



# PACIFIC EARTHQUAKE ENGINEERING RESEARCH CENTER

## **Seismic Demands for Performance-Based Design of Bridges**

**Kevin Mackie**

University of California, Berkeley

**and**

**Bozidar Stojadinovic**

University of California, Berkeley

# **Seismic Demands for Performance-Based Design of Bridges**

**Kevin Mackie**

University of California, Berkeley

**Božidar Stojadinović**

University of California, Berkeley

PEER Report 2003/16  
Pacific Earthquake Engineering Research Center  
College of Engineering  
University of California Berkeley  
August 2003

## ABSTRACT

The Pacific Earthquake Engineering Research Center is developing a probabilistic performance-based earthquake engineering framework, one component of which is a seismic demand model. Probabilistic seismic demand analysis was used to compute values of bridge-specific engineering demand parameters (EDP), such as curvature ductility, given ground motion intensity measures (IM), such as peak ground acceleration. A representative relation between chosen IM-EDP pairs forms the basis of the probabilistic seismic demand models (PSDM) presented.

The objective of this report was the development of an optimal PSDM for typical highway overpass bridges. An optimal model is defined as one that is practical, sufficient, effective, and efficient. For single-bent bridges with roller abutments, the optimal model comprises a spectral IM, such as  $Sa(T_1)$  and one of several EDPs. Different EDPs are considered for local (material stress), intermediate (column moment), and global (drift ratio) response quantities. Given the optimal PSDMs, bridge design parameter (such as column diameter) sensitivity studies were performed. Relations for each design parameter can be developed, giving bridge designers a quantitative tool for evaluating the effect of design choices on structural performance. The same PSDMs were then re-computed using incremental dynamic analysis (IDA) to assess the equivalency of response produced using the two analysis methods. Selection of an optimal PSDM was then extended to the case of multiple-bent bridges and bridges with different abutment models.

## **ACKNOWLEDGMENTS**

This work was supported in part by the Pacific Earthquake Engineering Research Center through the Earthquake Engineering Research Centers Program of the National Science Foundation under award number EEC-9701568.

The opinions presented in this report are solely those of the authors and do not necessarily represent the views of the sponsors.

The authors would also like to acknowledge the help of undergraduate student Heinz Kuo in the development of numerous instrumental procedures and computer software for the project. Further help was provided by Ryan Vignes under the PEER Center Summer Internship Program. The authors are also grateful to Professor C. Allin Cornell and a group of his graduate students at Stanford University for enlightening discussions about PSDMs.

# CONTENTS

<b>ABSTRACT .....</b>	<b>iii</b>
<b>ACKNOWLEDGMENTS .....</b>	<b>iv</b>
<b>TABLE OF CONTENTS .....</b>	<b>v</b>
<b>LIST OF FIGURES .....</b>	<b>vii</b>
<b>LIST OF TABLES .....</b>	<b>xi</b>
<b>1 INTRODUCTION .....</b>	<b>1</b>
<b>2 PROBABILISTIC SEISMIC DEMAND MODEL.....</b>	<b>7</b>
2.1 PSDA Ground Motions.....	8
2.2 PSDA Class of Structures .....	13
2.3 Design Parameters .....	15
2.4 PSDA Model .....	18
2.4.1 Column .....	18
2.4.2 Deck .....	22
2.4.3 Abutments.....	25
2.4.4 Pile Shafts .....	30
2.4.5 Loading.....	35
2.5 PSDA Analysis.....	35
2.5.1 Static Analysis .....	35
2.5.2 Modal Analysis .....	38
2.5.3 Dynamic Analysis .....	39
2.6 PSDA Intensity Measures and Engineering Demand Parameters.....	44
<b>3 OPTIMAL MODELS .....</b>	<b>49</b>
3.1 Sample Optimal PSDMs .....	51
3.1.1 Local Engineering Demand Parameters.....	52
3.1.2 Intermediate Engineering Demand Parameters .....	54
3.1.3 Global Engineering Demand Parameters .....	55
3.2 Verifying Optimal Model.....	56
3.3 Evaluation of Non-Optimal IM-EDP pairs .....	60
3.3.1 Poor Intensity Measures .....	60
3.3.2 Poor Engineering Demand Parameters .....	62
3.4 Vector Intensity Measures .....	63
<b>4 DESIGN PARAMETER SENSITIVITY .....</b>	<b>65</b>
4.1 Design Parameter Sensitivity: MODEL without Abutments .....	65
4.1.1 Design Trends .....	71
4.2 Design Parameter Sensitivity: MODEL with Abutments .....	72
4.3 Sensitivity to Period in Spectral Displacement .....	76
4.4 Sensitivity to Period in Arias Intensity .....	79
4.5 IM Robustness across Design Parameters .....	81
4.6 Abutment Model Sensitivity .....	83
4.6.1 Longitudinal Stiffness .....	84
4.6.2 Transverse Stiffness .....	85
4.6.3 Participating Mass.....	85

<b>5</b>	<b>INCREMENTAL DYNAMIC ANALYSIS.....</b>	<b>89</b>
5.1	Evolution of Median Value and Dispersion.....	93
5.2	Ground Motion Dependence .....	94
5.3	Verification of PSDA.....	95
<b>6</b>	<b>MULTIPLE-SPAN, MULTIPLE-BENT BRIDGES.....</b>	<b>99</b>
6.1	Multiple-Span Bridge Models .....	99
6.2	Transverse Irregularity.....	103
6.3	Sample Design Parameter Sensitivity.....	104
<b>7</b>	<b>CONCLUSIONS.....</b>	<b>107</b>
7.1	Optimal PSDMs.....	108
7.2	Structural demand hazard curves.....	109
7.3	Limitations .....	111
7.4	The Future .....	112
	<b>REFERENCES .....</b>	<b>115</b>
	<b>APPENDIX A NOTATION.....</b>	<b>123</b>
	<b>APPENDIX B GROUND MOTION RECORDS .....</b>	<b>127</b>
	<b>APPENDIX C ANALYSIS PROCEDURE DETAILS.....</b>	<b>133</b>
Appendix C.1	OpenSees .....	133
Appendix C.2	Pre-Processing.....	134
Appendix C.3	Analysis Description .....	137
Appendix C.3.1	Static Analysis.....	137
Appendix C.3.2	Modal and Dynamic Analysis .....	140
Appendix C.4	Post-Processing .....	145
Appendix C.4.1	IMCDM .....	145
Appendix C.4.2	IM.....	145
Appendix C.4.3	SPECTRAL.....	146
	<b>APPENDIX D VISUALIZATION .....</b>	<b>147</b>
Appendix D.1	Data Visualization.....	147
Appendix D.2	Model Visualization .....	153

## LIST OF FIGURES

Fig. 1.1	PEER performance-based engineering framework .....	3
Fig. 1.2	Probabilistic seismic demand model form.....	5
Fig. 2.1	Distribution of ground motion records in M-R space .....	10
Fig. 2.2	Spectra with original and resampled records (sampling period in legend) .....	11
Fig. 2.3	Spectral difference produced by down-sampling from 200->50 Hz.....	12
Fig. 2.4	Spectral difference produced by down-sampling from 100->50 Hz.....	13
Fig. 2.5	Bridge longitudinal and transverse configurations.....	14
Fig. 2.6	Longitudinal and transverse directions, including skew [Caltrans 1999] .....	15
Fig. 2.7	Single-bent bridge design parameters .....	16
Fig. 2.8	Typical column cross section modeled in UCFyber .....	19
Fig. 2.9	Confined and unconfined concrete constitutive relationships .....	20
Fig. 2.10	Reinforcing steel constitutive relationships .....	20
Fig. 2.11	Deck and column dimensions .....	21
Fig. 2.12	Box girder modeled in UCFyber.....	23
Fig. 2.13	NL deck transverse SPO.....	24
Fig. 2.14	NL deck longitudinal SPO.....	24
Fig. 2.15	NL deck transverse SPO (M- $\phi$ ).....	24
Fig. 2.16	NL deck longitudinal SPO (M- $\phi$ ).....	24
Fig. 2.17	Bilinear and trilinear abutment force-deformation relationships .....	27
Fig. 2.18	Type I pile shafts [Caltrans 1999] .....	31
Fig. 2.19	Location of plastic hinges over length of column and pile shaft .....	32
Fig. 2.20	Sampled closed-form and idealized <i>P</i> - <i>y</i> force-displacement relationships .....	33
Fig. 2.21	Force-displacement pushover .....	36
Fig. 2.22	Moment-curvature pushover.....	36
Fig. 2.23	Determination of yield displacement from static pushover curve .....	37
Fig. 2.24	Single-bent 1 <sup>st</sup> mode transverse .....	38
Fig. 2.25	Single-bent 2 <sup>nd</sup> mode longitudinal.....	38
Fig. 2.26	Displacement time history .....	39
Fig. 2.27	Column orbital displacements.....	39
Fig. 2.28	Sample moment-curvature plot.....	40
Fig. 2.29	Sample moment-rotation plot .....	40
Fig. 2.30	Comparison of time histories for different abutment cases .....	41
Fig. 2.31	Extreme steel fiber stress and strain time history.....	42
Fig. 2.32	Abutment gap closure time history .....	43
Fig. 3.1	$Sd_{TI}$ - $\sigma_{steel}$ , $\rho_s$ sensitivity longitudinal.....	52
Fig. 3.2	$Sa_{TI}$ - $\sigma_{steel}$ , $D_c/D_s$ sensitivity longitudinal.....	52
Fig. 3.3	$Sd_{TI}$ - $\sigma_{steel}$ , $f_y$ sensitivity .....	53
Fig. 3.4	$Sd_{TI}$ - $\sigma_{concrete}$ , $f'_c$ sensitivity .....	53
Fig. 3.5	$Sd_{TI}$ - $M_{max}$ , $D_c/D_s$ sensitivity longitudinal .....	54
Fig. 3.6	$Sd_{TI}$ - $M_{max}$ , $D_c/D_s$ sensitivity transverse .....	54
Fig. 3.7	$Sa_{TI}$ - $\mu_\phi$ , $D_c/D_s$ sensitivity longitudinal .....	55
Fig. 3.8	$Sa_{TI}$ - $\Delta$ , $D_c/D_s$ sensitivity longitudinal.....	55
Fig. 3.9	$Sa_{TI}$ - $\Delta$ , $D_c/D_s$ , $\mu \pm 1\sigma$ stripes .....	56

Fig. 3.10	$Sa_{T1-\Delta}$ , $D_c/D_s$ , M dependence .....	56
Fig. 3.11	$Sa_{T1-\Delta}$ , $D_c/D_s$ , R dependence .....	58
Fig. 3.12	$Sa_{T1-\Delta}$ , $D_c/D_s$ , bin dependence .....	58
Fig. 3.13	$Sa_{T1-\Delta}$ , $D_c/D_s$ , seismicity .....	58
Fig. 3.14	Arias- $\Delta$ , $D_c/D_s$ , seismicity.....	58
Fig. 3.15	PGA- $\Delta$ , $D_c/D_s$ sensitivity longitudinal. ....	60
Fig. 3.16	FR1- $\Delta$ , $D_c/D_s$ sensitivity longitudinal.....	60
Fig. 3.17	$I_c-\Delta$ , $D_c/D_s$ sensitivity longitudinal.....	61
Fig. 3.18	$A_{rms}-\Delta$ , $D_c/D_s$ sensitivity longitudinal.....	61
Fig. 3.19	$Sa_{T1-RDI}$ , $D_c/D_s$ sensitivity longitudinal .....	62
Fig. 3.20	$Sa_{T1-NHE}$ , $D_c/D_s$ sensitivity longitudinal.....	62
Fig. 3.21	Sd vector (3D), L/H longitudinal .....	64
Fig. 3.22	Sd vector (2D), L/H longitudinal .....	64
Fig. 4.1	L sensitivity, $Sd_{T1-\mu\Delta}$ .....	67
Fig. 4.2	L sensitivity, $Sa_{T1}-M_{max}$ .....	67
Fig. 4.3	L/H sensitivity, $Sa_{Cordova}-\Delta$ .....	68
Fig. 4.4	L/H sensitivity, $Sd_{T1}-\sigma_{steel}$ .....	68
Fig. 4.5	$D_c/D_s$ sensitivity, $Sd_{T1}-\Delta$ .....	69
Fig. 4.6	$D_c/D_s$ sensitivity, Arias- $\mu\Delta$ .....	69
Fig. 4.7	$\rho_s$ sensitivity, $Sa_{Cordova}-\mu\Delta$ .....	69
Fig. 4.8	$\rho_s$ sensitivity, $Sd_{T1}-M_{max}$ .....	69
Fig. 4.9	$Wt$ sensitivity, $Sa_{T1}-M_{max}$ .....	70
Fig. 4.10	$K_{soil}$ sensitivity, $Sa_{T1}-M_{max}$ .....	70
Fig. 4.11	$f_y$ sensitivity, $Sa_{T1}-\mu\Delta$ .....	70
Fig. 4.12	$f'_c$ sensitivity, $Sd_{T1}-\mu\Delta$ .....	70
Fig. 4.13	L sensitivity, $Sd_{T1}-\mu\Delta$ .....	73
Fig. 4.14	L sensitivity, $Sa_{T1}-M_{max}$ .....	73
Fig. 4.15	L/H sensitivity, $Sa_{Cordova}-\Delta$ .....	73
Fig. 4.16	L/H sensitivity, $Sd_{T1}-\sigma_{steel}$ .....	73
Fig. 4.17	$D_c/D_s$ sensitivity, $Sd_{T1}-\Delta$ .....	74
Fig. 4.18	$D_c/D_s$ sensitivity, Arias- $\mu\Delta$ .....	74
Fig. 4.19	$\rho_s$ sensitivity, $Sa_{Cordova}-\mu\Delta$ .....	75
Fig. 4.20	$\rho_s$ sensitivity, $Sd_{T1}-M_{max}$ .....	75
Fig. 4.21	skew sensitivity, Arias- $\Delta$ longitudinal.....	75
Fig. 4.22	skew sensitivity, Arias- $\Delta$ transverse.....	75
Fig. 4.23	$D_c/D_s$ sensitivity, $Sd_{T1}-M_{max}$ .....	76
Fig. 4.24	$D_c/D_s$ sensitivity, $Sd_{T1}-M_{max}$ .....	76
Fig. 4.25	$D_c/D_s$ sensitivity, $Sd_{T2}-M_{max}$ .....	78
Fig. 4.26	$D_c/D_s$ sensitivity, $Sd_{T2}-M_{max}$ .....	78
Fig. 4.27	T sensitivity, $Sd_{T1}-M_{max}$ .....	79
Fig. 4.28	T sensitivity, $Sd_{T1}-M_{max}$ .....	79
Fig. 4.29	T sensitivity, $I_A-M_{max}$ .....	80
Fig. 4.30	T sensitivity, $I_A-M_{max}$ .....	80
Fig. 4.31	Robustness across design parameters L/H, $D_c/D_s$ , L, and $Wt$ .....	82
Fig. 4.32	Comparison of robustness for different IMs.....	83

Fig. 4.33	$Ka_l$ (6") sensitivity, $CAD-\Delta$ .....	84
Fig. 4.34	$Ka_l$ (2") sensitivity, Arias- $\Delta$ .....	84
Fig. 4.35	$Ka_l$ sensitivity, $PGV-\Delta$ .....	86
Fig. 4.36	Mass sensitivity, $CAD-\mu_\Delta$ .....	86
Fig. 4.37	Abut sensitivity, $PGV-\Delta$ .....	86
Fig. 4.38	Abut sensitivity, Arias- $M_{max}$ .....	86
Fig. 5.1	PSDA $Sa_{TI}-\Delta$ , $D_c/D_s$ 4i.....	91
Fig. 5.2	IDA $Sa_{TI}-\Delta$ , $D_c/D_s$ 4i.....	91
Fig. 5.3	IDA/PSDA, $D_c/D_s$ ( $\Delta$ ) 4i.....	92
Fig. 5.4	IDA/PSDA, $D_c/D_s$ ( $\phi_{max}$ ) 4i.....	92
Fig. 5.5	IDA/PSDA, $D_c/D_s$ 4i $1\sigma$ stripes.....	93
Fig. 5.6	IDA/PSDA, $D_c/D_s$ ( $\Delta$ ) 3i.....	93
Fig. 5.7	IDA/PSDA, $D_c/D_s$ ( $\Delta$ ) 4j.....	95
Fig. 5.8	IDA/PSDA, $D_c/D_s$ ( $\Delta$ ) 8ij.....	95
Fig. 5.9	PSDA comparison, median.....	96
Fig. 5.10	IDA/PSDA, $D_c/D_s$ $1\sigma$ stripes.....	96
Fig. 6.1	Two-bent bridge design parameters.....	100
Fig. 6.2	Three-bent, 1 <sup>st</sup> mode (transverse).....	102
Fig. 6.3	Two-bent, 2 <sup>nd</sup> mode (longitudinal).....	102
Fig. 6.4	Multiple-bent, $Sa_{TI}-\Delta$ longitudinal.....	103
Fig. 6.5	Multiple-bent, $Sa_{TI}-M_{max}$ longitudinal.....	103
Fig. 6.6	Multiple-bent, Arias- $\Delta$ longitudinal.....	103
Fig. 6.7	Multiple-bent, $Sa_{TI}-\Delta$ transverse.....	103
Fig. 6.8	Three-bent irregular (transverse).....	104
Fig. 6.9	Effect of irregularity on efficiency.....	104
Fig. 6.10	$L_2$ sensitivity, $PGV-u_{max}$ longitudinal.....	105
Fig. 6.11	$R$ residual dep, $PGV-u_{max}$ longitudinal.....	105
Fig. 7.1	Structural demand hazard curve for $Sa_{TI}-\Delta$ PSDM.....	110
Fig. Appendix C.1	Sample finite element bridge model.....	134
Fig. Appendix D.1	Initial screen from <i>Demand.m</i> for running all PSDMs.....	147
Fig. Appendix D.2	PSDM plotting window.....	151
Fig. Appendix D.3	Initial screen from <i>Showbridge.m</i> for model visualization.....	155

## LIST OF TABLES

Table 2.1	Parameter variation ranges for a two-span overpass bridge .....	17
Table 2.2	Deck elastic properties.....	22
Table 2.3	Abutment stiffness and mass participation values .....	30
Table 2.4	Apparent abutment stiffness values.....	30
Table 2.5	Assumed soil properties for $K_{soil}$ groups .....	34
Table 2.6	Intensity measures .....	44
Table 2.7	Engineering demand parameters.....	46
Table 4.1	Bridge first and second mode periods for sample bridge configurations .....	66
Table 4.2	Bridge periods for $D_v/D_s$ sensitivity, longitudinal mode in italics .....	77
Table 4.3	Dispersion values for $S_d$ - $M_{max}$ , optimal in italics.....	78
Table 5.1	Ground motions used for IDA .....	91
Table 5.2	Dispersions of PSDA and IDA runs ( $S_{aT1}$ vs. $D$ ) .....	94
Table 5.3	PSDA comparison using different sets of ground motion bins.....	96
Table 6.1	Parametric variation ranges for a two-bent overpass bridge.....	101
Table 6.2	Parametric variation ranges for a three-bent overpass bridge.....	101
Table Appendix B.1	LMSR (large magnitude small distance).....	128
Table Appendix B.2	LMLR (large magnitude large distance) .....	129
Table Appendix B.3	SMSR (small magnitude small distance) .....	130
Table Appendix B.4	SMLR (small magnitude large distance).....	131
Table Appendix B.5	Near (large magnitude near-field effects).....	132

# 1 Introduction

Performance-based earthquake engineering (PBEE) describes a quantitative means for designers of structures to achieve predetermined performance levels or objectives in a specific hazard environment. Recent efforts have been aimed at moving away from traditional single limit state, deterministic, design techniques. Multiple performance objectives, each comprising a performance level at a seismic hazard level, require a significantly more complex design framework. SEAOC's Vision 2000 [SEAOC 1995] and the subsequent *Recommended Lateral Force Requirements* [SEAOC 1996] allowed for four performance objectives for each hazard intensity category. This uncoupled approach lacked rigorous acceptance criteria for each performance level, and was a deterministic solution to a probabilistic seismic input.

The Federal Emergency Management Agency (FEMA) and National Earthquake Hazards Reduction Program (NEHRP) advanced PBEE in practice with FEMA-273 [FEMA 1996] for the rehabilitation of existing buildings and FEMA-302 [FEMA 1997] for new buildings. These design frameworks addressed only the probabilistic evaluation of location-specific seismic hazards. The graduated arrays of performance levels are based on deterministic estimates of structural performance. Not only this, but performance was evaluated only at discrete intervals rather than over a performance continuum. These deficiencies have been confronted recently in the SAC Steel Project FEMA-350 document [FEMA 2000b] for new steel moment-resisting frame buildings and FEMA-356 [FEMA 2000a] for rehabilitation of buildings. One of the SAC project achievements was a design framework that provided a means for considering uncertainty and randomness simultaneously in both the demand and capacity. These uncertainties were addressed in a probabilistic manner, allowing specification of a level of confidence that a structure will achieve a given performance objective.

In the thrust to achieve a consistent reliability-based framework that is more general than that of the SAC project, the Pacific Earthquake Engineering Research Center (PEER) is developing a probabilistic framework for performance-based design and evaluation. The goal is to allow for fully probabilistic evaluation of the PBEE problem, decoupled into smaller and more easily definable portions. Performance objectives are defined in terms of annual probabilities of socio-economic decision variables ( $DV$ ) being exceeded in a seismic hazard environment of the urban region and site under consideration. While useful to owners and designers, a general probabilistic model directly relating decision variables to measures describing the site seismicity is too complex. Instead, the PEER performance-based design framework utilizes the total probability theorem to de-aggregate the problem into several interim probabilistic models that address sources of randomness and uncertainty more rigorously. This de-aggregation involves global or component damage measures ( $DM > z$ ), structural engineering demand parameters ( $EDP > y$ ), and seismic hazard intensity measures ( $IM > x$ ). Thus, the mean annual frequency (MAF) of a  $DV$  exceeding limit value  $w$  is [Cornell 2000]:

$$v_{DV}(w) = \int_z \int_y \int_x G_{DV|DM}(w | z) dG_{DM|EDP}(z | y) dG_{EDP|IM}(y | x) d\lambda_{IM}(x) dx dy dz \quad (1.1)$$

The interim probabilistic models are:

- $G_{DV|DM}(w | z)$  is a loss or performance model, predicting the probability of exceeding the value of a decision variable  $w$  (such as repair cost or down time), given a value of a Damage Measure (DM)  $z$ ;
- $G_{DM|EDP}(z | y)$  is a capacity model, predicting the probability of exceeding the value of a damage measure  $z$  (such as amount of spalling or crack density), given a value of a Demand Measure (EDP)  $y$ ;
- $G_{EDP|IM}(y | x)$  is a demand model, predicting the probability of exceeding the value of an engineering demand measure  $y$  (such as inter-story drift ratio or steel rebar strain), given a value of a seismic hazard intensity measure (IM)  $x$ ;
- $\lambda_{IM}(x)$  is a seismic hazard model, predicting the annual probability of exceeding the value of a seismic hazard intensity measure  $x$  (such as peak ground acceleration) in a given seismic hazard environment.

The de-aggregation of Equation 1.1 is possible only when the components are mutually independent, and if the capacity and demand models are independent of the seismic hazard environment. The intermediate variables (*DM*, *EDP*, *IM*) are chosen such that probability conditioning is not carried over from one model to the next. Additionally, the uncertainties over the full range of model variables need to be systematically addressed and propagated, making the selection of each interim model critical to the process. Nevertheless, these independent models can be designed separately and used interchangeably, making it easier to develop a general performance-based framework for seismic design and evaluation.

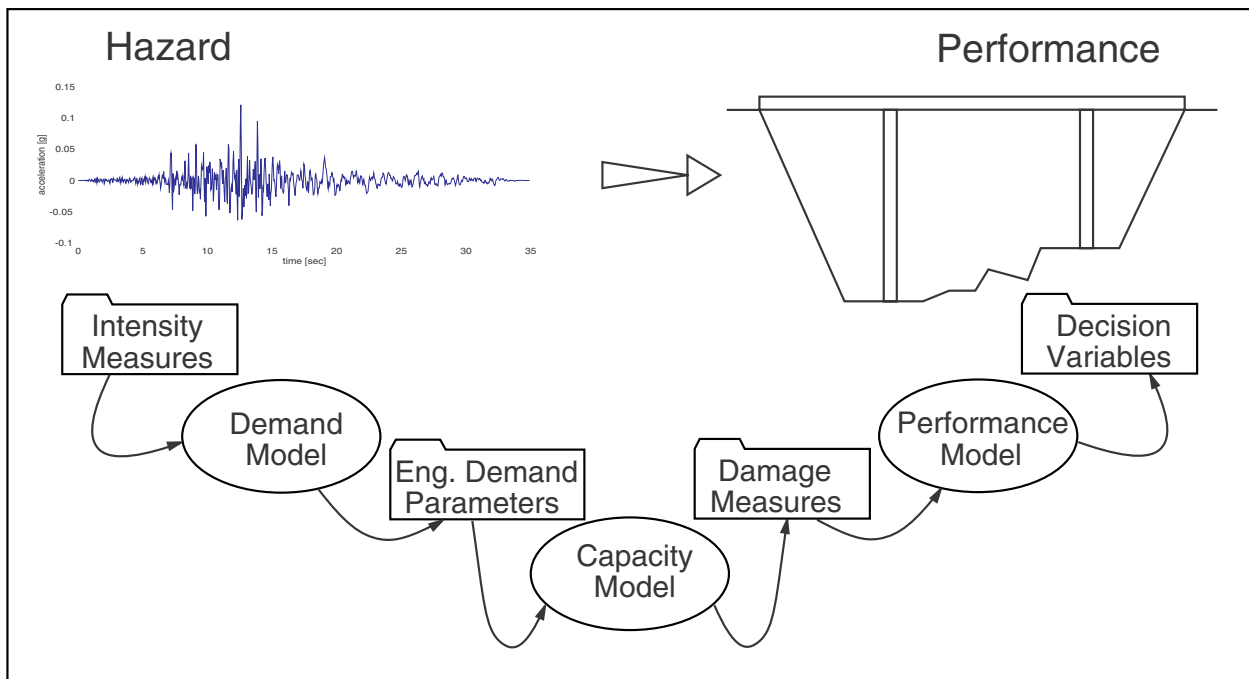


**Fig. 1.1 PEER performance-based engineering framework**

The hazard and performance de-aggregation process described above is depicted in Figure 1.1 for the case of a highway overpass bridge. First, seismic hazards, evaluated using a regional hazard model, are expressed using intensity measures. A demand model, built for this class of bridges, is then used to correlate hazard intensity measures to structural engineering demand parameters for this bridge. Next, a capacity model is used to relate structural engineering demand parameters to damage measures. Finally, damage measures are used to affect the loss in performance, evaluated in terms of decision variables. Decision variables

describe the performance of a typical overpass bridge after an earthquake in terms of its function in a traffic network in an urban region such as the San Francisco Bay Area. This includes reduction in lane load capacity and assessment of speed limits and traffic capacity, or duration of bridge closure and cost of bridge repair. The results of a performance-based evaluation of an overpass bridge in the San Francisco Bay Area would be mean annual probabilities of exceeding set values of a chosen suite of decision variables such as those mentioned above.

This report addresses one component of the de-aggregated performance-based design framework, the interim demand model, or the relation between structural demand and earthquake intensity. Other PEER researchers are addressing the other interim models. Probabilistic demand analysis is done in order to estimate the mean annual frequency ( $\nu$ ) of exceeding a given structural engineering demand measure ( $EDP > y$ ) in a postulated hazard environment ( $IM = x$ ), as detailed in Equation 1.2.

$$\nu_{EDP}(y) = \int_x G_{EDP|IM}(y|x) |d\lambda_{IM}(x)| dx \quad (1.2)$$

The result of probabilistic seismic demand analysis (PSDA) is shown in Figure 1.2. The data points represent individual outcomes of PSDA. They show the value of the EDP for a structure subjected to a ground motion characterized by a value of IM. Assuming a log-normal probability distribution of these outcomes, a straight line can be fit through the cloud of points. Parameters of this line define the PSDM, together with a measure of dispersion ( $\sigma$ ) of the actual data with respect to the least-squares fit line.

A probabilistic seismic demand model (PSDM) for typical California highway bridges is presented in this report. A PSDM relates EDPs to IMs in the probabilistic framework of Equation 1.1. The fundamentals of developing a PSDM, such as the choice of ground motions and their intensity measures, the choice of bridge design parameters and structural engineering demand parameters, and the analysis procedure (probabilistic seismic demand analysis) used to generate them are presented first. Sample PSDMs for a two-span single-bent highway overpass are derived and explored next. The single-bent overpass bridge was used to evaluate several properties of PSDMs. First, an optimal PSDM was developed to limit the number of IM-EDP pairs considered. Second, optimal PSDMs were used to assess their sensitivities to highway overpass bridge design parameters. Third, the method used to generate the PSDMs (probabilistic

seismic demand analysis) was compared against a different analysis method (Incremental Dynamic Analysis) for equivalency of results. Finally, these PSDMs were recomputed for multiple-bent highway overpass bridges. A discussion of how to incorporate PSDMs into PEER's performance-based seismic design framework, and their applicability to fragility estimates for highway network simulations concludes this report.

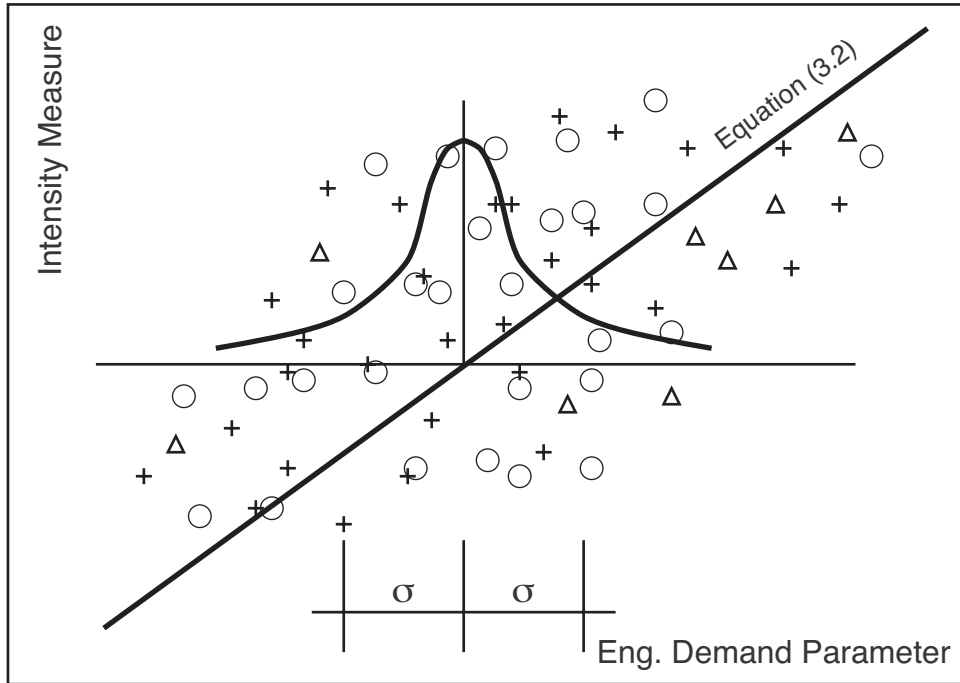


**Fig. 1.2 Probabilistic seismic demand model form**

Detailed information regarding the ground motion records used in this study and the bins into which they were grouped are included in Appendix B. The analysis tools used to generate the models and resulting data for this study are detailed further in Appendix C. All of the PSDM database plots in this study, and several of the figures of bridge models were generated with Matlab tools developed specifically for this project. Details on output from, and usage of, these tools are included in Appendix D.

Results from the PSDM investigations show that optimal models are generated when coupling spectral IMs (spectral acceleration for example) with an EDP in a range of scopes. The EDP is drift ratio at the global level, maximum column moment at the intermediate level, and

maximum steel stress at the local level. These choices of IM-EDP pairs are not dependent on the type of bridge considered (single-bent, multiple-bent, abutment included, abutment excluded, etc.), the variation of design parameters within each of these bridge choices, or the analysis method chosen to obtain the PSDM data. Therefore, the optimal PSDM becomes a very powerful tool in performance-based seismic design and evaluation of bridges.

## 2 Probabilistic Seismic Demand Model

In current practice, probabilistic seismic evaluation is routinely done as a part of performance-based design of important and expensive structures such as the new Oakland-San Francisco (“East Bay”) Bridge. In such projects, a complex nonlinear model of the structure is typically subjected to a large number of real and artificial ground motions to estimate the required probabilities of exceeding predetermined values of project-specific decision variables. Such computationally intensive approaches are applicable to unique structures only, and cannot be used in routine performance-based design. A de-aggregated performance-based design framework (Eq. 1.1) is a practical alternative for such non-unique structures. One reason for extensibility in this framework is that PSDA applies to an entire urban region, rather than to a unique location. Second, it applies to an array of possible decision variables, rather than a single one. And finally it applies to a class of structures, rather than to a unique structure. Resulting PSDMs are therefore quite general.

The probabilistic seismic demand model (PSDM) formulated herein is the outcome from probabilistic seismic demand analysis (PSDA). PSDA has previously been used [Shome 1998] to couple probabilistic seismic hazard analysis (PSHA) with demand predictions from nonlinear finite element analysis. This is done in order to estimate the mean annual frequency of exceeding a given demand, and results in a structural demand hazard curve [Luco 2001a] in a conjectured hazard environment. Such integration was not explicitly performed herein; rather, the demand model is emphasized. Extension to structural demand hazard curves is addressed at the end of the report.

The procedure used to formulate the PSDMs of interest involves five steps. First, a set of ground motions, representative of regional seismic hazard, is selected or synthesized. Instrumental in selecting these motions is categorizing them according to computable intensity

measures descriptive of their content and intensity. Second, the class of structures to be investigated is defined. Associated with this class are a suite of engineering demand parameters which can be measured during analysis to assess structural performance under the considered motions. Third, a nonlinear finite element analysis model is generated to model the class of structures selected, with provisions to vary designs of the class through the use of design parameters. Thus, a portfolio of structures is generated by different realizations of the design parameters. Fourth, nonlinear dynamic analyses are performed until all motions and structural model combinations have been exhausted. Fifth, a demand model is formulated between resulting ground motion intensity measures and structural engineering demand parameters.

## 2.1 PSDA GROUND MOTIONS

The PSDA method used herein to formulate the PSDMs involves the ground motion bin approach only. It would also be possible to perform the analysis using a standard Monte Carlo simulation [e.g., Foutch 1992] involving thousands of ground motions, or by generation of synthetic ground motions. Synthetic motions are site specific and include both expected acceleration time histories or motions generated based on design spectra. The bin approach, proposed and used by Shome and Cornell [Shome 1999], was used to subdivide ground motions into imaginary bins based on magnitude ( $M_w$ ), closest distance ( $R$ ), and local soil type. The use of magnitude and distance allows parallels between standard attenuation relationships and existing PSHA.

Advantages of the bin approach include the ability to assess the effect of generalized earthquake characteristics, such as frequency domain content or duration, on structural demands. For example, bins differentiate between near- and far-field earthquake types, rather than between individual near- and far-field records. Ground motion intensity can also be abstracted by scaling the earthquakes in a bin to the same level of intensity, such as spectral acceleration at the fundamental period of a structure. Second, the use of bins is substantial in limiting the number of ground motions selected for analysis. Shome and Cornell [Shome 98] show that, assuming a log-normal probability distribution of structural engineering demand parameters, the number of ground motions sufficient to yield response quantity statistics that have a required level of confidence is proportional to the square of a measure of dispersion in the demand model. They

also show [Shome 99] that the bin approach, and scaling motions within bins, by itself does not introduce bias into the relation between EDPs and ground motion IMs.

Four bins with 20 ground motions each were obtained from the PEER Strong Motion Database [PEER Strong Motion Catalog]. These motions are characteristic of non-near-field motions ( $R > 15$  km) recorded in California. The delineation between small (SM) and large (LM) magnitude bins was at  $M_w = 6.5$ . Ground motions with closest distance  $R$  ranging between 15 and 30 km were grouped into a small distance (SR) bin, while ground motions with  $R > 30$  km were in the large distance (LR) bin. All ground motions were recorded on NEHRP soil type D sites. The specific records selected were similar to those used by Krawinkler [Gupta 2000, Medina 2001] in a companion PEER research project related to building structures. The ground motions in the bins used by Krawinkler were chosen such that the median spectral shapes (and dispersions) of all bins were roughly equal when scaled to a common spectral value.

Several of the records used by Krawinkler had only horizontal ground motion accelerograms in the PEER database [PEER Strong Motion Catalog]. These records were then removed and replaced with an earthquake record from the PEER database with similar magnitude, distance, and PGA characteristics, but containing all three orthogonal component accelerograms. This allows for a fully three-dimensional analysis without the generation of artificial or rotated records. The distribution of motions selected within the four bins (in  $M_w$  and  $R$  space) is shown in Figure 2.1. Details of all the ground motion records used, including earthquake names, sensor location, magnitude, distance, soil type, faulting mechanism, and peak waveform ordinates are provided in Appendix B. This information was extracted from the ground motion record header or obtained from the PEER database and saved for later usage as possible IM candidates.

A fifth bin was added later, also containing 20 ground motions. This bin comprises ground motions from Luco's [Luco 2001b] nearby-field bin. These are high-magnitude earthquakes measured at a distance ( $R$ ) of less than 15 km. Structural response to earthquakes in this bin would then be expected to exhibit some near-field effects such as directivity, fling, and pulse response. The choice of records on medium soil (NEHRP D) provides a conservative

approach to determining performance, as the level of ground shaking on firm, dense soil (NEHRP B, C) and rock sites (NEHRP A) for an equivalent earthquake is less likely amplified in the range of periods expected for fundamental bridge modes.

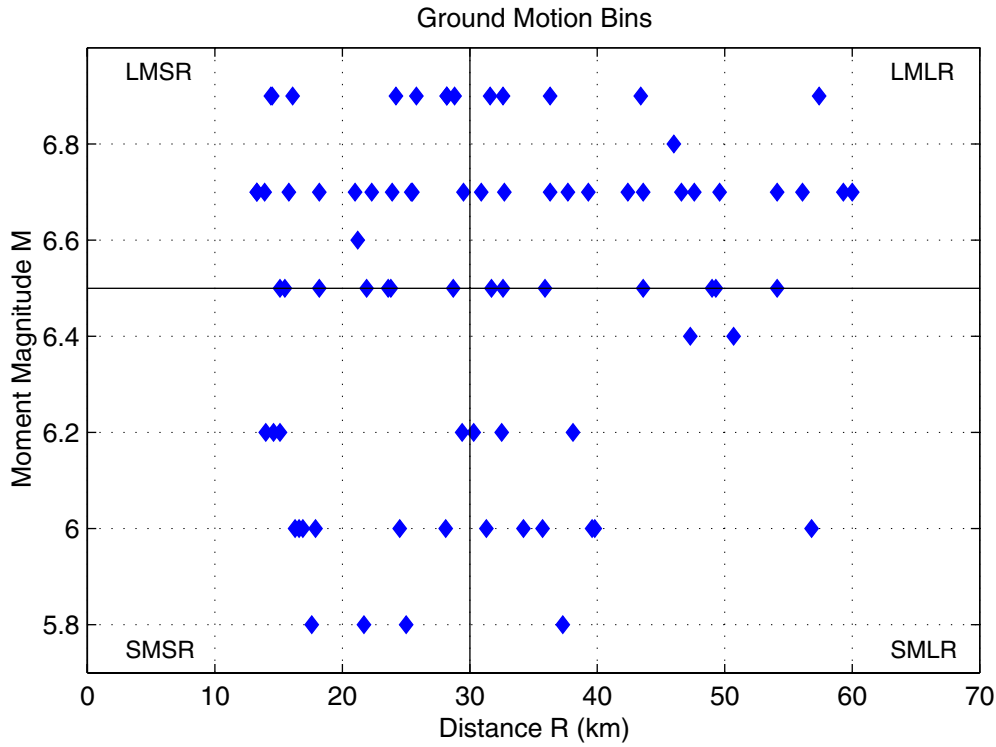


**Fig. 2.1 Distribution of ground motion records in M-R space**

The records used are not necessarily orthogonal in the two horizontal components. In this study, the bridge transverse direction was by default placed along the heading specified by the smaller degree designation of a record. This suggests the bridge span was oriented perpendicular to the fault, if strict directivity was being observed. For example, record CAP000.AT2 was assigned to the transverse direction (fault-parallel), CAP090.AT2 was assigned to the longitudinal direction (fault-normal), and CAP-UP.AT2 was assigned to the vertical direction. The intention was not to exactly capture fault-normal and fault-parallel effects like directivity but to utilize a large array of records to generate variation in bridge response.

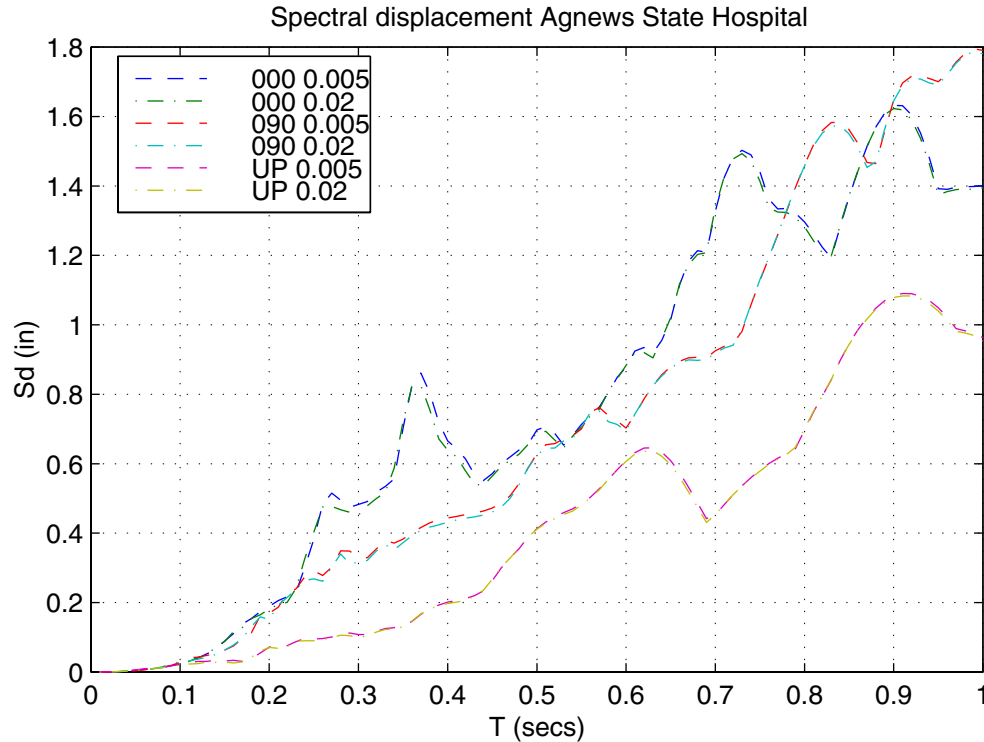


**Fig. 2.2 Spectra with original and resampled records (sampling period in legend)**

Each component of the earthquake records has been filtered to set all sampling frequencies to 50 Hz (0.02 sec). Some of the records have more sampling points, but because primary bridge modes of vibration occur at periods higher than 0.02 sec, little higher mode accuracy is lost in reducing all records to 0.02 sec sampling rate. A sample set of spectra generated using a SDF elastic oscillator from the Agnews State Hospital record (3 components) is shown in Figure 2.2, both original and resampled. Spectral differences between records which have been resampled with respect to the original records are shown in Figure 2.3 (original 200 Hz sampling frequency) and Figure 2.4 (original 100 Hz sampling frequency). An unconditionally stable integrator, the Newmark average acceleration method, was used for the small period values. As expected, large relative error occurs only at very low period (high frequency) values.

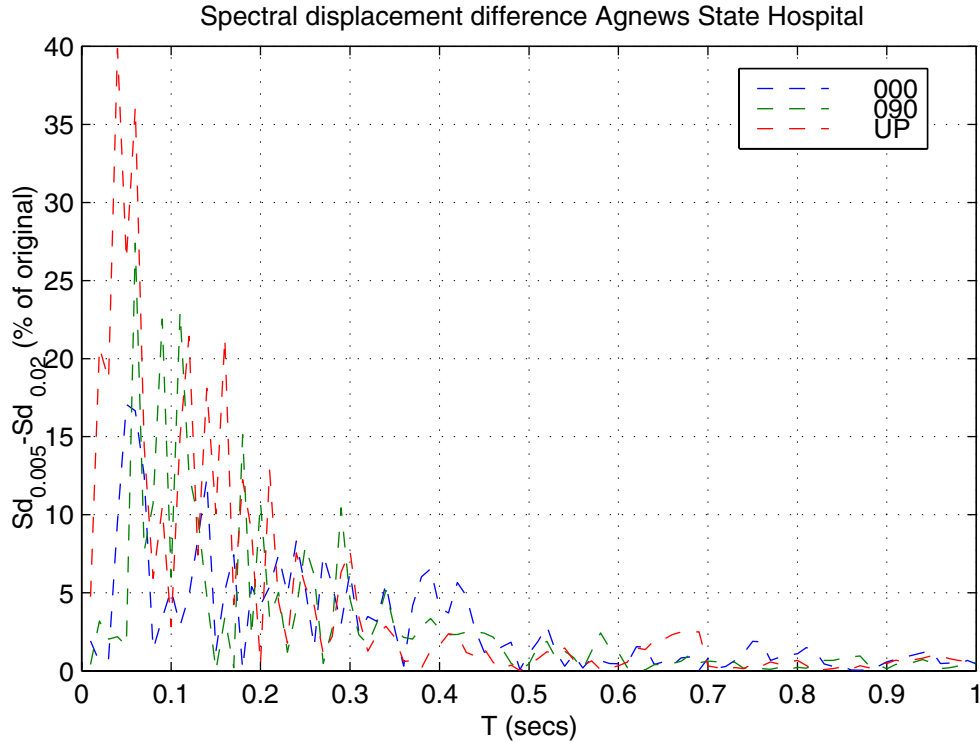


**Fig. 2.3 Spectral difference produced by down-sampling from 200->50 Hz**

The magnitude and frequency content of the records used was otherwise unaltered. Due to the absence of very high-magnitude California records, and in order to ensure nonlinear structural response, especially in the smaller intensity bins, the records were scaled by a factor of two. This scaling was achieved by a simple amplification of all the acceleration values during any of the probabilistic seismic demand model analyses. All processing of the records, except scaling, has been performed before the records were stored for analyses. Therefore, intensity measures independent of scaling were also calculated and stored in the record headers. This process is fully detailed in Section AIII.3. To allow for IDA support, intensity measures dependent on the scaled intensity were computed instantaneously during every analysis.

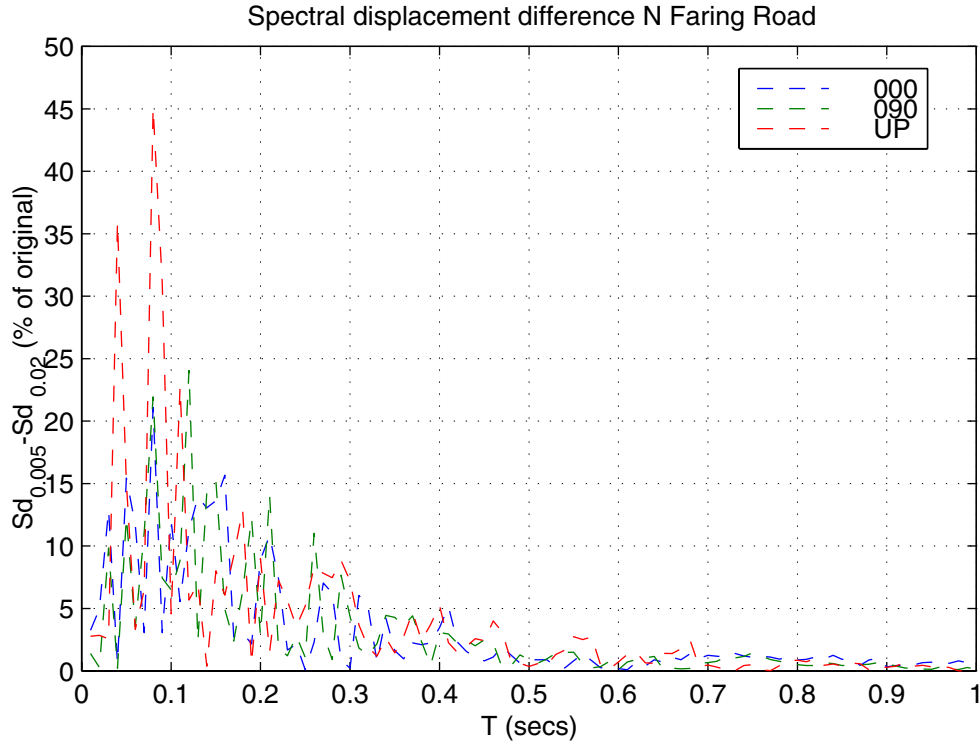


**Fig. 2.4 Spectral difference produced by down-sampling from 100->50 Hz**

## 2.2 PSDA CLASS OF STRUCTURES

In this study, typical new California highway overpass bridges were selected as the class of structures. A class is defined by geometry, components, and methods of design. Ideally, each of these can be investigated in a parameter sensitivity study using the resulting PSDMs. The bridges presented in this report were designed according to *Caltrans Bridge Design Specification and Seismic Design Criteria* [Caltrans 1999] for reinforced concrete bridges. These specifications were largely based on the guidelines set forth in ATC-32 [ATC 1996]. Consistent with the displacement-based design approach used by Caltrans for new bridges, it was assumed such that columns develop plastic hinges in flexure rather than experience shear failure.

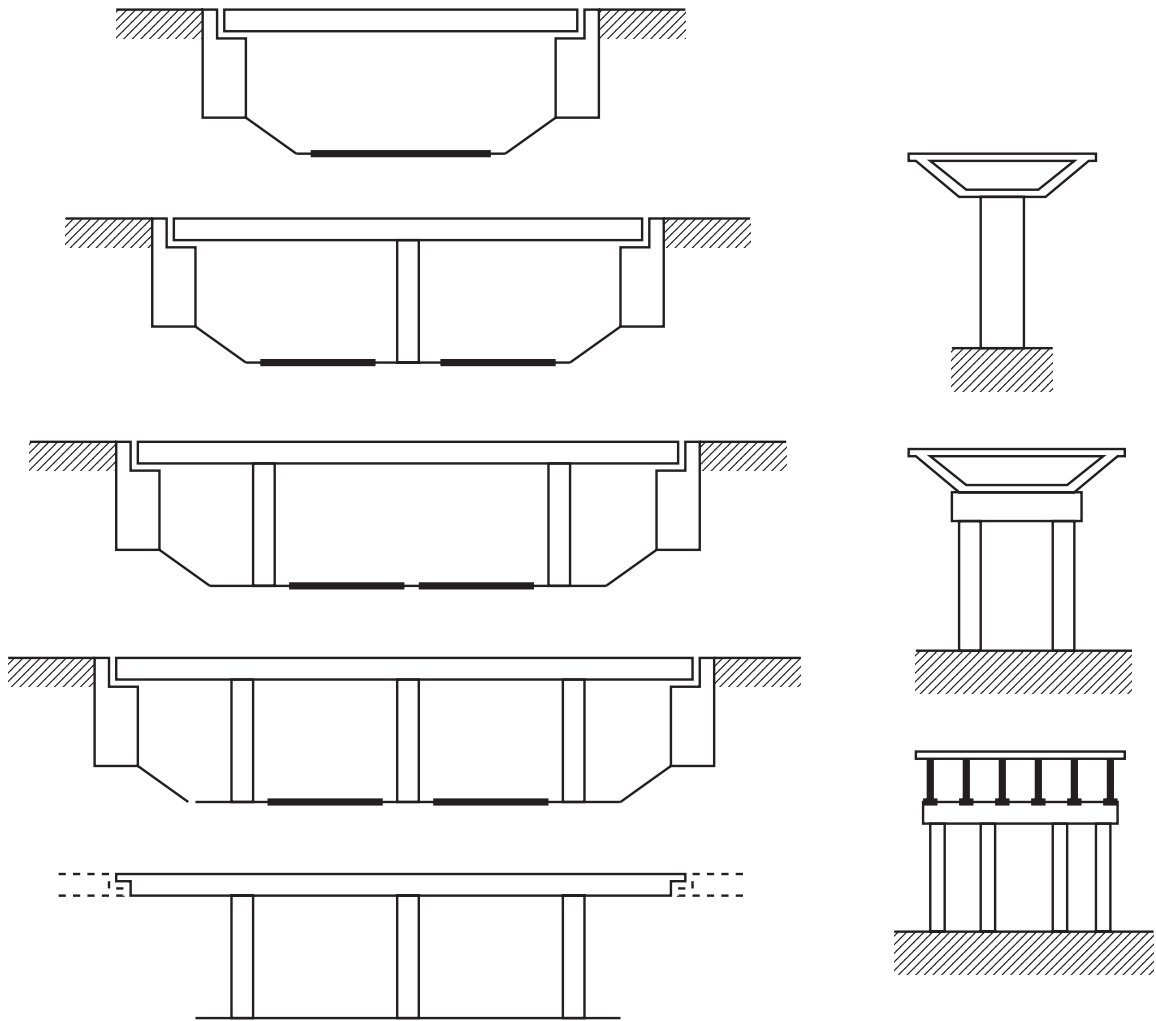


**Fig. 2.5 Bridge longitudinal and transverse configurations**

Longitudinal structural configurations for bridges in this class are shown in Figure 2.5. They are: single-span, two-span, and three-span overpasses (including abutments) and stand-alone components of multi-span viaducts divided at expansion joints. In the transverse direction, typical California overpasses have single-, two-column, or multi-column bents (Fig. 2.5). Only single-column bents (in the transverse direction) were considered for all of the bridges in this study. At abutments and expansion joints these bridges have varying degrees of restraint. Diagrammatical definitions of the longitudinal and transverse directions are shown for an arbitrary bridge in Figure 2.6. Common to all bridge types is a single-column bent with uniform circular cross section over the complete column height above grade, continuing into an integral Type I pile shaft foundation. All bridges are of reinforced concrete construction, including a continuous reinforced concrete box girder superstructure, as designed by Caltrans [Yashinsky

2000]. The portfolio of bridges considered in the beginning of this study was limited to single-column per bent, single-bent overpass highway bridges with two equal spans. The bridge class was extended to include bridges with more than one bent later in the study.

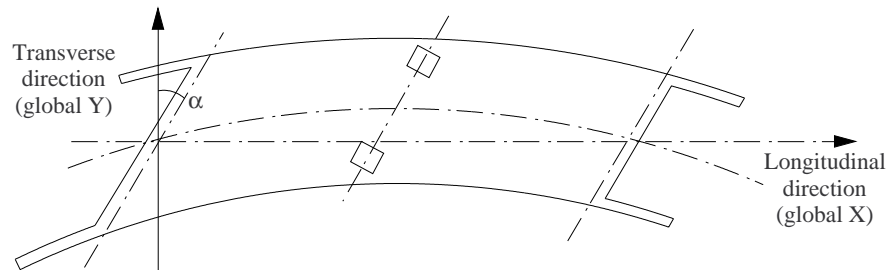


**Fig. 2.6 Longitudinal and transverse directions, including skew [Caltrans 1999]**

Each individual bridge generated for analysis was not intended to correspond directly to any existing bridge design. Rather, a bridge portfolio was developed to represent a class of highway overpass bridges with varying designs. The portfolio would then cover a full range of bridge design possibilities. Starting from a realistic base bridge configuration, a suite of bridges was developed by varying certain design parameters. This spectrum of designs in the portfolio was made possible by the parametric variation of these bridge design parameters, using acceptable engineering ranges for each. Each parameter was varied against the base configuration, not necessarily against all the other parameters. This limited the number of bridges analyzed to a scope acceptable for the rigorous amount of computations required.

### **2.3 DESIGN PARAMETERS**

Analyses have been performed for ten different design parameters. These are detailed in Table 2.1 along with the ranges assigned to each of the parameters. Four equally spaced values of each parameter were chosen initially. Performance of the bridge due to all variations can be plotted against a suite of intensity measures using the enclosed plotting utility. Included in the legend of each plot are details as to the exact value used for each parameter in each instantiation. Note that Table 2.1 is only directly applicable to the case of the single-bent bridge, as shown graphically in

Figure 2.7. Introduction of new design parameters for multiple-bent bridges is discussed in Chapter 6.

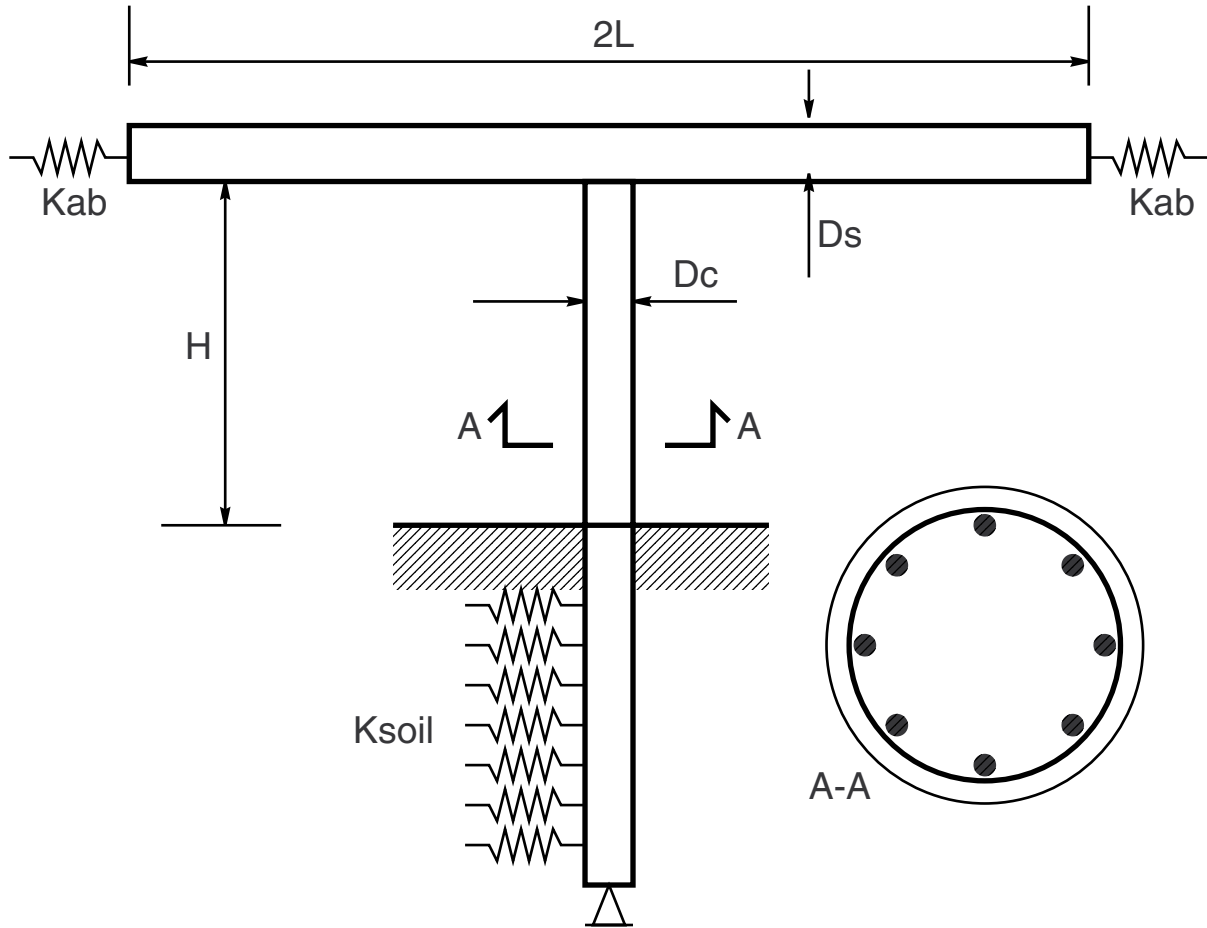


**Fig. 2.7 Single-bent bridge design parameters**

The skew angle ( $\alpha$ ) of the deck at the abutments was measured from the vertical (Fig. 2.6). The vertical is defined as a line perpendicular to the centerline of the bridge deck along the transverse axis, in the same plane. The span length parameter ( $L$ ) was applied directly to each of the equal spans. Column height above grade was then obtained from the span-to-column height ratio ( $L/H$ ). As the span-to-column height ratio ( $L/H$ ) was varied, the length ( $L$ ) was held constant, thereby only altering the column height ( $H$ ). Conversely, as  $L$  was varied, the  $L/H$  ratio remained constant, thereby making the  $L$  design parameter a measure of the overall size of the bridge, not just the span lengths.

**Table 2.1 Parameter variation ranges for a two-span overpass bridge**

Description	Parameter	Range
Degree of skew	$\alpha$	0–60°
Span length	$L$	18–55 m (60–180 ft)
Span-to-column height ratio	$L/H$	1.2–3.5
Column-to-superstructure dimension ratio	$D_c/D_s$	0.67–1.33
Reinforcement nominal yield strength	$f_y$	470–655 Mpa (68–95 ksi)
Concrete nominal strength	$f'_c$	20–55 Mpa (3–8 ksi)
Longitudinal reinforcement ratio	$\rho_{s,long}$	1–4%
Transverse reinforcement ratio	$\rho_{s,trans}$	0.4–1.1%
Pile soil stiffness	$K_{soil}$	USGS A, B, C, D
Additional bridge dead load	$Wt$	10–75% self-weight
Abutment models	$Abut$	Various

The column-to-superstructure dimension ratio ( $D_c/D_s$ ) was used to size the column, given a fixed superstructure deck depth detailed below. The ranges of this parameter were governed by the Caltrans SDC [Caltrans 1999]. Material properties were varied for both concrete and reinforcing steel. Steel nominal yield strength ( $f_y$ ) ranges from  $f_{ye}$  in the SDC document to higher values that can be expected for modern reinforcing steel. These steel properties were applied to the column as both longitudinal ( $\rho_{s,l}$ ) and transverse ( $\rho_{s,t}$ ) reinforcement. Bar sizes are detailed below. Nominal unconfined concrete strength ( $f'_c$ ) varies from strengths universally available in construction to high strength, as typical for modern construction practice.

To account for different bridge sites, an attempt to model soil properties was implemented through the use of nonlinear soil P-y springs ( $K_{soil}$ ) acting on the pile shafts. The properties of these springs were determined from properties typical to USGS soil groups A, B, C, and D, or their corresponding NEHRP soil groups B, C, D, and E. The final parameter was additional bridge dead load ( $Wt$ ) applied in percentages of the existing bridge self-weight. The additional load increases the column axial load ratio, as reported in output data, and makes the column more susceptible to nonlinear geometric effects.

The abutment parameter is discussed in more detail in the discussion of abutment modeling (Section 2.4.3). While no particular values were assigned to the abutment parameter, separate abutment models proposed by other researchers were instantiated. A parametric variation of stiffness and mass properties of the abutments was also completed in order to cover a realistic range of values.

## 2.4 PSDA MODEL

The importance of choosing a nonlinear analysis tool and understanding its limitations cannot be underestimated. This tool should enable sufficiently accurate modeling of the class of structures under investigation, perform stable nonlinear time-history analysis of the structure, and enable easy extraction and post-processing of various structural response quantities after an analysis. More importantly, this analysis tool must be calibrated to give a level of confidence in the response quantities it produces. The PEER OpenSees [McKenna 2000, OpenSees] platform was selected as the nonlinear finite element engine for PSDA.

### 2.4.1 Column

Reinforced uniformly circular concrete column cross sections were used throughout. The diameter of the columns was determined from the  $D_c/D_s$  design parameter. All columns have perimeter longitudinal reinforcement. Longitudinal bars are all #11 (1.410 in. diameter, 1.56 in.<sup>2</sup> cross-sectional area), evenly spaced at a radius determined using 1.5 in. cover and the diameter of transverse reinforcement. Transverse spiral reinforcement was used to confine the concrete, consisting of #6 bars (0.750 in. diameter, 0.44 in.<sup>2</sup> cross-sectional area).

The columns were modeled in OpenSees using fully three-dimensional fiberized nonlinear beam-column elements [Neuenhofer 1998]. Nonlinear geometry effects were addressed through inclusion of P- $\Delta$  effects for the columns. Column cross sections were discretized into 96 and 24 radially defined fibers in the core and cover concrete, respectively. A typical cross section is shown in Figure 2.8. Constitutive models used for concrete were based on the Kent-Scott-Park stress-strain relation [Kent 1971], as modeled in OpenSees [OpenSees].

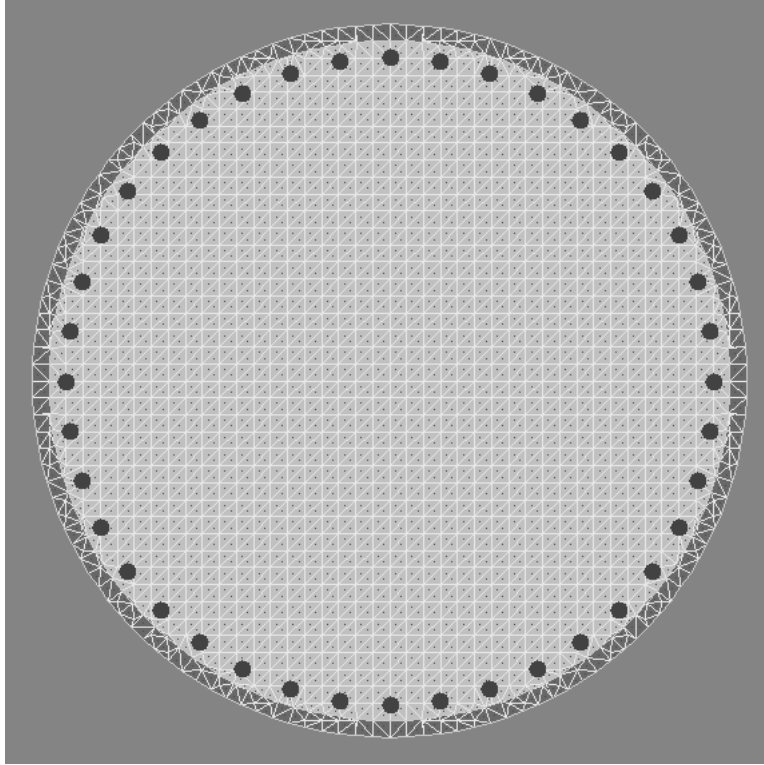


**Fig. 2.8 Typical column cross section modeled in UCFyber**

For this study, the maximum confined concrete stress (Eq. 2.1) was determined from the Mander confined concrete model [Mander 1988].

$$f'_{cc} = f'_c \left( -1.254 + 2.254 \sqrt{1 + \frac{7.94 f'_l}{f'_c}} - 2 \frac{f'_l}{f'_c} \right) \quad (2.1)$$

where  $f'_l$  was determined for spiral confinement from Equation 2.2.

$$f'_l = \frac{1}{2} \rho_{s,trans} f_y \left( \frac{1 - \frac{s'}{2d_s}}{1 - \rho_{s,long}} \right) \quad (2.2)$$

where  $s'$  is the clear spacing between spirals, and  $d_s$  is the centerline diameter of the spirals. A sample confined and unconfined concrete stress-strain relationship is shown in Figure 2.9, with the convention that the compressive stress and strain are negative.

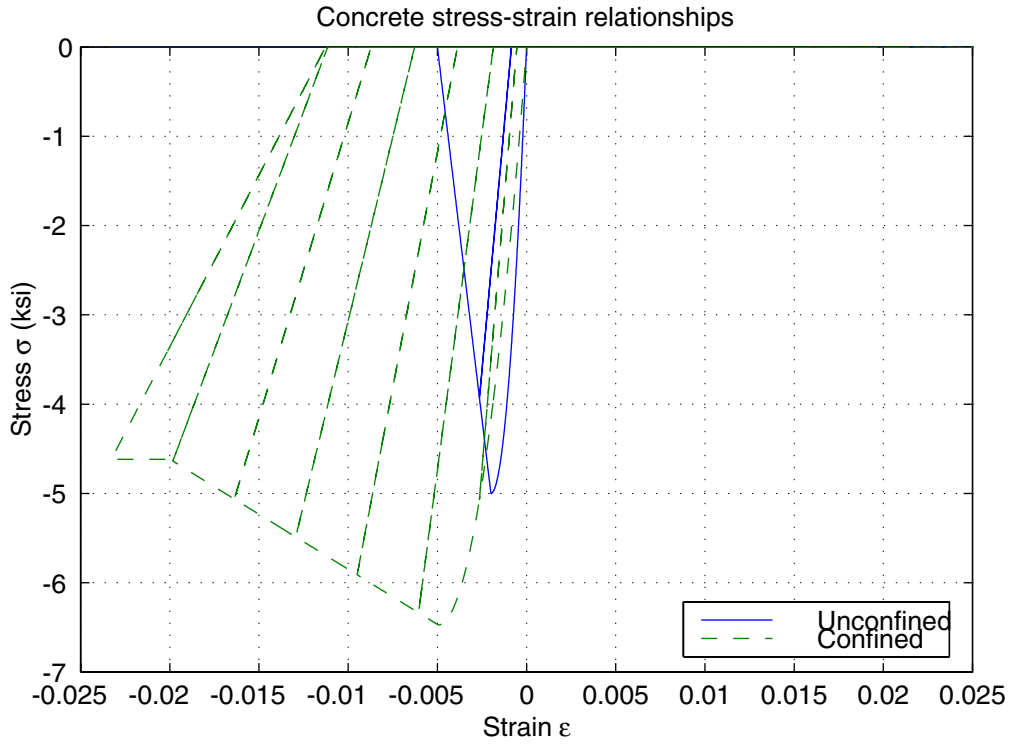


**Fig. 2.9** Confined and unconfined concrete constitutive relationships

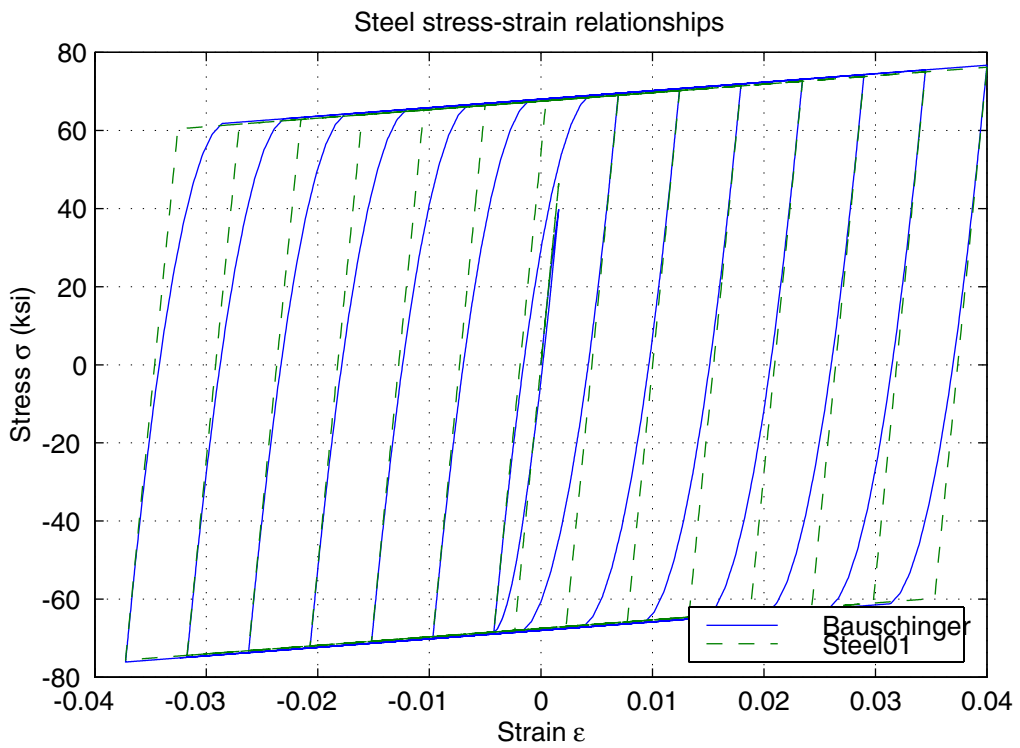


**Fig. 2.10** Reinforcing steel constitutive relationships

The constitutive model used for the steel reinforcement was a simple elastic-plastic bilinear model. The steel has initial stiffness  $E=29000$  ksi, and post-yield hardening stiffness of 1.5% pre-yield stiffness, or 435 ksi. As defined in Caltrans SDC [Caltrans 1999], the ultimate steel strain in tension was limited to 0.09. A sample steel stress-strain relationship is shown in Figure 2.10.

While initial bridge models used the elastic-plastic steel model in OpenSees (Steel01), subsequent analyses have incorporated a more complex steel model. All results shown herein used the latter steel model. The basic hysteresis rules and properties are the same as described above; however, the Bauschinger effect was included. Including the Bauschinger effect gives a more realistic estimate of energy dissipation during cyclic loading. Instead of using a simply linear strain-hardening approximation, the Bauschinger steel model hardens at a slope of 1.5% (of the elastic modulus) until a strain of 0.07, after which it starts to soften at a slope of 0.75% (of the elastic modulus) until it reaches an ultimate fracture strain of 0.12. While this strain is higher than that prescribed by Caltrans, modern steels can be expected to easily achieve such ultimate strain. It was desired to affect some stiffness plateau in the global system; therefore this softening was included.

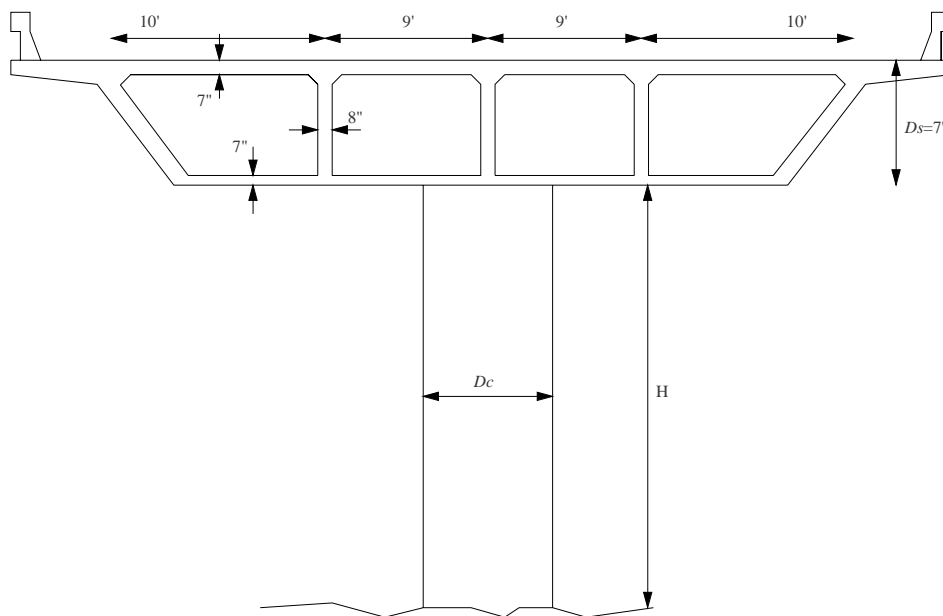


**Fig. 2.11 Deck and column dimensions**

### 2.4.2 Deck

The deck cross section is of reinforced concrete box girder construction. A typical 3-lane (design traffic lane width 3.6m), 4-cell box girder was used, with a width of 36 ft and a depth ( $D_s$ ) of 7 ft. See Figure 2.11 for dimensions. Area, moment of inertia, and torsional properties were computed and used in the OpenSees model, as shown in Table 2.2.

**Table 2.2 Deck elastic properties**

$I_Y$	10299150 in. <sup>4</sup>
$I_Z$	164711680 in. <sup>4</sup>
A	8960 in. <sup>2</sup>
J	31020600 in. <sup>4</sup>
E (5, 6, 8 ksi)	4108, 4500, 5196 ksi

The deck was modeled as a linear-elastic beam element, with properties described above. The flexural stiffness,  $I_{eff}=0.75I$ , and torsional stiffness,  $J_{eff}=0.25J$ , were modified to approximate a cracked stiffness as recommended by ATC-32 [ATC 1996]. The Young's Modulus,  $E$ , was determined for concrete only from  $E_c = w^{1.5} \sqrt{f'_c}$  (ksi units,  $w$  unit weight in pcf). Each span was discretized into five equal sub-spans, with mass determined from self-weight properties lumped at each of these nodes. The bridge decks were all assumed straight, since skewness only affects the angle of abutment connection, not the radius of curvature of the deck. Each bridge deck node has six mass terms, three translational (masses) and three rotational (moment of inertias).

As the deck deforms and is resisted by abutment supports, the global lateral-resisting-force properties of the bridge continue at a constant slope due to the presence of the elastic material in the model. In order to model bridge collapse, a nonlinear deck model may need to be used. To investigate this, a fiberized beam-column element was used.

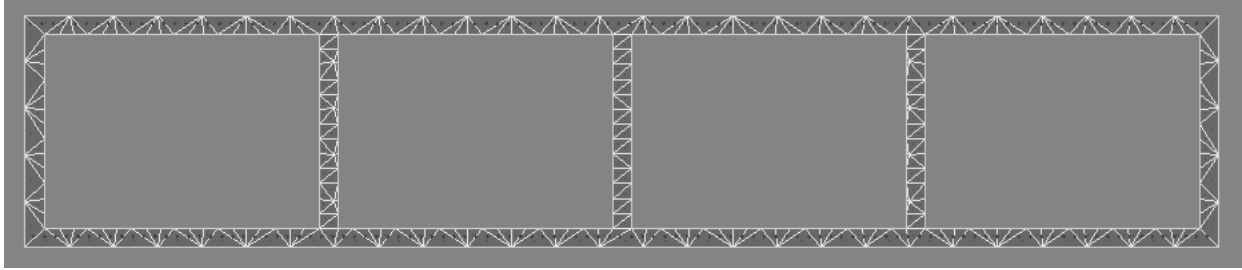


**Fig. 2.12 Box girder modeled in UCFyber**

To maintain the distribution of mass used in the elastic analyses, the nonlinear deck was discretized into two elements per span with 4 integration points each, and a distributed mass (mass/unit length), to achieve the same total mass. Rotational mass terms were again lumped at the nodes.

To generate the nonlinear model, the box girder section was modeled in UCFyber [Chadwell] using unconfined concrete boxes as shown in Figure 2.12. Steel reinforcement (box girder was assumed not to be post-tensioned) was then placed both in the soffit and deck slabs. A single row of #5 bars ( $0.31 \text{ in.}^2$ ) in the soffit provided 0.35% steel reinforcement ratio. Two rows of #5 bars, one at each face of the deck slab, each provide 0.20% and 0.40% steel reinforcement ratio, respectively. Such reinforcement ratios are typical for bridge box girders designed by Caltrans. Given the box girder dimensions shown above, this results in a total of 35 bars in the soffit and 60 bars in the deck slab.

The models were compared by conducting pushover analyses of the bridge model with a linear and nonlinear deck model. A sample transverse static pushover curve (SPO) is shown in Figure 2.13 to evaluate the contribution of the nonlinear deck to ultimate and yield values. A longitudinal pushover is shown in Figure 2.14. The corresponding moment-curvature diagrams for the top of the column in the transverse (Fig. 2.15) and longitudinal (Fig. 2.16) directions are also shown for comparison.

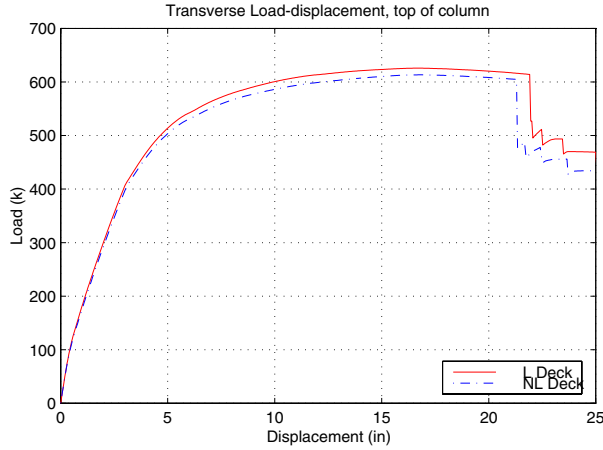


**Fig. 2.13 NL deck transverse SPO**

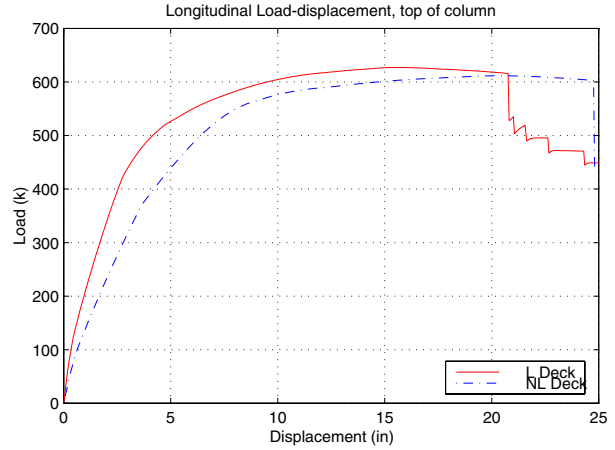


**Fig. 2.14 NL deck longitudinal SPO**

Moments introduced into the column were somewhat reduced for the nonlinear bridge deck model, whereas yield values were the same as those from the linear deck model. In the longitudinal pushover analysis, the deck is forced to deform between the column and roller abutment supports. This causes the nonlinear (NL) deck model to exhibit a stiffness change from the elastic model. However, the effect of the nonlinear deck model on the overall behavior of the bridge is not significant (see ultimate force). Thus, the linear deck model was retained.

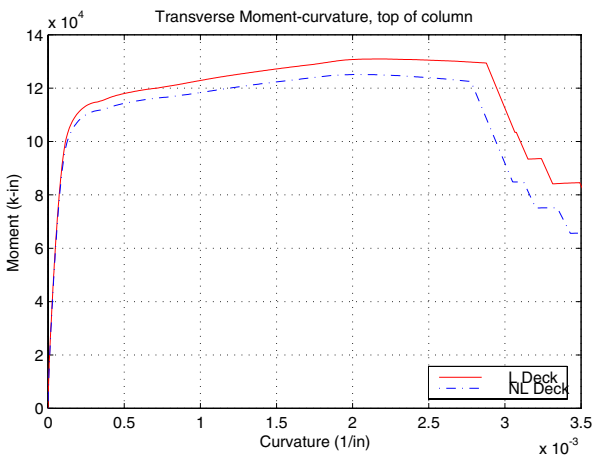


**Fig. 2.15 NL deck transverse SPO (M- $\phi$ )**

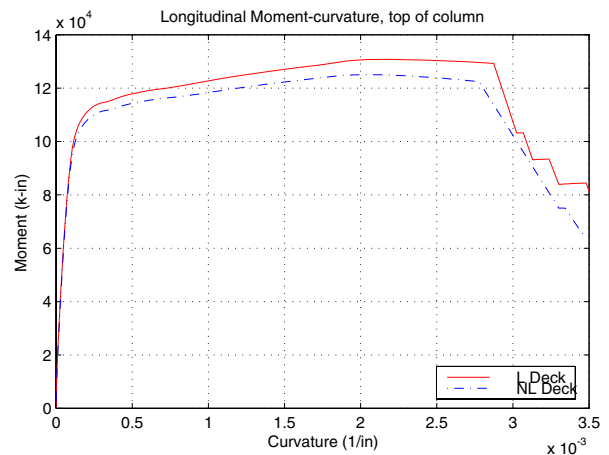


**Fig. 2.16 NL deck longitudinal SPO (M- $\phi$ )**

### 2.4.3 *Abutments*

There are numerous examples of abutment models for use in analytical bridge studies, based on both empirical observations and theory. Three main categories can be discerned for these types of models. The first attempts to model abutment properties by simply providing a roller support in order to maximize column demand. The second category uses spring and gap elements to model properties of the abutment structural and soil systems. The difference between the first two categories indicates how significantly the relative stiffness of the abutments affects the global bridge response. The third category addresses soil and embankment contributions to the stiffness and inertia of the abutment.

A rigid link oriented in the transverse direction was added to the last deck element where the abutment was to be modeled. This link has a width intended to model the actual deck width, and constrains the displacement of all the abutment nodes. For the case of roller boundary conditions, vertical restraints are placed at both ends of this transverse link. The roller abutment case was labeled “abut 0.”

For the case where abutment stiffness and strength properties were defined (second category), a combination of the methods used by Caltrans [Caltrans 1999], Goel and Chopra [Goel 1997], and Maroney [Maroney 1994a] was implemented. Numerical values used in the OpenSees model are summarized in Table 2.3 following their derivation. A total of five spring and gap elements were then added in parallel between this link and rigid supports. These elements were spaced transversely to account for torsional response at the abutments, as shown in Fenves and Ellery [Fenves 1998]. The extreme two elements in the array were longitudinal gap materials with vertical springs. The intermediate two elements were springs modeling the bearing pads in both the longitudinal and transverse directions. Finally, the center element was a transverse spring with zero gap to model the transverse abutment stiffness. Calibration of these elements is discussed hereafter.

The abutment was assumed to be seat-type with a gap between the backwall and the deck [Priestley 1996]. An initial gap of 6 in. was assumed. The deck rests on elastomeric bearing pads. These fabric or steel reinforced pads have 15500 Kpa tensile strength, 34500 Kpa low

temperature stiffness ( $E$ ), 750 Kpa shear modulus ( $G$ ) and can deform up to 350% before failure [Caltrans 1999]. Two bearing pad springs (2 in. thick) with elastic-perfectly-plastic behavior were added to the array described above. Bearing pad spring stiffnesses were derived from  $k_{bp} = \frac{GA}{h}$  where  $Ah$  is the pad volume. Yield force and yield displacement were determined from the properties listed above.

To model the opening and closing of the gap, two gap elements were placed into the array for resistance in the longitudinal direction. The hysteretic behavior of such an element is shown in Figure 2.17. As shown, the gap elements only resist compression forces and the damage to the abutment backwall is cumulative. The stiffness and ultimate strength properties were determined based on backwall and backfill soil-dissipating mechanisms (Eq. 2.3). The stiffness also includes an empirical pile (Eq. 2.4) resistance term [Eq. Goel 1997].

$$R_{soil} = \sqrt{\frac{D_s}{8}} (7.7 \text{ ksf}) A_{deck} \quad (2.3)$$

$$R_{pile} = 40k / \text{pile} \quad (2.4)$$

These values provide an ultimate strength that was assumed to occur at 1 in. Maximum deformation was assumed to be 2.4 in. A list of material properties for each spring is shown in Table 2.3.

The transverse direction was modeled as a single spring that resists displacement in both directions (tension and compression) due to abutment wing walls. Similar to the longitudinal direction, damage is cumulative and only compression resistance is provided by the walls. Total transverse resistance is then the wing walls (Eq. 2.5) coupled with 3/4 of the pile resistance determined in the longitudinal direction [e.g., Goel 1997].

$$\begin{aligned} V_{ww} &= \phi(V_c + V_s) \\ &= \phi \left( 0.95 \sqrt{f'_c} A_{ww} + \frac{A_v f_y d}{s} \right) \end{aligned} \quad (2.5)$$

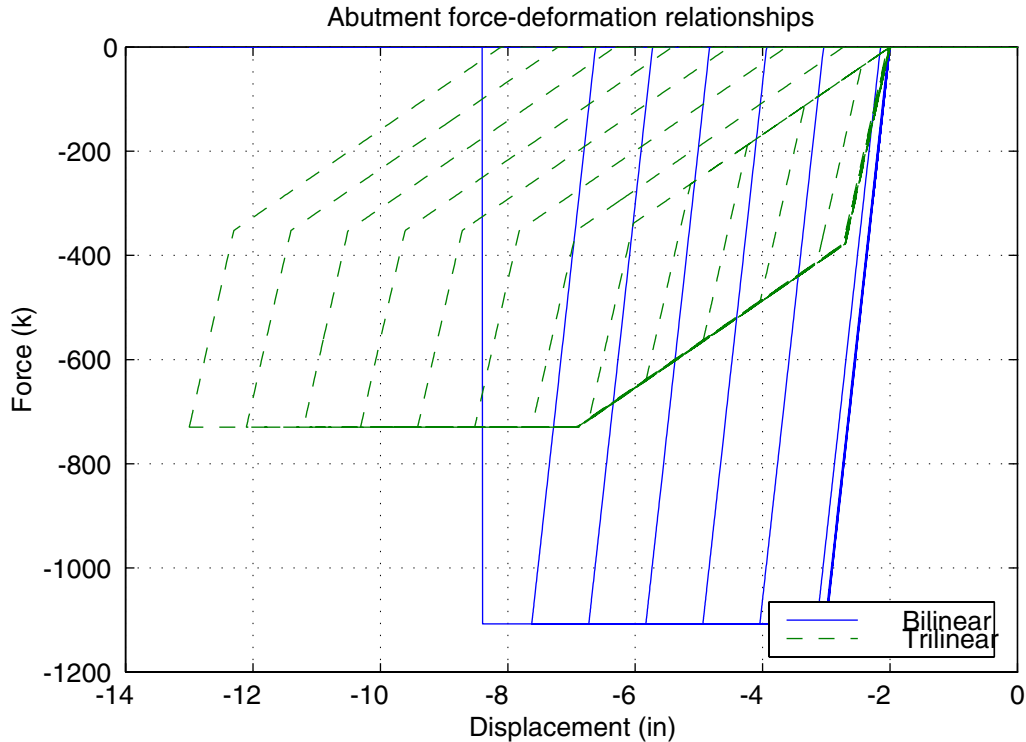


**Fig. 2.17 Bilinear and trilinear abutment force-deformation relationships**

Finally, a vertical uplift spring was also provided. With a high stiffness, this is equivalent to a vertical support condition at the abutment. Using values appropriate for the bridges considered, the idealized bilinear abutment force-displacement relation yields a stiffness of 2215 k/in. and 627 k/in. in the longitudinal and transverse directions, respectively. This abutment model was labeled “abut 1,” and the force-deformation relationship is plotted in Figure 2.17 as “bilinear.”

Large-scale abutment tests provided an empirical verification of abutment stiffness values for use in the longitudinal direction [Maroney 1994b]. An idealized trilinear backbone with normalized ordinates allowed adaptation of the backbone to values specific to a given bridge. Tests indicated that both the initial stiffness and ultimate strength values predicted by the Caltrans method were high. Resulting stiffness and strength values are shown in Table 2.3. The transverse direction uses a slightly reduced value from the Caltrans procedure. This abutment model was labeled “abut 2,” and the force-deformation relationship is plotted in Figure 2.17 as “trilinear.”

In order to improve bounds for the parametric variation of stiffness and mass properties, several alternative methods for determining abutment properties were investigated. These belong to the third category of abutments described above: those which account for embankment flexibility and inertial effects. These methods primarily develop relationships between embankment properties and response in the transverse direction for a plane strain case.

Assuming a symmetric soil embankment with defined trapezoid cross-sectional properties ( $w$ =crown width,  $H$ =embankment height,  $1/S$ =slope of sides), soil shear moduli ( $G$ ), and unit weight ( $\gamma$ ), the stiffness per unit length of the embankment can be determined [Wilson 1990] by Equation 2.6.

$$\bar{k}_t = \frac{2SG}{\ln\left(1 + 2S\frac{H}{w}\right)} \quad (2.6)$$

The maximum soil shear modulus was determined from sample embankment material [Maroney 1994b] and a shear wave velocity. Reduction of the shear modulus due to shear strain level (shear strain of  $1e-3$ ) was then calculated using a relationship such as Idriss and Seed [Seed 1970]. The total stiffness was then derived from an estimated wing wall length. This can be assumed to be approximately 20–30% of the deck width in order to produce larger displacement demand. This length was purposely underestimated to make the transverse stiffness low.

Wilson and Tan [Wilson 1990] also allow calculation of a vertical stiffness from the same cross section, using the elastic stiffness of the soil in place of the shear modulus. The longitudinal stiffness was assumed the same as the transverse, as shown in Table 2.3. This abutment model was labelled “abut 3,” and uses the bilinear force-deformation relationship (Fig. 2.17).

A similar embankment procedure was proposed by Zhang and Makris [Zhang 2001]. The transverse stiffness was generalized to any embankment geometry and allows for both the stiffness and damping calculation for dynamic abutment response. Only the spring stiffness was used herein (damping was not simulated using complex stiffness), derived for the transverse (Eq. 2.7) and vertical directions. The distance between the crown and the imaginary intersection of the embankment sides is  $z_0$ . The total stiffness was derived from the critical length  $L_c$  (Eq. 2.8).

The  $S$  was kept consistent with the terminology in Wilson and Tan. The longitudinal and transverse directions were again assumed the same. This abutment model was labeled “abut 4” when used without mass, “abut 8” when mass was incorporated.

$$\bar{k}_t = \frac{wG}{z_0 \ln\left(\frac{z_0 + H}{z_0}\right)} \quad (2.7)$$

$$L_t \approx 0.7 \sqrt{\frac{wH}{S}} \quad (2.8)$$

In addition to abutment stiffness, the other fundamental factor governing abutment response is the inertial force generated during earthquakes. Inertia was included in the analysis model by using a point mass at the abutments. Coupled with the stiffness quantities above, this is equivalent to single-degree-of-freedom systems attached to each end of the bridge. Determining the mass participating in abutment response is highly uncertain and is usually approximated by a critical length of embankment. Different researchers have proposed participating lengths that best match recorded data [Wissawapaisal 2000; Zhang 2001], as shown in Table 2.3. As suggested by Wissawapaisal, this critical length may vary based on earthquake intensity as well.

To provide a further data point for the assessment of participating mass, the mass expression derived by Werner was used [Werner 1994]. This was accomplished using an effective embankment length,  $d$ , assumed to be a quarter of the deck length (Eq. 2.9). The mass density ( $\rho_s$ ) is related to  $\gamma$  above by  $g$ . The mass computed was on the order of the other methods.

$$m = \frac{\rho_s(w + SH)Hd}{4} \quad (2.9)$$

Hysteretic damping was not included in any of the abutment models, only 2% Rayleigh damping for the entire system. This is not realistic, as it has been shown that energy dissipation at the abutments can amount to as much as 20% of critical damping in the fundamental transverse mode and greater than 40% in the longitudinal mode [Zhang 2001]. However, the

sensitivity to mass and stiffness in abutment modeling is more crucial in determining maximum response, as investigated herein.

**Table 2.3 Abutment stiffness and mass participation values**

<b>Proposed by</b>	<b>Longitudinal Ka<sub>l</sub> (k/in.)</b>	<b>Transverse Ka<sub>t</sub> (k/in.)</b>	<b>Vertical Ka<sub>v</sub> (k/in.)</b>	<b>Participating mass (k s<sup>2</sup>/in.)</b>
Caltrans	2215	627	NA	7.4
Maroney	1080, 168	487	NA	NA
Wilson & Tan	587	587	1643	7.4
Zhang & Makris	1006	1006	2817	12.6
Werner	NA	NA	NA	5.7

**Table 2.4 Apparent abutment stiffness values**

<b>Proposed by</b>	<b>Longitudinal period (sec)</b>	<b>Transverse period (sec)</b>	<b>Vertical period (sec)</b>
Caltrans	0.36	0.68	NA
Maroney	0.48	0.77	NA
Wilson & Tan	0.71	0.71	0.42
Zhang & Makris	0.70	0.70	0.42

Abutment stiffness information is presented using the fundamental period as a measure for comparison. These abutment periods do not reflect the actual system modes, but rather are an indication of the influence of the abutments (Table 2.4).

#### **2.4.4 Pile shafts**

The Type I integral pile shafts used in this study feature a continuous amount of longitudinal reinforcement running through both the column and pile shaft. There is no increase in concrete cover below grade (Fig. 2.18, left). Any lap splices and discontinuous longitudinal reinforcement were assumed to be located outside of the expected plastic hinge zones. In this

configuration, the expected location of plastic hinging was at the column-deck connection and in the pile shaft below grade.

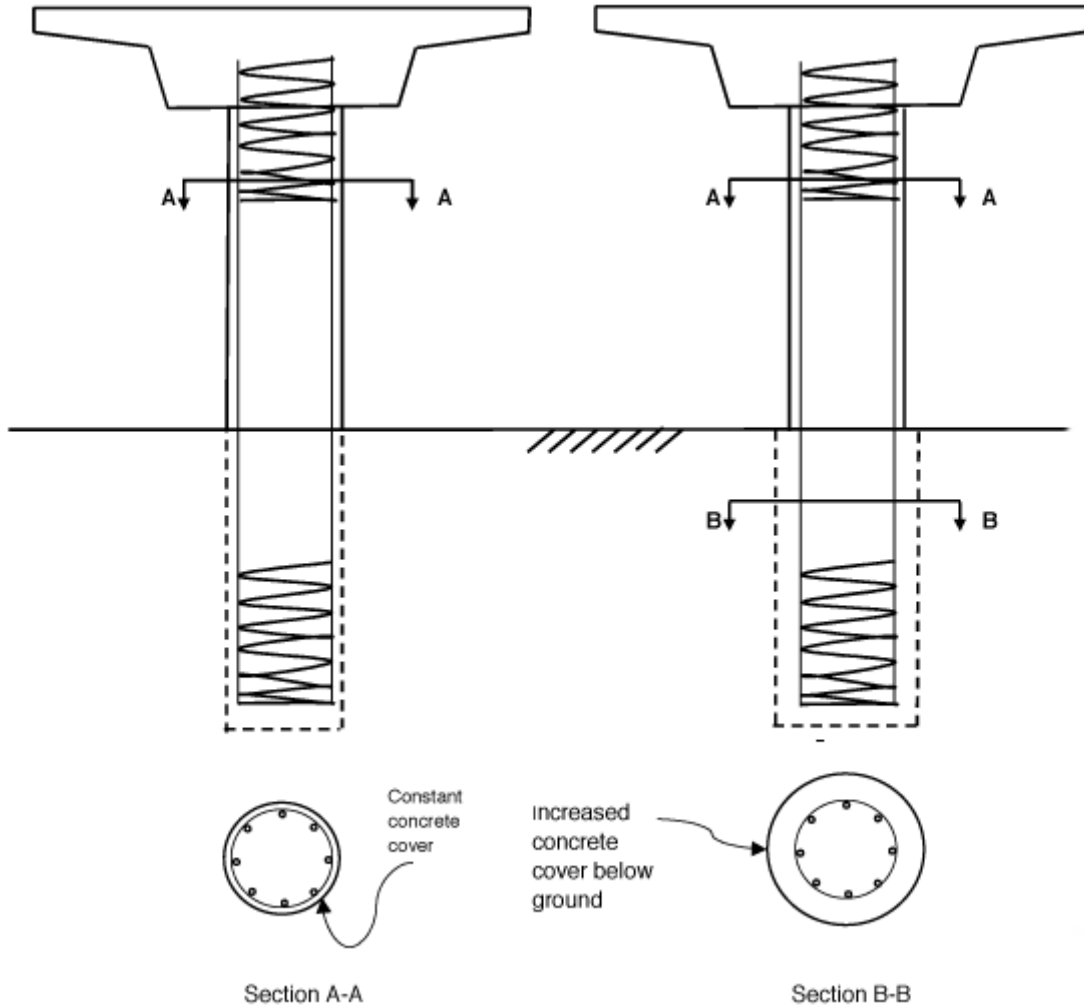


**Fig. 2.18 Type I pile shafts [Caltrans 1999]**

These assumptions can be confirmed by plotting a typical maximum moment diagram over the height of the column and pile shaft Figure 2.19. The moment and curvature distributions were generated from a longitudinal pushover analysis at ultimate load. Plastic hinging is concentrated at the top of the column, whereas hinging is distributed below grade (spread-plasticity).

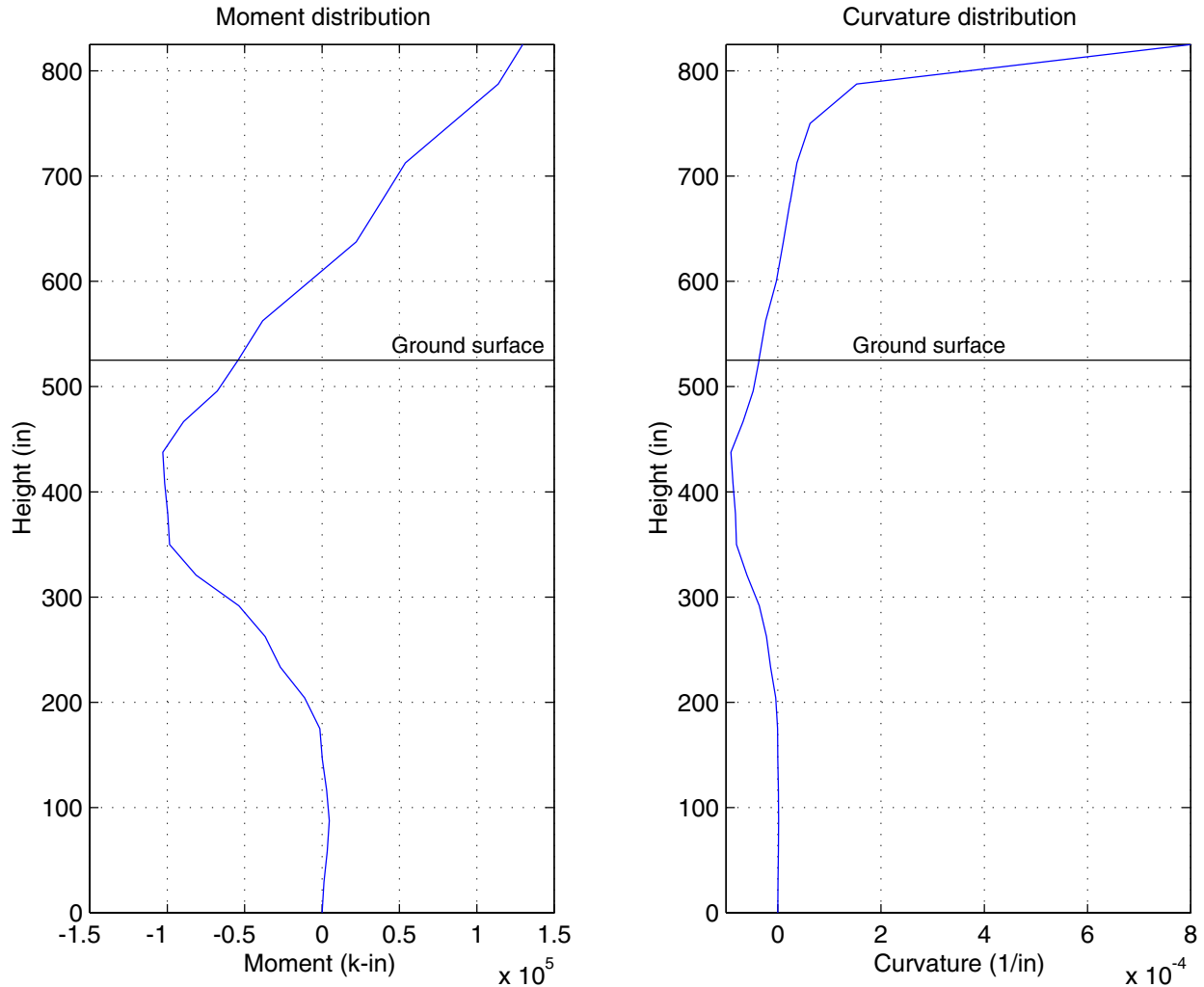


**Fig. 2.19 Location of plastic hinges over length of column and pile shaft**

The pile shaft cross section and reinforcement were identical to that of the column, as described above. Pile shaft length was arbitrarily assumed to be 1.75 times the length of the column above grade. As in the SDC, plastic hinges in these types of pile shafts were expected to form below ground. The pile shafts were discretized into six elements for the express purpose of accommodating seven (one at each node) soil  $P$ - $y$  springs to model the soil stiffness acting on the pile shaft. Mass was assigned to each pile shaft node based on pile self-weight properties.

Another reason for choosing the said pile shaft length was to accommodate curvature changes allowed by four integration points along the length of each pile shaft element. This is especially critical due to the aspect ratio of large diameter circular cross sections and the

performance of finite element fiberized beam-column models with small lengths possibly on the order of the plastic hinge length. A spring oriented in both longitudinal and transverse directions with the same stiffness properties was placed at each pile shaft node. The node at the ground surface was assigned a torsional single point constraint.

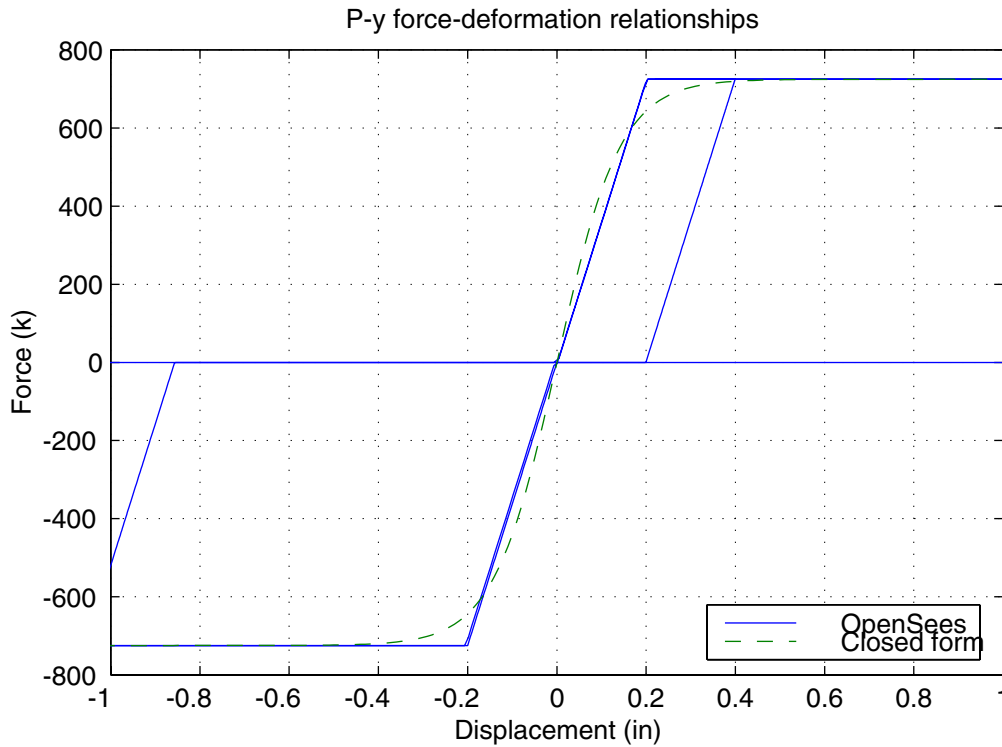


**Fig. 2.20** Sample closed form and idealized *P-y* force-displacement relationships

The properties assigned to the soil springs were derived from load-deflection curves (*P-y* curves) for cohesionless soils [API 1993]. The ultimate lateral-bearing capacity is defined in Equation 2.10.

$$p_u = \min \left\{ \begin{array}{l} (C_1 x + C_2 D) \gamma' x \\ C_3 D \gamma' x \end{array} \right. \quad (2.10)$$

where  $C_1, C_2, C_3$  are constants from Figure G8-1 [API 1993]

$x$  depth below grade

$\gamma'$  effective soil weight

$\phi'$  angle of internal friction

$D$  average pile diameter

Load-deflection behavior ( $P$ - $y$ ) was then determined by the relation:

$$P = Ap_u \tanh \left[ \frac{kx}{Ap_u} y \right] \quad (2.11)$$

where  $A=0.9$  constant for cyclic loading

$k$  initial modulus of subgrade reaction from Figure G8-2 [API 1993]

$y$  lateral deflection

The initial modulus was amplified in proportion to the diameter for the presence of large-diameter pile shafts as recommended in ATC-32 [ATC 1996]. However, to control the magnitude of  $k$ , the square root of the diameter was used instead [Fenves 1988].

Four different soil types were investigated, these corresponding to the USGS A, B, C, and D categories. Assumed properties for each of these soil types to calculate load deflection behavior are shown in Table 2.5. The water table was assumed below the site of interest, therefore, the spring stiffnesses may be artificially higher than in more realistic analyses. A sample load deflection relationship is shown in Fig 2.20. To approximate the relationship by a bilinear hysteretic model, the same algorithm applied to determine  $u_y$  for static pushovers (Fig. 2.23) was applied to  $P$  above to derive an effective stiffness and ultimate strength.

**Table 2.5 Assumed soil properties for  $K_{soil}$  groups**

	<b>USGS A</b>	<b>USGS B</b>	<b>USGS C</b>	<b>USGS D</b>
Vs (ft/s)	> 2500	1200-2500	600-1200	< 600
$\phi$ (°)	42	39	35	29
$\gamma$ (pcf)	147	135	121	95

The use of a pile shaft and  $P$ - $y$  springs allows for some rotation and displacement of the bridge column at ground level. This is more realistic than assuming a fixed-base column; however, the material models assumed for the  $P$ - $y$  springs will necessarily make the soil artificially stiff. This is because the shear modulus of soil degrades with increasing shear strain, behavior not captured by the bilinear relationship of Figure 2.19.

### **2.4.5 Loading**

Two load cases were considered for every analysis. The first is a constant gravity load (dead load). The gravity loading was determined from the mass properties assigned to the deck nodes in the deck description above. The dead load was supplemented by a comparatively small traffic live load HS-20 equivalent lane load of 0.64 k/ft. The loading is concentrated at each of the deck nodes, not distributed continuously across the span. The second load case involves either lateral loads or dynamic loading as described in the following section on PSDA Analysis.

## **2.5 PSDA ANALYSIS**

Nonlinear models were generated for each of the 160 bridge configurations and analyzed for each ground motion. Each routine involves a static pushover analysis to determine yield values, a modal analysis to determine natural frequency and mode shape information, and a dynamic time-history analysis to determine demand.

### **2.5.1 Static Analysis**

All analyses call a bridge generation script, whose components have been previously described in the PSDA model. Static analysis was controlled by the ModelS.tcl input file (see Appendix C). The routines executed include a static pushover analysis in the bridge longitudinal direction, a static pushover in the bridge transverse direction, and a set of data extraction routines to save the data to a database. Static analysis always sets the longitudinal abutment gap to be infinity in order to maximize the column demands, and to measure the yield information for the column specifically. Therefore, the bearing pads were also excluded from the pushover analyses.

For the case of a single-bent bridge, longitudinal pushover analysis was performed by incrementing the lateral load at the top of the column and monitoring displacement until failure. A standard Newton-Raphson solution strategy was used. For all the analyses investigated, the application of gravity loads takes place initially, with a single static load step to enforce equilibrium, followed by further static or dynamic analysis. A resulting force-displacement plot

(Fig. 2.21) shows not only the location of yield, but shows the post-degradation of strength as various components of the bridge model experience failure (steel longitudinal reinforcement for example). Force-displacement and moment curvature (Fig. 2.22) were recorded for yield extraction. Also monitored in the longitudinal direction was the moment and curvature distribution at failure along the total length of column and pile shaft. This allows the determination of the plastic hinge locations (Fig. 2.19). As the location of the pile shaft hinge was not known a-priori, a time history at this location was never recorded.

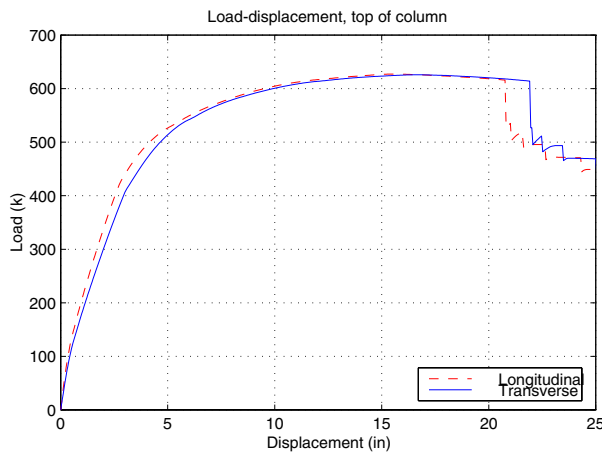


**Fig. 2.21 Force-displacement pushover**

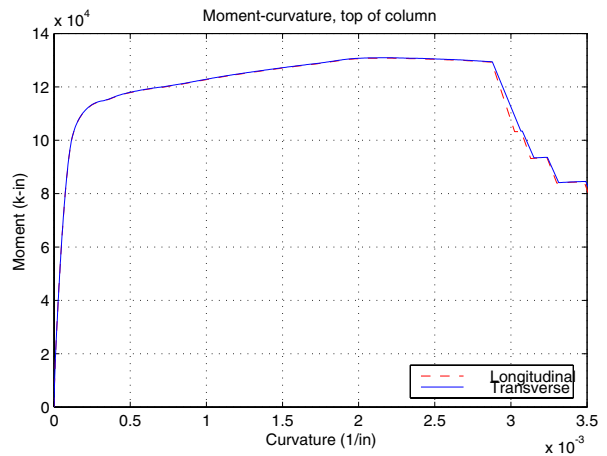


**Fig. 2.22 Moment-curvature pushover**

A similar procedure was applied to the transverse direction, also without abutment contribution. As would be expected then, for the case of the single-column, single-bent bridge, the pushover diagrams are quite similar in the longitudinal and transverse directions. They are only slightly influenced by the transverse array at the abutments. Data were then analyzed to determine yield displacement and curvature values for each direction. Ultimate force and moment are clearly defined on the pushover plots; however, the automation of yield displacements required an algorithm to select a unique value. To standardize the yield state in this study, the yield displacement (or curvature) was specified as the displacement at which the 66% percentile ( $\frac{2}{3} F_{\max}$ ) slope intersects the force line midway between  $F_{\max}$  and  $\frac{2}{3} F_{\max}$  (i.e.,  $\frac{5}{6} F_{\max}$ ). This yield deformation algorithm is illustrated on a sample pushover curve in Figure 2.23.

While single-bent bridges use standard static pushover techniques for both longitudinal and transverse directions, multiple-bent bridges require a modification of the procedure in the transverse direction. Similar to the modal pushover procedure for buildings [Chopra 2001] and the pushover analysis in the N2 method [Fajfar 1997], the distribution of lateral forces is determined from the shape of the fundamental transverse mode, weighted by tributary mass. Displacements at column tips were then monitored along with shear forces induced in the columns, such as base shear in buildings. This allows for nonregular bridges to be accurately analyzed as well, producing separate yield data for different bents. Nonregularity frequently occurs when the properties of each bent are varied from each other.

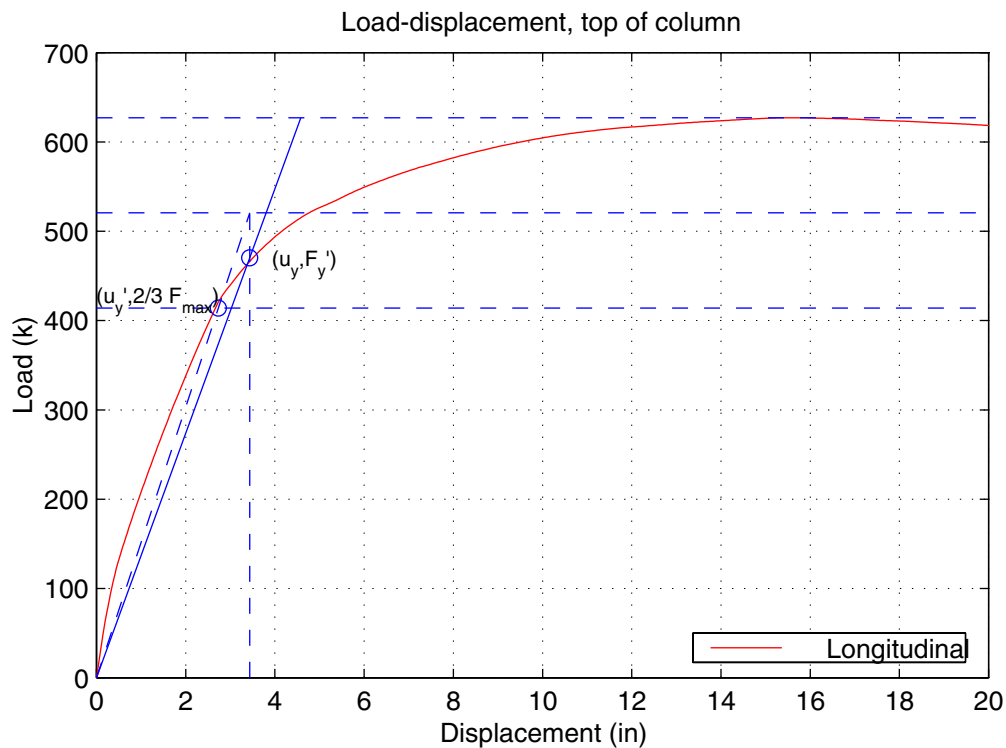


**Fig. 2.23 Determination of yield displacement from static pushover curve**

With the availability of a fully three-dimensional model and transverse mode information, a new regularity-like index ( $RI^*$ ) was developed (Eq. 2.12) to indicate the expected introduction of higher mode response. While the index proposed by Isakovic and Fischinger [Isakovic 2001] depends on the analysis method (and differences between),  $RI^*$  is a function of the model only. The normalizing constant in the denominator is derived from a purely transverse

translational mode. The mode in the numerator is derived in the absence of abutments, therefore irregularity is a function of bridge geometry only. Multiple-bent bridge regularity is discussed in more detail in Chapter 6.

$$RI^* = \left( \frac{1}{L} \int_0^L \bar{\phi}(x) dx \right) * 100\% \approx \frac{\sum_{i=1}^n \frac{dx_i}{2} (\bar{\phi}_i + \bar{\phi}_{i-1})}{\sum_{i=1}^n dx_i} * 100\% \quad (2.12)$$

### 2.5.2 Modal Analysis

Modal analysis is the first step controlled by the dynamic analysis control file (ModelD.tcl; see Appendix C). It was performed before each analysis (elastic stiffness), as well as after each analysis, to assess the change in natural frequencies at the onset of damage in the bridge. Only the first two modes were extracted and saved, as they correspond directly to the longitudinal and transverse modes of the bridge. For the assumed roller boundary condition at the abutments, the fundamental mode for all three bent types was in the transverse direction. This mode involves a simple transverse translation of the deck (Fig. 2.24). The second mode involves a longitudinal translation of the superstructure, coupled with small rotations of the columns and supports (Fig. 2.25). When abutment models were added, transverse stiffness (from the abutments) becomes dominant (over the longitudinal stiffness) due to the gap in the longitudinal direction before abutment impact. Hence the fundamental mode of the bridge shifts to the longitudinal mode described above, and the second mode transverse.

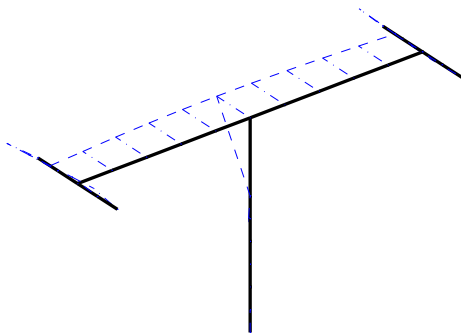


Fig. 2.24 Single-bent 1<sup>st</sup> mode transverse

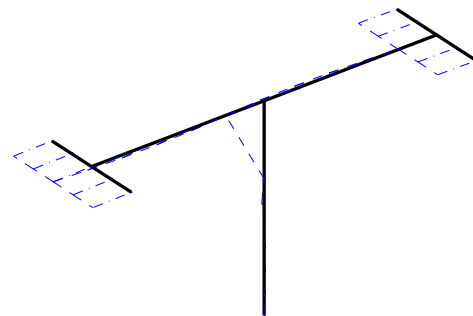
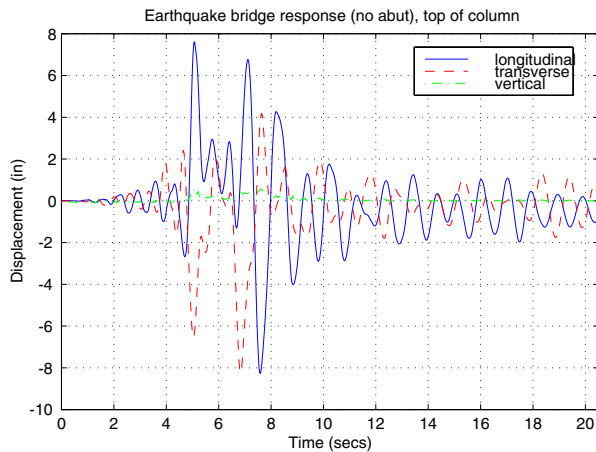


Fig. 2.25 Single-bent 2<sup>nd</sup> mode longitudinal

Sample period information for various bridge configurations is listed in Table 4.1. The fundamental period values range from 0.39 for short bridges to 3.9 for long-span bridges. Second mode periods vary similarly from 0.30 to 3.3.

### 2.5.3 Dynamic Analysis

The actual transient analyses were performed for all ground motions and bridge instantiations, as controlled by ModelD.tcl (Appendix C). The computation time required was somewhat reduced by reducing the dynamic time step to 0.02 sec as described in PSDA Ground Motions (Section 2.1). A static analysis was performed first to allow application of the gravity loads. Following this, the constant average acceleration Newmark numerical integrator was used with 2% Rayleigh damping to perform the dynamic time steps. Numerous quantities were monitored and then passed to the data extraction routines to extract maximum dynamic quantities, such as stress, strain, moment, displacements, etc.



**Fig. 2.26 Displacement time history**

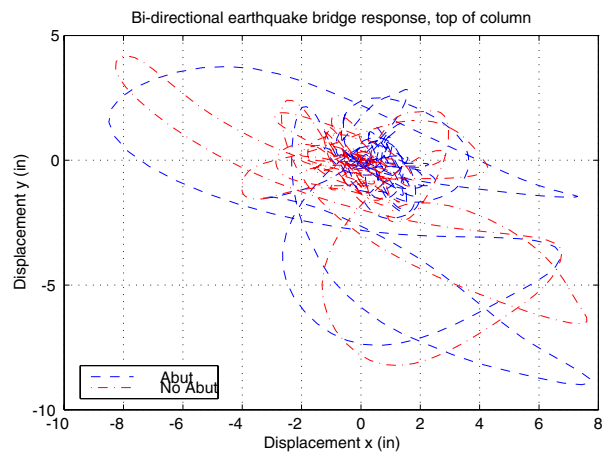


**Fig. 2.27 Column orbital displacements**

A selection of results is presented below from the dynamic analysis resulting from the LMSR record LOS (Appendix B). The base bridge configuration was used, as described further in Chapter 3, with a roller boundary condition for the abutments initially. The resulting time history displacement response at the top of the single-column bent is shown in Figure 2.26. Similarly, a plot of orbital displacements (longitudinal and transverse displacement paths) is

shown in Figure 2.27. Moment-curvature at the top of the column (Fig. 2.28) and moment-rotation (Fig. 2.29) are shown subsequently.

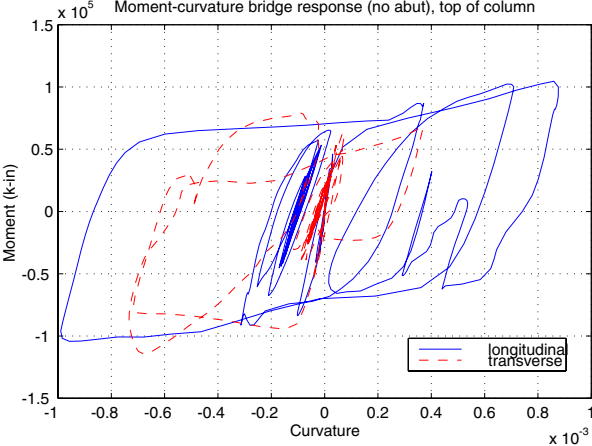


**Fig. 2.28** Sample moment-curvature plot

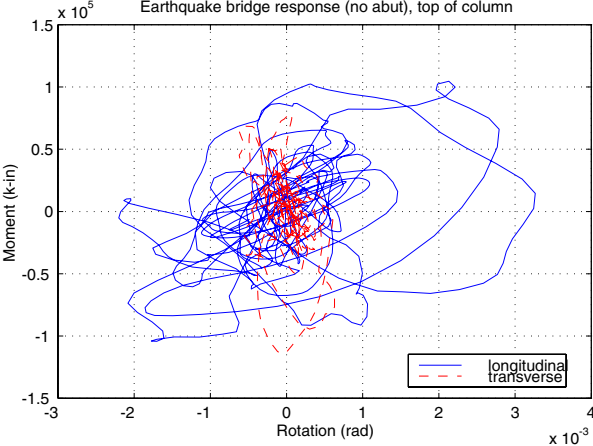


**Fig. 2.29** Sample moment-rotation plot

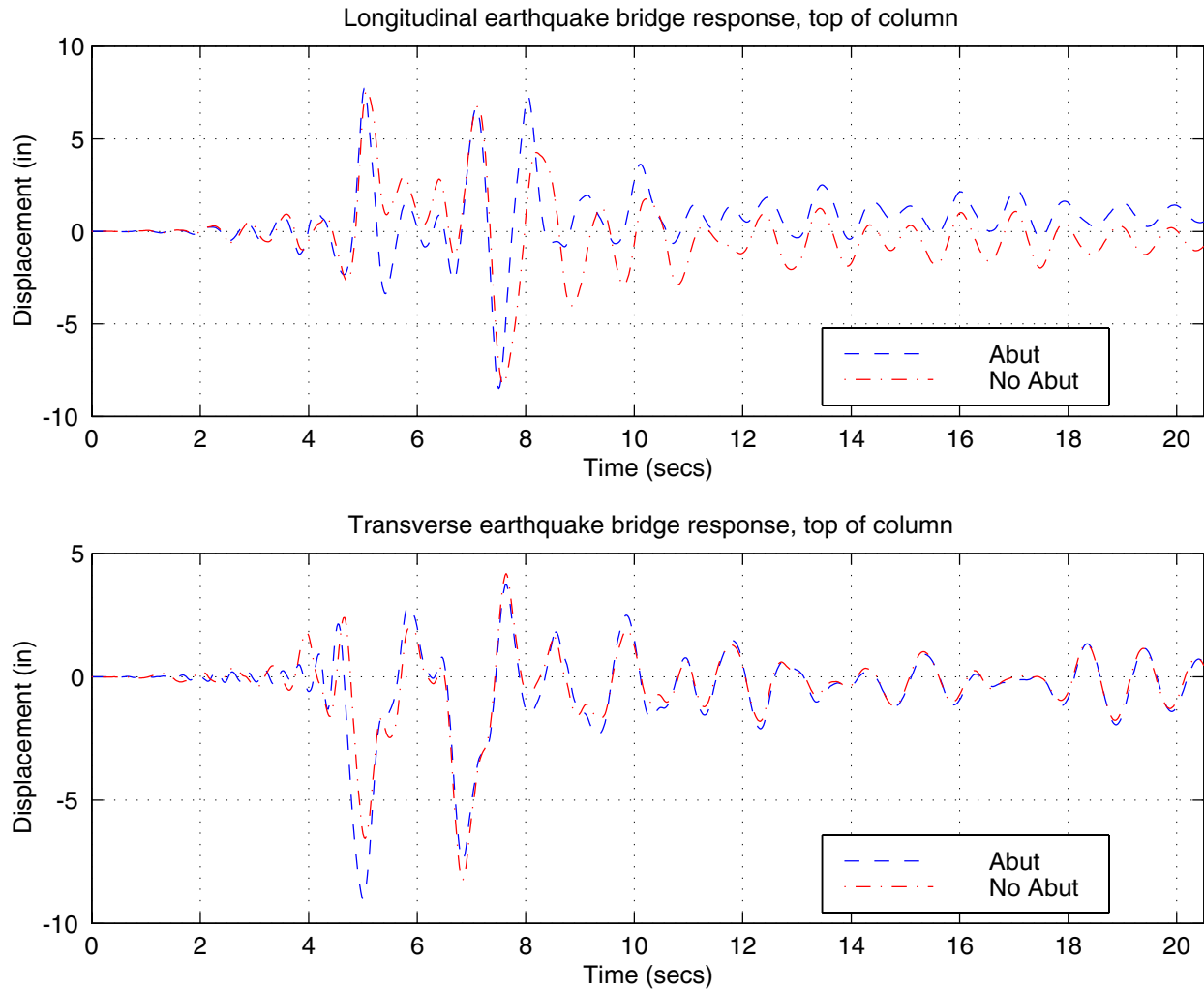


**Fig. 2.30 Comparison of time histories for different abutment cases**

In order to determine the hysteretic energy dissipated during earthquake motion, the moment-rotation diagram needs to be integrated numerically. However, due to the spread of plastic hinging at the top of the column, the final Gauss-Lobatto integration point sampled does not necessarily contain the maximum rotation. Therefore, the moment-curvature diagram was used instead. The curvature was assumed to act over a plastic hinge length  $L_p$  defined in Equation 2.13 [Caltrans 1999]. The nominal longitudinal rebar diameter ( $d_{bl}$ ) is defined from the #11 bars used in the column, and  $L'$  is the length from the maximum moment at the top of the column to the inflection point. This was determined from Figure 2.19.

$$L_p = 0.08L' + 0.15f_y d_{bl} \geq 0.3f_y d_{bl} \quad (\text{Eq. 2.13})$$

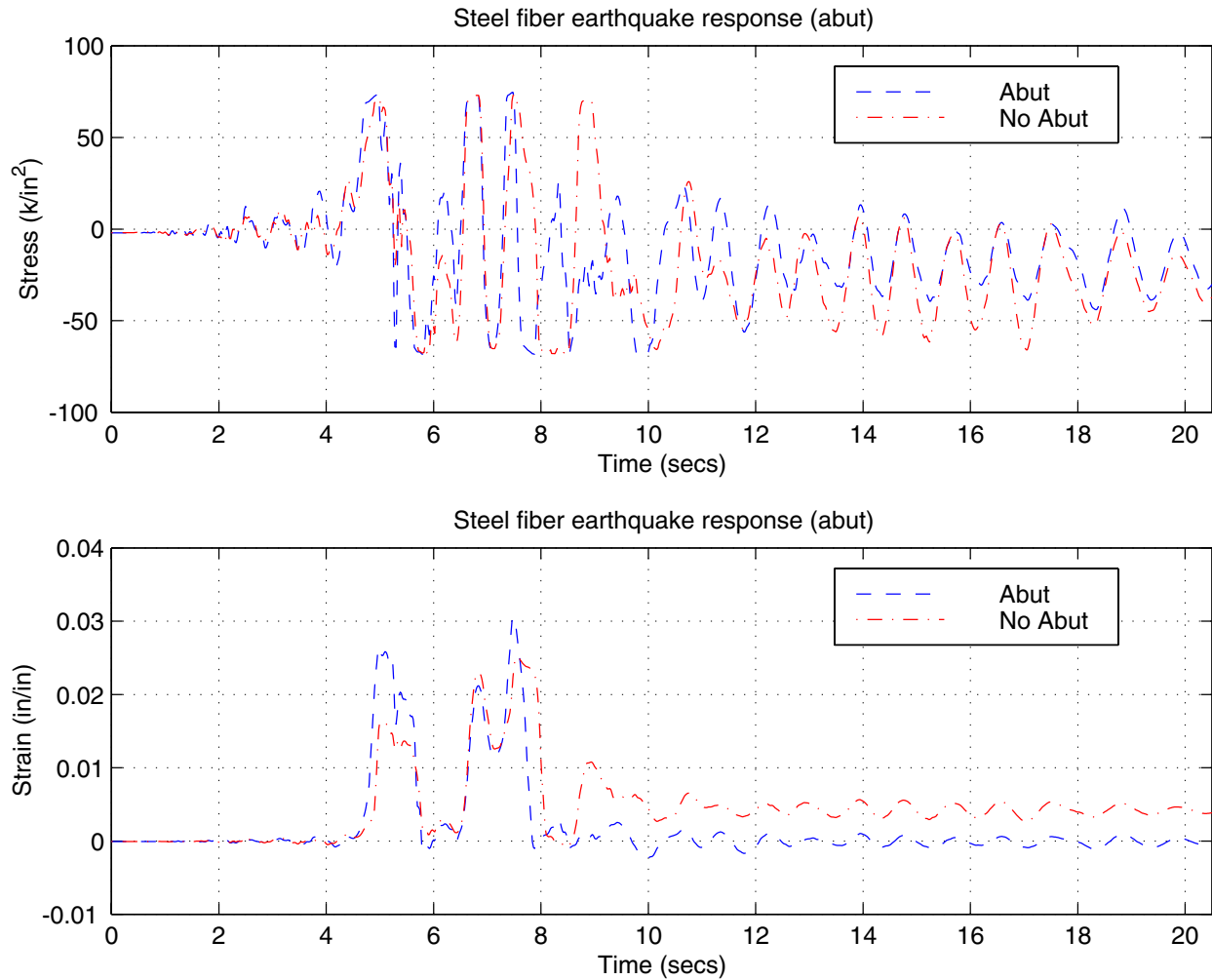


**Fig. 2.31 Extreme steel fiber stress and strain time history**

A sample abutment model (“abut 2”) was introduced to the base bridge configuration and some of the dynamic results are reproduced below for comparison to the roller case. This abutment model introduces only a gap/spring element, therefore, there is no mass modification as with several of the abutment models. Figure 2.30 shows a comparison of displacement time histories at the top of the column.

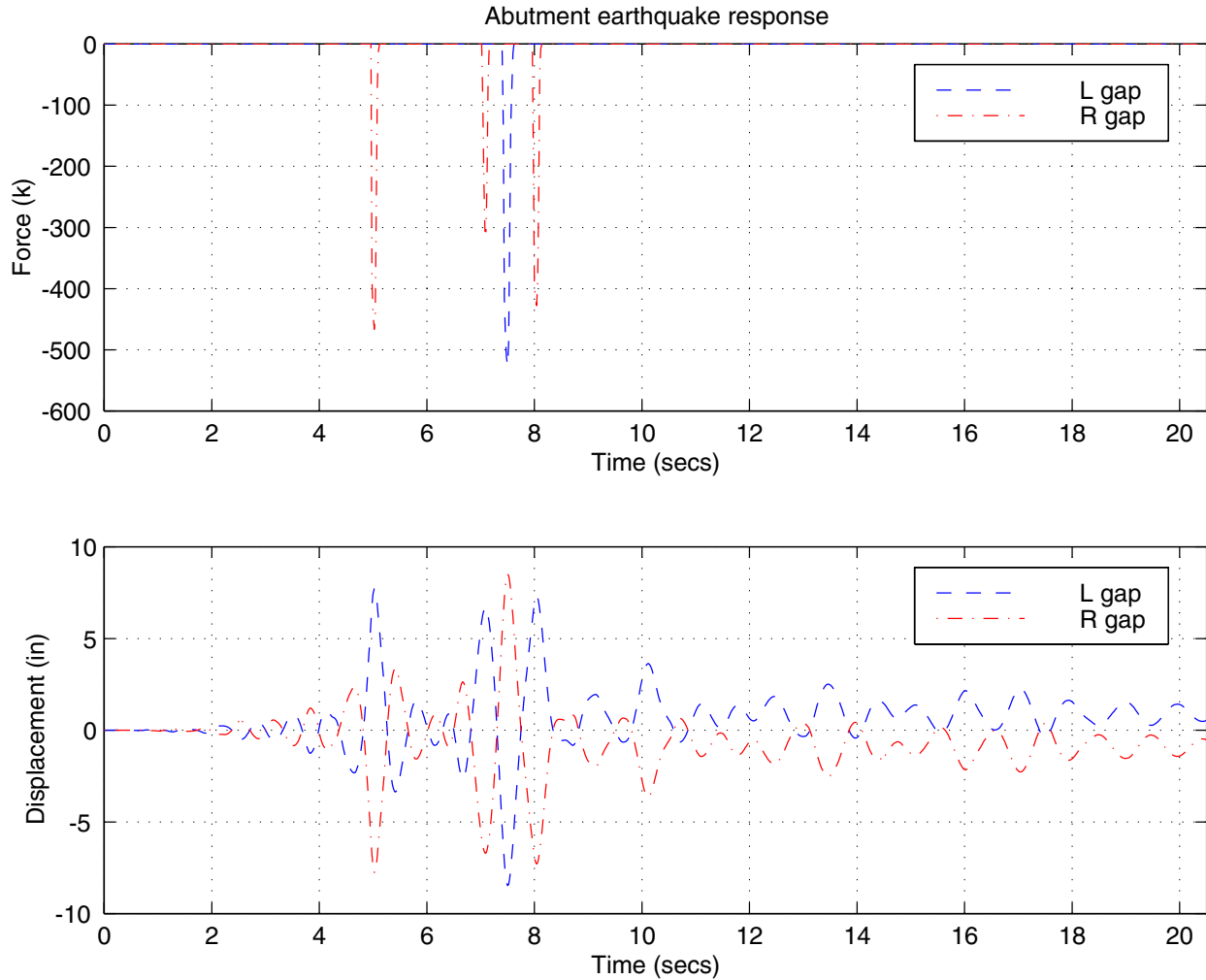


**Fig. 2.32 Abutment gap closure time history plot**

Any number of response quantities can be extracted from the model for post-processing. One such automated extraction routine examines the time histories for extreme steel and concrete fibers in the column. A sample stress and strain comparison for a particular steel fiber is shown in Figure 2.31. Finally, in any of the abutment models, response at the abutments can also be examined. Force-deformation relations will follow those material models described in the Abutment section (Section 2.4.3), however, force and displacement time histories can be examined for gap closure in the longitudinal direction. The left gap (L gap) generated a force only when the gap (6" in this case) was exceeded. Similarly, the displacement history for the right gap (R gap) case is reversed, and this gap closes when displacements occur in the opposite direction (Fig. 2.32).

## 2.6 PSDA INTENSITY MEASURES AND ENGINEERING DEMAND PARAMETERS

The final step in PSDA is to combine all the analyses of interest into PSDMs, which relate ground motion specific intensity measures (IM) to class-specific structural engineering demand parameters (EDP). Given the wide array of IMs and EDPs for every analysis, it was critical to select an optimal PSDM so as to narrow the amount of data processed.

The ground motion IMs used in this study are shown in Table 2.6. They range from spectral quantities, across duration and energy related quantities, to frequency content characteristics. Each IM is ground motion specific and independent of the bridge model, except for period-based spectral quantities. The IMs were derived primarily from those geotechnical quantities listed in Kramer [Kramer 1996]. All of the spectral quantities were calculated given the first and second mode bridge periods from the modal analysis. As listed below, the only post-earthquake spectral quantity is the inelastic spectral displacement using the damaged natural periods.

**Table 2.6 Intensity measures**

IM	Name	Formula	Units
$D$	Duration	-	s
$M_w$	Magnitude	-	-
$R$	Epicentral distance	-	km
$T_D$	Strong motion duration	$t(0.95I_A) - t(0.05I_A)$	s
$PGA$	Peak ground acceleration	$\max \ddot{u}_g(t) $	g
$PGV$	Peak ground velocity	$\max \dot{u}_g(t) $	cm/s
$PGD$	Peak ground displacement	$\max u_g(t) $	cm
$T_1, T_2$	Natural vibration periods	-	s
$T_{1dmg}, T_{2dmg}$	Post-eqk vibration periods	-	s
$Sa$	Elastic spectral acceleration, 5% damping	-	cm/s <sup>2</sup>

**Table 2.6—Continued**

IM	Name	Formula	Units
$S_v$	Elastic spectral velocity, 5% damping	-	cm/s
$S_d$	Elastic spectral displacement, 5% damping	-	cm
$S_{d,inelastic}$	Inelastic spectral displacement, 5% damping, 50k yield strength	-	cm
$S_{d,dmg,inelastic}$	Damaged inelastic spectral displacement, 5% damping, 50k yield strength	-	cm
$I_A$	Arias Intensity	$\frac{\pi}{2g} \int_0^D [\ddot{u}_g(t)]^2 dt$	cm/s
$I_v$	Velocity Intensity	$\frac{1}{\dot{u}_{g,max}} \int_0^D [\dot{u}_g(t)]^2 dt$	cm
CAV	Cumulative absolute velocity	$\int_0^D  \ddot{u}_g(t)  dt$	cm/s
CAD	Cumulative absolute displacement	$\int_0^D  \dot{u}_g(t)  dt$	cm
$A_{rms}$	Root mean square acceleration	$\sqrt{\frac{1}{T_D} \int_0^{T_p} [\ddot{u}_g(t)]^2 dt}$	cm/s <sup>2</sup>
$I_c$	Characteristic intensity	$A_{rms}^{1.5} T_D^{0.5}$	cm/s
$FR_1$	Frequency ratio 1	$\frac{\dot{u}_{g,max}}{\ddot{u}_{g,max}}$	s
$FR_2$	Frequency ratio 2	$\frac{u_{g,max}}{\dot{u}_{g,max}}$	s
$S_a, Cordova$	Sa predictor [Cordova 2000]	$Sa(T_1) \sqrt{\frac{Sa(2T_1)}{Sa(T_1)}}$	cm/s <sup>2</sup>

The bridge EDPs were chosen from the PEER database of experimental results for concrete bridge components [Hose 2000, PEER Capacity Catalog]. The database details specific discrete limit states for each of the EDPs considered. By mirroring the component database, it is possible to directly evaluate damage in a bridge, given the analysis demands. This method suffers from only having discrete limit states for comparison, but it does provide a direct correlation between demand and damage, as required in Equation 1.1. The engineering demand parameters range from global, such as drift ratio, to intermediate, such as cross-sectional curvature, to local, such as material strains. Several other descriptive measures were also added to assess the loading (axial load ratio) and relative strength of the bridge (R factors). The axial load ratios range from 7.9% to 12.6% and the R factors range from 1 to 11.6. All the EDPs in this study are shown in Table 2.7. For the equations defining the strength reduction factors,  $m$  is the total mass of the bridge column and superstructure.  $F_y'$  is the yield force obtained from Figure 2.23.

**Table 2.7 Engineering demand parameters**

Name	Formula	Units
Axial load ratio	$ALR = \frac{P}{f'_c A_g}$	%
Yield displacement	$u_y$	In.
Yield curvature	$\phi_y$	1/in.
Yield energy	$E_y = \int_0^{u(\max(F))} F(u) du$	k-in.
Maximum displacement	$u_{\max} = \max( u(t) )$	In.
Drift ratio	$\Delta = \frac{u_{\max}}{H}$	%
Maximum curvature	$\phi_{\max} = \max( \phi(t) )$	1/in.
Maximum moment	$M_{\max} = \max( M(t) )$	k-in.
Maximum steel strain	$\epsilon_{s, \max} = \max( \epsilon_s(t) )$	%
Maximum steel stress	$\sigma_{s, \max} = \max( \sigma_s(t) )$	ksi

**Table 2.7—Continued**

Name	Formula	Units
Maximum concrete strain	$\varepsilon_{c,max} = \max( \varepsilon_c(t) )$	%
Maximum concrete stress	$\sigma_{c,max} = \max( \sigma_c(t) )$	ksi
Residual displacement	$u_{resid} =  u(t_{max}) $	in.
Residual displacement index	$RDI = \frac{u_{resid}}{u_y}$	%
Hysteretic energy	$HE = \oint_{\theta} M(\theta) d\theta$	k-in.
Normalized hysteretic energy	$NHE = \frac{HE}{E_y}$	%
R factor (capacity spectrum)	$R_{CS} = \frac{m \cdot Sa_{avg,bin}(T)}{F'_y}$	-
R factor (USGS)	$R_{USGS} = \frac{m \cdot Sa_{2\%-50\%year}(T)}{F'_y}$	-
Displacement ductility	$\mu_{\Delta} = \frac{u_{max}}{u_y}$	-
Curvature ductility	$\mu_{\phi} = \frac{\phi_{max}}{\phi_y}$	-
Plastic rotation	$\theta_{pl} = \frac{u_{max} - u_y}{H}$	rad

In each subsequent PSDM figure, the data were plotted in log-log scale, with the demand measure on the abscissa and the intensity measure on the ordinate (Fig. 1.2). This is a standard method for plotting any IM-EDP relationship (stemming from a pushover curve axis designation) even though the demand measure is regarded as the dependent variable in all the models. Each demand model was constructed in the longitudinal and transverse directions independently. Where applicable, the demand model was also generated for the vertical direction, although these were not the focus of attention for developing optimal models.

### 3 Optimal Models

This chapter addresses the search for an optimal PSDM among the possible IM (Table 2.6) and EDP (Table 2.7) combinations. Optimal is defined henceforth as being practical, sufficient, effective, and efficient. An IM-EDP pair is “practical” if it has some direct correlation to known engineering quantities and makes engineering sense. Specifically, IMs derived from known ground motion parameters and EDPs from resulting nonlinear analysis are practical. Correlation between analytical models and experimental data lend further practicality to the EDPs of the demand model. A further criterion for evaluating practicality is whether or not the IM is readily described by available attenuation relationships or other sources of hazard data.

As discussed in Equation 1.1, the PEER performance-based design framework achieves de-aggregation of the hazard and demand model if and only if the IM-EDP pair does not have a statistical dependence on ground motion characteristics, such as magnitude and distance. Such demand models with no conditional dependence are termed “sufficient” [Cornell 2002]. Sufficiency is further investigated in the sample models presented below.

“Effectiveness” of a demand model is determined by the ability to evaluate Equation 1.1 (or Eq. 1.2) in a closed form. For this to be accomplished, it was assumed the EDPs followed a log-normal distribution [Shome 1999]. Thus an equation describing the demand model can be written as Equation 3.1.

$$EDP = a(IM)^b \quad (3.1)$$

to which a linear, or piecewise-linear, regression in log-log space can be applied to determine the coefficients (Eq. 3.2). Demand models lending themselves to this form allow closed-form integration of Equation 1.1 and casting the entire framework in an LRFD type format [Yun 2002]. An example of such an implementation is the SAC project [Cornell 2002, FEMA 2000b]

for steel moment frames that proved to be crucial for wide adoption of probabilistic performance-based design in practice.

$$\ln(EDP) = A + B \ln(IM) \quad (3.2)$$

“Efficiency” is the amount of variability of an EDP given an IM. Specifically, linear regression provides constants in Equation 3.2, as well as the distribution of data about the linear, or piecewise linear, fit (example shown in Fig. 1.2). The measure used to evaluate efficiency is the dispersion (Eq. 3.3), defined as the standard deviation of the logarithm of the demand model residuals [Shome 1999]. Equation 3.3 is for the case of a bilinear least squares fit. An efficient demand model requires a smaller number of nonlinear time-history analyses to achieve a desired level of confidence. In general, dispersion is a measure of randomness, or aleatory uncertainty, but is not the only source of uncertainty. Not investigated in this study was the epistemic uncertainty derived from such issues as modeling, nonlinearity, approximate analysis methods, and limited number of ground motions considered [Cornell 2002].

$$\sigma = \sqrt{\frac{\sum_{i=1}^n (\ln(EDP_{i,fit}) - \ln(EDP_i))^2}{n-3}} \quad (3.3)$$

The use of bilinear and linear fitting routines were made in the data presented in this report. Some PSDMs lend themselves to bilinear fits in order to reduce the calculated dispersion.

The traditional relation between peak ground acceleration and structural response is practical, but is neither efficient nor effective across larger period ranges. A number of intensity measure-demand measure pairs presented in the literature in recent years have been aimed at performance-based design of buildings. Thus, a principal milestone in the development of a PSDM for highway overpass bridges is the search for an optimal intensity and demand measure pair for this class of structures.

Several important distinctions should be made regarding the choice of IMs in the PSDMs of this chapter. First, efficiency is not the only measure for evaluation of optimality. Therefore, while some models exhibit lower dispersions than others, this alone does not make them optimal. Careful attention should be paid to practicality, effectiveness, and sufficiency. Second, among

the models that *are* deemed optimal (specifically, they are practical, effective, and efficient), dispersion then becomes the measure of which PSDM is considered the “best.” PSDMs with dispersions on the order of 0.20 to 0.30 are considered superior. However, the final PSDM selected not only exhibits all of these characteristics, but also does so for PSDMs generated for structures across a wide range of periods (see Section 4.5).

### 3.1 SAMPLE OPTIMAL PSDMS

Presented below is a small subset of the parametric study, focusing on the parameters that produce an optimal demand model. All of the design parameters presented are in reference to a base bridge configuration. The base configuration includes two 18.2 m (60 ft) spans, a single-column bent 7.6 m high (30 ft), with a 1.6 m (5.25 ft) diameter circular column, 2% longitudinal reinforcement, and 0.7% transverse reinforcement. Only one parameter was varied from the base configuration at a time. The range of values for each design parameter was intended to cover the complete spectrum of possible bridge designs, even if independent values are uncommon in design practice. The base bridge was on a USGS class B (NEHRP C) soil site. Design parameters referenced in this chapter were limited to the percent of column longitudinal reinforcement ( $\rho_{s, long}$ ), column- to superstructure-depth ratio ( $D_c/D_s$ ), and unconfined concrete strength ( $f'_c$ ). The  $R_{CS}$  factors for the base bridge (LMSR bin) are 2.4 and 2.9 for the longitudinal and transverse directions, respectively. For the SMLR bin, the  $R_{CS}$  factors drop to unity (earthquakes do not produce inelastic behavior). The  $R_{USGS}$  factors for the base bridge are 4.8 and 5.6 for the longitudinal and transverse directions, respectively.

Given the varying engineering usefulness of each of the EDPs calculated, an optimal demand model for each was developed. Several of the computed engineering demand parameters were mutually dependent and one was neglected. For example, displacement ductility and drift ratio are related by a constant (yield displacement). Residual displacements yielded poor IM-EDP relationships and were therefore also neglected (see Chapter 4). The remaining EDPs considered can be categorized as either local, intermediate, or global.

### 3.1.1 Local Engineering Demand Parameters

Local demand quantities, such as material stress in the column, proved to be good performance indicators. Peak stress values in both steel and concrete materials were computed at the critical column cross section. In order to maintain comparability with the other EDPs considered, a PSDM for steel stress ( $\sigma_{\text{steel}}$ ) was first developed using  $\rho_s$  (Fig. 3.1) and  $D_c/D_s$  (Fig. 3.2) as the parameters of variation. These produce very efficient fits, largely due to the plateauing behavior at high stress levels. The bilinear fits largely reflect a bilinear material stress-strain envelope when the strain is thought of as a function of earthquake intensity. In either case, stronger and stiffer bridges show trends toward reduced demand.

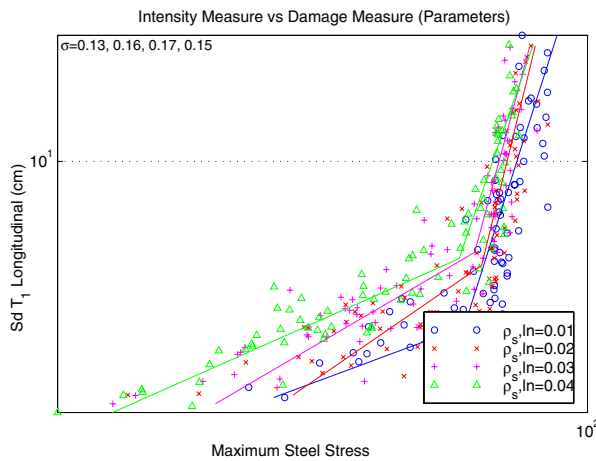


Fig. 3.1  $Sd_{T1}$ - $\sigma_{\text{steel}}$ ,  $\rho_s$  sensitivity longitudinal

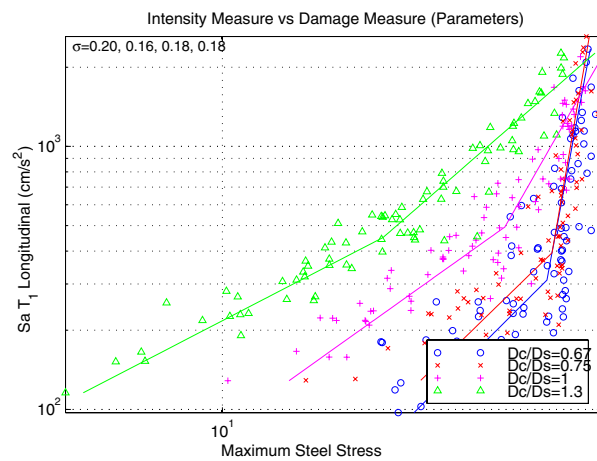
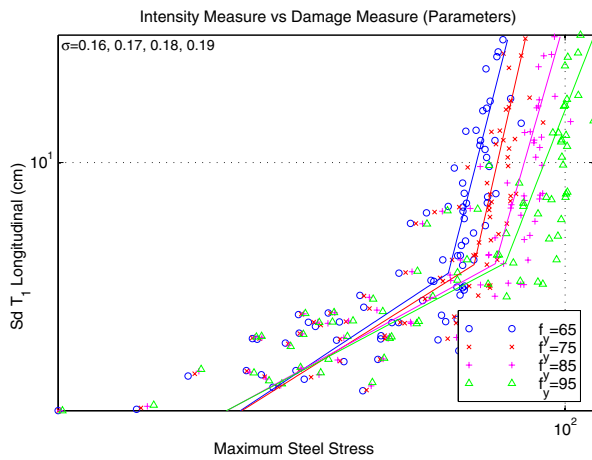


Fig. 3.2  $Sa_{T1}$ - $\sigma_{\text{steel}}$ ,  $D_c/D_s$  sensitivity longitudinal

While fundamental mode periods were roughly equivalent for variation of the longitudinal reinforcing ratio, the use of  $Sd$  can be confusing, since changing design parameters also modifies the bridge period (e.g., stiffness in the  $D_c/D_s$  case, Fig. 3.2). In the  $\rho_s$  case (Fig. 3.1), a line of constant intensity can be drawn across the plot to determine performance. However, this cannot be done with  $Sa$  in Figure 3.2. Therefore, an IM was sought which was necessarily independent of the period, but still exhibited properties of an optimal PSDM. Results indicate the use of Arias intensity or PGV as period-independent IMs yield models with dispersions approximately 50% higher than  $Sd$ .

An instructive PSDM is developed when the steel yield strength and concrete compressive strength were varied parametrically. As may be expected, these models were

efficient and effective. Steel stress and concrete stress models are shown in Figures 3.3 and 3.4, respectively. Similar to the previous steel stress model (Fig. 3.2), the bilinear steel stress-strain diagram becomes apparent in the results. Specifically, changing the yield strength has no effect on performance in the elastic range. However, as the yield strength increases, so does the amount of stress attracted. The concrete stress PSDM yields interesting behavior, as the separate maximum trends of unconfined and confined concrete can be discerned. Therefore, each value of  $f'_c$  depicts two plateau regions. As with steel, the stronger designs attract more stress.



**Fig. 3.3**  $Sd_{TI}$ - $\sigma_{steel}, f_y$  sensitivity

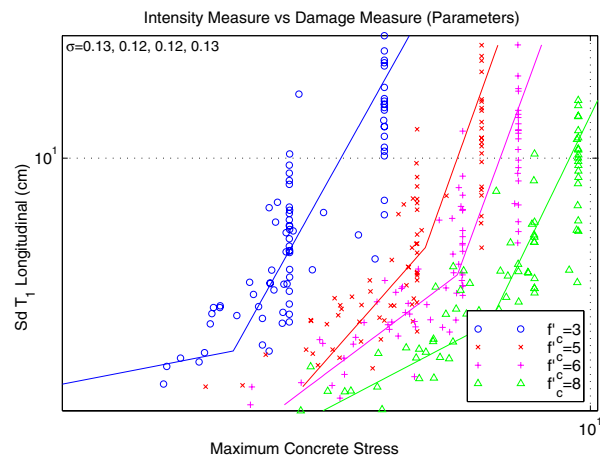


**Fig. 3.4**  $Sd_{TI}$ - $\sigma_{concrete}, f'_c$  sensitivity

While all of the local stress-based PSDMs developed show good qualities in terms of effectiveness and efficiency, none of them are practical from an engineering testing standpoint. At a local level, the only measure quantifiable during experimentation is strain. Deriving stress from this quantity would require analytical material models. Therefore, PSDMs using local material strains were also investigated, but not shown here due to their lack of efficiency. The steel strain model dispersion changes minimally between the use of  $Sd_{TI}$ ,  $PGV$ , or Arias intensity as the IM. The steel model shows stiffer designs reduce demand, while the concrete strain model shows a similar trend for stronger designs. The increase in dispersion when using strain-based PSDMs (on the order of 100%) over stress-based PSDMs was enough to direct attention to the intermediate and global engineering demand parameters.

### 3.1.2 Intermediate Engineering Demand Parameters

Figure 3.5 shows the ensuing PSDM for maximum moment in the longitudinal direction. The optimal IM for parametric variation of column diameter- to superstructure depth- ratio ( $D_c/D_s$ ) was first mode spectral displacement ( $Sd_{T1}$ ). Spectral displacement of the second mode period ( $Sd_{T2}$ ) provides an appropriate extension of this relationship to the transverse direction (Fig. 3.6), although it should be noted that  $T_1$  can be used in place of  $T_2$  in the transverse direction and still maintain efficiency. The determination of optimal period is investigated in Section 4.3. As would be expected, the stiffer the column was made, the more force it attracted. More flexible structures resulted in higher dispersion. Results indicate the use of Arias intensity or PGV yields models with dispersions approximately 40% higher than  $Sd_{T1}$ . In addition,  $PGV$  and Arias intensity demand models exhibit higher dispersion for stiffer structures, indicating unpredictable behavior of these IMs except in the extreme low period regime ( $T < 0.3$  sec).

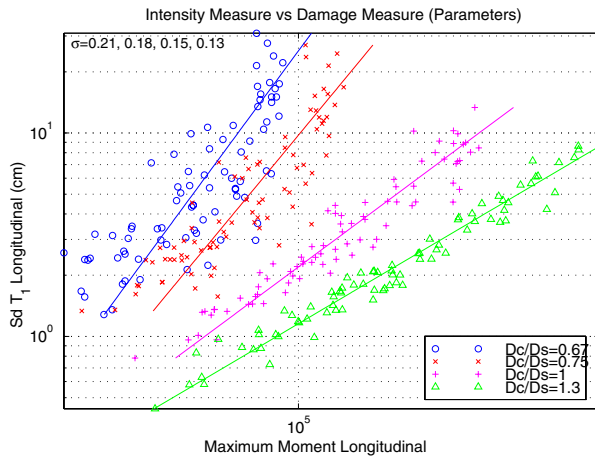


**Fig. 3.5**  $Sd_{T1}$ - $M_{max}$ ,  $D_c/D_s$  sensitivity longitudinal

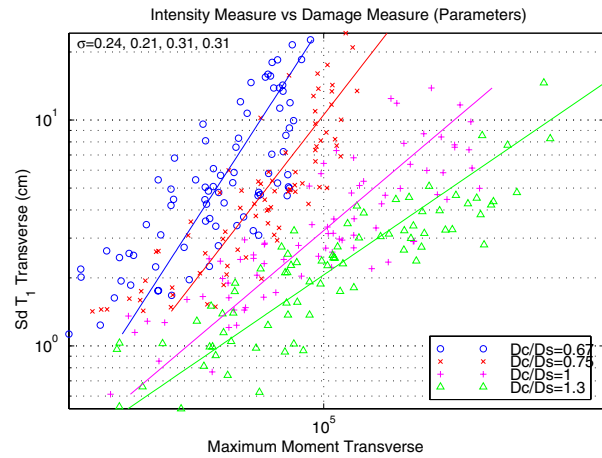


**Fig. 3.6**  $Sd_{T1}$ - $M_{max}$ ,  $D_c/D_s$  sensitivity transverse

It should be noted that there was a strong sensitivity of the optimal IM-EDP pair to the period (stiffness) of the structure under consideration. This trend was exhibited between stiffer/stronger structures and the demand model dispersion values. Figures 3.5–3.8 are typical, showing reduction in dispersion as the stiffness/strength of the structure was increased (by

design parameter variation). Some IMs were more susceptible to this increase, specifically period independent measures such as Arias intensity, cumulative absolute velocity (CAV), and *PGA*. The dependence of efficiency on the design parameter (and hence system period) is investigated more systematically in Section 4.5. The need for an IM that is independent of this phenomenon motivates the robustness requirement for an optimal IM.

Column curvature ductilities are investigated next. The most efficient and effective fits were once more obtained by using  $Sd_{T1}$  as the IM. The PSDM varying  $D_c/D_s$  for curvature ductility is shown in Figure 3.7,  $Sa_{T1}$  as the IM for an example (spectral quantities can be used interchangeably). Dispersions were roughly independent of selection of either  $D_c/D_s$  or  $\rho_s$ . The large period dependence of the dispersions in this model should be noted. As discussed earlier, it may be useful for the designer to consider period-independent parameters. Therefore, to eliminate  $Sd$  intensity shifts due to variation in  $T_1$ , the use of Arias intensity, Characteristic intensity, or *PGV* as an IM, increases dispersions by approximately 20% over  $Sd_{T1}$ .

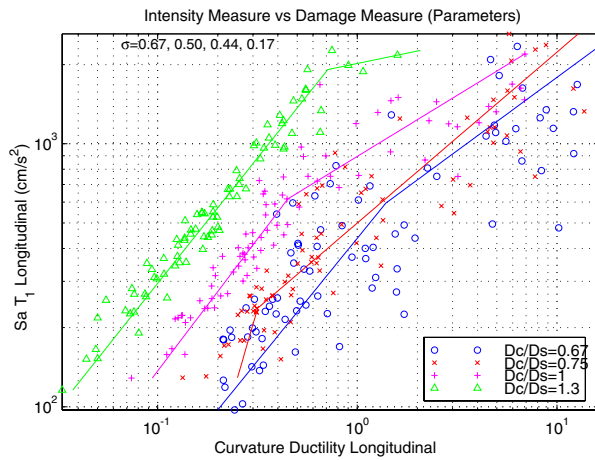


**Fig. 3.7**  $Sa_{T1}-\mu_\phi, D_c/D_s$  sensitivity longitudinal

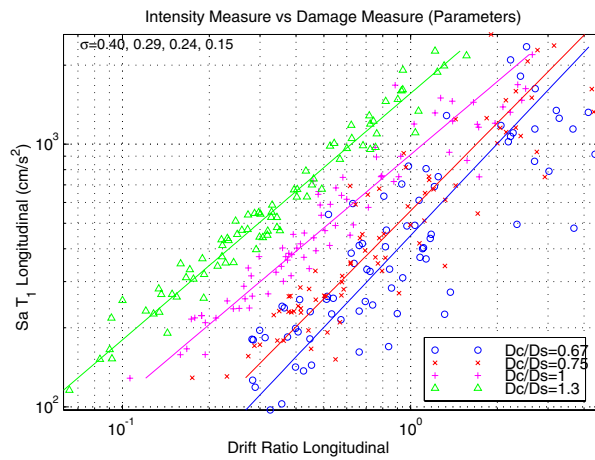


**Fig. 3.8**  $Sa_{T1}-\Delta, D_c/D_s$  sensitivity longitudinal

### 3.1.3 Global Engineering Demand Parameters

The final PSDM developed was for longitudinal drift ratio. The optimal model was obtained by varying  $D_c/D_s$  and again using  $Sa_{T1}$  as the IM (Fig. 3.8). Other possibilities include incorporating Arias intensity, *CAV*, or inelastic spectral displacement of the first mode as the IM. These options increase dispersions by approximately 33%–40% from using  $Sa_{T1}$ . Note the efficiency of

the fit for the high stiffness parameter,  $D_c/D_s = 1.3$ , as would be expected for structures that remain largely elastic.

### 3.2 VERIFYING OPTIMAL MODEL

From the previously discussed models, the relationship between  $Sa_{TI}$  and longitudinal drift ratio for the column diameter ( $D_c/D_s$ ) parameter variation (Fig. 3.8) was selected to investigate other demand model properties. As with any of the models, it is possible to generate not only the mean, but the  $\mu \pm 1\sigma$  (16<sup>th</sup> and 84<sup>th</sup> percentile) distribution stripes. These stripes were calculated as (Eq. 3.4):

$$EDP_{\pm 1\sigma, j} = \sqrt{\left( \sigma \left( 1 + N^{-1} + \frac{(IM_j - \mu(IM))^2}{\sum_{i=1}^N (IM_i - \mu(IM))^2} \right) \right)} \quad (3.4)$$

This probability distribution is shown in Figure 3.9 for the above example case.

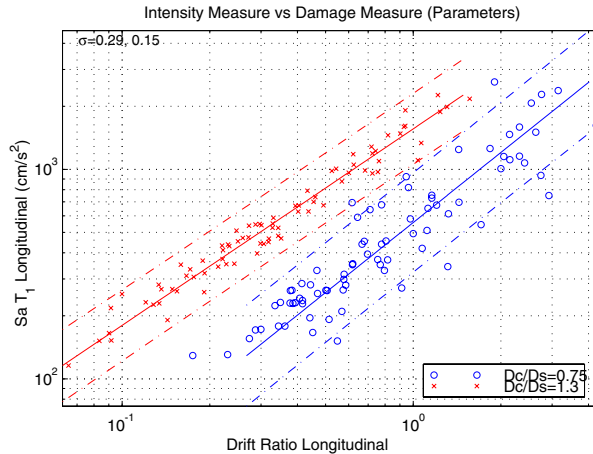


Fig. 3.9  $Sa_{TI}-\Delta, D_c/D_s, \mu \pm 1\sigma$  stripes

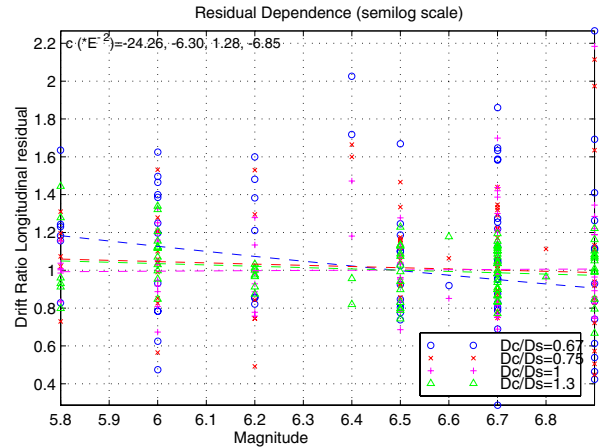


Fig. 3.10  $Sa_{TI}-\Delta, D_c/D_s, M$  dependence

Efficiency and effectiveness have already been established, however; sufficiency and practicality remain to be confirmed. The classification of practicality is, unfortunately, a subjective exercise. In the perception of the EDP holding a particular definition in the engineering sense, maximum material stress is then also practical. However, in terms of

instrumentation and physical test specimens, stress by itself is an indeterminable physical quantity. A clearly practical EDP is the global drift ratio.

Sufficiency is required to determine whether the total probability theorem can be used to de-aggregate the various components of the PEER framework equation. This cannot be done if there are any residual dependencies on  $M$ ,  $R$ , etc. Equation 3.5 can be used if the demand model is statistically independent; otherwise Equation 3.6 must be utilized, necessarily complicating evaluation of Equation 1.1.

$$V_{EDP}(y) = \int P_{EDP|IM}(y|x) |d\lambda_{IM}(x)| dx \quad (3.5)$$

$$V_{EDP}(y) = \iiint P_{EDP|IM,M,R}(y|x,m,r) f_{IM|M,R}(x|m,r) f_{M,R}(m,r) dm dr dx \quad (3.6)$$

To assess this sufficiency, regression on the IM-EDP pair residuals was performed, conditioned on  $M$ ,  $R$ . The same formulation can also be applied to assess dependence on strong motion duration. The resulting sufficiency plots for the PSDM of interest are shown in Figures 3.10 and 3.11. The first takes moment magnitude ( $M_w$ ) from the database of IMs and plots it versus the residual of the chosen IM-EDP fit. Similarly, the second plots residual versus closest distance ( $R$ ). The slopes of the linear regression lines in the plot are shown at the top of each of the plots. Small slope values for all parameters indicate that these demand models have the sufficiency required to neglect the conditional probability as described above.

A more rigorous definition of sufficiency can also be used when the regression lines described above are ambiguous. Fitting of residual data is equivalent to the multivariate linear regression of Equation 3.7.

$$\ln(EDP) = A + B\ln(IM) + C(M) + D(R) \quad (3.7)$$

While median coefficient values are shown in the plots, it is also possible to obtain statistics for an arbitrary confidence interval. If there is no residual dependence on  $M$ ,  $R$ , the coefficients  $C$  and  $D$  are zero somewhere within the defined confidence interval. For purposes of this paper, no residual dependence on a 90% confidence interval is termed sufficient.

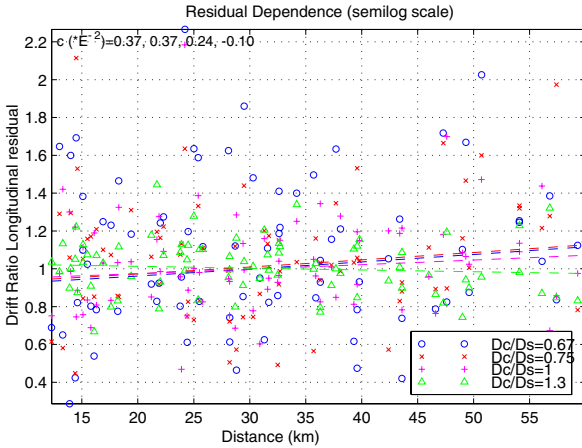


**Fig. 3.11**  $Sa_{TI}-\Delta, D_c/D_s, R$  dependence

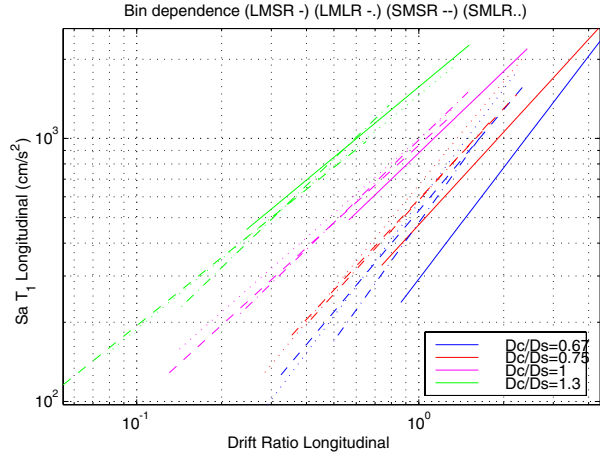


**Fig. 3.12**  $Sa_{TI}-\Delta, D_c/D_s$ , bin dependence

The use of the bin approach also needs to be evaluated to determine what, if any, bias has been introduced into the results from different bins. A seismicity plot was generated by fitting the data based on each of the four bins to the same cloud of points (Fig. 3.13). The regression in this case was too scattered to show any definite trends, however, it can be noted that the higher intensity earthquakes (LMSR) produce higher demand. For a given earthquake intensity, however, the demand should be roughly the same between bins (Fig. 3.14), as can be shown by a structure-independent IM.

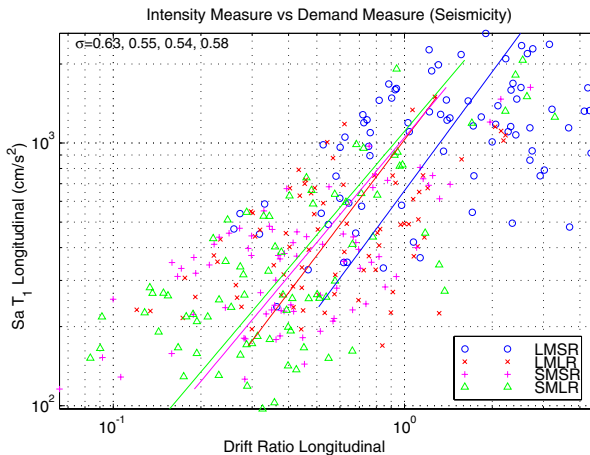


**Fig. 3.13**  $Sa_{TI}-\Delta, D_c/D_s$ , seismicity

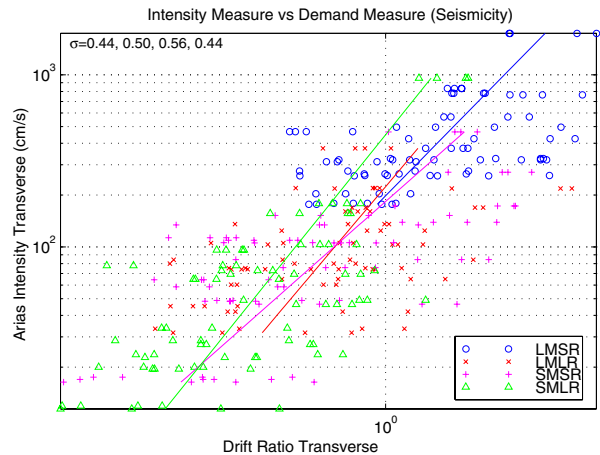


**Fig. 3.14** Arias- $\Delta, D_c/D_s$ , seismicity

In order to uncouple the different design parameter variations in the seismicity plot, it was necessary to plot 16 lines, one for each of the bins and each of the design parameter values

(Fig. 3.12). To minimize the clutter, only linear fit lines are shown; the data points have been removed. In order for the model to be independent of the choice of bins, the lines of same color (corresponding to individual design parameter values) should exhibit the same slope at a given intensity level. As bins have different concentrated ranges of intensities, care should be taken not to bias the slope of the fit lines in these regions.

In summary, it was found that first mode spectral displacement ( $Sd_{T_I}$ ) was the optimal *existing* IM when coupled with a variety of EDPs. These EDPs include local measures (maximum material stresses), intermediate measures (maximum column moment), and global measures (drift ratio). Regardless of the fundamental vibration mode shape,  $T_I$  remains the optimal period at which to sample the spectral quantities. This is useful for avoiding confusion over whether the longitudinal or transverse bridge response is being considered. With a small trade-off in efficiency, the use of period-independent Arias intensity as the IM was also acceptable as an optimal IM. Advantages to using period-independent IMs become readily apparent when varying bridge design parameters (Chapter 4).

The spectral values can be considered as superior IM quantities as they not only incorporate measures of the motion frequency content, but are directly related to modal response of the given structure. Arias intensity does not include this structure-dependent information, but does, however, include the cumulative effect of energy input from the ground motion. There are several practical reasons to utilize Arias intensity though, given that it can be used to compare structures at constant intensity levels, and has been recently described by an attenuation relationship [Travasarou 2002].

As described after the definition of an optimal PSDM, this chapter does not address the issue of finding the lowest dispersion only. Further increases in efficiency of the demand models beyond the basic spectral quantities used here is possible and was further pursued in later chapters using various spectral combinations (Chapter 4). These are not included here as they are only effective and efficient on a case-by-case basis. Also, they are not currently described by attenuation relationships, and are possibly difficult to scale to the same intensity level, making them an impractical choice.

### 3.3 EVALUATION OF NON-OPTIMAL IM-EDP PAIRS

Not all possible IM-EDP pairs can be considered optimal. Primarily, these pairs are discarded when they fail to meet the effectiveness criteria. Characteristic of these PSDMs is the inability to discern any trends, linear or otherwise, in the data, which results in extremely large dispersion values. Subsequently, the PSDMs are also not efficient. Care should also be taken when effective and efficient models are discovered, as they do not necessarily satisfy sufficiency requirements. For any particular class of structures and ground motion bins considered, sufficiency needs to be verified and not necessarily assumed.

#### 3.3.1 Poor Intensity Measures

There were numerous examples of IMs that cause effectiveness problems in PSDMs. This is indicative of the failure of these IMs to correctly capture the content of the earthquake records that is causing structural response. Of particular note were peak ground acceleration ( $PGA$ ), peak ground displacement ( $PGD$ ), velocity intensity ( $I_v$ ), root mean square acceleration ( $A_{rms}$ ), Characteristic intensity ( $I_c$ ), frequency ratio 1 ( $FR_1$ ), and frequency ratio 2 ( $FR_2$ ). Maintaining global drift as the EDP in several optimal PSDMs, the lack of predictor qualities in the aforementioned IMs can be seen in Figure 3.15 ( $PGA$ ) and Figure 3.16 ( $FR_1$ ).

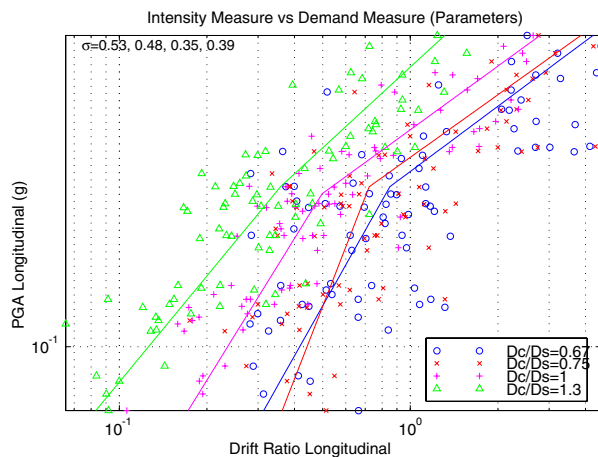


Fig. 3.15  $PGA-\Delta, D_c/D_s$  sensitivity longitudinal

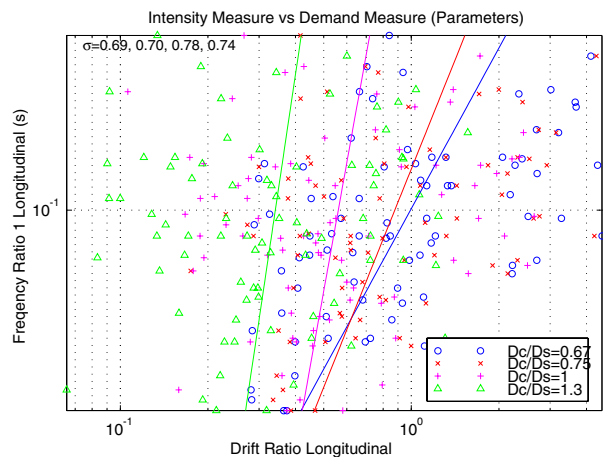
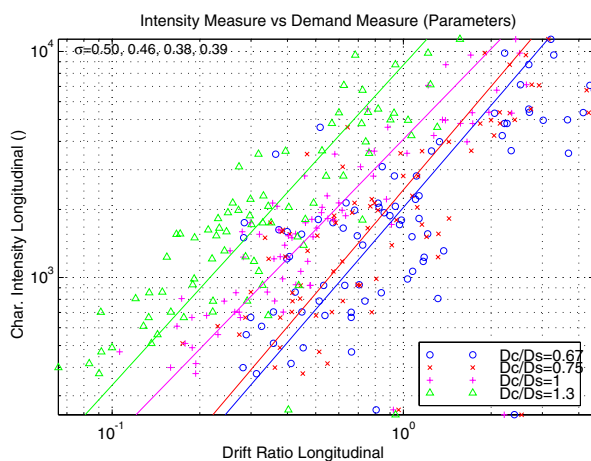


Fig. 3.16  $FR_1-\Delta, D_c/D_s$  sensitivity longitudinal

Several relationships are evident in the poor IM quantities. The first was the use of peak acceleration, velocity, or displacement values rather than the use of a range of values in the record. Depending on the fundamental period of the structure, a larger *PGA* does not necessarily indicate larger response. *PGA* only has good correlation with response of structures with very small periods, as it is a spectral quantity for the zero second period structure. Most of the bridge structures of concern have first mode periods between 0.5 and 1.0 sec, thus explaining lack of correlation with *PGA*. *PGD* is a similar displacement based quantity. When considering pulse or fling type earthquakes, these two IMs may have more correlation to response. The frequency ratio IMs are simply ratios of the various peak values, and therefore do not introduce new information to predict response more accurately.

The second trend of note was the lack of duration quantities in predicting response.  $I_c$  (Fig. 3.17) and  $A_{rms}$  (Fig. 3.18) both use strong motion duration information, coupled with a cumulative measure of the acceleration record, however neither results in useful PSDMs. For these two IMs, the PSDMs exhibited a lack of efficiency and were therefore rejected. The lack of information yielded by duration quantities has been confirmed by other researchers with regard to reinforced concrete column components in bridges [Gardoni 2002] and slope stability and permanent ground deformations in geotechnical engineering [Travasrou 2002].



**Fig. 3.17**  $I_c$ - $\Delta$ ,  $D_c/D_s$  sensitivity longitudinal

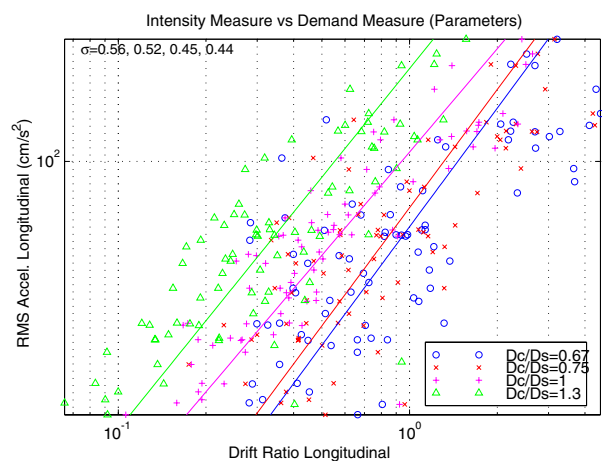


**Fig. 3.18**  $A_{rms}$ - $\Delta$ ,  $D_c/D_s$  sensitivity longitudinal

### 3.3.2 Poor Engineering Demand Parameters

Similarly, some of the EDPs considered in this study independently (of the IM used) cause a non-effective PSDM. When coupled with a spectral IM quantity, it was found that residual displacement, *RDI*, hysteretic energy, and normalized hysteretic energy all generated poor PSDMs. As residual displacement and *RDI* are related by yield displacement, and hysteretic energy and *NHE* by yield energy, they are both statistically dependent quantities. Therefore, the same trends were exhibited in the resulting PSDMs. *RDI* is shown in Figure 3.19 and *NHE* in Figure 3.20.

Residual displacement was poor due to sensitivity to the analysis method used, especially in finite element analysis. Not only this, but *RDI* is also dependent on the earthquake record in an essentially nonlinear manner. Even large magnitude earthquakes causing highly nonlinear response can have zero residual displacement. Conversely, earthquakes with lower intensities may cause permanent displacement. Using SDOF oscillators, residual displacement was found to depend on the shape of the material hysteretic behavior [Kawashima 1998], not stiffness, mass, or earthquake bin. *RDI* then effectively becomes another structure-dependent intensity measure, as it indicates the cumulative effect of yield excursions at each given location in the material constitutive laws.

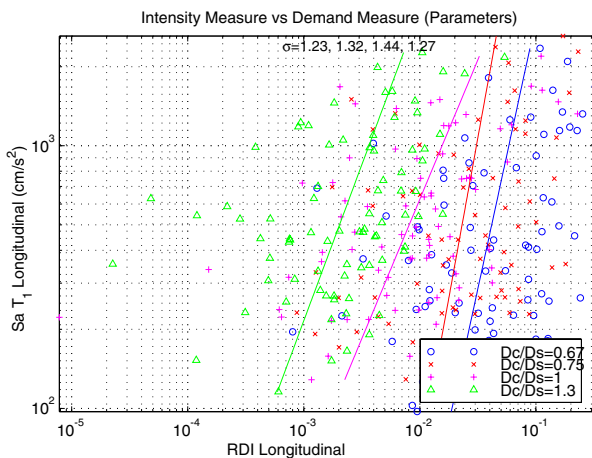


**Fig. 3.19** *Sa<sub>T1</sub>-RDI, D<sub>c</sub>/D<sub>s</sub> sensitivity longitudinal*

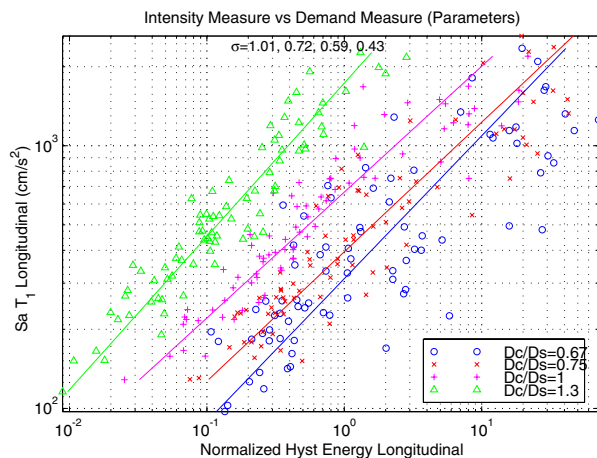


**Fig. 3.20** *Sa<sub>T1</sub>-NHE, D<sub>c</sub>/D<sub>s</sub> sensitivity longitudinal*

### 3.4 VECTOR INTENSITY MEASURES

Of further interest in the pursuit of optimal PSDMs is the selection of a vector of IM quantities rather than a single scalar value. The purpose of selecting this vector is to better describe the content of the ground motion that influences structural performance. By finding a better predictor, it is possible to use fewer ground motion records to obtain a desired level of confidence in the model dispersion. The trade-off being Equation 1.1 can no longer be de-aggregated as there are conditional probabilities associated with the IMs in the vector.

While not performed explicitly in this study, using the results and supplied visualization routines, it is possible to investigate a two-component vector IM. A sample vector IM PSDM is shown in Figure 3.21. The second IM component was chosen as the ratio of spectral displacements. The denominator was chosen as  $Sd$  at  $T_2$ , however, it could be arbitrarily selected at a period that is expected to provide better correlation with the EDP of interest. The ratio of spectral quantities doesn't increase as the records are scaled (PSDM produced using IDA analysis method).

Instead of fitting a line through the data, a best fit plane is sought. Since the spectral ratio doesn't increase with scaling, it was possible to take a slice through a  $Sd_{T1}/Sd_{T2}$  plane (look down the  $Sd_{T1}/Sd_{T2}$  axis) and plot the resulting 2D array of data in log-log space (Fig. 3.22). The resulting PSDM was in the same format as those investigated in this chapter and can be analyzed accordingly. Although not shown in Figure 3.22, the dispersion values were 0.26, 0.31, 0.26, and 0.32, respectively. These are comparable to the standard 4-record IDA (see Chapter 5) used to produce the basic  $SdTI-\Delta$  PSDM; therefore no dispersion gain is realized in this example.

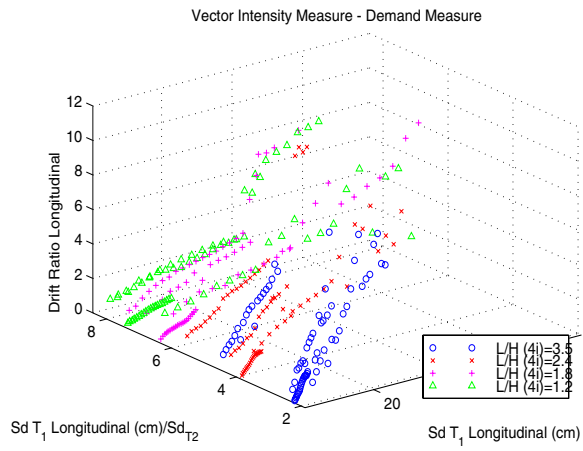


**Fig. 3.21** *Sd* vector (3D), *L/H* longitudinal

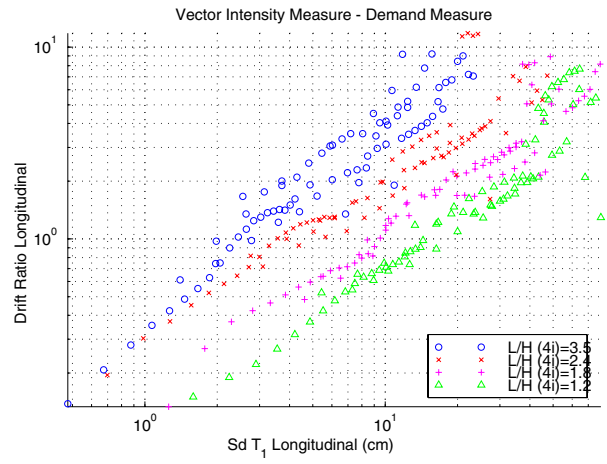


**Fig. 3.22** *Sd* vector (2D), *L/H* longitudinal

## 4 Design Parameter Sensitivity

This chapter investigates the use of the PSDM as a tool for evaluating performance changes resulting from the variation of bridge design parameters. Split into two sections, the first section of the chapter focuses on single-bent bridges with roller abutments, and the second focuses on the same single-bent bridges, but includes an analytical abutment model.

### 4.1 DESIGN PARAMETER SENSITIVITY: MODEL WITHOUT ABUTMENTS

All of the parameters presented are in reference to the same base bridge configuration as in the Optimal chapter (Chapter 3). This configuration was two 18.2 m (60 ft) spans, a single-column bent 7.6 m above grade (30 ft), with a 1.6 m (5.25 ft) diameter circular column, 2% longitudinal reinforcement, 0.7% transverse reinforcement, USGS class B (NEHRP C) soil, and a Type I pile shaft foundation. Once again, the variation of design parameters from this base configuration (Table 2.1) was intended to cover the complete spectrum of possible bridge designs, even if independent values are uncommon in design practice. Roller conditions are assumed for the abutments. Different abutments models are considered in more detail later in this chapter (Section 4.6).  $R$  factors for the base bridge are listed in Section 3.1.

In the parametric study of this chapter, the IMs were limited to the spectral quantities and Arias intensity only. First mode spectral displacement ( $Sd_{T1}$ ),  $Sa_{T1}$ , and  $Sv_{T1}$  were used interchangeably, as the dispersions in the PSDMs were independent of the choice of spectral quantity. While calibrated for buildings that exhibit definite in-plane mode shapes, it was determined that the IM proposed by Cordova (Table 2.6) also generated effective fits for the bridge model utilized. This IM contains terms to account for both elastic response and inelastic response by including information pertaining to a longer period value than  $T_1$ . The extended

period factor ( $2T_1$ ) is effective in capturing linear fits in the higher intensity range as it can be related to  $\sqrt{\mu_\Delta}$ .

Of the total possible EDP combinations, only a few were selected for the design parameter study. Two global EDPs, used in current bridge design practice, are the column drift ratio ( $\Delta$ ) and displacement ductility ( $\mu_\Delta$ ). These are two kinematically dependent measures that can be used interchangeably in the PSDMs. The other EDPs that yielded optimal PSDMs were maximum column moment ( $M_{max}$ ), and intermediate EDP, and steel material stress ( $\sigma_{steel}$ ), a local EDP.

The consequence of choosing spectral quantities for the demand model is the period dependence of the IM. Since the initial elastic stiffness was used to compute the measure of  $Sd_{T1}$ , design parameters that vary the stiffness of the bridge system will cause intensity shifts in the demand models for a given earthquake. Alternate IMs, which introduced more dispersion, were Arias intensity and PGV. To alleviate the IM period dependence, these IMs can be used when comparing engineering demand parameters. In this case, the result is a single line of constant IM value parallel to the EDP axis that aids direct evaluation of varying design parameters on performance.

**Table 4.1 Bridge first and second mode periods for sample bridge configurations**

Configuration	T <sub>1</sub>	T <sub>2</sub>	Configuration	T <sub>1</sub>	T <sub>2</sub>
Base bridge	0.64	0.55	$\rho_{s,long} = 0.01$	0.66	0.58
$L = 27$ m (1080")	1.18	1.00	$\rho_{s,long} = 0.03$	0.62	0.53
$L = 37$ m (1440")	1.87	1.58	$\rho_{s,long} = 0.04$	0.61	0.51
$L = 55$ m (2160")	3.92	3.28	$K_{soil} = A$	0.62	0.53
$L/H = 3.5$	0.48	0.41	$K_{soil} = C$	0.67	0.59
$L/H = 1.8$	0.82	0.72	$K_{soil} = D$	0.79	0.70
$L/H = 1.2$	1.21	1.08	$Wt = 0.25$	0.68	0.59
$D_c/D_s = 0.67$	0.72	0.64	$Wt = 0.5$	0.74	0.64
$D_c/D_s = 1.0$	0.49	0.39	$Wt = 0.75$	0.80	0.69
$D_c/D_s = 1.3$	0.39	0.30	$Wt = 1.50$	0.96	0.83

Specifically, the design parameters used in this study were  $L/H$ ,  $D_c/D_s$ ,  $L$ , and  $K_{soil}$ . They were chosen as they affect the period of the bridge, evident in the period differences within parameter groups (Table 4.1). The initial stiffness of the bridge was only minimally influenced by the amount of reinforcement (longitudinal and transverse) in the reinforced concrete column section. The only parameter that alters the mass, and accordingly the spectral values, is the additional dead weight,  $Wt$ . In order to understand the effect of design parameters, constant intensity lines have been added to the figures below.

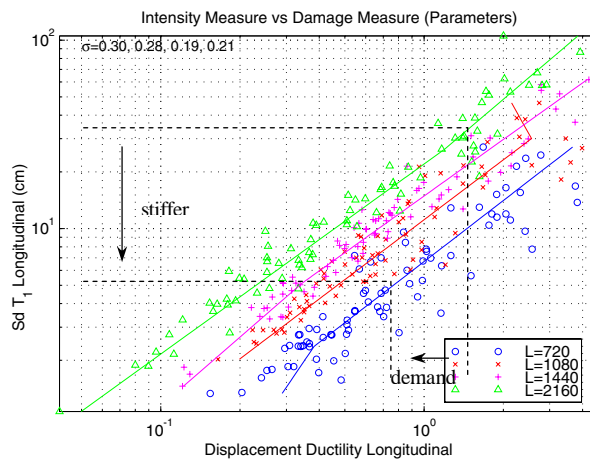


**Fig. 4.1**  $L$  sensitivity,  $Sd_{T1}-\mu_{\Delta}$

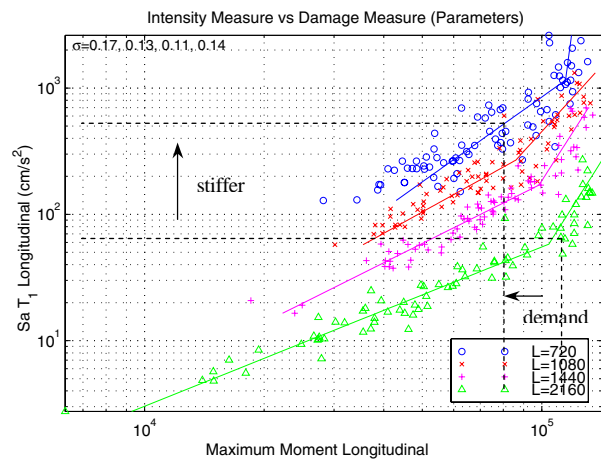


**Fig. 4.2**  $L$  sensitivity,  $Sa_{T1}-M_{max}$

Two optimal models for the span length parameter ( $L$ ) sensitivity are shown in Figures 4.1 and 4.2, respectively. Also shown on the figures are sample design trends when evaluating performance by varying the span length. Reducing the bridge span directly reduces the  $\mu_{\Delta}$  demand. The same was true of  $\Delta$  as they are related by properties of the column (yield displacement). The fits in Figure 4.1 provide desirable relationships, as they are linear, leading to simplified design equations. Figure 4.2 is typical of the reduced dispersion obtained by a bilinear least-squares fit. Also of note was the trend toward reduced dispersion in more flexible structures, given  $L$ ,  $\mu_{\Delta}$ , and  $Sd$ . This trend was opposite to many other models discussed here.

The span- to column height-ratio ( $L/H$ ) parameter models exhibit the same behavior as span length models when considering  $M_{max}$  and  $\Delta$ . The span was held constant, while column heights were varied to the specification of the parameter. Shown in Figure 4.3 is the model pairing  $\Delta$  with  $Sa_{Cordova}$  using a linear fit. Increasing stiffness results in reduced demand at a given intensity. Figure 4.4 shows the trends in models that use local demand quantities, such as  $\sigma_{steel}$  in this instance. This figure indicates that increased stiffness does not result in improved performance for all intensity levels. As determined in Chapter 3, local EDP models exhibit high efficiency. The slope of the fits corresponds directly to the rate of change of performance (demand). Steep slopes result in minimal demand changes, while shallow slopes produce large demand reductions for small variations in design parameter values.

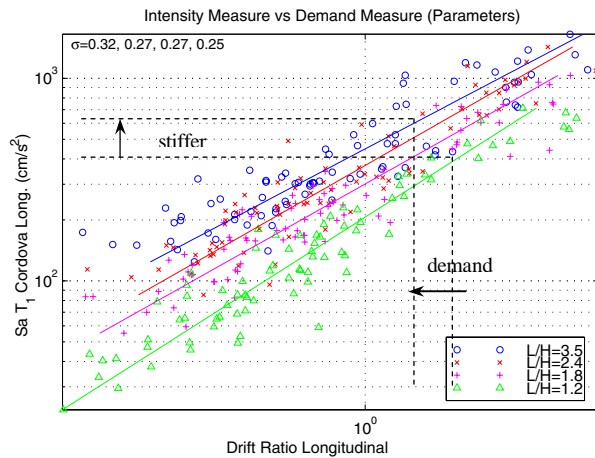


**Fig. 4.3**  $L/H$  sensitivity,  $Sa_{Cordova}$ - $\Delta$

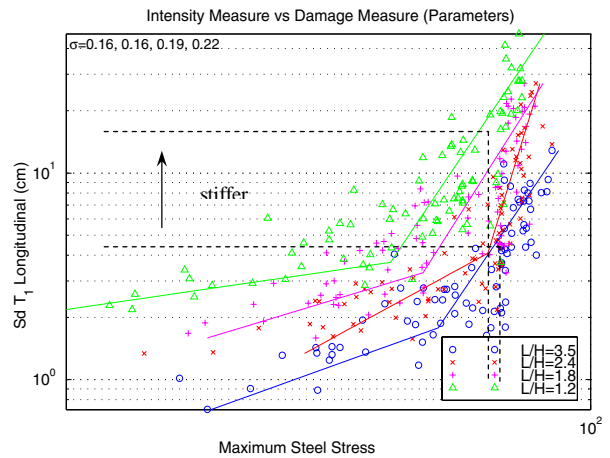


**Fig. 4.4**  $L/H$  sensitivity,  $Sd_{T1}$ - $\sigma_{steel}$

Variation of column-to-superstructure dimension ratio ( $D_c/D_s$ ) was based on varying the column diameter as the superstructure depth and properties were held fixed throughout. Therefore, for higher stiffness columns (larger diameter), a larger performance gain was realized (Figs. 4.5 and 4.6). The design parameter (and thus period) dependent change in dispersions between a period-dependent (Fig. 4.5) and period-independent (Fig. 4.6) IM can be assessed directly. Piecewise linear fits with negative slopes are merely a function of fewer data points in the high-intensity range and subsequent attempts by the bilinear fit algorithm to reduce dispersion.

The steel reinforcement ratio ( $\rho_s$ ) is one of the parameters not causing intensity shifts in spectral plots. The use of the optimized linear IM,  $Sa_{Cordova}$ , allows the reduction in demand to be immediately correlated to the design strength (Fig. 4.7). A linear increase in reinforcement does not correspond to a linear decrease in demand, however. The sensitivity of performance at lower reinforcing ratios was more pronounced. Similarly for forces, increasing the reinforcing amount has a drastic effect on the amount of moment attracted to the column (Fig. 4.8). Evident are two linear regimes for each design parameter, as may be expected of an idealized bilinear moment-curvature relation of the column cross section.

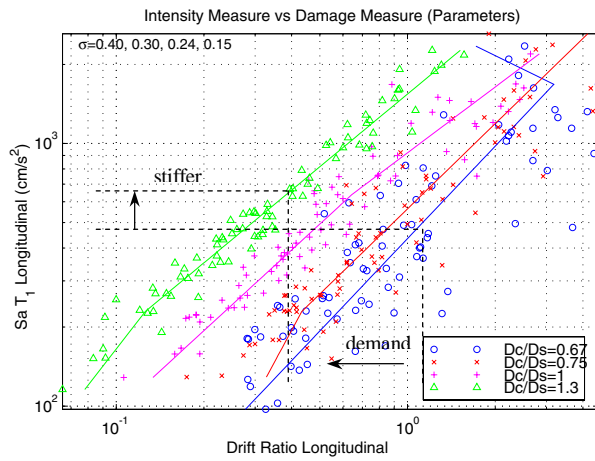


Fig. 4.5  $D_c/D_s$  sensitivity,  $Sd_{T1}-\Delta$

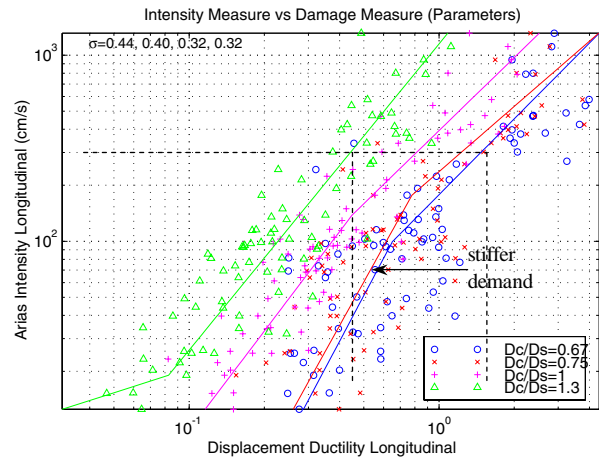


Fig. 4.6  $D_c/D_s$  sensitivity, Arias- $\mu_\Delta$

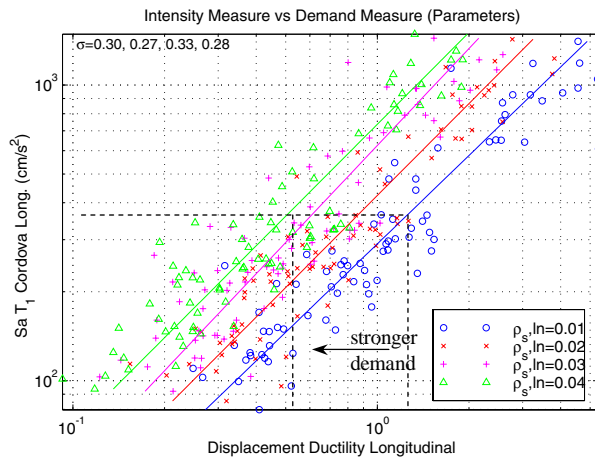


Fig. 4.7  $\rho_s$  sensitivity,  $Sa_{Cordova}-\mu_\Delta$

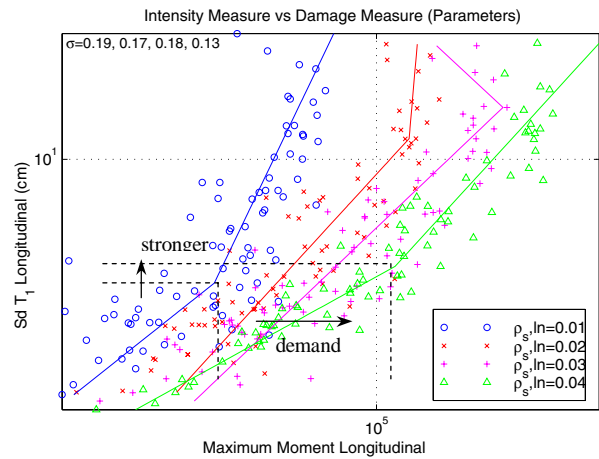


Fig. 4.8  $\rho_s$  sensitivity,  $Sd_{T1}-M_{max}$

As seen in Table 4.1, the small change in period attributed to bridge mass results in a similarly small moment demand reduction. However, when a large mass was considered (150%), significant P- $\Delta$  effects caused an increase in moment demand, as shown in Figure 4.9. In the context of the response spectrum, larger mass can be equated with a flexible structure, or longer period. Similar to Figure 4.2 then, dispersions decrease with longer-period design parameter models, however, the period ranges covered by these parameters are significantly longer than any of the other parameters considered. This phenomena was independent of whether a force- or displacement-based EDP was used, given the  $L$  or  $Wt$  design parameter.

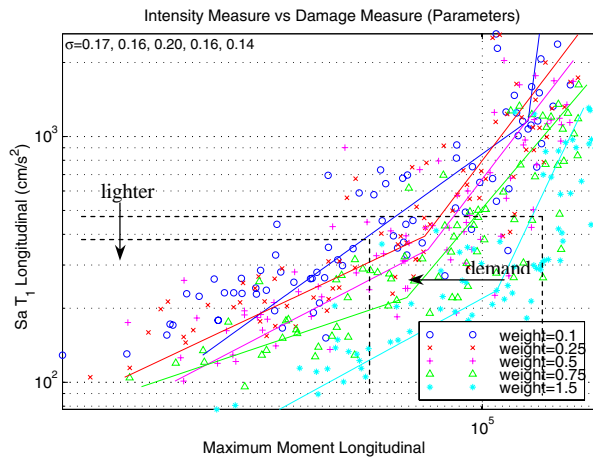


Fig. 4.9  $Wt$  sensitivity,  $Sa_{T1}-M_{max}$

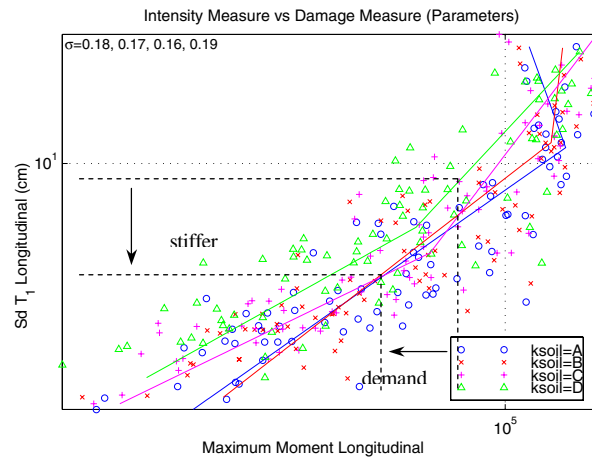


Fig. 4.10  $K_{soil}$  sensitivity,  $Sa_{T1}-M_{max}$

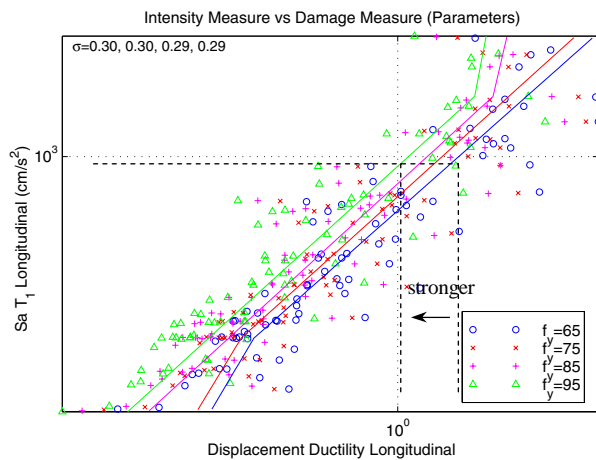


Fig. 4.11  $f_y$  sensitivity,  $Sa_{T1}-\mu_{\Delta}$

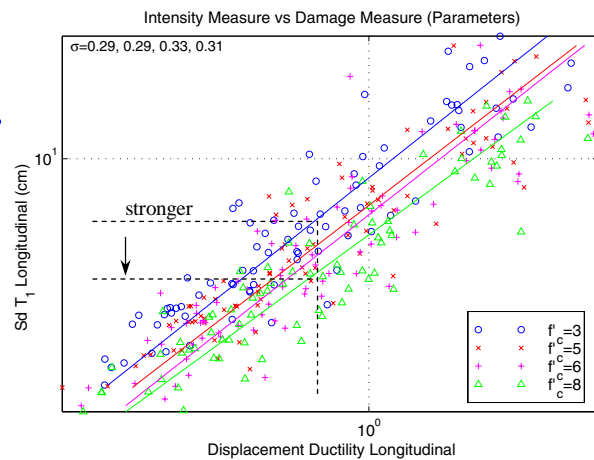


Fig. 4.12  $f'_c$  sensitivity,  $Sd_{T1}-\mu_{\Delta}$

Figure 4.10 shows the relationships for variation of soil stiffness,  $K_{soil}$ . While there was a reduction in demand when considering either a rock or soft soil site, the difference between a USGS B or C site was small. This is largely due to the fact there was no soil stiffness or strength degradation included in the model, as discussed in Section 2.4.4. Again, the negative bilinear fit slopes are a result of large dispersion in a few data points at high-intensity levels.

As would be expected, stronger steel reinforcement ( $f_y$ ) in Figure 4.11 causes a reduction in the demand and an increase in force attracted. Period independency allows a constant intensity comparison in this case. While changing only the concrete strength would result in a very similar trend as Figure 4.11, Figure 4.12 shows that the reinforced concrete strength actually causes a sizable shift in spectral quantities. However, also as expected, concrete strength has a small influence on the global bridge performance.

The only design parameters not mentioned in this section are the deck skew angle ( $\alpha$ ) and the percent of transverse column reinforcement ( $\rho_{s,trans}$ ). The base bridge configuration has simply supported boundary conditions at the abutment, therefore the skew angle has no effect. See Section 4.2 for the effect of skew angle on response of a bridge with abutments. No results are shown for  $\rho_{s,trans}$  because in the current model, shear is accounted for by modification of the confined concrete material model. The net effect of adding more transverse reinforcement is to raise the peak concrete compressive strength, therefore,  $\rho_{s,trans}$  and  $f'_c$  are highly correlated quantities. Thus, as with  $f'_c$ , increasing  $\rho_{s,trans}$  has minimal influence on the global bridge performance, as currently modeled.

#### **4.1.1 Design Trends**

Given the trends outlined in the models above, one model (Fig. 4.6) was selected in order to develop a set of design equations using design parameter  $D_c/D_s$  that can be used explicitly by designers without coupling to Equation 1.1. In order to facilitate ease of use, a model with period independence was selected. This was done at the expense of efficiency, albeit eliminating  $T$  as a

design variable directly. The use of  $Sd_{TI}$  (Fig. 4.5) would have resulted in a decrease in dispersion of approximately 33% compared to Arias intensity.

Using the regression data and Equation 3.2, the design equation can be written as Equation 4.1.

$$\ln(EDP) = (5.84x^2 - 11.81x + 1.23) + (-1.08x^2 + 1.85x + 0.021)\ln(IM) \quad (4.1)$$

with  $x=D_c/D_s$ ,  $EDP=\mu_\Delta$ , and  $IM=Arias$  intensity. For a particular case of  $x=1.15$ , the design equation reduces to Equation 4.2.

$$\ln(EDP) = -4.623 + 0.721 \ln(IM) \quad (4.2)$$

For example, in order to reduce  $\mu_\Delta$  from 3 to 2 (33% reduction), given an earthquake event with an Arias intensity of 750 cm/s, the polynomial in Equation 4.1 can be solved. The resulting design requires increasing the column diameter ratio  $D_c/D_s$  from 0.65 to 0.90 (38% increase); whereas, reducing  $\mu_\Delta$  from 2.5 to 1.67 (33%) requires diameter ratio ( $D_c/D_s$ ) increase from 0.78 to 0.99 (27%).

## 4.2 DESIGN PARAMETER SENSITIVITY: MODEL WITH ABUTMENTS

While the trends and sensitivities above were all derived for the case of the roller boundary condition at the abutments, this section will show that the use of a more realistic abutment model does not significantly influence these trends. The same PSDMs were derived as the above cases and can be directly compared. The abutment model used in all the following cases was “abut 2” (see Section 2.4.3 for definition). This model adds stiffness to the longitudinal and transverse directions, but no mass.

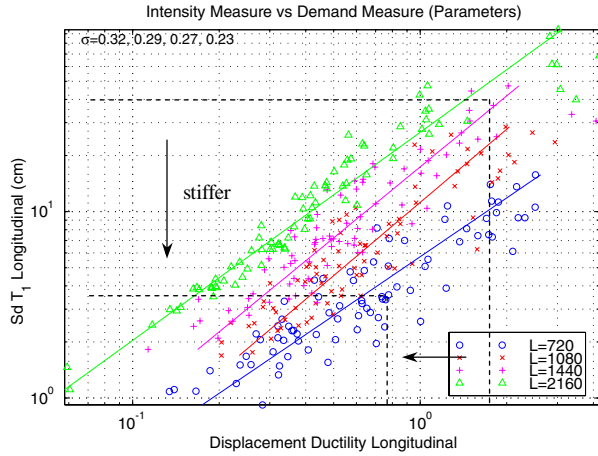


**Fig. 4.13**  $L$  sensitivity,  $Sd_{T1}-\mu_{\Delta}$

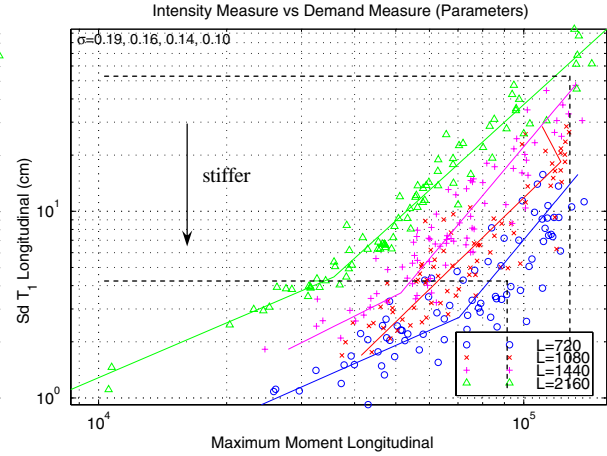


**Fig. 4.14**  $L$  sensitivity,  $Sa_{T1}-M_{max}$

Figure 4.13 shows span  $L$  sensitivity and is equivalent to Figure 4.1. As stiffness was increased (span becomes shorter), the demand decreased. The lines of constant intensity for this period-dependent IM are shown on Figure 4.1. As the abutment stiffness affects the overall bridge stiffness, however, these lines should be adjusted to reflect the new spectral values. The long span period increases, as does the corresponding  $Sd$ ; therefore, the demand decrease for making the bridge stiffer is larger than for the no abutment case (Fig. 4.13). Similarly, Figure 4.2 is replotted using  $Sd_{T1}$  instead of  $Sa$  to mimic the  $Sd$  trends of Figure 4.13.

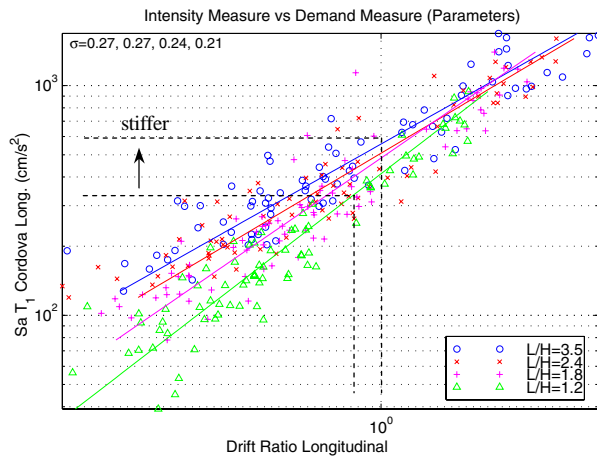


**Fig. 4.15**  $L/H$  sensitivity,  $Sa_{Cordova}-\Delta$

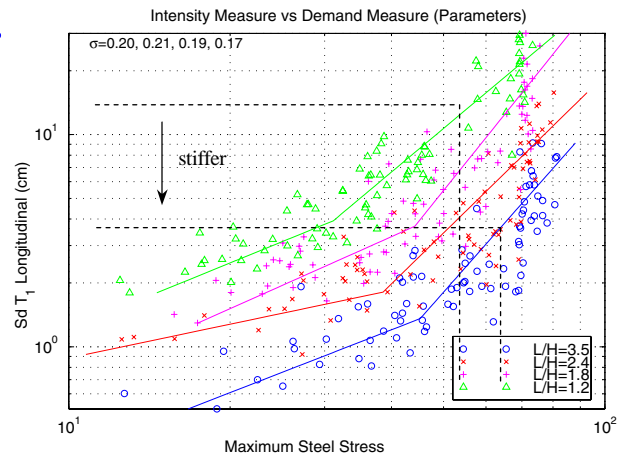


**Fig. 4.16**  $L/H$  sensitivity,  $Sd_{T1}-\sigma_{steel}$

When considering  $L/H$  sensitivity, there was a slight difference from the no abutment case. Increasing stiffness (making  $H$  shorter with constant  $L$ ) resulted in a slight increase in demand (Fig. 4.15), the reverse case of Figure 4.3. This shift in performance was also seen in Figure 4.16. Compared with the minimal performance change in Figure 4.4, in slight increase in stress was expected as the stiffness was increased. It should be noted that while it is possible to effect an undesirable change in performance by increasing stiffness through  $H$ , the change in demand is on the order of the dispersion, therefore changing  $H$  has little real impact.

Due to the added abutment stiffness, enlarging the column ( $D_c$ ) has a reduced effect on demand (Fig. 4.17) compared to Figure 4.5. Figure 4.18 shows more clearly the improvement in performance with increased stiffness ( $D_c$ ) due to the use of the period-independent IM Arias intensity.

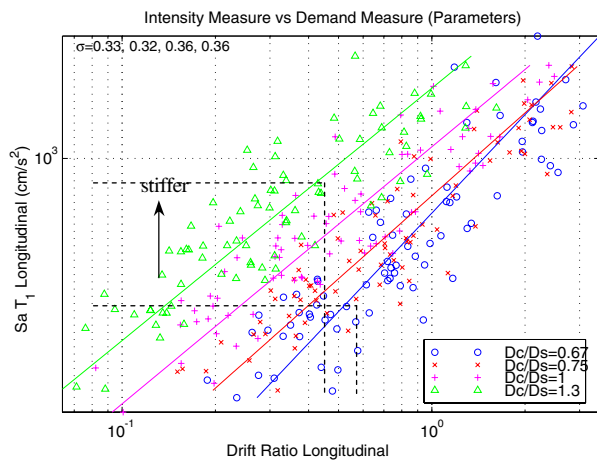


**Fig. 4.17**  $D_c/D_s$  sensitivity,  $Sd_{T1-\Delta}$

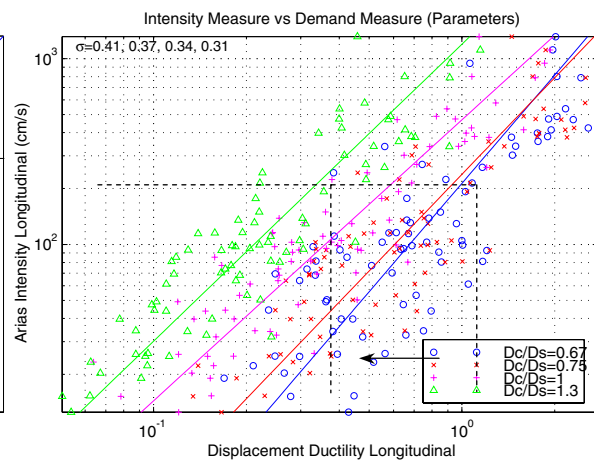


**Fig. 4.18**  $D_c/D_s$  sensitivity, Arias- $\mu_A$

Figure 4.19 shows identical trends to Figure 4.7. More steel reinforcement in the longitudinal direction has a marked improvement in performance. Changing the reinforcement ratio has little effect on the initial stiffness period, therefore allowing the horizontal constant intensity line to be drawn. Similarly, Figure 4.20 shows a large increase in force attracted with more reinforcement, as in Figure 4.8.

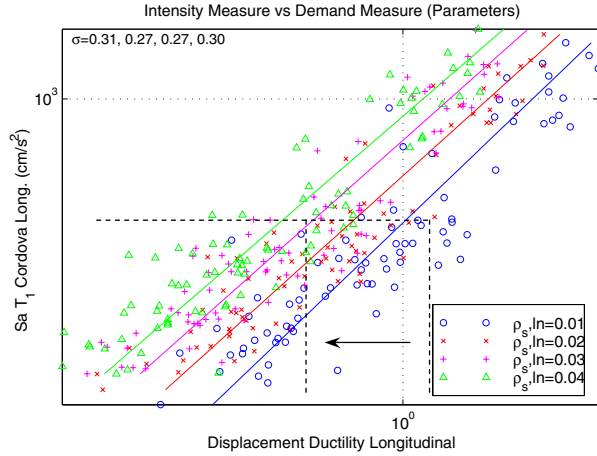


Fig. 4.19  $\rho_s$  sensitivity,  $Sa_{Cordova} - \mu_{\Delta}$

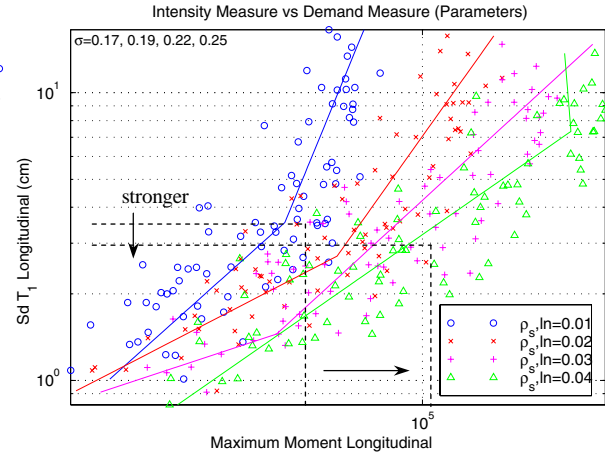


Fig. 4.20  $\rho_s$  sensitivity,  $Sd_{T1} - M_{max}$

Finally, the deck skew angle ( $\alpha$ ) is introduced as a design parameter for the bridge model with abutments. The effects of skew in the longitudinal direction are minimal (Fig. 4.21); however, transverse behavior is considerably different as the gap varies along the width of the bridge deck. As the deck rotates about the column axis, impact of the deck with the abutment occurs at one extreme of the deck cross section while the opposite extreme is pulling away. In the bridge model implemented, this results in lower stiffness being imparted by the abutments. Figure 4.22 shows the increase in transverse drift demand as the skew angle increases. Using an array of elements at the end of each bridge span only, however, limits modeling of the true deck behavior. For example, compressive struts may develop from the deck ends that impact the abutments that are not accounted for in the current model.

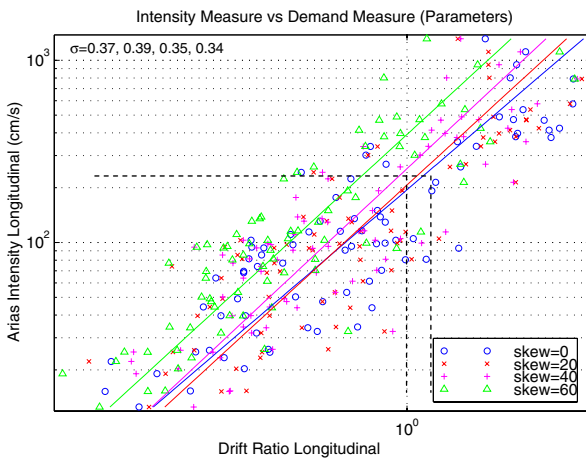


Fig. 4.21 Skew sensitivity, Arias- $\Delta$  longitudinal

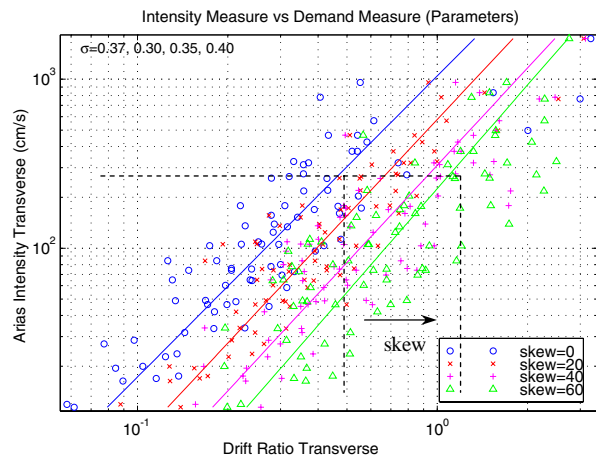


Fig. 4.22 Skew sensitivity, Arias- $\Delta$  transverse

In summary, as seen in Figures 4.13–4.20, the addition of abutment stiffness has negligible effect on the general PSDM trends developed for the no abutment case (specific response values differ). Given the sensitivity to abutment stiffness in Section 4.6, the trends in the PSDMs can be applied to any of the abutment stiffness models.

### 4.3 SENSITIVITY TO PERIOD IN SPECTRAL DISPLACEMENT

An interesting phenomenon can be derived from examination of the PSDMs shown previously. Specifically, the use of a spectral quantity at the first mode period becomes the optimal IM, regardless of whether the direction of concern was longitudinal or transverse. This is counter-intuitive, as the first and second modes were dominated by transverse and longitudinal deck motion only. An example illustrates this fact using  $D_c/D_s$  sensitivity in the presence of abutments and an intermediate demand measure,  $M_{max}$ . Figure 4.23 shows this PSDM for the transverse direction using  $Sd_{T1}$ , Figure 4.24 for the longitudinal direction using  $Sd_{T1}$ . For the case of abutment stiffness, the fundamental mode was in the longitudinal direction. The second mode was in the transverse direction. Bridge period values are summarized in Table 4.2.

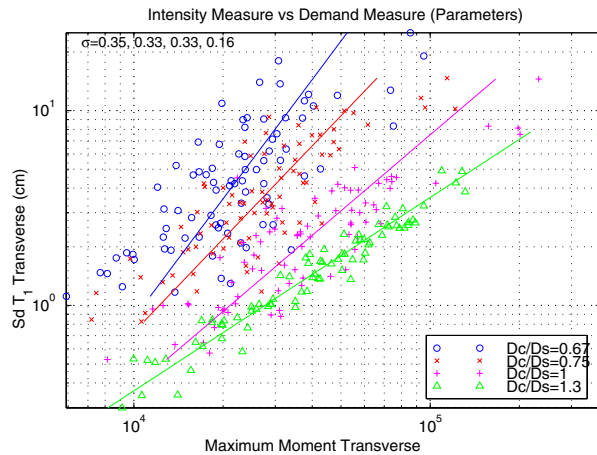


Fig. 4.23  $D_c/D_s$  sensitivity,  $Sd_{T1}-M_{max}$

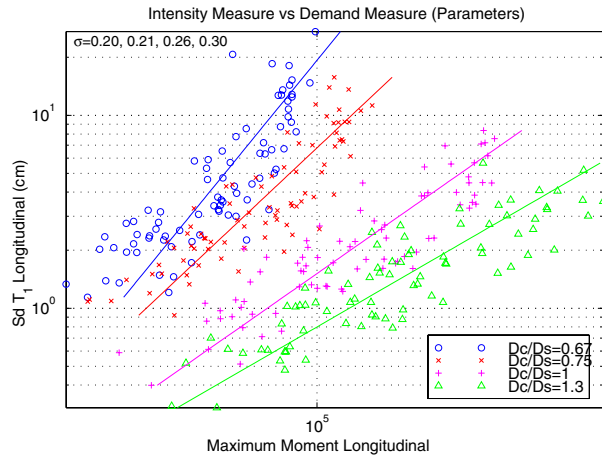


Fig. 4.24  $D_c/D_s$  sensitivity,  $Sd_{T1}-M_{max}$

**Table 4.2 Bridge periods for  $D_c/D_s$  sensitivity, longitudinal mode in italics**

$D_c/D_s$	Abutment		No Abutment	
	$T_1$	$T_2$	$T_1$	$T_2$
0.67	<i>0.61</i>	0.25	0.72	<i>0.64</i>
0.75	<i>0.53</i>	0.24	0.64	<i>0.55</i>
1.0	<i>0.38</i>	0.23	0.49	<i>0.39</i>
1.3	<i>0.30</i>	0.22	0.39	<i>0.30</i>

Figures 4.25 (transverse) and 4.26 (longitudinal) show the same information, plotted with  $Sd_{T2}$ . As can be seen by the dispersion values shown in the figure windows and summarized in Table 4.3, the highest efficiency was gained from using  $Sd_{T1}$ . The only instance where this does not hold true was for the transverse direction for the weaker columns ( $D_c/D_s = 0.67, 0.75$ ). For these two cases,  $Sd_{T2}$  was the more efficient measure.

A study was performed to determine the sensitivity of the model dispersion to the values of period used in the spectral displacement. The period was varied from 0.15 to 0.85 for all of the  $D_c/D_s$  values (0.67, 0.75, 1.00, 1.30). The resulting plots show a clear minimization problem. Figure 4.27 shows model efficiency,  $\sigma$ , as a function of period, as used in  $Sd$ , for the first two  $D_c/D_s$  values. Figure 4.28 shows the same information for the last two  $D_c/D_s$  values. Both figures address the response in the longitudinal and transverse direction. Actual transverse and longitudinal periods are also indicated on the plots as vertical lines.

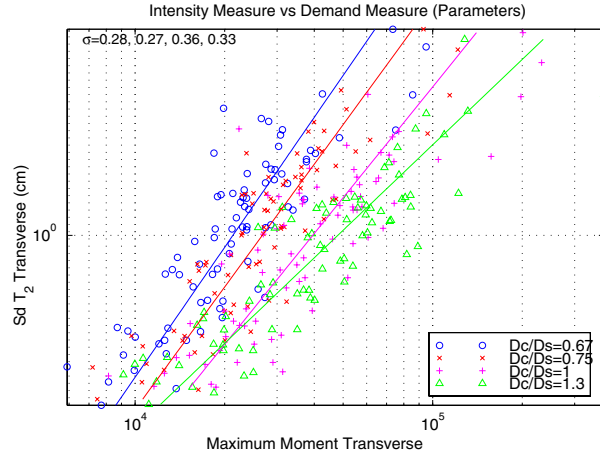


Fig. 4.25  $D_c/D_s$  sensitivity,  $Sd_{T_2}-M_{max}$

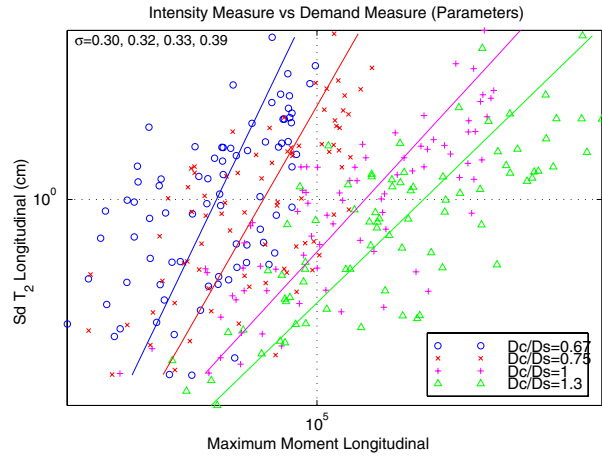


Fig. 4.26  $D_c/D_s$  sensitivity,  $Sd_{T_2}-M_{max}$

Table 4.3 Dispersion values for  $Sd-M_{max}$ ; optimal in italics

		Abutment				No Abutment				
Transverse	$T_1$	0.35	0.33	0.33	0.16	T1	<i>0.24</i>	<i>0.21</i>	<i>0.31</i>	<i>0.31</i>
	$T_2$	<i>0.28</i>	<i>0.27</i>	0.36	0.33	T2	0.25	0.23	0.35	0.37
Longitudinal	$T_1$	<i>0.20</i>	<i>0.21</i>	0.26	0.36	T1	<i>0.21</i>	<i>0.18</i>	<i>0.15</i>	<i>0.13</i>
	$T_2$	0.30	0.32	0.33	0.39	T2	0.23	0.21	0.24	0.30

For all parameter values in both the longitudinal and transverse direction, the optimal period was greater than that predicted by the fundamental and second mode periods. This optimal period can be related by a constant to the period of interest in each case. For the longitudinal direction, this constant is 1.30. Similarly, the transverse direction constant is 1.35. This suggests the real optimal IM of interest in Chapter 3 is Equation 4.3.

$$Sd_{Optimal} = Sd(kT_x) \quad (4.3)$$

where  $k$  is the constant enumerated above and  $T_x$  is the period corresponding to the direction (longitudinal or transverse) of interest. In a similar manner, the model dispersion sensitivity to period can be evaluated for different PSDM. For example, using the  $Sd-\Delta$  PSDM with  $D_c/D_s$  sensitivity, the constant  $k$  is once again derived to be 1.30 in the longitudinal direction and 1.35 in the transverse direction.

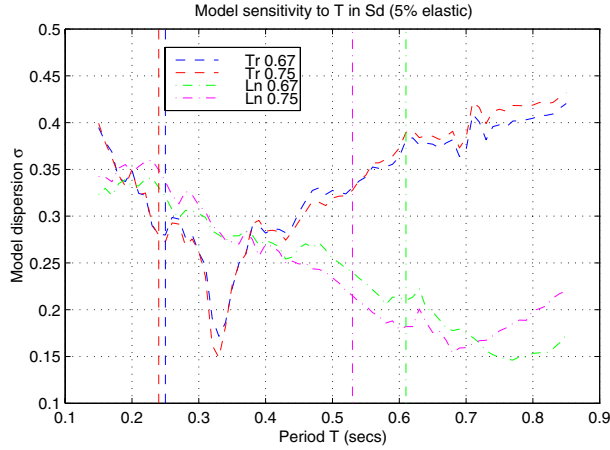


**Fig. 4.27**  $T$  sensitivity,  $Sd_{TI}-M_{max}$

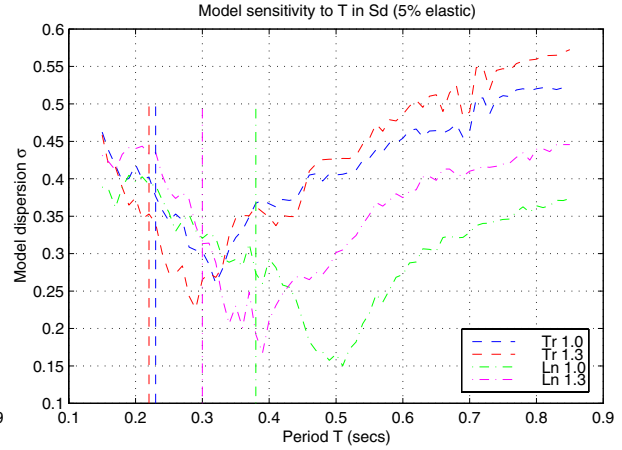


**Fig. 4.28**  $T$  sensitivity,  $Sd_{TI}-M_{max}$

This preliminary data support a relationship between an equivalent secant period and the displacement ductility demand on the bridge. Considering a bilinear relationship between force and displacement, the initial elastic stiffness ( $K_i$ ) is related to the secant stiffness ( $K_s$ ) by Equation 4.4.

$$K_i = \mu_\Delta K_s \quad (4.4)$$

$$T_s = \sqrt{\mu_\Delta} T_i$$

If linear strain hardening ( $\eta$  = strain-hardening ratio) is added to the above relationship, the correlation between secant and initial periods is defined by Equation 4.5.

$$T_s = \sqrt{\frac{\mu_\Delta}{1 + \eta(\mu_\Delta - 1)}} T_i \quad (4.5)$$

To obtain  $k=1.3$ , the required average displacement ductility demand ( $\mu_\Delta$ ) is 1.7 (Eq. 4.4) and 1.85 (Eq. 4.5) for a 10% strain-hardening ratio. Figure 4.1. shows a sample PSDM using  $\mu_\Delta$  as the EDP value. A ductility demand of approximately 2 is appropriate and corresponds to the predicted equation values. With the current data set, however, it is not possible to verify whether these trends hold for larger ductility demands in the high-intensity region or for weaker structures.

#### 4.4 SENSITIVITY TO PERIOD IN ARIAS INTENSITY

Traditionally Arias intensity has been calculated using only the recorded acceleration record. However, a similar procedure to the spectral quantities can also be applied, specializing Arias

intensity to a given period. Using a SDOF oscillator with 5% damping, the acceleration time history response for a given period was then integrated to obtain the period-dependent Arias intensity value.

A study was once again performed to determine the sensitivity of the model dispersion to the values of period used in  $I_A$ . The same period and parameter variations were used as above. As might be expected, the resulting plots show a similar trend to the spectral quantities. Figure 4.29 shows the model efficiency as a function of period, as used in  $I_A$ , for the first two  $D_r/D_s$  values. Figure 4.30 shows the same information for the last two  $D_r/D_s$  values. Actual transverse and longitudinal periods are also indicated on the plots as vertical lines.

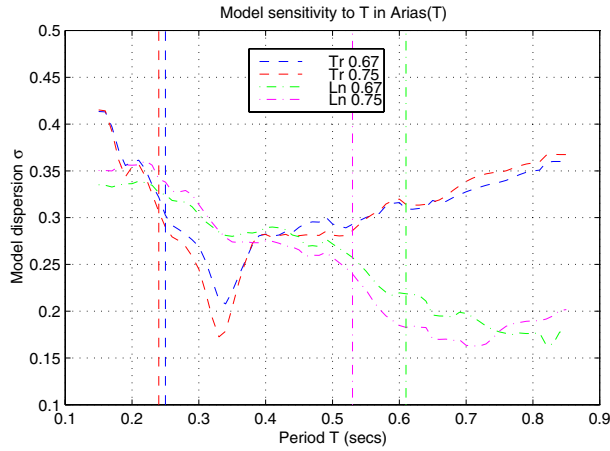


**Fig. 4.29**  $T$  sensitivity,  $I_A$ - $M_{max}$

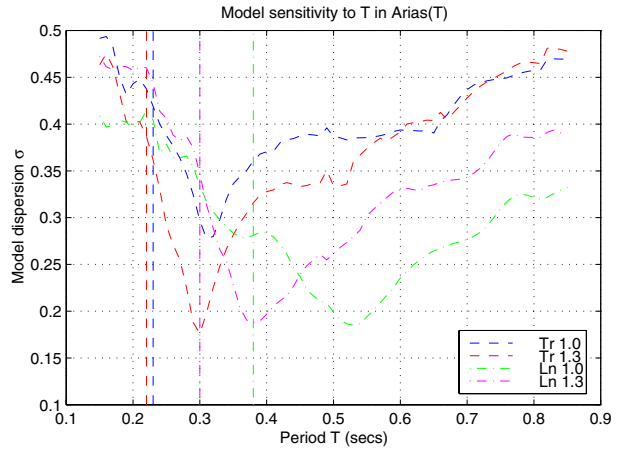


**Fig. 4.30**  $T$  sensitivity,  $I_A$ - $M_{max}$

Once again, the optimal period (for efficiency) was related to the structural period by a constant in all cases. For the longitudinal and transverse directions, this constant is 1.35. Similarly, the transverse direction constant is 1.35. This suggests the optimal Arias quantity is not the original ground motion, but the one related to structural period as Equation 4.6.

$$I_{A,Optimal} = I_A(kT_x) = \frac{\pi}{2g} \int_0^D [\ddot{u}_{kT, \zeta=5\%}(t)]^2 dt \quad (4.6)$$

Comparison of Figure 4.27 with 4.29 and Figure 4.28 with 4.30 indicate the ground motion intensity information carried by the maximum of a period-specific time history (spectral quantity such as  $Sd$ ) is similar to the cumulative effect of the acceleration reversals ( $I_A$ ) when predicting structural response.

Another interesting conclusion from a comparison of the figures is that the lowest possible dispersion obtained (approximately 0.15) is achieved by both the spectral and Arias quantities. Since the spectral quantities are simply period-dependent  $PGA$ ,  $PGV$ , and  $PGD$  values, and the period-dependent Arias IM is calculated from the same period filtered record, there may be a whole family of period-dependent IMs that could be considered. However, given that they yield similar dispersion values, it may be implied that the dispersion reduction is due to the SDOF filter rather than to the subsequent IM chosen. Therefore, instead of investigating other period-dependent IMs derived from a SDOF filtered record, it may make more sense to search for another filter which provides a more efficient PSDM.

#### **4.5 IM ROBUSTNESS ACROSS DESIGN PARAMETERS**

Not explicitly stated in Chapter 3, a further requirement for an IM to be classified as optimal is its usefulness across a large range of periods common to design. This implicit assumption is in large part the cause for rejection of such IMs as  $PGA$  or  $CAV$ . While these IMs may give efficient correlations for low-period structures (stiff), they lose efficiency in the longer periods. Given the practicality, efficiency, effectiveness, and sufficiency of  $Sa_{T1}$ , this IM is selected to investigate robustness across design parameters. Robustness describes the rate of change of efficiency with period. The method used to evaluate robustness is the dispersion of a PSDM, given the IM and a set of bridges with specific design parameters varied.

Figure 4.31 shows the period sensitivity of both  $Sa_{T1}$  and  $PGA$  across four different parameter groups. These parameter groups are chosen because they cause period shifts; therefore such quantities as  $\rho_{s, long}$  were omitted. The period values are normalized with respect to the period of the base bridge configuration (Table 4.1) and the dispersions are normalized with respect to the PSDM for the base bridge configuration. These normalized quantities facilitate

comparisons between not only different IMs (and consequently different efficiencies) but also between different choices of the EDP ( $\Delta$  and  $M_{max}$  are considered here) used in the PSDM. Given a  $\pm$  one standard deviation band on robustness,  $Sa_{T1}$  falls completely within this range (Fig. 4.31, upper pane). Not only this, but the efficiency improves in the long- and short-period ranges. In contrast,  $PGA$  (Fig. 4.31, lower pane) rapidly loses robustness at higher periods. This phenomenon is in addition to  $PGA$ 's lack of efficiency.

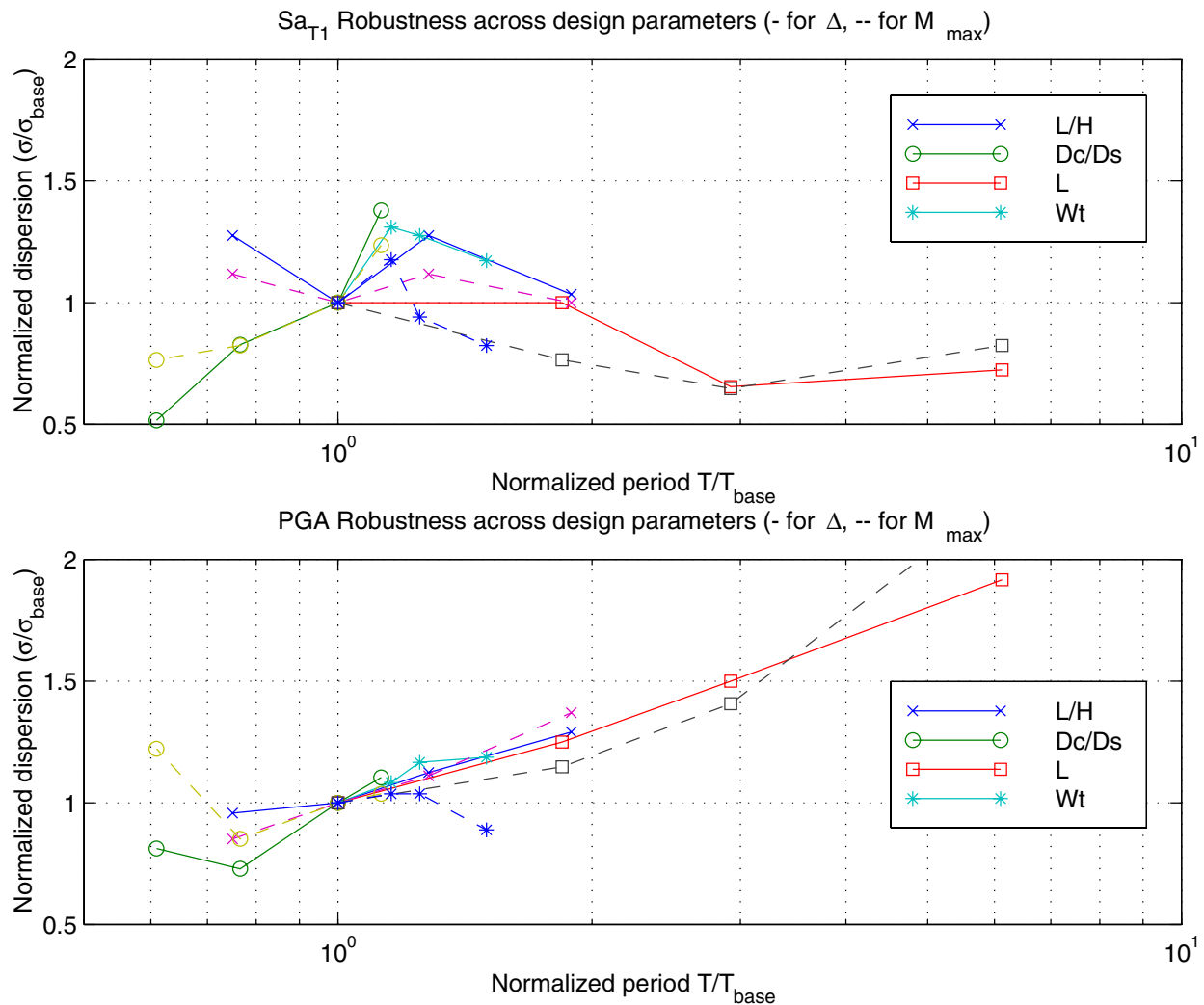


**Fig. 4.31 Robustness across design parameters  $L/H$ ,  $D_c/D_s$ ,  $L$ , and  $Wt$**

To simplify the robustness trends, a linear regression of Figure 4.31 was performed such that the resulting trends between different IMs can be more easily assessed. Figure 4.32 shows the robustness for an additional IM,  $CAV$ . As in the previous figure,  $CAV$  continues to lose

efficiency at higher periods, albeit a somewhat more effective measure than *PGA*. Therefore, the previous conclusion regarding  $S_{aT_I}$  being the optimal IM remains true when robustness in the presence of different design parameters is considered.

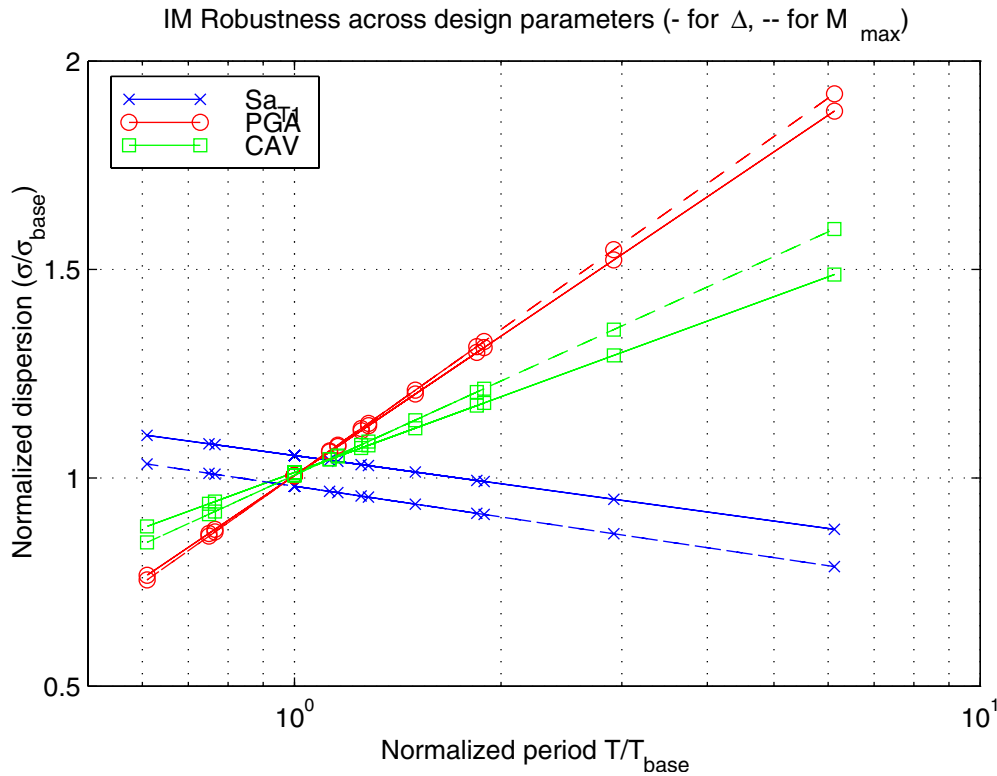


**Fig. 4.32 Comparison of robustness for different IMs**

#### 4.6 ABUTMENT MODEL SENSITIVITY

The previous design parameter sensitivities were all derived for the base bridge configuration, with only rollers at the abutments (Section 4.1) and the “abut 2” model (Section 4.2). In this section, abutment models were introduced on the ends of both spans. Sensitivity studies were performed by varying, in turn, the longitudinal stiffness, transverse stiffness, and participating mass of both abutments. Stiffness values range from 0 (no abutment case, only rollers) to 1000 k/in. Mass values range from 0 to 8 ks<sup>2</sup>/in. To differentiate between the effect of increasing

abutment stiffness and mass, longitudinal stiffnesses were varied for the cases of no mass and a median mass.

The resulting PSDMs shown below are not necessarily the optimal PSDMs for the given IM-EDP combinations. Optimal models utilize first mode spectral acceleration for the IM. Period-independent IMs have been used in order to isolate the effect of stiffness change on the response only, not on the IM as well.

#### 4.6.1 Longitudinal Stiffness

Longitudinal response in the presence of varying stiffness was difficult to evaluate in the case of bridges with seat-type abutments. Abutment stiffness was only activated once sufficient column deformations had caused the gap to close. Several studies were therefore performed. To evaluate stiffness only, response with the case of 0 abutment mass was performed first. For cases of large gaps (6"), response was identical in all except the high-intensity region. In this study there were insufficient data in this range to evaluate the abutment sensitivity. Therefore, the gap was reduced to 2" to better assess stiffness sensitivity. Figure 4.34 shows the response at varying stiffness levels. After gap closure, stiffer abutments reduced response. Even the lower stiffness bound provided improved response over the no abutment case.

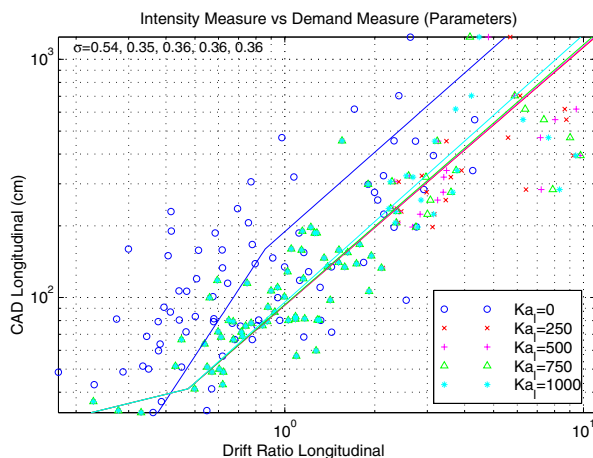


Fig. 4.33  $Ka_l$  (6") sensitivity, CAD- $\Delta$

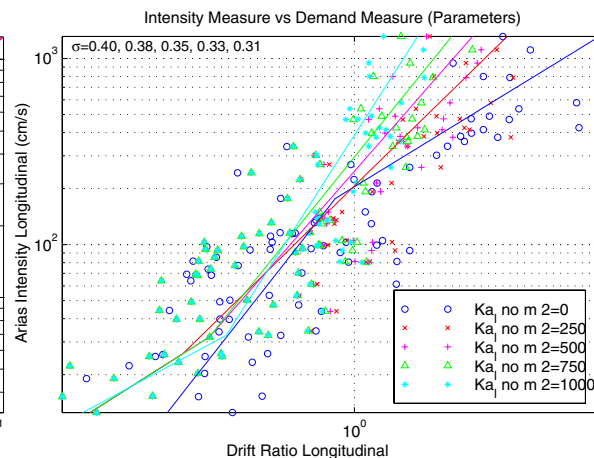


Fig. 4.34  $Ka_l$  (2") sensitivity, Arias- $\Delta$

Finally, a median value of mass was added to the abutments and the 6" gap study repeated. The added inertia at the abutments was sufficient to cause significant gap closure, in contrast to

the no-mass case described above. However, the mass appeared to dominate the response, as there was no appreciable difference between stiffness levels (Fig. 4.33). At very high intensities, the 1000 k/in. stiffness median response began to decrease, indicating that in large earthquake events, a stiffer abutment will contribute to decreasing the response before abutment failure.

#### 4.6.2 *Transverse Stiffness*

The effects of increasing abutment stiffness were more readily observed in the transverse direction, as there was no gap before mobilizing the total abutment stiffness. As seen in Figure 4.35, the increase in transverse stiffness in the presence of embankment inertia has little effect on the response. As expected though, the stiffer abutments reduce median response at all intensity levels. Excluding abutments (mass and stiffness) from the model yields similar results as does a low stiffness abutment in the presence of inertial forces, especially for smaller intensities. Making this assumption, however, is highly nonconservative in the high-intensity region.

#### 4.6.3 *Participating Mass*

As indicated by the stiffness sensitivities in the presence of mass, the participating mass was more critical to bridge response. Figure 4.36 shows the increasing contribution of participating mass to the total response at higher intensities. This verified the observations by Wissawapaisal and Aschheim [Wissawapaisal 2000], as reduced mass was required to maintain a response level as intensity was increased. Similarly, at constant intensities, the response increased with more participating mass. This sensitivity can be described by Equation 4.7 ( $m$  = desired mass).

$$\ln EDP = (0.014m^2 - 0.269m - 3.75) + (-0.005m^2 + 0.088m + 0.713) \ln(IM) \quad (4.7)$$

The abutment models from several authors described in the Abutment section (Section 2.4.3) were then used to determine their PSDM sensitivity. As an example case, they were applied to a two-bent bridge model, described in the multiple-bent chapter (Chapter 6). The results are applicable to both single- and multiple-bent bridges investigated. Figure 4.37 shows a comparison of different models in the longitudinal direction, Figure 4.38 in the transverse direction. As in the single-bent case, models that vary only longitudinal stiffness have near

identical response (“abut 2” [Maroney 1994b], “abut 4” [Zhang 2001] no mass). The only difference arose when the mass was also altered (“abut 7” [Maroney 1994b] with mass, “abut 8” [Zhang 2001] with mass).

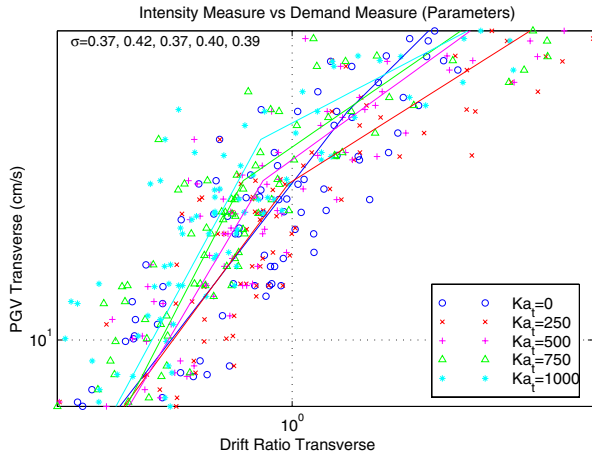


**Fig. 4.35**  $K_a$  sensitivity,  $PGV-\Delta$

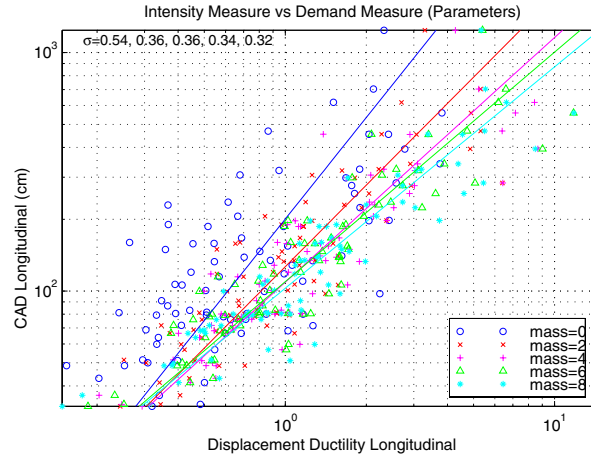


**Fig. 4.36** Mass sensitivity,  $CAD-\mu_{\Delta}$

As suggested earlier, it is not conservative to assume that there is no mass at the abutments. The abutment models containing stiffness only (no mass) affected higher demand than assuming no abutment at all (roller case). In the transverse direction, there was once again a difference between mass and stiffness cases. The no-abutment case provided a conservative alternative at lower intensities, but was not conservative at high intensities.

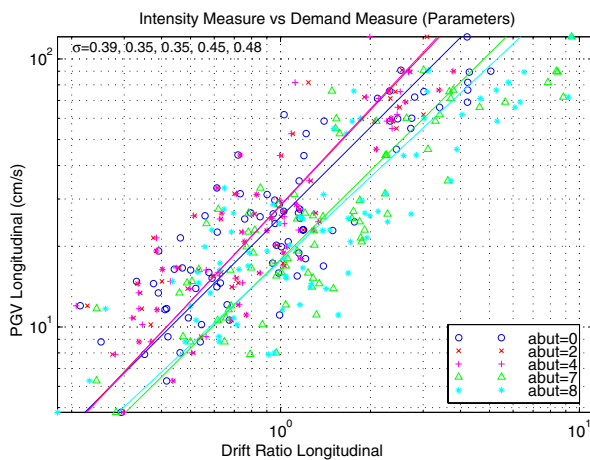


**Fig. 4.37** Abut sensitivity,  $PGV-\Delta$

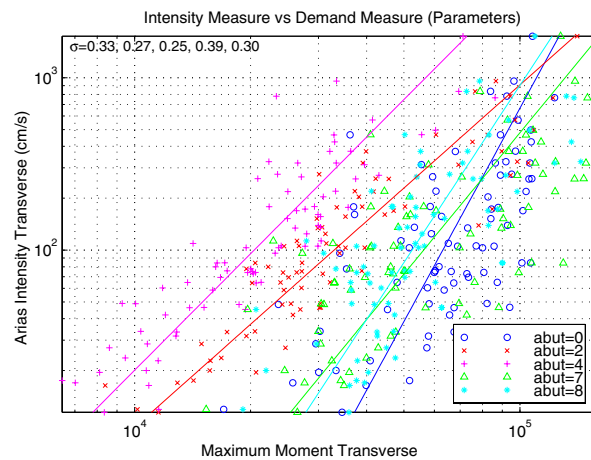


**Fig. 4.38** Abut sensitivity,  $Arias-M_{max}$

The participating length of the embankment, and hence the mass associated with the abutment, was the most critical parameter. Neglecting to include mass in the analysis underpredicted the response, even if large longitudinal or transverse stiffness was applied. In the absence of inertial forces, global response was insensitive to the selection of longitudinal stiffness. Therefore, any of the abutment models discussed are sufficient for approximating the longitudinal stiffness.

Transverse stiffness values have a larger effect in the absence of inertia, due in part to the fact that no gap closure is required to mobilize the abutment. However, given the predominance of mass on the response, transverse stiffness sensitivity is also reduced to the point where any of the abutment models are sufficient. Further studies are needed to investigate the dependence of the participating embankment length on bridge length, ground motion intensity and other factors. Inel provides some recommended embankment lengths [Inel 2001] for different levels of ground motions for use in an equivalent SDOF system to account for abutment flexibility. These range from 2–4 m for high-intensity shaking and 4–8 m for low and moderate intensities and can be used for initial mass estimates.

As a simplified model, it is possible to conservatively analyze a given bridge with only rollers at the abutments. This assumption is valid only at lower intensities due to the trade-off introducing stiffness and mass to the abutment incurs. However, introduction of more complex abutment models do not necessarily improve the accuracy of the solution when improperly calibrated.

In summary, the PSDMs can be used directly by designers as structural demand hazard curves. They allow assessment of the effects of structural design parameter variations on structural performance. Design decisions can be made on the trade-off between quantifiable performance levels and the resulting changes in design and material requirements, as shown by design Equations 4.1 and 4.2. While these equations are predictive for all ranges, the modularity of the approach allows subsequent resolution refinement of both parameter ranges as well as the parameters themselves. In order to facilitate the use of PSDMs as decision-making tools, an IM that is robust must be used to properly compare different design parameter effects.

## 5 Incremental Dynamic Analysis

The PSDMs in this study can be formulated using two analysis methods, probabilistic seismic demand analysis (PSDA) and incremental dynamic analysis (IDA). The first method attempts to represent seismicity through a wide selection of many ground motions, grouped into bins. The latter method achieves the same by stepwise incrementation of a select few ground motion records. Comparison of resulting PSDMs was considered in this chapter. Specifically, the equivalency of the two methods and instances when they can be used interchangeably are investigated.

PSDA uses a bin approach, where a portfolio of ground motions was chosen to represent the seismicity of an urban region. IDA is the dynamic equivalent to a familiar static pushover analysis. Given a structure and a ground motion, IDA is done by conducting a series of nonlinear time-history analyses. The intensity of the ground motion, measured using an IM, is incrementally increased in each analysis. An EDP, such as global drift ratio, is monitored during each analysis. The extreme values of an EDP are plotted against the corresponding value of the ground motion IM for each intensity level to produce a dynamic pushover curve for the structure and the chosen earthquake record. To achieve comparison with an equivalent PSDA, IDA intensities must cover a similar range.

A comparison of PSDA and IDA results for typical California single-column-bent reinforced concrete highway overpass bridges is presented in this chapter. The PSDA and IDA were conducted using the same portfolio of recorded ground motions. Probabilistic seismic demand models (PSDMs) were computed in two ways:

- (1) For an interval of IM values, centered about a value used in IDA, EDPs were obtained from a PSDA done by using a portion of the ground motion portfolio such that the ground motion IMs are in the chosen interval.
- (2) For a given IM, EDP data were obtained using IDA.

Such IDA-PSDA comparisons were done for a number of IM-EDP pairs. The differences between the two methods and the conditions that IMs and EDPs need to satisfy to ensure that IDA and PSDA results are statistically equivalent are discussed. The results of this chapter can be used to streamline the process of developing probabilistic seismic demand models for a performance-based seismic design framework.

The only variance between the two analysis tools presented was in the first step described in the PSDA analysis method (Section 2.5). A sample PSDM generated using PSDA is shown in Figure 5.1. It will be used to compare the two analysis methods throughout this chapter. The theory behind IDA lies in the ability to take a small subset of ground motions from a larger catalog or series of bins and reuse the same motion to mimic variable intensities. This variation in intensity is achieved by incrementally increasing the amplitude of the ground motion record [Vamvatsikos 2002]. Careful selection of PSDA bins described above ensures that intensity values are clustered at approximately the same values as the increments used in IDA, allowing comparable demand results. Ideally, a ground motion could be scaled until the structure collapses, generating a dynamic pushover plot. However, given the limitations of the model used herein, the bridge continues to gain stiffness until numerical instability causes loss of convergence. Certain ground motions generate regions of intermediate instability that yield inaccurate (nonconverged) measures of demand in these regions. Therefore, the region of interest has been purposely limited to the intensity ranges covered by PSDA.

Example IDA curves are shown in Figure 5.2. Usually plotted in linear scale, each curve depicts one ground motion as it was incremented. The use of bin scaling can be substantial in limiting the number of ground motions selected for analysis. Assuming that the standard errors of estimation are the calculated dispersions divided by the root of number of records used [Shome 1999], the  $1\sigma$  confidence band, given a dispersion of 0.15 and 4 records, is 7.5% wide.

Accordingly, one ground motion has been selected from each of the PSDA bins, denoted as series “4i” and “4j” (Table 5.1).

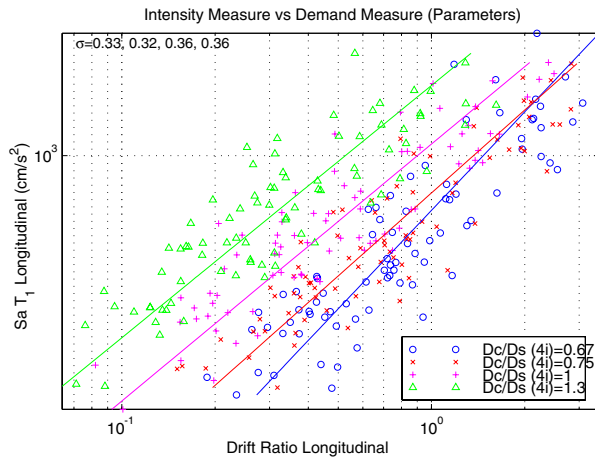


Fig. 5.1 PSDA  $Sa_{TI-\Delta}$ ,  $D_c/D_s$  4i

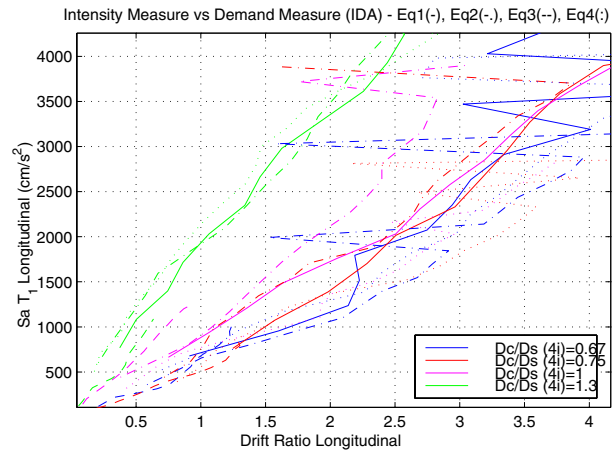


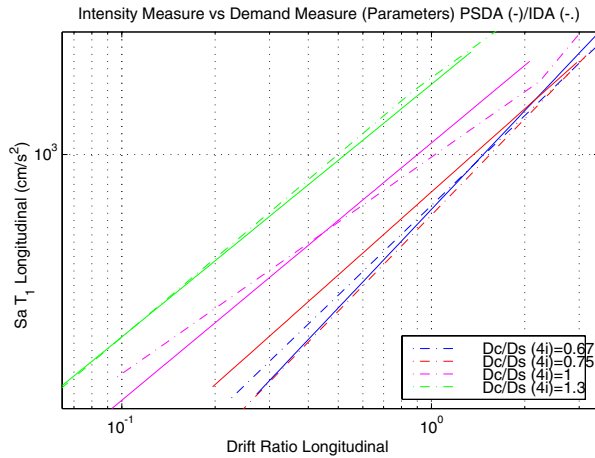
Fig. 5.2 IDA  $Sa_{TI-\Delta}$ ,  $D_c/D_s$  4i

Table 5.1 Ground motions used for IDA

Bin	Series “4i”	Series “4j”
LMSR	Northridge, 1994, Canyon County	Loma Prieta, 1989, Hollister City Hall
LMLR	Loma Prieta, 1989, SLAC Lab	Borrego Mtn., 1968, El Centro #9
SMSR	Livermore, 1980, Eastman Kodak	Imperial Valley, 1979, Chihuahua
SMLR	Imperial Valley, 1979, Delta	Morgan Hill, 1984, Capitola

Only those PSDMs determined to be optimal (see Chapter 3) were compared in this study. Of primary interest when using IDAs is the evolution of the median values (effectiveness), and dispersion (efficiency). The IMs used to describe ground motion characteristics were specifically limited in this comparison to first mode spectral acceleration ( $Sa_{TI}$ ) and an optimized spectral acceleration measure [Cordova 2000] defined in Table 2.6. This measure ( $Sa_{Cordova}$ ) was used as an example of how to reduce the real dispersion (Fig. 5.5), as opposed to reducing the model dispersion predicted by the various PSDMs shown.

Initial comparisons use the same computational effort, as both incorporate 80 nonlinear analyses per bridge configuration. PSDA attains this from the four bins of 20 motions, while IDA scales four motions 20 times.



**Fig. 5.3 IDA/PSDA,  $D_c/D_s$  ( $\Delta$ ) 4i**

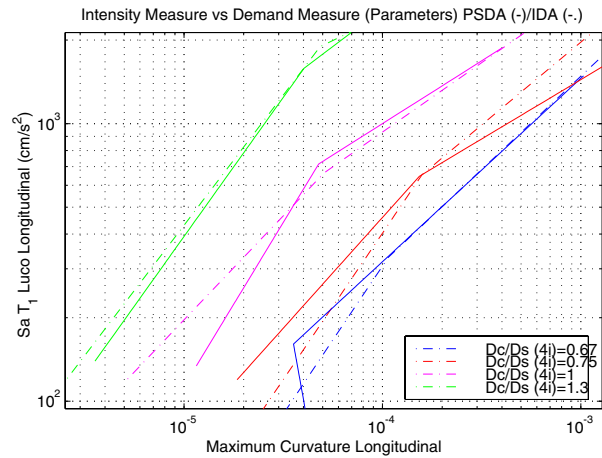


**Fig. 5.4 IDA/PSDA,  $D_c/D_s$  ( $\phi_{max}$ ) 4i**

Due to the “pushover” nature of IDA, it tends to capture demand values at the upper end of the spectrum. However, in order to facilitate comparison in the same data ranges, the IDA and PSDA ranges were reduced to the same interval. Considering the same PSDM developed above using both analysis methods, the data median and distribution were subsequently compared. Figure 5.3 shows the median contrast plot. IDA analysis results are shown in dotted lines, PSDA in solid. Ideally, the median values would agree between methods. The differences between IDA and PSDA for this PSDM are, indeed, small, especially for stiffer bridges (higher  $D_c/D_s$ ). As the location of the bilinear fit intersection was determined by the least-squares algorithm to minimize dispersion, PSDMs may differ substantially, as shown in Figure 5.4. This was, in particular, true of the PSDMs for intermediate ( $\phi_{max}$  Fig. 5.4) and local EDPs ( $\sigma_{steel}$ ). For the PSDM shown (Fig. 5.3), median lines agree for all but  $D_c/D_s=0.75$ , especially for higher stiffness bridge configurations.

More critical for PSDM use is dispersion. In Figure 5.1, the resultant PSDA dispersions are 0.33, 0.33, 0.36, and 0.36. For initial IDA comparisons, these dispersions were assumed to be the real dispersions associated with the given PSDM. The IDA plot (Fig. 5.2), when cast as a

PSDM, yields dispersions of 0.27, 0.32, 0.27, and 0.18, respectively. To compare dispersions directly, PSDMs from Figure 5.3 are plotted using one sigma ( $\mu+1\sigma$  or 84<sup>th</sup> percentile) stripes in Figure 5.5. It should be noticed that the  $1\sigma$  distribution using IDA lies below the PSDA envelope of true dispersions for all parameter values (Fig. 5.5). Drawing from these results, the estimated dispersion for the model was underpredicted using IDA even if the median values agreed for this ground motion subset. This does not mean, however, that using IDA reduces the true dispersion of the PSDM. The true dispersion can only be reduced with a different IM-EDP pair, as was done using the optimized spectral acceleration quantity (Table 2.6).

### 5.1 EVOLUTION OF MEDIAN VALUE AND DISPERSION

The worth of using IDA could be further increased if fewer analyses were required to attain the same level of confidence in the median which we associate with the PSDA method. Figure 5.6 repeats the comparison of median values except that the IDA data use only 3 ground motions (“3i” removes LMSR bin) amplified 20 times. This 25% reduction in analysis effort results in similar fits for high stiffness bridge configurations ( $D_c/D_s = 1.3$ ), but an increasing deviation for all others. Up to 50% deviation (between PSDA and IDA median lines) exists.

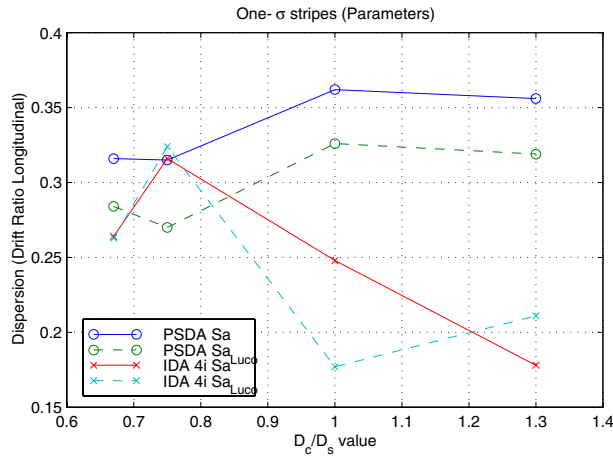


Fig. 5.5 IDA/PSDA,  $D_c/D_s$  4i  $1\sigma$  stripes

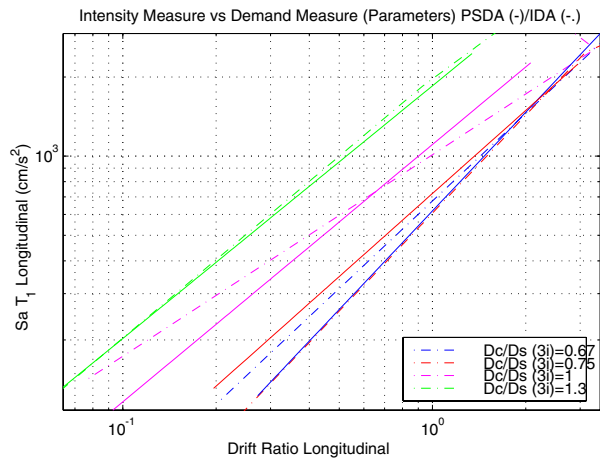


Fig. 5.6 IDA/PSDA,  $D_c/D_s$  ( $\Delta$ ) 3i

Table 5.2 shows the evolution of dispersion with reduction of computation effort for the models shown. The significant reduction in the estimated dispersion for fewer analyses indicates a loss of confidence in the median. Therefore, reducing computational effort as described above

provides uncertain results. A better IDA approach would be to use 5 motions amplified 16 times or 8 motions amplified 10 times each. As indicated in Table 5.2, the estimated dispersions approach the true dispersions as the number of records was increased.

**Table 5.2 Dispersions of PSDA and IDA runs ( $Sa_{TI}$  vs.  $\Delta$ )**

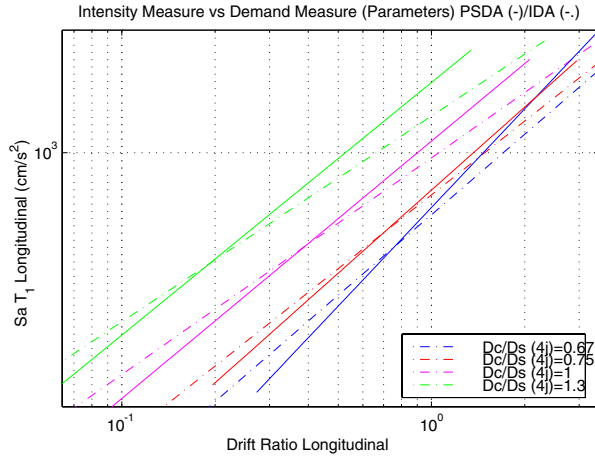
	Type	$D_e/D_s = 0.67$	$D_e/D_s = 0.75$	$D_e/D_s = 1.0$	$D_e/D_s = 1.3$
PSDA	4i	0.32	0.32	0.36	0.36
PSDA	16	0.33	0.32	0.36	0.35
IDA	4i	0.26	0.32	0.25	0.18
IDA	3i	0.23	0.31	0.26	0.21
IDA	2i	0.21	0.18	0.29	0.21
IDA	4j	0.29	0.31	0.35	0.25
IDA	8ij	0.30	0.36	0.31	0.27

## 5.2 GROUND MOTION DEPENDENCE

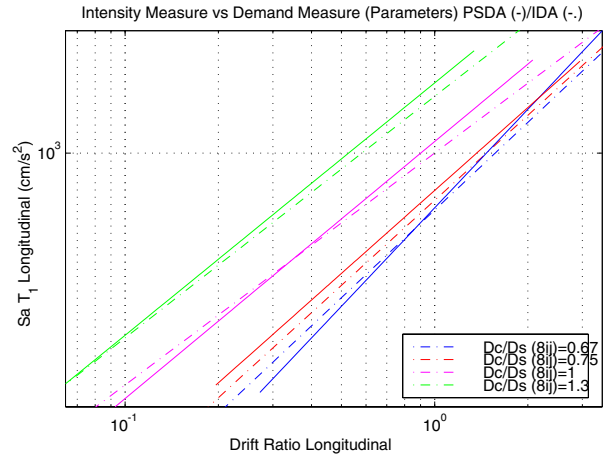
Another issue of contention when performing IDA is the selection of ground motions. The bin approach allows for incorporation of wide ranges of frequency content and amplitude variation, simply by choice of different earthquakes (by locations and site effects). However, if only one motion is selected from each bin, the results may become biased. To explore this, a second set of IDA ground motions was selected, group “j” (Table 5.1). The median and  $1\sigma$  analysis plots were once again performed for this new subset of motions, and compared to the same PSDA results as in Figure 5.3.

Figure 5.7 shows the change in median slope with the new motions. As the median lines intersect at intensity levels close to the median of the range of interest, the difference in demand for a given intensity was small. However, when used as predictors for performance at higher levels of shaking, the results will diverge substantially. As discussed, a better choice would be 8 motions (“8ij”) amplified 10 times each (Fig. 5.8). The median values show better agreement than both Figures 5.3 and 5.7. Corresponding dispersions for both “4j” and “8ij” are shown in Table

5.2 and the  $1\sigma$  stripe plot (Fig. 5.10). Dispersion for the 8 motion IDA approaches the real dispersion.



**Fig. 5.7 IDA/PSDA,  $D_c/D_s$  ( $\Delta$ ) 4j**



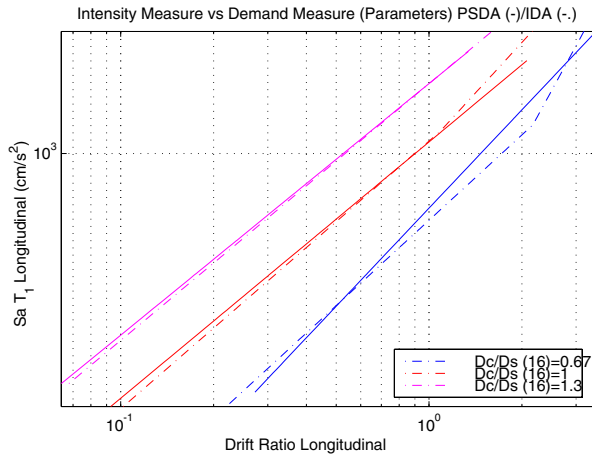
**Fig. 5.8 IDA/PSDA,  $D_c/D_s$  ( $\Delta$ ) 8ij**

### 5.3 VERIFICATION OF PSDA

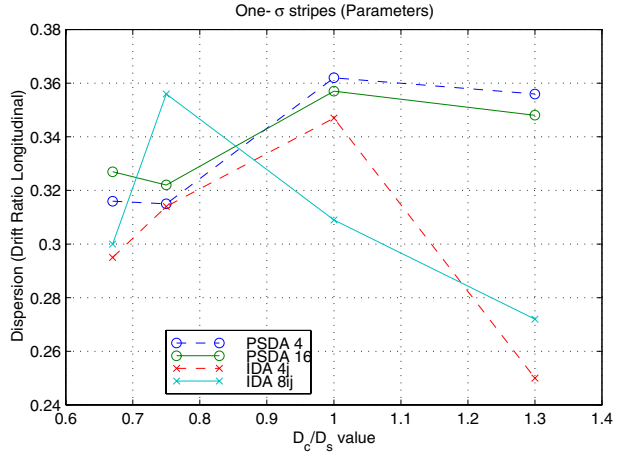
Thus far, all the IDA-PSDA comparisons have been addressed against a baseline PSDA set of results, assumed to correctly predict the median and dispersion. However, there is no guarantee that the number of motions used in the bin approach is sufficient to guarantee accurate representation of the median and dispersion. At the expense of computation time, it was possible to create a denser array of ground motions in the  $M_w, R$  bin matrix. This was accomplished with the addition of three ground motion bins created by Luco and Cornell [Luco 2001b] to the existing ones from Krawinkler [Medina 2001]. Each of the near-field, intermediate-field, and far-field bins contain 75 ground motions, bringing the total number of motions considered to 250 (duplicate motions were removed). These bins provide a larger subset of information in the higher intensity (near-field) region, which may be useful in comparison with the upper reaches of the IDAs. However, as before, the regions of interest were standardized.

Figure 5.9 shows the median values for each of the bridge configurations. The original PSDA data are once again in solid lines, while the expanded ground motion set is shown in dotted

lines. The  $1\sigma$  stripes are shown in Figure 5.10. Dispersions for both ground motion selections are also shown in Table 5.3. As can be seen, the 80 motion (four bin) subset provides a sufficiently accurate representation of expected behavior. On average, median values differed by less than 5%, and dispersions were roughly equivalent, verifying the initial PSDA assumptions.



**Fig. 5.9 PSDA comparison, median**



**Fig. 5.10 IDA/PSDA,  $D_c/D_s$   $1\sigma$  stripes**

Given the optimal PSDM formed from the IM-EDP pair  $Sa_{T1}$  and global  $\Delta$ , the two demand analysis tools, PSDA and IDA, can be used interchangeably to compute the probability of exceeding specified structural demand levels, i.e. to formulate PSDMs for performance-based analysis. Similarly, other optimal PSDMs can be generated with either IDA or PSDA. Other IM-EDP combinations can be used to reduce the real dispersion of the model if efficiency is critical.

**Table 5.3 PSDA comparison using different sets of ground motions bins**

	$D_c/D_s = 0.67$			$D_c/D_s = 1.0$			$D_c/D_s = 1.3$		
	$B$	$A$	$\sigma$	$B$	$A$	$\sigma$	$B$	$A$	$\sigma$
<b>Std.</b>	0.803	-5.164	0.32	1.022	-7.162	0.36	1.041	-7.834	0.36
<b>16</b>	0.924	-5.843	0.33	0.978	-6.865	0.36	1.020	-7.673	0.35

With the same computational effort, the median and  $1\sigma$  least-squares fits for both methods produce results with similar confidence levels in the median as long as an adequate number of ground motions are considered for the IDA. According to the PSDM presented in this study, just using 8 motions will slightly underpredict dispersion. Using more motions will cause the median

and dispersion values between the two methods to converge. For stiffer bridge configurations, it was possible to reduce the number of IDAs used with a subsequent decrease in confidence of predicting the EDP. The IDA method is sensitive to the choice of ground motions, however; therefore it is recommended that the number of analyses not be reduced and a representative set of motions be carefully selected from the regional seismic hazard database of interest.

Realistically, if more than 10 motions are required for dispersion agreement, or low confidence in IDA results is expected for bilinear PSDMs involving local and intermediate EDPs, the PSDA method should be used as it provides sufficient variation in ground motion content. When performing site specific risk analysis, it is often preferable to perform a stripe analysis. Given a particular ground motion intensity of interest, it is possible to scale the selected motions to a single intensity, creating a “stripe” of response information. The PSDA motions have not been scaled to the same IM; therefore, stripe analysis information can more readily be obtained from existing IDA data, as each motion has already been scaled to numerous different IM values.

## 6 Multiple-Span, Multiple-Bent Bridges

This chapter presents PSDMs developed for multi-span highway overpass bridges. These overpass bridges have two, three, or four spans (Fig. 2.5); circular columns with integral pile shafts; and continuous box girder superstructures the same as for single-bent models. PSDMs that demonstrate commonality with optimal PSDMs derived for single-bent bridges are presented. The influence of multiple bridge spans on their seismic behavior, such as the effect of higher mode response, was also investigated. Of particular interest was whether optimal PSDMs remain optimal for all bridge bent configurations considered because as bridge designs become more complex, it becomes less likely they can be expected to respond in single-degree-of-freedom fashion. The PSDMs derived herein give designers a tool to enable optimization of bridge layout for the expected level of seismic performance specific to their site. Not only can they be used to assess design parameter variation on response, but also to demonstrate whether higher mode response contributes significantly as irregularity of the bridge is increased.

### 6.1 MULTIPLE-SPAN BRIDGE MODELS

In this study, typical new California highway overpass bridges were selected as the class of structures for demand analysis. Configurations in this study were limited to single-, two-, and three-bent (two-, three-, and four-span), single-column per bent, reinforced concrete bridges, with spans that were not necessarily equal. This selection of spans was intended to cover a large range of frames used in stand-alone analyses. These are typical of long overpass bridges with segments separated by expansion joints, where individual frames are expected to perform independently [Caltrans 1999].

For each configuration, bridge design can be varied through a series of design parameters. These include the parameters developed for single-bent bridges (Table 2.1), as well

as those specific to multi-span bridges. Additional parameters for two- and three-bent bridges are shown in Tables 6.1 and Table 6.2, respectively. The two-bent base configuration includes 27.4-36.6-27.4 m (90-120-90 ft) spans, 7.6m (30 ft) above-grade columns of diameter 1.7 m (5.6 ft), 2% longitudinal, and 0.8% transverse reinforcement. Definitions of the design parameters for the two-bent case are shown graphically in Figure 6.1.

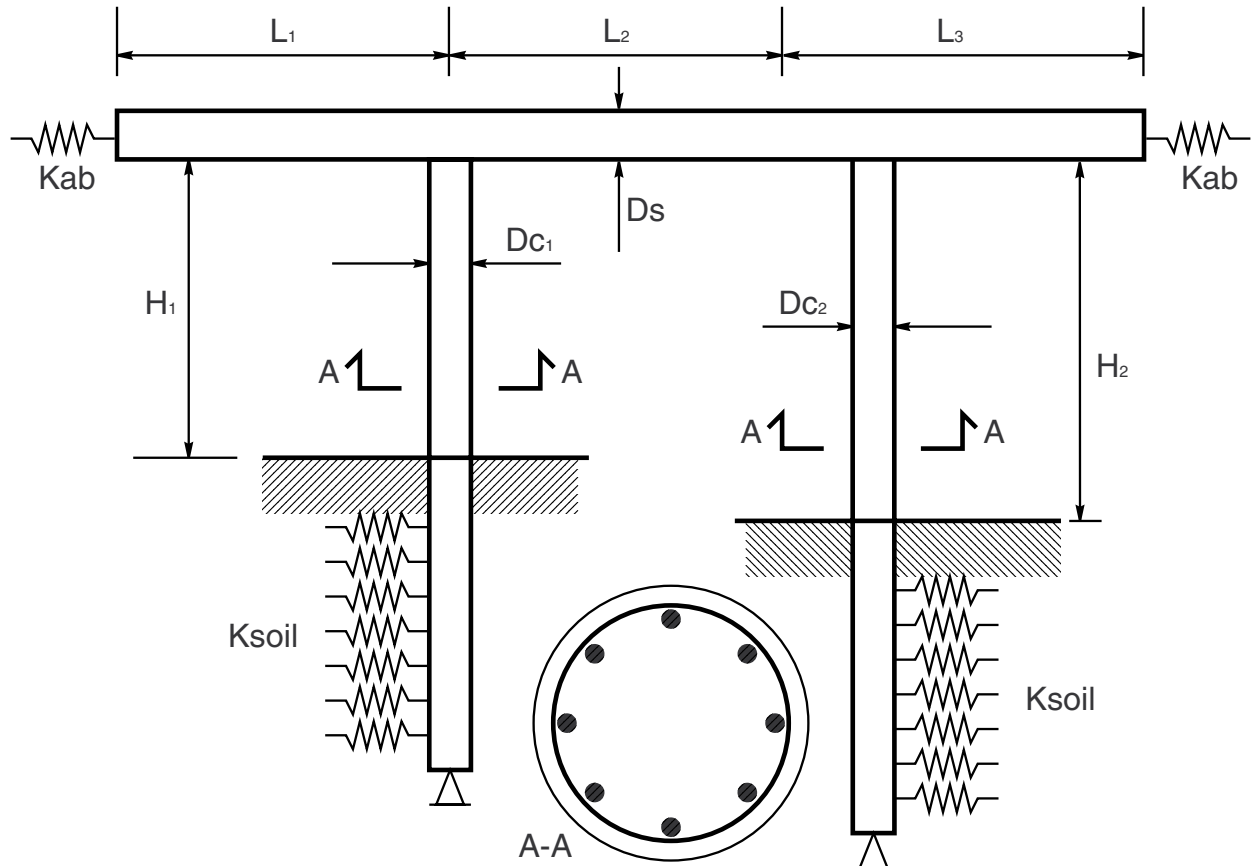


**Fig. 6.1 Two-bent bridge design parameters**

The three-bent bridge model adopts the same configuration as the two-bent model, adding another 36.6 m (120 ft) interior span. A limited subset of design parameters were selected for runs, therefore,  $L_1$  was fixed at 27.4 m (90 ft) and  $L_3$  at 36.6 m (120 ft). Similarly, the properties of the left column were fixed at  $L_1/H_1=1.8$  and  $D_{c1}D_s=0.8$ . The right column properties were fixed at  $L_1/H_1=2.4$  and  $D_{c1}D_s=0.8$ . All base bridges were on a USGS class B (NEHRP C) soil site. For this particular study, the abutment conditions were set as roller. The

ability to extend PSDMs using various abutment models to multi-span bridges was shown in Chapter 4.

The IMs in this chapter were limited to the spectral quantities, Arias intensity, and peak ground velocity (*PGV*) only. As before, first mode spectral displacement ( $Sd_{T1}$ ), acceleration ( $Sa_{T1}$ ), and velocity ( $Sv_{T1}$ ) were used interchangeably, as the dispersions in the PSDMs were independent of the choice of spectral quantity. EDPs in this chapter were limited to the column drift ratio ( $\Delta$ ), maximum column moment ( $M_{max}$ ), and maximum displacement ( $u_{max}$ ).

**Table 6.1 Parametric variation ranges for a two-bent overpass bridge**

<b>Description</b>	<b>Parameter</b>	<b>Range</b>
Degree of skew	$\alpha$	0–60°
Span length left	$L_1$	18–55 m (90–210 ft)
Span length right	$L_2$	18–55 m (90–210 ft)
Span-to-column height ratio	$L_2/H_1$	1.2–3.5
Column-to-superstructure dimension ratio	$D_c/D_s$	0.67–1.33
Longitudinal reinforcement ratio	$\rho_{s,long}$	1–4%
Abutment models	<i>Abut</i>	Various

**Table 6.2 Parametric variation ranges for a three-bent overpass bridge**

<b>Description</b>	<b>Parameter</b>	<b>Range</b>
Degree of skew	$\alpha$	0–60°
Span length middle	$L_2$	18–55 m (90–210 ft)
Span-to-column height ratio	$L_2/H_2$	1.2–3.5
Column-to-superstructure dimension ratio	$D_c/D_s$	0.67–1.33
Abutment models	<i>Abut</i>	Various

For the assumed roller boundary condition at the abutments, the fundamental mode for all three-bent types was in the transverse direction. This mode involves a simple transverse translation of the deck (Fig. 6.2). The second mode involves a longitudinal translation of the

superstructure, coupled with small rotations of the columns and supports (Fig. 6.3). When abutment models were added, transverse stiffness becomes dominant due to the gap in the longitudinal direction before abutment impact. Hence the fundamental mode of the bridge becomes longitudinal, and the second mode transverse.

From the single-bent bridge study, optimal PSDMs were  $Sa-\Delta$  and  $Sa-M_{max}$ . The same PSDMs were evaluated in terms of efficiency and sufficiency for multi-bent bridges. To assess the applicability of the optimal PSDMs from single-bent bridge analyses, the data for all bent types are presented on the same plot. Figure 6.4 shows the PSDM formed between  $Sa_{T1}$  and  $\Delta$ . Of interest was the decrease in dispersion between using  $Sa_{T1}$  over  $Sa_{T2}$ , even though the fundamental mode of the two- and three-bent bridges was in the transverse direction. Note, however, that this does not mean there is a relationship between transverse spectral quantities and longitudinal deformations. Instead, this suggests the spectral quantity producing optimal dispersions may not be a simple function of bridge modes, but a combination of them. This approach was investigated in part using the single-bent bridge elsewhere [Mackie 2002b]. The PSDM between  $Sa_{T1}$  and maximum column moment ( $M_{max}$ ) is shown in Figure 6.5.

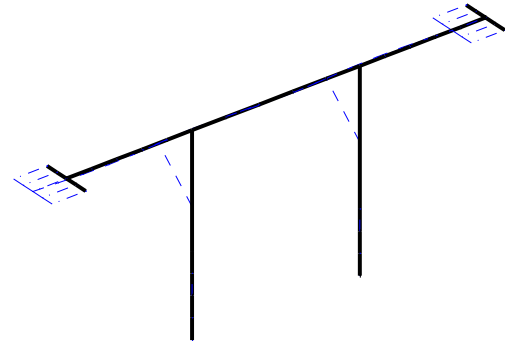
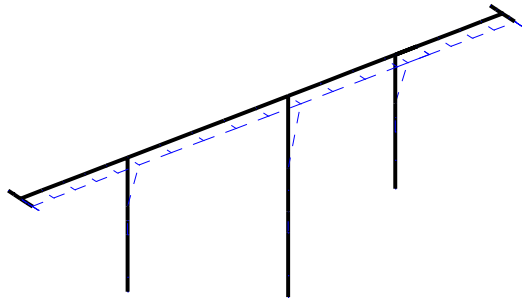


**Fig. 6.2 Three-bent, 1<sup>st</sup> mode (transverse)**      **Fig. 6.3 Two-bent, 2<sup>nd</sup> mode (longitudinal)**

In order to better understand the trends indicated in a stiffness- or mass-varying PSDM, it is helpful to use a non-period-dependent IM. The PSDM formed using Arias intensity and  $\Delta$  is shown in Figure 6.6. While the dispersions increase, this PSDM allows the use of lines of constant intensity to observe an increase in demand as the number of bents is decreased.

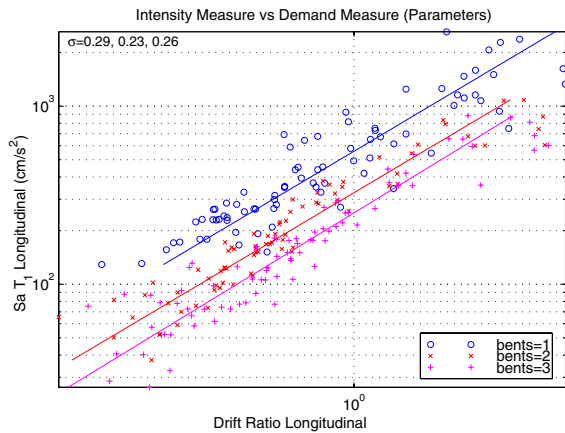


Fig. 6.4 Multiple-bent,  $Sa_{T1}-\Delta$  longitudinal

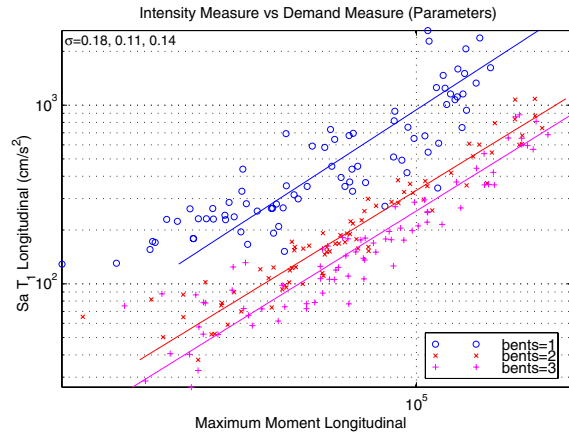


Fig. 6.5 Multiple-bent,  $Sa_{T1}-M_{max}$  longitudinal

## 6.2 TRANSVERSE IRREGULARITY

All of the above PSDMs can be extended to the transverse direction as well. This was especially critical when considering bridges with irregular transverse response. Figure 6.7 shows the  $Sa_{T1}-\Delta$  PSDM for the case of single, two, and three bents all with a  $RI^*$  of 100% (regular). The trends and dispersions are similar to that in the longitudinal direction. Furthering the assessment of which period to use in the spectral computation, using  $T_1$  reduces dispersion values over the use of  $T_2$ .

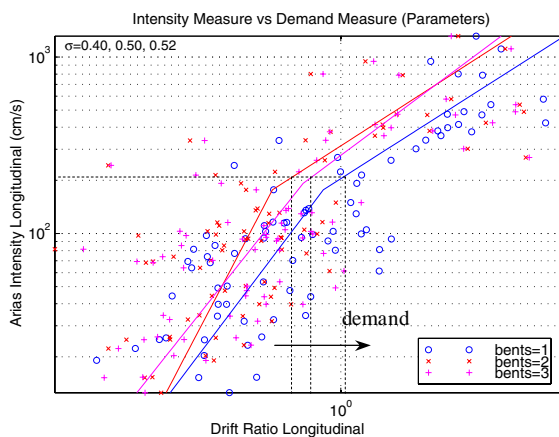


Fig. 6.6 Multiple-bent,  $Arias-\Delta$  longitudinal

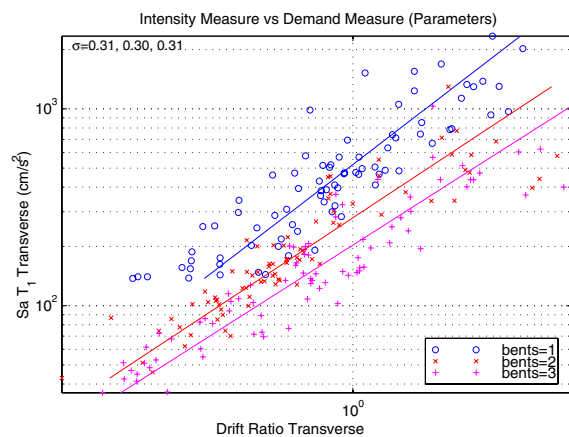
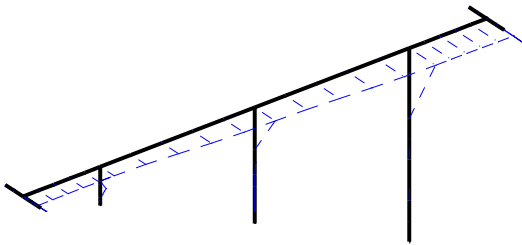
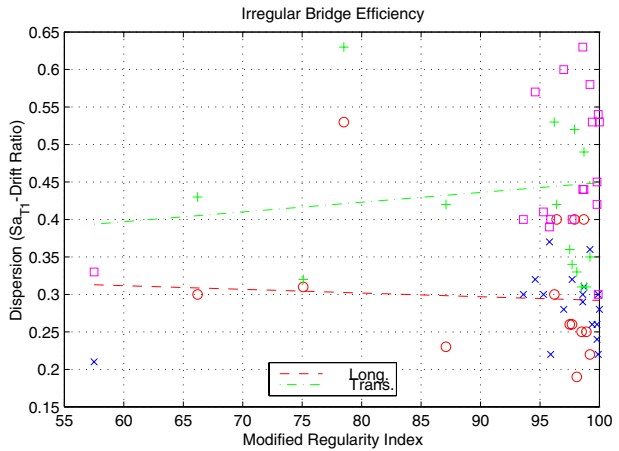


Fig. 6.7 Multiple-bent,  $Sa_{T1}-\Delta$  transverse

Given a wide variation in the span length and column stiffness in each bent, it was not possible to generate a fundamental transverse mode not dominated by transverse deck translation at all the bents. Therefore, the modified regularity index falls in the ranges of 55–100% for all configurations investigated. As it is possible to generate PSDMs with arbitrary IM-EDP pairs, it is constructive to investigate whether higher mode participation in these highly irregular bridges considerably influences the efficiency of PSDMs using spectral quantities for the IM. A sample irregular bridge with transverse mode indicated is shown in Figure 6.8. From a range of bridge configurations, the relationship between  $RI^*$  and dispersion for  $Sa_{TI}-\Delta$  was developed. From Figure 6.9 it is apparent that  $Sa_{TI}$  captures longitudinal and transverse response, regardless of  $RI^*$ .



**Fig. 6.8 Three-bent irregular (transverse)**



**Fig. 6.9 Effect of irregularity on efficiency**

### 6.3 SAMPLE DESIGN PARAMETER SENSITIVITY

Designers can use PSDMs to assess the effect of changing certain design parameters on the response of the bridge. This was accomplished by varying bridge design parameters; in this case (Fig. 6.10) the three-bent bridge was chosen and the middle span lengths ( $L_2$ ) were being varied. From the line of constant intensity shown, increasing  $L_2$  increases the bridge demand as expected. The EDP was shifted to maximum longitudinal displacement ( $u_{max}$ ) rather than  $\Delta$  as varying  $L_2$  also affects the column heights ( $L/H$  ratios remain constant). Note that maximum

displacement and drift generate PSDMs with the same dispersion, and therefore can be used interchangeably. Finally, this PSDM can be investigated to ensure there was no residual dependence on  $M_w$  and  $R$ , as assumed.  $R$  dependence is depicted in Figure 6.11. As desired, the slope of the lines is approximately horizontal, indicating lack of  $R$  dependence. The same trend is true of  $M_w$  but is not shown here.

Further design parameters for multi-span bridges are not shown herein, but are described in Appendix C and in the data provided at [http://peer.berkeley.edu/Products/PEERReports/reports-2003/0316\\_appCD.html](http://peer.berkeley.edu/Products/PEERReports/reports-2003/0316_appCD.html). Arbitrary pairings of IMs, EDPs, design parameters, and bent configurations are possible.

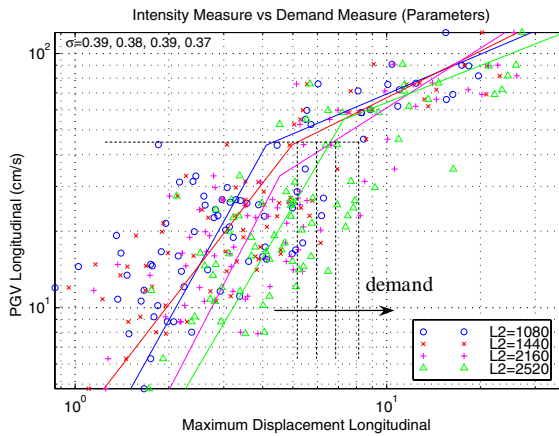


**Fig. 6.10**  $L_2$  sensitivity,  $PGV-u_{max}$  longitudinal

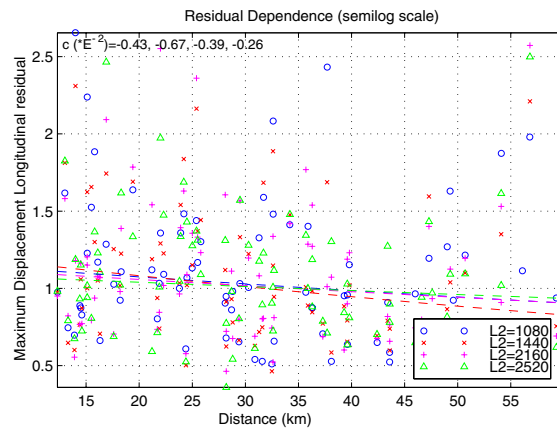


**Fig. 6.11**  $R$  residual dep,  $PGV-u_{max}$  longitudinal

In summary, when applied to multiple span highway bridges, the criteria required for de-aggregation are maintained in the resulting PSDMs, thus allowing seamless integration into the PEER framework. More importantly, the same IM-EDP pairs derived as optimal for single-bent bridges are also optimal for multiple-bent. The wide use of spectral acceleration in current practice makes it a useful property for bridges.

As tools for designers, the PSDMs for multiple span bridges are especially useful as they are not subject to deterioration of effectiveness or sufficiency due to bridge irregularity. Optimality of IM-EDP pairs is maintained across a broad range of irregular configurations. This

standardization allows designers to evaluate bridge response without an initial requirement that a bridge design qualify as an “ordinary standard bridge” [Caltrans 1999].

## 7 Conclusions

Probabilistic seismic demand models (PSDMs) for typical California highway overpass bridges were presented in this report. They were developed using probabilistic seismic demand analysis (PSDA) for a class of real structures. A PSDM relates engineering demand parameters (EDPs) to intensity measures (IMs) in the PEER Center probabilistic framework of Equation 1.1. The fundamentals of developing a PSDM were presented and applied to a two-span, single-bent highway overpass. This single-bent bridge was used to evaluate the selection of an optimal PSDM, to assess sensitivity of PSDMs to bridge design parameters, and to compare different analysis methods (PSDA and IDA) for equivalency of results. Finally, the single-bent PSDMs were extended to multiple-bent bridges.

While preparing for PSDA an analyst should consider the following issues:

1. Choice of ground motion intensity measures and structural engineering demand parameters should be made to produce a practical, sufficient, effective, and efficient PSDM. Guidelines for making such choices are presented below.
2. When choosing the ground motions for PSDA, care should be taken to avoid bias, yet to accurately represent the seismicity of the region for which PSDMs are being developed.
3. Understanding the capabilities and shortcomings of the tool used to model and analyze the structure is essential for proper interpretation of PSDMs.
4. A class of structures is represented by a base structure and a number of instantiations developed by varying a set of design parameters. Therefore, good design of the base structure and prudent choice of design parameters are essential for successful development of PSDMs showing design trends.
5. The computational effort required to develop PSDMs for a class of structures and the complexity of the database required to track the results of a large number of analyses

should not be underestimated. Task scheduling, database and visualization tools should be designed and implemented with care.

6. The analysis method for demand analysis should be selected with care. For arbitrary PSDMs and those with design parameter sensitivity, it is recommended that PSDA be performed. For stripe analysis, existing IDA data should be used.
7. For the class of highway bridges selected, the choice of optimal PSDM and design parameter sensitivity can be extended to single-, two-, or three-bent, single-column bridges. This covers an overwhelming number of bridge configurations in Northern California.

Probabilistic seismic demand models for a class of structures provide information about the probability of exceeding critical levels of chosen structural engineering demand parameters in a given seismic hazard environment. PSDMs have two major uses. Standing alone, PSDMs are design tools, as they provide information on how variations of structural design parameters change the expected demand on the structure. Such sensitivity data can be used to efficiently design structures for performance. When coupled with probabilistic seismic hazard analysis (PSHA), the PSDMs then become structural demand hazard curves. Second, PSDMs can be used in a performance-based seismic design framework, such as the one developed by PEER. In such design frameworks, PSDMs are coupled with ground motion intensity models on one side and structural element fragility models on the other side to yield probabilities of exceeding structural performance levels for a structure in a given seismic hazard environment.

## **7.1 OPTIMAL PSDMS**

From a large combination of IM-EDP pairs, a selection of optimal pairs was made based on the criteria of practicality, effectiveness, efficiency, and sufficiency. “Practical” suggests that the PSDM is realistic in an engineering sense. “Effective” describes the ability to fit a linear or piecewise linear form to the data for use in the closed-form solutions of Equation 1.1. “Efficient” describes the dispersion around these linear fits. For utility as a design tool, robustness, the requirements of effectiveness and efficiency across all periods of interest, need

also be a feature of the PSDM. Finally, a “sufficient” model has no residual dependence on  $M_w$  and  $R$ , allowing de-aggregation of hazard.

For all of the models considered, the spectral quantities ( $S_{aT_I}$ ,  $S_{vT_I}$ ,  $S_{dT_I}$ ) at the fundamental period ( $T_I$ ) of the bridge produced optimal models. The use of  $T_I$  can be extended to PSDMs in the longitudinal and transverse directions, regardless of the direction of the fundamental vibration mode. While this lack of sensitivity simplifies implementation, it indicates the presence of an optimal period not necessarily at a system eigenvalue. For a select few PSDMs, this optimal period was determined to be  $1.3T_I$ . By varying the period at which Arias intensity is computed (making it a period-dependent IM as well), similar conclusions can be drawn about the optimal period in the resulting PSDMs.

Coupled with these IMs, the complementary EDPs were separated based on scope of the response quantity. For local EDPs, such as material stresses and strains, the optimal PSDMs were determined to be steel ( $\sigma_{steel}$ ) and concrete stress ( $\sigma_{concrete}$ ). Intermediate EDPs include section behavior, with the optimal choice being maximum column moment ( $M_{max}$ ). Finally, the optimal global EDP quantity is the column drift ratio ( $\Delta$ ).

The only drawback of coupling the spectral IM or variable period  $I_A$  quantities to any of these EDPs is the period dependence of many of the design parameters. As a tool to assess performance sensitivities to design parameters, it is useful to employ period-independent IMs in the above PSDMs to more clearly identify design trends. As detailed in Chapter 3, no single period-independent IM provides the same efficiency as PSDMs containing a spectral IM. Of those investigated, the most consistent across different models and design parameters are Arias Intensity and  $PGV$ .

## 7.2 STRUCTURAL DEMAND HAZARD CURVES

The PSDM is part of the relation described in Equation 1.2. This can be extended to a structural demand hazard curve [Luco 2001a] by integrating the PSDM with a PSHA. As an example of how this can be done with the data derived in this report, the  $S_{aT_I}-\Delta$  PSDM with the bridge column aspect ratio parameter ( $D_c/D_s$ ) sensitivity for the no-abutment case of a single-bent

bridge was selected. Typical PSHA provides the probability of exceeding a given earthquake intensity, usually in terms of *PGA* or spectral acceleration. This relation has been expressed in exponential form (Eq. 7.1) by several researchers [e.g., Cornell 2002].

$$v_{IM}(x) = k_0 x^{-k} \tag{7.1}$$

By using this relationship, Equation 1.2 can be integrated directly, or the exponential fit to the PSDM (Eq. 3.1) can be used to integrate in closed form. The final form of Equation 1.2 then becomes:

$$v_{EDP}(y) = k_0 \left[ \left( \frac{y}{a} \right)^{\frac{1}{\delta}} \right]^{-k} \exp \left[ \frac{k^2}{2b^2} \sigma^2 \right] \tag{7.2}$$

As discussed in the Chapter 3, the ability to evaluate in closed form is termed “effectiveness.” Given the PSDM of Fig. 3.8, the structural demand hazard curve (Fig. 7.1) was developed for an example site in Berkeley, California. Probabilities of exceeding certain levels of ground motion were determined from the USGS zip code data [USGS], as was done when evaluating the strength factor,  $R_{USGS}$  (Table 2.7).

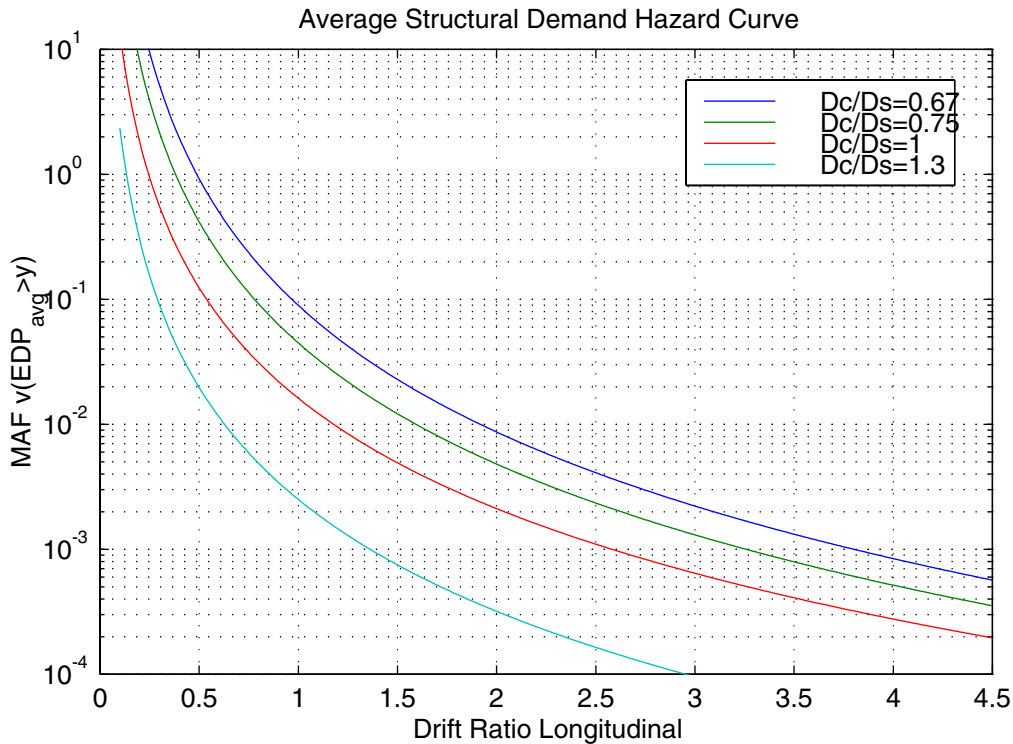


**Fig. 7.1 Structural demand hazard curve for  $Sa_{TI}-\Delta$  PSDM**

### 7.3 LIMITATIONS

There are several limitations inherent in the PSDMs produced in this study. These are primarily related to modeling, and can be systematically addressed in future studies. The PSDA method used is for a specific class of structures, not a generic SDOF oscillator. The model of this class of structures is therefore more accurate at predicting performance, but also subject to modeling error and lack of knowledge issues. Uncertainty due to lack of knowledge is addressed systematically in the PEER framework [Cornell 2002] as epistemic uncertainty. In order to reduce epistemic uncertainty, the current model has several shortcomings to be remedied.

The assumption of no shear failure in the columns was not correct, even considering modern ductile designs according to the Caltrans displacement based methodology. Due to the limitations of the fiberized beam-column element in OpenSees, shear interaction was not included. However, shear can be incorporated into the model on the section level (at numerical integration points). Future versions of the bridge model will aggregate nonlinear shear force-shear strain behavior derived empirically or analytically.

While more accurate than a fixed or partially restrained column base boundary condition, the use of pile shafts with  $P$ - $y$  springs to model soil-pile-structure-interaction is not ideal. The springs represent only the immediate soil deformation and do not account for free-field response or radiation damping. While it is possible to model all of the soil elements and add them to the bridge finite element mesh, this is quite cumbersome because there are no actual site conditions being modeled for this class of structures. The use of assumed USGS soil properties was only a method of varying the stiffness of the soil below grade, not as specific site investigation data. The obvious shortcoming of not including soil elements to attenuate ground motions as they propagate upwards is when using multiple-bent bridges. The input motion at the base of these pile shafts is not identical, as assumed in the current implementation.

Finally, the most important modeling issue is related to the use of abutment models. As illustrated in the chapter on sensitivity (Chapter 4), the current procedures for calibrating the abutment stiffness properties are sufficient for usage. However, given the large mass sensitivity, a better calibrated abutment mass model is necessary. An alternative model is one coupled with a full soil finite element mesh as described above. This would allow for mass and stiffness participation from the abutments due to both soil and structural element to be determined implicitly. Such a model has been implemented for the Humboldt Bay Bridge [Conte 2000], however, the current computational intensity would be prohibitive for the case of PSDA.

#### **7.4 THE FUTURE**

Given the well-documented state of the demand model for California highway bridges, the next step involves extending this information into the capacity domain in order to derive bridge fragility curves. Fragility curves predict the probability of exceeding a prescribed level of performance given an earthquake intensity. Fragility curves can be used specifically in the case of evaluating a single bridge in the Caltrans network. All of the bridges in this system are cataloged according to bridge class type and certain geometrical features such as number of spans and skew, as contained in the National Bridge Inventory (NBI) database (from Federal Highway Administration). Given that the demand models produced herein are for a specific class of bridges, the most commonly occurring class in California was selected. Reinforced concrete, prestressed concrete bridges, bents, and viaducts account for 87% of the total. With the use of single-, two-, and three-bent reinforced concrete bridges in the complete (with abutments) or stand-alone (no abutments) configurations derived in this study, most of this class of structures can be evaluated. Other PEER research is focused on determining damage measures and limit states given certain levels of demand using experimental procedures [PEER Capacity Catalog, PEER Reinforced Concrete Column Performance Database]. This information is useful in integration of Equation 1.1 and in determination of these desired fragilities.

The usefulness of bridge fragilities is further expanded in the context of the highway network simulation being developed by PEER [Kiremidjian 1999]. This simulation of the San Francisco Bay Area's traffic capacity in the event of an earthquake aims to predict not only loss

of traffic-load-carrying capacity, but damage to various pieces of the infrastructure and the cost to repair. Therefore, the total cost of the earthquake event scenario is broken down into the loss of operation cost and the repair or replacement cost. The repair or replacement cost is directly related to the bridge or component damage. For this to be determined, the experimental capacities described above are required. However, in order to determine the operational cost, the loss of vehicular capacity, lane closures, speed limits, etc need to be determined. These functional engineering demand parameters are not readily determinable from the component damage states and fragilities. Currently, the method for determining lane and bridge closures is based on arbitrarily selected states of damage that are assigned based on reconnaissance information [e.g., HAZUS 1997].

A bridge damaged in an average sense will be subjected to a push-under analysis due to traffic loads to determine pre- and post-earthquake capacities by using the state of knowledge of the given class of highway bridges. This loss in performance can then be related probabilistically to the intensity of the earthquake in a method similar to an IDA. Fragility curves for operational losses can then be determined and applied to the network. Similarly, fragilities for these bridges can also be developed for aftershock scenarios. Once a real earthquake occurs, these aftershock scenario estimates can be updated by using a technique such as Bayesian updating.

## REFERENCES

API (1993). *Recommended practice for planning, designing, and constructing fixed offshore platforms — Load and resistance factor design*. American Petroleum Institute, Washington D.C., Report No. RP2A-LRFD.

ATC-32 (June 1996). *Improved Seismic Design Criteria for California Bridges*. Applied Technology Council, Redwood City, California, Report No. ATC-32.

Caltrans (July 1999). *Seismic Design Criteria 1.1*. California Department of Transportation.

Chadwell, C. UCFyber and OSP software. <http://www.zevent.com>.

Chopra, A.K. and Goel, R.K. (2001). *A Modal Pushover Analysis Procedure to Estimate Seismic Demands for Buildings*, Report No. 2001/03, Pacific Earthquake Engineering Research Center, University of California, Berkeley.

Conte, J., Seible, F., and Elgamal, A. (2000). “Seismic Response and Fragility Assessment of Bridge Systems,” *PEER Project No. 5172000*, Pacific Earthquake Engineering Research Center, University of California, Berkeley.

Cordova, P.P., Mehanny, S.S.F., Deierlein, G.G., and Cornell, C.A. (March 2000). “Development of a two-parameter seismic intensity measure and probabilistic assessment procedure,” *The Second U.S.-Japan Workshop on Performance-Based Earthquake Engineering Methodology for Reinforced Concrete Building Structures*. Report No. 2000/10, Pacific Earthquake Engineering Research Center, University of California, Berkeley.

Cornell, C.A., and Krawinkler, H. (2000). “Progress and Challenges in Seismic Performance Assessment,” *PEER Center News Spring 2000*, 3(2).

Cornell, C.A., Jalayer, F., Hamburger, R.O., and Foutch, D.A. (April 2002). "Probabilistic basis for 2000 SAC/FEMA steel moment frame guidelines," *Journal of Structural Engineering*, 128(4): 526-533.

Fajfar, P., Gaspersic, P., and Drobnic, D. (1997). "A simplified nonlinear method for seismic damage analysis of structures," In *Seismic Design Methodologies for the Next Generation of Codes, Proceedings of the International Workshop*, Bled, Slovenia.

FEMA-273 (1996). *NEHRP Guidelines for the Seismic Rehabilitation of Buildings*, Federal Emergency Management Agency, Washington D.C., Report No. FEMA-273.

FEMA-302 (1997). *NEHRP Recommended Provisions for Seismic Regulations for New Buildings and Other Structures*, Federal Emergency Management Agency, Washington D.C., Report No. FEMA-302.

FEMA-356 (2000a). *Prestandard and Commentary for the Seismic Rehabilitation of Buildings*, Federal Emergency Management Agency, Washington D.C., Report No. FEMA-356.

FEMA-350 (July 2000b). *Recommended Seismic Design Criteria for New Steel Moment-Frame Buildings*, Washington D.C., Report No. FEMA-350.

Fenves, G.L. and Ellery, M. (1998). *Behavior and failure analysis of a multiple-frame highway bridge in the 1994 Northridge earthquake*, Report No. 98/08, Pacific Earthquake Engineering Research Center, University of California, Berkeley.

Foutch, D.A., Yu, C.-Y., and Wen, Y.K. (1992). "Reliability of steel frame buildings under seismic load," In *Proceedings of the Tenth World Conference on Earthquake Engineering*, A. A. Balkema, Rotterdam, Vol. 8.

Gardoni, P. (2002). "Probabilistic models and fragility estimates for structural components and systems," *Ph.D. Dissertation*, Dept. of Civil and Environmental Engineering, University of California, Berkeley.

Goel, R.K. and Chopra, A. (February 1997). "Evaluation of bridge abutment capacity and stiffness during earthquakes," *Earthquake Spectra*, 13(1): 1-23.

Gupta, A. and Krawinkler, H. (January 2000). "Behavior of ductile of SRMFs at various hazard levels," *Journal of Structural Engineering*, 126(ST1): 98-107.

HAZUS. (1997). *Earthquake loss estimation methodology*. Technical Manual. National Institute of Building Sciences for Federal Emergency Management Agency.

Hose, Y., Silva, P., and Seible, F. (2000). "Development of a performance evaluation database for concrete bridge components and systems under simulated seismic loads," *Earthquake Spectra*, 16(2): 413-442.

Inel, M. (2001). "Design strategies for the performance based seismic design of short bridges," *Ph.D. Dissertation*, Dept. of Civil and Environmental Engineering, University of Illinois, Urbana-Champaign.

Isakovic, T. and Fischinger, M. (2001). "Analysis and design of RC viaducts in moderate seismicity regions of Europe," In *Proceedings of the 4th International Symposium on Earthquake Engineering for the Moderate Seismicity Regions*, Seoul, Korea.

Kawashima, K., MacRae, G.A., Hoshikuma, J., and Nagaya, K. (May 1998). "Residual displacement response spectrum," *Journal of Structural Engineering*, 124(5): 523-530.

Kent, D.C. and Park, R. (July 1971). "Flexural members with confined concrete," *Journal of Structural Engineering*, 97(ST7): 1969-1990.

Kiremidjian, A., Chiu, S., and Moore, J. (1999). "Seismic Risk Model for a Designated Highway System," *PEER Project 1041999*, Pacific Engineering Earthquake Research Center, University of California, Berkeley.

Kramer, S.L. (1996). *Geotechnical Earthquake Engineering*, Prentice Hall, Upper Saddle River, New Jersey.

Luco, N., Cornell, C.A., and Yeo, G.L. (2001a). "Annual limit-state frequencies for partially-inspected earthquake-damaged buildings," In *8th Int'l Conference on Structural Safety and Reliability*, International Association for Structural Safety and Reliability (IASSAR), Denmark.

Luco N. (2001b). "Probabilistic seismic demand analysis, SMRF connection fractures, and near source effects," Ph.D. Dissertation, Dept. of Civil and Environmental Engineering, Stanford University, California.

Mackie, K., and Stojadinović, B. (Nov/Dec 2001). "Probabilistic Seismic Demand Model for California Highway Bridges," *Journal of Bridge Engineering*, 6(6): 468-481.

Mackie, K., and Stojadinovic, B. (2002a). "Optimal Probabilistic Seismic Demand Model for Typical Highway Overpass Bridges," In *Proceedings of the 12th European Conference on Earthquake Engineering*, Elsevier Science Ltd.

Mackie, K. and Stojadinović, B. (2002b). "Design parameter sensitivity in Probabilistic Seismic Demand Models," In *Proceedings of the 7<sup>th</sup> US National Conference on Earthquake Engineering*, Boston, Massachusetts.

Mackie, K. and Stojadinović, B. (2002c). "Relation between Probabilistic Seismic Demand Analysis and Incremental Dynamic Analysis," In *Proceedings of the 7<sup>th</sup> US National Conference on Earthquake Engineering*, Boston, Massachusetts.

Mander, J.B., Priestley, M.J.N., and Park, R. (August 1988). “Theoretical stress-strain model for confined concrete,” *Journal of the Structural Engineering*, 114(ST8): 1804-1826.

Maroney, B., Kutter, B., Romstad, K., Chai, Y.H., and Vanderbilt, E. (1994a). “Interpretation of large scale bridge abutment test results,” In *Proceedings of 3rd Annual Seismic Research Workshop*, California Department of Transportation, Sacramento, CA.

Maroney, B.H., and Chair, Y.H. (1994b). “Seismic design and retrofitting of reinforced concrete bridges,” In *Proceedings of 2nd International Workshop*, Earthquake Commission of New Zealand, Queenstown, New Zealand: 255-76.

MathWorks. MATLAB software. <http://www.mathworks.com>.

McKenna, F. and Fenves, G.L. (2000). “An object-oriented software design for parallel structural analysis,” In *Proceedings of the Advanced Technology in Structural Engineering*, Structures Congress 2000, ASCE, Washington, D. C.

Medina, R., Krawinkler, H., and Alavi, B. (July 2001). “Seismic drift and ductility demands and their dependence on ground motions,” In *Proceedings of the US-Japan Seminar on Advanced Stability and Seismicity Concepts for Performance-Based Design of Steel and Composite Structures*, Kyoto, Japan.

Neuenhofer, A., and Filippou, F.C. (June 1998). “Geometrically nonlinear flexibility-based frame finite element,” *Journal of Structural Engineering*, 124(6): 704-711.

OpenSees. <http://www.opensees.org>. Web page.

PEER Capacity Catalog.

[http://www.structures.ucsd.edu/PEER/CapacityCatalog/capacity\\_catalog.html](http://www.structures.ucsd.edu/PEER/CapacityCatalog/capacity_catalog.html). Web page.

PEER Reinforced Concrete Column Performance Database.

<http://maximus.ce.washington.edu/~peera1/>. Web page.

PEER Strong Motion Catalog. <http://peer.berkeley.edu/smcat>. Web page.

Priestley, M.J.N., Seible, F., and Calvi, G.M. (1996). *Seismic Design and Retrofit of Bridges*, John Wiley and Sons, Inc., New York, New York.

Seed, H.B. and Idriss, I.M. (1970). *Soil moduli and damping in soils, design equation and curves*, Report No. EERC 70-10, Earthquake Engineering Research Center, University of California, Berkeley.

Shome, N., Cornell, C.A., Bazzurro, P., and Caraballo, J.E. (June 1998). "Earthquakes, records, and nonlinear responses," *Earthquake Spectra*, 14(3): 467-500.

Shome, N., and Cornell, C.A. (1999). "Probabilistic seismic demand analysis of nonlinear structures," *Reliability of Marine Structures Report No. RMS-35*, Dept. of Civil and Envir. Engineering, Stanford University, California.

Structural Engineers Association of California. (1995). *A framework for performance based design*, Report No. Vision 2000, Sacramento, California.

Structural Engineers Association of California, (1996). *Recommended lateral force requirements and commentary*, ed. Shea, G.H., Sacramento, California.

Travasarou, T., Bray, J.D., and Abrahamson, N.A. (2002). "Empirical attenuation relationship for Arias Intensity." Submitted to *Journal of Earthquake Engineering and Structural Dynamics*.

USGS. National Seismic Hazard Mapping Project Zip Code Look-up for Ground Motion Values. <http://eqint.cr.usgs.gov/eq/html/zipcode.shtml>. Web page.

Vamvatsikos, D. and Cornell, C.A. (March 2002). "Incremental dynamic analysis," *Earthquake Engineering and Structural Dynamics*, 31(3): 491-512.

Werner, S.D. (1994). "Study of Caltrans' seismic evaluation procedure for short bridges," In *Proceedings of 3<sup>rd</sup> Annual Seismic Research Workshop*, Sacramento, CA.

Wilson, J.C. and Tan, B.S. (August 1990). "Bridge Abutments: Formulation of Simple Model for Earthquake Response Analysis," *Journal of Engineering Mechanics*," 116(8): 1828-1837.

Wissawapaisal, C. and Aschheim, M. (September 2000). *Modeling the transverse response of short bridges subjected to earthquakes*, Technical Report No. 00-05, Mid-America Earthquake Center, University of Illinois, Urbana-Champaign, IL.

Yashinsky, M. and Ostrom, T. (February 2000). "Caltrans' new seismic design criteria for bridges," *Earthquake Spectra*, 16(1): 285-307.

Zhang, J. and Makris, N. (March 2001). *Seismic Response Analysis of Highway Overcrossings Including Soil-Structure Interaction*, PEER Report No. 2001/02, Pacific Engineering Earthquake Research Center, University of California, Berkeley.

Yun, S.Y., Hamburger, R.O., Cornell, C.A., and Foutch, D.A. (2002). "Seismic performance for steel moment frames." Submitted to *Journal of Structural Engineering*.

## Appendix A Notation

The following symbols were used in this report.

$D_c$	=	column diameter (single-bent)
$D_{c1}$	=	column diameter of left column (where appropriate)
$D_{c2}$	=	column diameter of right column (two-bent) or middle column (three-bent)
$D_{c3}$	=	column diameter of right column (three-bent)
$d_s$	=	centerline diameter of column spirals
$D_s$	=	superstructure depth
$DM$	=	damage measure
$DV$	=	decision variable
$E$	=	Young's modulus
$EDP$	=	engineering demand parameter
$f'_c$	=	concrete 28-day unconfined compressive strength
$f'_{cc}$	=	maximum confined concrete compressive strength
$f'_l$	=	effective lateral concrete confining stress
$f_y$	=	steel reinforcement yield stress
$H$	=	column height above grade (single-bent)
$H_1$	=	column height above grade of left column (where appropriate)
$H_2$	=	column height above grade of right column (two-bent) or middle column (three-bent)
$H_3$	=	column height above grade of right column (three-bent)
$I_y$	=	moment of inertia about local y axis
$I_z$	=	moment of inertia about global Z axis
$IM$	=	intensity measure
$J$	=	torsional moment of inertia
$k$	=	optimal period constant

$K_i$	=	initial stiffness
$K_s$	=	secant stiffness
$K_{soil}$	=	USGS soil group below grade of columns
$k_l$	=	longitudinal abutment stiffness
$k_t$	=	transverse abutment stiffness
$\bar{k}_t$	=	transverse embankment stiffness per unit length
$L$	=	span length (single-bent)
$L'$	=	length from maximum moment to point of inflection
$L_1$	=	span length of left span (where appropriate)
$L_2$	=	span length of middle span (two-bent) or second span from the left (three-bent)
$L_3$	=	span length of second span from right (three-bent)
$L_c$	=	critical abutment embankment length
$L_p$	=	plastic hinge length
LM	=	large magnitude
LR	=	large distance
$m$	=	mass
$M_{max}$	=	maximum column moment (k-in.)
$M_w$	=	moment magnitude
$R$	=	closest distance (km)
$RI^*$	=	modified regularity index (Eq. 2.12)
$s'$	=	clear spacing between column spirals
$Sa_{T1}$	=	first mode spectral acceleration
$Sd_{T1}$	=	first mode spectral displacement
$Sv_{T1}$	=	first mode spectral velocity
SM	=	small magnitude
SR	=	small distance
$T_1$	=	first mode bridge period
$T_2$	=	second mode bridge period
$T_i$	=	initial elastic period
$T_s$	=	equivalent secant period

$u_y$	=	yield displacement
$W_t$	=	additional dead weight of the superstructure (%)
$\alpha$	=	degree of deck skewness (degrees)
$\Delta$	=	drift ratio
$\gamma$	=	effective weight of soil (force/volume)
$\eta$	=	strain-hardening ratio of equivalent force-displacement system
$\nu$	=	mean annual frequency of exceedance
$\rho_{s,long.}$	=	steel longitudinal reinforcement ratio (%)
$\rho_{s,trans.}$	=	steel transverse reinforcement ratio (%)
$\sigma$	=	PSDM dispersion (Eq. 3.3)
$\sigma_{concrete}$	=	stress in concrete fiber
$\sigma_{steel}$	=	stress in steel fiber
$\phi'$	=	angle of internal soil friction (degrees)
$\bar{\phi}(x)$	=	mode shape normalized to a maximum value of 1.0
$\bar{\phi}_i$	=	value of $\bar{\phi}(x_i)$
$\phi_y$	=	yield curvature

## Appendix B Ground Motion Records

Specific information detailing all the ground motion records used in this study is contained in the tables of this appendix. The tables are separated according to bin. All of the records and record information were obtained from the PEER strong motion catalog (PEER Strong Motion Catalog). Values of *PGA*, *PGV*, and *PGD* are shown for informational purposes only. In reality, values were calculated when the acceleration record is integrated by the IM processing routines (Appendix C).

Table Appendix B.1 LMSR (Large magnitude small distance)

Table Appendix B.2 LMLR (Large magnitude large distance)

Table Appendix B.3 SMSR (Small magnitude small distance)

Table Appendix B.4 SMLR (Small magnitude large distance)

Table Appendix B.5 Near (Large magnitude near-field effects)

Table BII.1 - LMSR (Large Magnitude, Small Distance)

Record ID	Event	Year	M	R (km)	Station	Soil	Mechanism	fHP (Hz)			fLP (Hz)			PGA (g)			PGV (cm/s)			PGD (cm)		
								x	y	z	x	y	z	x	y	z	x	y	z	x	y	z
AGW	Loma Prieta	1989	6.9	28.2	Agnews State Hospital	D	reverse-obliqu	0.20	0.20	0.20	30.0	30.0	42.0	0.159	0.172	0.093	17.6	26.0	8.3	9.8	12.6	4.4
CAP	Loma Prieta	1989	6.9	14.5	Capitola	D	reverse-obliqu	0.20	0.20	0.20	40.0	48.0	50.0	0.443	0.529	0.541	29.3	36.5	19.4	5.5	9.1	2.6
G03	Loma Prieta	1989	6.9	14.4	Gilroy Array #3	D	reverse-obliqu	0.10	0.10	0.10	40.0	33.0	50.0	0.367	0.555	0.338	44.7	35.7	15.5	19.3	8.2	7.0
G04	Loma Prieta	1989	6.9	16.1	Gilroy Array #4	D	reverse-obliqu	0.20	0.20	0.20	30.0	28.0	42.0	0.212	0.417	0.159	37.9	38.8	14.6	10.1	7.1	5.1
GMR	Loma Prieta	1989	6.9	24.2	Gilroy Array #7	D	reverse-obliqu	0.20	0.20	0.20	35.0	40.0	48.0	0.323	0.226	0.115	16.6	16.4	5.6	3.3	2.5	2.9
HCH	Loma Prieta	1989	6.9	28.2	Hollister City Hall	D	reverse-obliqu	0.10	0.10	0.10	30.0	29.0	32.0	0.215	0.247	0.216	45.0	38.5	14.9	26.1	17.8	7.1
HDA	Loma Prieta	1989	6.9	25.8	Hollister Differential Array	D	reverse-obliqu	0.10	0.10	0.10	33.0	40.0	38.0	0.279	0.269	0.154	35.6	43.9	8.4	13.1	18.5	4.2
SVL	Loma Prieta	1989	6.9	28.8	Sunnyvale - Colton Ave.	D	reverse-obliqu	0.10	0.10	0.10	32.0	40.0	50.0	0.209	0.207	0.104	36.0	37.3	8.6	16.9	19.1	4.1
CNP	Northridge	1994	6.7	15.8	Canoga Park - Topanga Can.	D	reverse-slip	0.10	0.05	0.05	30.0	30.0	30.0	0.420	0.356	0.489	60.8	32.1	14.2	20.2	9.1	5.5
FAR	Northridge	1994	6.7	23.9	LA - N Faring Rd.	D	reverse-slip	0.13	0.13	0.20	30.0	30.0	30.0	0.242	0.273	0.191	29.8	15.8	8.9	4.7	3.3	1.7
FLE	Northridge	1994	6.7	29.5	LA - Fletcher Dr.	D	reverse-slip	0.15	0.13	0.30	30.0	30.0	30.0	0.240	0.162	0.109	26.2	10.7	6.9	3.6	2.9	1.2
GLP	Northridge	1994	6.7	25.4	Glendale - Las Palmas	D	reverse-slip	0.10	0.13	0.30	30.0	30.0	30.0	0.206	0.357	0.127	7.4	12.3	4.3	1.8	1.9	0.4
HOL	Northridge	1994	6.7	25.5	LA - Hollywood Stor FF	D	reverse-slip	0.20	0.20	0.20	23.0	23.0	23.0	0.358	0.231	0.139	27.5	18.3	9.2	3.0	4.8	2.3
NYA	Northridge	1994	6.7	22.3	La Crescenta-New York	D	reverse-slip	0.10	0.30	0.13	30.0	30.0	30.0	0.159	0.178	0.106	11.3	12.5	3.9	3.0	1.1	0.9
LOS	Northridge	1994	6.7	13.0	Canyon Country - W Lost Cany	D	reverse-slip	0.10	0.05	0.20	30.0	30.0	30.0	0.482	0.410	0.318	45.1	43.0	20.3	12.6	11.8	5.2
RO3	Northridge	1994	6.7	12.3	Sun Valley - Roscoe Blvd	D	reverse-slip	0.10	0.10	0.10	30.0	30.0	30.0	0.443	0.303	0.306	38.2	22.1	12.5	10.0	7.8	5.0
PEL	San Fernando	1971	6.6	21.2	LA - Hollywood Stor Lot	D	reverse-slip	0.20	0.20	0.50	35.0	35.0	35.0	0.174	0.210	0.136	14.9	18.9	4.3	6.3	12.4	1.5
B-ICC	Superstition Hills	1987	6.7	13.9	El Centro Imp. Co. Cent	D	strike-slip	0.10	0.10	0.10	38.0	40.0	47.0	0.258	0.358	0.128	40.9	46.4	8.4	20.2	17.5	4.9
B-IVW	Superstition Hills	1987	6.7	24.4	Wildlife Liquef. Array	D	strike-slip	0.10	0.10	0.10	40.0	50.0	50.0	0.207	0.181	0.408	34.5	29.9	6.0	21.0	19.9	3.9
B-WSM	Superstition Hills	1987	6.7	13.3	Westmorland Fire Station	D	strike-slip	0.10	0.10	0.10	40.0	35.0	50.0	0.211	0.172	0.249	31.0	23.5	8.7	20.3	13.0	4.2

Given R is closest to fault rupture, red indicates hypocentral distance

Table BII.2 - LMLR (Large Magnitude, Large Distance)

Record ID	Event	Year	M	R (km)	Station	Soil	Mechanism	fHP (Hz)			fLP (Hz)			PGA (g)			PGV (cm/s)			PGD (cm)		
								x	y	z	x	y	z	x	y	z	x	y	z	x	y	z
A-ELC	Borrego Mountain	1968	6.8	46.0	El Centro Array #9	D	strike-slip	0.20	0.20	0.20	12.8	12.5	16.4	0.057	0.130	0.030	13.2	26.3	3.3	10.0	12.2	2.0
A2E	Loma Prieta	1989	6.9	57.4	APEEL 2E Hayward Muir Sch.	D	reverse-obliqu	0.20	0.20	0.20	25.0	30.0	40.0	0.139	0.171	0.095	11.5	13.7	3.8	5.7	3.9	2.4
FMS	Loma Prieta	1989	6.9	43.4	Fremont - Emerson Court	D	reverse-obliqu	0.10	0.10	0.10	32.0	31.0	38.0	0.141	0.192	0.067	12.9	12.7	8.6	8.4	5.5	6.4
HVR	Loma Prieta	1989	6.9	31.6	Halls Valley	D	reverse-obliqu	0.20	0.20	0.20	22.0	22.0	28.0	0.103	0.134	0.056	13.5	15.4	8.4	5.5	3.3	4.1
SJW	Loma Prieta	1989	6.9	32.6	Salinas - John & Work	D	reverse-obliqu	0.10	0.10	0.10	28.0	30.0	42.0	0.112	0.091	0.101	15.7	10.7	6.7	7.9	8.6	2.4
SLC	Loma Prieta	1989	6.9	36.3	Palo Alto - SLAC Lab.	D	reverse-obliqu	0.20	0.20	0.20	28.0	33.0	40.0	0.278	0.194	0.090	29.3	37.5	10.2	9.7	10.0	2.8
BAD	Northridge	1994	6.7	56.1	Covina - W. Badillo	D	reverse-slip	0.20	0.20	0.30	30.0	30.0	30.0	0.079	0.100	0.043	7.0	5.8	2.9	1.6	1.2	0.7
CAS	Northridge	1994	6.7	49.6	Compton - Castlegate St.	D	reverse-slip	0.20	0.10	0.40	30.0	30.0	30.0	0.136	0.088	0.046	7.1	6.8	2.6	2.2	3.4	0.4
CEN	Northridge	1994	6.7	30.9	LA - Centinela St.	D	reverse-slip	0.20	0.13	0.13	30.0	30.0	30.0	0.322	0.465	0.109	22.9	19.3	10.6	5.5	3.5	3.8
DEL	Northridge	1994	6.7	59.3	Lakewood - Del Amo Blvd.	D	reverse-slip	0.20	0.13	0.80	30.0	30.0	30.0	0.123	0.137	0.058	10.4	11.2	1.6	2.9	2.0	0.2
DWN	Northridge	1994	6.7	47.6	Downey - Co. Maint. Bldg.	D	reverse-slip	0.20	0.20	0.20	23.0	23.0	23.0	0.230	0.158	0.146	11.3	13.8	3.9	2.1	2.3	0.3
JAB	Northridge	1994	6.7	46.6	Bell Gardens - Jaboneria	D	reverse-slip	0.13	0.13	0.13	30.0	30.0	30.0	0.068	0.098	0.049	7.6	7.4	3.5	2.5	3.5	1.9
LH1	Northridge	1994	6.7	36.3	Lake Hughes #1	D	reverse-slip	0.12	0.12	0.12	23.0	23.0	23.0	0.077	0.087	0.099	9.5	9.4	7.0	2.4	3.7	3.4
LOA	Northridge	1994	6.7	42.4	Lawndale - Osage Ave.	D	reverse-slip	0.13	0.13	0.13	30.0	30.0	30.0	0.152	0.084	0.053	8.0	8.5	3.5	2.6	2.9	1.8
LV2	Northridge	1994	6.7	37.7	Leona Valley #2	D	reverse-slip	0.20	0.20	0.20	23.0	23.0	23.0	0.063	0.091	0.058	7.2	7.5	7.1	1.6	1.6	2.1
PHP	Northridge	1994	6.7	43.6	Palmdale - Hwy 14 & Palmdale	D	reverse-slip	0.20	0.20	0.20	46.0	46.0	46.0	0.067	0.061	0.040	16.9	14.8	8.0	8.0	7.2	5.5
PIC	Northridge	1994	6.7	32.7	LA - Pico & Sentous	D	reverse-slip	0.20	0.20	0.20	46.0	46.0	46.0	0.186	0.103	0.065	14.3	12.2	5.3	2.4	3.7	1.7
SOR	Northridge	1994	6.7	54.1	West Covina - S. Orange Ave.	D	reverse-slip	0.10	0.20	0.20	30.0	30.0	30.0	0.067	0.063	0.049	5.8	5.9	2.7	2.7	1.3	1.0
SSE	Northridge	1994	6.7	60.0	Terminal Island - S. Seaside	D	reverse-slip	0.13	0.13	0.13	30.0	30.0	30.0	0.194	0.133	0.048	12.1	13.7	3.1	2.3	2.7	1.5
VER	Northridge	1994	6.7	39.3	LA - E Vernon Ave.	D	reverse-slip	0.10	0.20	0.20	30.0	30.0	30.0	0.153	0.120	0.063	10.1	9.2	3.4	1.8	1.7	1.2

Given R is closest to fault rupture, red indicates hypocentral distance

Table BII.3 - SMSR (Small Magnitude, Small Distance)

Record ID	Event	Year	M	R (km)	Station	Soil	Mechanism	fHP (Hz)			fLP (Hz)			PGA (g)			PGV (cm/s)			PGD (cm)		
								x	y	z	x	y	z	x	y	z	x	y	z	x	y	z
H-CAL	Imperial Valley	1979	6.5	23.8	Calipatria Fire Station	D	strike-slip	0.10	0.10	0.10	40.0	40.0	40.0	0.078	0.128	0.055	13.3	15.4	3.9	6.2	10.9	2.8
H-CHI	Imperial Valley	1979	6.5	28.7	Chihuahua	D	strike-slip	0.05	0.05	0.05	-	-	-	0.254	0.270	0.218	30.1	24.9	5.1	12.9	9.1	1.3
H-E01	Imperial Valley	1979	6.5	15.5	El Centro Array #1	D	strike-slip	0.10	0.10	0.10	40.0	40.0	40.0	0.134	0.139	0.056	10.7	16.0	3.8	7.0	10.0	2.1
H-E12	Imperial Valley	1979	6.5	18.2	El Centro Array #12	D	strike-slip	0.10	0.10	0.10	40.0	40.0	40.0	0.116	0.143	0.066	21.8	17.6	6.7	12.1	11.3	5.3
H-E13	Imperial Valley	1979	6.5	21.9	El Centro Array #13	D	strike-slip	0.20	0.20	0.20	40.0	40.0	40.0	0.139	0.117	0.046	13.0	14.7	3.2	5.8	7.3	1.7
H-WSM	Imperial Valley	1979	6.5	15.1	Westmorland Fire Station	D	strike-slip	0.10	0.10	0.10	40.0	40.0	40.0	0.110	0.074	0.082	21.9	21.2	6.8	10.0	16.6	2.6
A-SRM	Livermore	1980	5.8	21.7	San Ramon Fire Station	D	strike-slip	0.20	0.15	0.30	15.0	15.0	20.0	0.040	0.058	0.016	4.0	3.3	2.0	1.2	1.0	0.4
A-KOD	Livermore	1980	5.8	17.6	San Ramon - Eastman Kodak	D	strike-slip	0.20	0.08	0.40	20.0	20.0	30.0	0.076	0.154	0.042	6.1	18.9	2.8	1.7	6.1	0.5
M-AGW	Morgan Hill	1984	6.2	29.4	Agnews State Hospital	D	strike-slip	0.20	0.20	0.20	13.0	14.0	18.0	0.032	0.032	0.016	5.5	5.0	3.2	2.1	2.3	1.6
M-G02	Morgan Hill	1984	6.2	15.1	Gilroy Array #2	D	strike-slip	0.10	0.20	0.20	37.0	31.0	37.0	0.212	0.162	0.578	12.6	5.1	10.8	2.1	1.4	0.9
M-G03	Morgan Hill	1984	6.2	14.6	Gilroy Array #3	D	strike-slip	0.10	0.10	0.10	32.0	37.0	42.0	0.200	0.194	0.395	12.7	11.2	9.9	3.5	2.4	1.2
M-GMR	Morgan Hill	1984	6.2	14.0	Gilroy Array #7	D	strike-slip	0.10	0.10	0.10	30.0	31.0	40.0	0.113	0.190	0.428	6.0	7.4	5.4	1.8	2.1	0.9
PHN	Point Mugu	1973	5.8	25.0	Port Hueneme	D	reverse-slip	0.15	0.20	0.20	30.0	25.0	30.0	0.083	0.112	0.047	4.6	14.8	2.2	0.8	2.6	0.4
BRA	Westmorland	1981	5.8	22.0	5060 Brawley Airport	D	strike-slip	0.70	0.15	0.60	33.0	40.0	40.0	0.171	0.169	0.101	5.8	12.7	2.2	0.5	3.1	0.2
NIL	Westmorland	1981	5.8	19.4	724 Niland Fire Station	D	strike-slip	0.25	0.30	0.30	40.0	33.0	33.0	0.176	0.105	0.126	6.6	5.6	2.9	0.8	0.7	0.5
A-CAS	Whittier Narrows	1987	6.0	16.9	Compton - Castlegate St.	D	reverse	0.28	0.09	0.50	25.0	25.0	25.0	0.333	0.332	0.167	14.1	27.1	3.3	1.5	5.0	0.2
A-CAT	Whittier Narrows	1987	6.0	28.1	Carson - Catskill Ave.	D	reverse	0.55	0.18	0.50	25.0	25.0	25.0	0.059	0.042	0.037	2.4	3.8	1.3	0.3	0.8	0.2
A-DWN	Whittier Narrows	1987	6.0	18.3	14368 Downey - Co Maint Bldg	D	reverse	0.25	0.20	1.00	30.0	30.0	40.0	0.141	0.221	0.177	13.4	28.8	3.3	1.6	4.0	0.2
A-W70	Whittier Narrows	1987	6.0	16.3	LA - W 70th St.	D	reverse	0.20	0.30	0.30	25.0	25.0	25.0	0.151	0.198	0.077	8.7	19.5	2.8	1.5	2.5	0.5
A-WAT	Whittier Narrows	1987	6.0	24.5	Carson - Water St.	D	reverse	0.30	0.20	0.50	25.0	25.0	25.0	0.133	0.104	0.046	11.3	9.0	2.0	1.5	1.9	0.2

Given R is closest to fault rupture, red indicates hypocentral distance

Table BII.4 - SMLR (Small Magnitude, Large Distance)

Record ID	Event	Year	M	R (km)	Station	Soil	Mechanism	fHP (Hz)			fLP (Hz)			PGA (g)			PGV (cm/s)			PGD (cm)		
								x	y	z	x	y	z	x	y	z	x	y	z	x	y	z
B-ELC	Borrego	1942	6.5	49.0	El Centro Array #9	D	unknown	0.10	0.10	0.10	15.0	15.0	20.0	0.044	0.068	0.033	4.0	3.9	1.1	1.4	1.4	0.3
H-C05	Coalinga	1983	6.4	47.3	Parkfield - Cholame 5W	D	reverse-obliqu	0.20	0.20	0.50	22.0	22.0	30.0	0.131	0.147	0.034	10.0	10.8	2.3	1.3	1.1	1.1
H-C08	Coalinga	1983	6.4	50.7	Parkfield - Cholame 8W	D	reverse-obliqu	0.50	0.20	0.20	21.0	23.0	27.0	0.100	0.098	0.024	8.0	8.6	3.3	1.3	1.5	0.9
H-CC4	Imperial Valley	1979	6.5	49.3	Coachella Canal #4	D	strike-slip	0.20	0.20	0.20	40.0	40.0	40.0	0.128	0.115	0.038	15.6	12.5	3.6	3.0	2.3	0.7
H-CMP	Imperial Valley	1979	6.5	32.6	Compuertas	D	strike-slip	0.20	0.20	0.20	-	-	-	0.147	0.186	0.075	9.5	13.9	2.9	2.5	2.9	1.0
H-DLT	Imperial Valley	1979	6.5	43.6	Delta	D	strike-slip	0.05	0.05	0.05	-	-	-	0.351	0.238	0.145	33.0	26.0	14.8	19.0	12.1	8.6
H-NIL	Imperial Valley	1979	6.5	35.9	Niland Fire Station	D	strike-slip	0.10	0.10	0.10	40.0	30.0	40.0	0.069	0.109	0.034	8.3	11.9	3.8	5.3	6.9	2.0
H-PLS	Imperial Valley	1979	6.5	31.7	Plaster City	D	strike-slip	0.10	0.10	0.10	40.0	40.0	40.0	0.057	0.042	0.026	5.4	3.2	2.4	1.9	1.3	1.0
H-VCT	Imperial Valley	1979	6.5	54.1	Victoria	D	strike-slip	0.20	0.05	0.05	-	-	-	0.167	0.122	0.059	8.3	6.4	1.6	1.1	2.1	0.7
A-STP	Livermore	1980	5.8	37.3	Tracy - Sewage Treatment Plant	D	strike-slip	0.08	0.15	0.20	15.0	20.0	20.0	0.073	0.050	0.021	7.6	7.5	3.1	1.8	2.4	1.0
M-CAP	Morgan Hill	1984	6.2	38.1	Capitola	D	strike-slip	0.20	0.20	0.20	28.0	30.0	35.0	0.142	0.099	0.045	8.1	4.9	2.1	1.6	0.6	0.4
M-HCH	Morgan Hill	1984	6.2	32.5	Hollister City Hall	D	strike-slip	0.20	0.20	0.20	24.0	19.0	25.0	0.071	0.071	0.118	9.0	7.4	3.9	3.8	1.6	1.1
M-SJB	Morgan Hill	1984	6.2	30.3	San Juan Bautista	C	strike-slip	0.10	0.10	0.10	21.0	21.0	21.0	0.036	0.044	0.052	4.4	4.3	2.7	1.5	1.7	1.4
H06	N. Palm Springs	1986	6.0	39.6	San Jacinto Valley Cemetery	D	strike-slip	0.20	0.20	0.50	31.0	38.0	40.0	0.063	0.069	0.053	4.4	3.1	1.8	1.2	1.0	0.3
INO	N. Palm Springs	1986	6.0	39.6	Indio	D	strike-slip	0.10	0.10	0.10	35.0	35.0	40.0	0.117	0.064	0.087	12.3	6.6	3.1	3.6	2.2	1.4
A-BIR	Whittier Narrows	1987	6.0	56.8	Downey - Birchdale	D	reverse	0.15	0.28	0.60	25.0	25.0	25.0	0.299	0.243	0.230	37.8	13.7	4.1	5.0	1.9	0.3
A-CTS	Whittier Narrows	1987	6.0	31.3	LA - Century City CC South	D	reverse	0.30	0.20	0.40	25.0	25.0	30.0	0.063	0.051	0.021	5.4	3.5	1.7	0.8	0.6	0.3
A-HAR	Whittier Narrows	1987	6.0	34.2	LB - Harbor Admin FF	D	reverse	0.25	0.60	0.20	25.0	30.0	25.0	0.071	0.058	0.028	7.3	4.1	1.6	0.9	0.6	0.4
A-SSE	Whittier Narrows	1987	6.0	35.7	Terminal Island - S. Seaside	D	reverse	0.28	0.20	0.28	25.0	25.0	25.0	0.041	0.042	0.021	3.1	3.9	1.2	1.0	1.0	0.3
A-STC	Whittier Narrows	1987	6.0	39.8	Northridge - Saticoy St.	D	reverse	0.20	0.23	0.25	25.0	25.0	25.0	0.118	0.161	0.084	5.1	8.4	2.4	0.8	0.7	0.4

Given R is closest to fault rupture, red indicates hypocentral distance

Borrego magnitude not from Silva database

Table BII.5 - Near (Nearby-Field)

Record ID	Event	Year	M	R (km)	Station	Soil	Mechanism	fHP (Hz)			fLP (Hz)			PGA (g)			PGV (cm/s)			PGD (cm)		
								x	y	z	x	y	z	x	y	z	x	y	z	x	y	z
I-ELC	Imperial Valley	1940	7.0	8.3	El Centro Array #9	D	strike-slip	0.20	0.20	0.20	15.0	15.0	15.0	0.215	0.313	0.205	30.2	29.8	10.7	23.9	13.3	9.2
C08	Parkfield	1966	6.1	5.3	Cholame #8	D	strike-slip	0.20	0.20	0.20	20.0	20.0	24.0	0.273	0.246	0.116	11.3	10.2	4.3	3.2	3.6	1.5
H-AEP	Imperial Valley	1979	6.5	8.5	Aeropuerto Mexicali	D	strike-slip	0.20	0.20	0.20	-	-	-	0.260	0.327	0.142	24.9	42.8	5.6	3.8	10.1	2.3
H-BCR	Imperial Valley	1979	6.5	2.5	Bonds Corner	D	strike-slip	0.10	0.10	0.10	40.0	40.0	40.0	0.775	0.588	0.425	45.9	45.2	12.2	14.9	16.8	4.0
H-CXO	Imperial Valley	1979	6.5	10.6	Calexico Fire Station	D	strike-slip	0.20	0.10	0.10	40.0	40.0	40.0	0.202	0.275	0.187	16.0	21.2	6.7	9.2	9.0	2.5
H-ECC	Imperial Valley	1979	6.5	7.6	EC County Center FF	D	strike-slip	0.10	0.10	0.10	35.0	40.0	50.0	0.235	0.213	0.246	68.8	37.5	18.1	39.4	16.0	9.7
H-E05	Imperial Valley	1979	6.5	1.0	El Centro Array #5	D	strike-slip	0.10	0.10	0.10	40.0	40.0	40.0	0.379	0.519	0.537	90.5	46.9	38.5	63.0	35.4	19.7
H-SHP	Imperial Valley	1979	6.5	11.1	SAHOP Casa Flores	D	strike-slip	0.20	0.20	0.20	-	-	-	0.506	0.287	0.379	30.9	19.6	9.2	5.6	2.7	1.5
H-PVP	Coalinga	1983	6.4	8.5	Pleasant Valley P.P. - bldg	D	reverse-obliqu	0.20	0.20	0.20	22.0	20.0	30.0	0.285	0.380	0.206	19.1	32.4	12.3	2.6	6.4	2.5
M-HVR	Morgan Hill	1984	6.2	3.4	Halls Valley	D	strike-slip	0.20	0.20	0.20	30.0	26.0	28.0	0.312	0.156	0.110	39.4	12.5	12.2	7.7	1.8	1.3
A-JAB	Whittier Narrows	1987	6.0	9.8	Bell Gardens - Jaboneria	D	reverse-slip	0.10	0.25	0.40	25.0	25.0	25.0	0.212	0.219	0.095	21.8	18.9	2.7	4.8	2.5	0.4
A-SOR	Whittier Narrows	1987	6.0	10.5	West Covina - S. Orange Ave.	D	reverse-slip	0.23	0.23	0.50	25.0	25.0	25.0	0.179	0.137	0.131	7.0	10.6	3.7	1.8	1.8	0.2
GOF	Loma Prieta	1989	6.9	12.7	Gilroy - Historic Bldg.	D	reverse-obliqu	0.20	0.20	0.20	40.0	38.0	52.0	0.241	0.284	0.149	24.0	42.0	11.1	3.7	11.1	6.0
G02	Loma Prieta	1989	6.9	12.7	Gilroy Array #2	D	reverse-obliqu	0.20	0.20	0.20	31.0	40.0	40.0	0.322	0.367	0.294	39.1	32.9	14.6	12.1	7.2	4.7
JEN	Northridge	1994	6.7	6.2	Jensen Filter Plant	D	reverse-slip	0.20	0.08	0.30	-	-	-	0.593	0.424	0.400	99.3	106.2	34.1	24.0	43.1	8.9
NWH	Northridge	1994	6.7	7.1	Newhall - Fire Station	D	reverse-slip	0.12	0.12	0.12	23.0	23.0	23.0	0.590	0.583	0.548	97.2	75.5	31.5	38.1	17.6	16.3
RRS	Northridge	1994	6.7	7.1	Rinaldi Receiving Station	D	reverse-slip	-	-	-	-	-	-	0.472	0.838	0.852	73.0	166.1	50.7	19.8	28.8	11.7
SPV	Northridge	1994	6.7	8.9	Sepulveda VA	D	reverse-slip	0.00	0.10	0.10	-	-	-	0.939	0.753	0.467	76.6	84.8	33.2	15.0	18.7	9.6
SCS	Northridge	1994	6.7	6.2	Sylmar - Converter Station	D	reverse-slip	-	-	-	-	-	-	0.897	0.612	0.586	102.8	117.4	34.6	47.0	53.5	25.4
SYL	Northridge	1994	6.7	6.4	Sylmar - Olive View Med FF	D	reverse-slip	0.12	0.12	0.12	23.0	23.0	23.0	0.843	0.604	0.535	129.6	78.2	19.1	32.7	16.1	8.5

Given R is closest to fault rupture, red indicates hypocentral distance

## **Appendix C    Analysis Procedure Details**

All of the analysis routines in this study were performed using PEER's OpenSees (Open System for Earthquake Engineering Simulation) [McKenna 2000, OpenSees] finite element platform. Several supplemental routines were added to provide pre- and post-analysis functionality to the analysis modules. These routines are specifically related to the calculation of ground motion dependent intensity measures and bridge model specific response parameters. All subsequent data interpretation and visualization were then conducted with associated Matlab [MathWorks] routines (see Appendix D).

### **APPENDIX C.1    OPENSEES**

The bridge as described in Section 2.4 was implemented in OpenSees by using a fully three-dimensional nonlinear model. Geometry was defined from the selection of design parameters; however, all variations shown in this appendix are on the single-column bent, two-equal-span overpass model. Extensions to this bridge class were investigated with similar implementations and were detailed in the multiple-bent bridge chapter (Chapter 6). A sample finite element bridge model is shown in Figure Appendix C.1. The array of transverse elements at bridge ends are used to provide accurate abutment models. See Section 2.4.3 for more details.

OpenSees was compiled and run on a Linux platform running on a Dell 1 GHz machine. Owing to the complexity and number of calculations involved, complete parametric studies took several weeks to run. One dynamic analysis (single bridge, single ground motion record) runs in approximately 8 minutes.

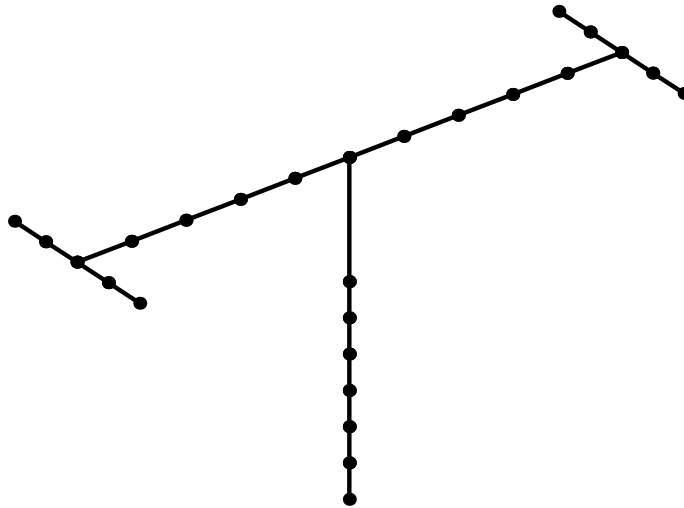


**Fig. Appendix C.1 Sample finite element bridge model**

The structure of a complete OpenSees analysis is contained in a file named Parameters.tcl. This file takes parameter information from a specified text file, and loops over all parameter variations in the file until complete. Each parameter group was sent through a static analysis (ModelS.tcl), a dynamic analysis (ModelD.tcl), and a data combination routine (Combine.tcl). Here is a sample line from the parameter input file:

```
# options: param_num directory skew L LoH fy fc rho DcDs soil wt rho_t deck abut ida
#
# BASE BRIDGE
001 ../motion/iLMSR/ 0 720 2.4 68.0 5.0 0.02 0.75 B 0.10 0.007 0 2 1
```

## **APPENDIX C.2 PRE-PROCESSING**

The only pre-processing required for the analyses was for the ground motions. The following is a description of how to pre-process the ground motions for use with the OpenSees model (note, filenames and command line usage shown in *italics*):

1. Download the ground motions (3 components always) from PEER strong motion database [PEER Strong Motion Catalog]. The three components normally correspond to fault-normal,

fault-parallel, and vertical directions, or some permutation of this combination. Filenames should be of the form \*.AT2.

2. From the directory containing the downloaded ground motions desired run:

```
cnv *.AT2
```

or `cnv` (read from file “*indir*”; see below)

This creates two files for every ground motion file present. The \*.*data* file is simply the record written as a single-column format, with all of the text header information stripped out. The \*.*info* file pulls the pertinent information out of the header such as *dt* (time step size), number of points, and an assigned number in the directory. After the \*.*data* and \*.*info* files have been created, the original \*.AT2 files can be removed to save space.

Note, if after running *index* (step 3) below, the number of earthquakes (1 earthquake=3 components mentioned above) does not agree with the number of files divided by 3, (ie 225 files means there should be 75 earthquake numbers output from *index*) then the files are not being input in the correct order to *cnv* in step 2. To correct the problem, do this:

```
ls *.AT2 > indir
cnv
```

The new *indir* file will contain the correct order of files and running *cnv* without any arguments defaults to reading from the file named *indir*.

3. From the same directory run:

```
index
```

This creates a file named *Index.tcl* that lists the filename roots of each of the earthquake triplets as well as their assigned number from part 2. Check to see whether the number of earthquakes = total files/3, (see Note above). If not, repeat part 2 using the *indir* file method.

4. Copy the Matlab file *filterup.m* into the directory with the files. Then run this Matlab script to resample the frequency of the ground motions. Usually they are on the order of *dt*=0.005 or *dt*=0.01. To save computation time for the range of periods concerned with this model, they can be sampled down to *dt*=0.02. To run the script:

```
cp filterup.m directory_name
matlab
filterup
```

This script automatically overwrites the old files, so if you do not want resampling, do not run this script. After this step, you can delete the non *\*.info* and *\*.data* files from the directory.

5. To add other ground motion information specified in the Silva database [PEER Strong Motion Catalog] but which is not included in the file headers, you must prepare the list yourself and save the results to a text file. This information can then be incorporated into the *\*.info* files using the program *im*.

From the same directory, run:

```
im OUR_records.txt
```

or:

```
../im ../OUR_records.txt
```

if you do not want to copy the files around from directory to directory. The format for the text file is:

```
!KEY M R PGA1 PGA2 PGA3 PGV1 PGV2 PGV3 PGD1 PGD2 PGD3
```

The directions used inside the OpenSees models are:

direction 1 (x-axis): fault normal - specified 2nd in Index.tcl

direction 2 (y-axis): fault parallel - specified 1st in Index.tcl

direction 3 (z-axis): vertical - specified 3rd in Index.tcl

!KEY is the code for the ground motion used in *Index.tcl* (ie. AGW000), without the three digit record orientation information (ie. AGW). It is not necessary to complete all the *PGA* (peak ground acceleration), *PGV* (peak ground velocity), and *PGD* (peak ground displacement) records with actual information, as the program will compute these values accurately on the fly. However, data placeholders must be present. Less than 12 columns of data for each line in the file will generate an error.

6. From the OpenSees *Parameters.tcl* input file, specify the directory where the *Index.tcl* file is located. It will load motion information from corresponding *\*.data* files and add the *\*.info* data to the summary files.

## APPENDIX C.3 ANALYSIS DESCRIPTION

### Appendix C.3.1 Static Analysis

Static analysis is controlled by the *ModelS.tcl* input file. Below is the Tcl skeleton of this file:

```
# ModelS.tcl: generic input shell for use with all static models
# Units: kip, in
# Kevin Mackie, 2001/02/01
# mackie@ce.berkeley.edu
#
# Takes structural input parameters from higher
# level procedure and outputs data to files for computation of yield
# quantities (displacement, curvature, etc).
# Performs static pushovers only.

proc ModelS {param_group directory skew L LoH fy fc rho_s DcDs ksoil wt rhos_trans deck abut ida}
{

set gap_in 100

# -----
# Perform the pushover analysis for yield condition data
# Load displacement only
# Longitudinal Direction only

source GenerateBridge.tcl
GenerateBridge $skew $L $LoH $fy $fc $rho_s $DcDs $ksoil $wt $rhos_trans $deck $gap_in $abut

set fstub [format "s1%04i" $param_group]

# Record top of column
recorder Node [format "%snd081.out" $fstub] disp -load -node 8 -dof 1

# Record section deformations in columns
recorder Element 1 -file [format "%ssf011.out" $fstub] section 1 forces
recorder Element 1 -file [format "%ssd011.out" $fstub] section 1 deformations
```

```

# Record section deformations in left pile shafts
recorder Element 20 -file [format "%ssf201.out" $fstub] section 1 forces
recorder Element 20 -file [format "%ssd201.out" $fstub] section 1 deformations

# Record deck movement at abutments
recorder Node [format "%snd031.out" $fstub] disp -load -node 3 -dof 1 2 3
recorder Node [format "%snd131.out" $fstub] disp -load -node 13 -dof 1 2 3

# Record left gap properties
recorder Element 40 -file [format "%sef401.out" $fstub] forces
recorder Element 40 -file [format "%sed401.out" $fstub] deformations

# Reference lateral loads
pattern Plain 5 Linear {
  #   node  FX   FY   FZ   MX   MY   MZ
  load   8   1.0  0.0  0.0  0.0  0.0  0.0
}

# Load control with variable load steps
#           init  Jd   min  max
integrator LoadControl 10.0  3   5.0 10.0

# continue up linear path with load control
analysis Static
analyze 50

# change integrator for displacement monitoring
#           node dof  dU1  Jd  minLam  maxLam
integrator DisplacementControl  8  1  0.1  3   0.05  0.1

# Perform the pushover analysis until failure
while { $static_slope > -0.1 && $static_cnt < 800 } {
  set res [analyze 1]
  if {$res < 0} {
    puts "Pushover analysis failed\n"
    set static_slope -10;
  }
  incr static_cnt
}

puts "Finished longitudinal pushover analysis..."

# -----

```

```

# Perform the pushover analysis for yield condition data
# Transverse Direction only

source GenerateBridge.tcl
GenerateBridge $skew $L $LoH $fy $fc $rho_s $DcDs $ksoil $swt $rhos_trans $deck $gap_in $abut

set fstub [format "st%04i" $param_group]

# Record top of column
recorder Node [format "%snd082.out" $fstub] disp -load -node 8 -dof 2

# Record deck movement at abutments
recorder Node [format "%snd031.out" $fstub] disp -load -node 3 -dof 1 2 3
recorder Node [format "%snd131.out" $fstub] disp -load -node 13 -dof 1 2 3

# Record section deformations in columns
recorder Element 1 -file [format "%ssf011.out" $fstub] section 1 forces
recorder Element 1 -file [format "%ssd011.out" $fstub] section 1 deformations

# Record left gap properties
recorder Element 40 -file [format "%sef401.out" $fstub] forces
recorder Element 40 -file [format "%sed401.out" $fstub] deformations

# Reference lateral loads
pattern Plain 5 Linear {
  #   node FX   FY   FZ   MX   MY   MZ
  load 8   0.0  1.0  0.0  0.0  0.0  0.0
}

# Load control with variable load steps
#
#           init  Jd   min  max
integrator LoadControl 10.0 3 5.0 10.0

# continue up linear path with load control
analysis Static
analyze 50

# change integrator for displacement monitoring
#
#           node dof  dU1  Jd  minLam  maxLam
integrator DisplacementControl 8 2 0.1 3 0.05 0.1

# Perform the pushover analysis under dynamic monitoring of failure
while { $static_slope > -0.1 && $static_cnt < 800 } {

```

```

set res [analyze 1]
if {$res < 0} {
    puts "Pushover analysis failed\n"
    set static_slope -10;
}
incr static_cnt
}

puts "Finished transverse pushover analysis..."

# -----
# Analyze data files for yield information
source AnalysisS.tcl
AnalysisS $skew $L $LoH $fy $fc $rho_s $DcDs $ksoil $wt $rhos_trans $param_group

# -----
# remove static recorder files to save space
set fstub [format "s1%04i" $param_group]
file delete [format "%snd031.out" $fstub]

}

```

### ***Appendix C.3.2 Modal and Dynamic Analysis***

Modal analysis is the first step controlled by the dynamic analysis control file (*ModelD.tcl*). The actual transient analyses are performed for all ground motions and bridge instantiations, as controlled by *ModelD.tcl*. The computation time required was somewhat reduced by reducing the dynamic time step to 0.02 seconds as described in Chapter 2. Below is the Tcl skeleton of this file:

```

# ModelD.tcl: generic input shell for use with dynamic models
# Units: kip, in
# Kevin Mackie, 2001/08/01
# mackie@ce.berkeley.edu
#
# Takes ground motion and structural input parameters from higher
# level procedure and outputs data to files for computation of UCSD
# output quantities. Performs dynamic excitation and modal analysis only
# Returns period information.

proc ModelD {param_group directory sf skew L LoH fy fc rho_s DcDs ksoil wt rhos_trans deck abut
ida} {

```

```

# -----
# set up earthquake files and parameters

set indxfile [open [format "%sIndex.tcl" $directory] "r"]
set total_eqks 0
while {-1 != [gets $indxfile line] } {
    set total_eqks [expr $total_eqks+1]
    scan $line "%s %s %s" eqk_fp($total_eqks) eqk_fn($total_eqks) eqk_fv($total_eqks)
}
close $indxfile

# -----
# begin loop of analysis for each ground motion triplet above
for {set loop_var 1} {$loop_var<=$total_eqks} {incr loop_var} {

puts "Parameter group $param_group: EQ $eqk_fv($loop_var)"

# ground motion data for this run (they must have corresponding dt vals)
set fp [format "%s%s.AT2" $directory $eqk_fp($loop_var)]
set fn [format "%s%s.AT2" $directory $eqk_fn($loop_var)]
set fv [format "%s%s.AT2" $directory $eqk_fv($loop_var)]

# -----
# iterate with increasing intensity if ida=1

source Transient.tcl
if { $ida == 1 } {
    # perform ida before moving onto next record
    while { $ida_stop==0 } {
        puts "    Intensity level: $ida_level"
        set Tret [Transient $param_group $skew $L $LoH $fy $fc $rho_s $DcDs $ksoil $wt $rhos_trans
$deck $abut $ida $ida_level $ida_cnt $fn $fp $fv]

        set ida_level [expr $ida_level+$ida_incr]
        set ida_cnt [expr $ida_cnt + 1]
        if { $ida_level > $IDAMAX } {
            set ida_stop 1
        }
    }
} else {
    # just perform a single transient analysis for this record
    # all record scaled by factor of sf (2 usually)

```

```

    set Tret [Transient $param_group $skew $L $LoH $fy $fc $rho_s $DcDs $ksoil $wt $rhos_trans
$deck $abut $ida $sf $ida_cnt $fn $fp $fv]
}
}
return $Tret
}

```

The interim file sourced is *Transient.tcl* that actually performs the modal and dynamic analyses.

The Tcl skeleton of this file is as follows:

```

# Transient.tcl: sets up and runs arbitrary transient run
# Units: kip, in
# Kevin Mackie, 2001/06/06
# mackie@ce.berkeley.edu
#
# Takes all parameters from ModelD.tcl and runs transient analysis.
# Allows multiple runs on same record as required for IDA
# Performs Earthquake excitation transient analysis

proc Transient {param_group skew L LoH fy fc rho_s DcDs ksoil wt rhos_trans deck abut ida level
ida_cnt fn fp fv} {

# load ground motion data parameters
set file [open [format "%s.info" $fn] "r"]
scan $line "%i %lf %u" points dt eqk_num
close $file

set filen [format "%s.data" $fn]
set filep [format "%s.data" $fp]
set filev [format "%s.data" $fv]

# -----
# Perform eigen analysis (initial stiffness)

source GenerateBridge.tcl
GenerateBridge $skew $L $LoH $fy $fc $rho_s $DcDs $ksoil $wt $rhos_trans $deck $gap_in $abut

# perform eigenvalue analysis for first two modes
set eigenvalues [eigen 5]
set omega1 [lindex $eigenvalues 0]
set omega2 [lindex $eigenvalues 1]

# -----

```

```

# Perform Earthquake excitation transient analysis

GenerateBridge $skew $L $LoH $fy $fc $rho_s $DcDs $ksoil $wt $rhos_trans $deck $gap_in $abut

# Create a recorder which writes to output
recorder Node [format "%snd08.out" $fstub] disp -time -node 8 -dof 1 2 3

# Record section deformations at the left column
recorder Element 1 -file [format "%ssf011.out" $fstub] section 1 forces
recorder Element 1 -file [format "%ssd011.out" $fstub] section 1 deformations

# Record corresponding rotations for energy calculations
recorder Node [format "%snr011.out" $fstub] disp -node 1 -dof 4 5 6

# Record left gap properties
recorder Element 40 -file [format "%sef401.out" $fstub] forces
recorder Element 40 -file [format "%sed401.out" $fstub] deformations

# Record fiber stress and strain at max location
for {set i 20} {$i < $conc_fibers} {incr i} {
recorder Element 1 -file [format "%sffc%03i.out" $fstub $i] section 5 fiber $i stress
recorder Element 1 -file [format "%sfdc%03i.out" $fstub $i] section 5 fiber $i strain
}

# Record fiber stress and strain at max location
for {set i $conc_fibers} {$i < $conc_fibers+$steel_fibers} {incr i} {
recorder Element 1 -file [format "%sffs%03i.out" $fstub $i] section 5 fiber $i stress
recorder Element 1 -file [format "%sfds%03i.out" $fstub $i] section 5 fiber $i strain
}

# define earthquakes      filename      dt          factor
set path1 "Path -filePath $filen -dt $dt -factor [expr $g*$level]"
set path2 "Path -filePath $filep -dt $dt -factor [expr $g*$level]"
set path3 "Path -filePath $filev -dt $dt -factor [expr $g*$level]"

#
tag dir
pattern UniformExcitation 2 1 -accel $path1
pattern UniformExcitation 3 2 -accel $path2
pattern UniformExcitation 4 3 -accel $path3

# Rayleigh damping for first 2 modes assuming 2% viscous damping
# C = alphaM * M + betaK * Kcurrent + betaKi * Kinit + betaKc * Kcommit
#
gamma beta alphaM betaK

```

```

integrator Newmark 0.5 0.25 $alphaM 0.0 0.0 $betaK

analysis Transient
set res [analyze [expr $points+25] $dt]
if {$res < 0} {
    puts "Dynamic analysis failed\n"
}

# -----
# Perform eigen analysis (post earthquake stiffness)

# perform eigenvalue analysis for first two modes
set eigenvalues [eigen 5]
set omega1dmg [lindex $eigenvalues 0]
set omega2dmg [lindex $eigenvalues 1]

# -----
# Analyze data to extract displacement/force information
source AnalysisD.tcl
AnalysisD $skew $L $LoH $fy $fc $rho_s $DcDs $ksoil $wt $rhos_trans $eqk_num $param_group $ida
$ida_cnt

# append ground motion specific data, ie Sd, Sa, etc
# using program cdm which uses central difference to compute
# spectral response quantities, generates information which is
# added to ground motion .info files
set Treturn "$Tn1 $Tn2 $Tn1dmg $Tn2dmg"

set imanaly "/home/mackie/motion/imcdm"
# note fp in 2 dir : fn in 1 dir : fv in 3 dir
exec $imanaly $fn 1 $Tn1 $Tn2 $level $Tn1dmg $Tn2dmg
exec $imanaly $fp 2 $Tn1 $Tn2 $level $Tn1dmg $Tn2dmg
exec $imanaly $fv 3 $Tn1 $Tn2 $level $Tn1dmg $Tn2dmg

# end of analysis
# -----

# -----
# remove dynamic recorder files to save space
file delete [format "%snd08.out" $fstub]

return $Treturn
}

```

## APPENDIX C.4 POST-PROCESSING

Post-processing was required to complete the process of generating demand models relating intensity measures (IM) to engineering demand parameters (EDP). The *Combine.tcl* function takes all of the post-processed information from both the static and dynamic routines and combines them along with other required IMs and other data. To facilitate this, several C routines are called which take the intensity level desired and output an array of IMs directly related to the period and intensity of interest.

### *Appendix C.4.1 IMCDM*

```
// Kevin Mackie, 2001/06/11
// mackie@ce.berkeley.edu
//
// Generates Intensity Measures from ground motion files for use with OpenSees
// Front end to the intensity measure engines. Takes specific ground
// motion files from the Tcl scripts and adds IM's to *.AT2.info files by
// way of im_analysis. Allows for dynamic scaling of records and variable
// periods.
//
// INPUT : file - ground motion file in format *.AT2
//         dirs - direction applied in (fn_1, fp_2, fv_3)
//              note though that fp is the lowest # in the index file
//         T1, T2 - 1st and 2nd mode periods for spectral quantities
//         sf - scale factor on ground motion
//         <T1dmg, T2dmg> - optional post earthquake periods
// OUTPUT : none
//
// spawns im_analysis.c
//
// to compile: cc -lm imcdm.c -o imcdm
// to run: imcdm ../motion/LMSR/LOS270.AT2 1 0.56 0.28 2.5
```

### *Appendix C.4.2 IM*

```
// Kevin Mackie, 2001/06/11
// mackie@ce.berkeley.edu
//
```

```

// Generates Intensity Measures from ground motion files for use with OpenSees
// Looks for ground motion information file in
// path specified in command line, usually named OUR_records.txt
// which has the following header format:
//      !KEY M R PGA1 PGA2 PGA3 PGV1 PGV2 PGV3 PGD1 PGD2 PGD3
// Will only operate in directories where the Index.tcl file has already
// been created. It adds information from information_file to each of the
// *.AT2.info files indexed in Index.tcl.
//
// INPUT  : Info_File - full path to information file described above
// OUTPUT : none (adds information to *.AT2.info files)
//
// spawns im_analysis.c
//
// to compile: cc -lm im.c -o im
// to run: im information_file

```

### ***Appendix C.4.3      SPECTRAL***

```

// Kevin Mackie, 2001/06/11
// mackie@ce.berkeley.edu
//
// Generates Intensity Measures from ground motion files for use with OpenSees
// Front end to spectral analysis using the central difference method.
// This routine simply prepares file for use and maintains back
// compatibility with older Tcl scripts by outputting Sd to a file:
//      "f%04isum_motion.out" <- eqk_num
//
// INPUT  : motion - filename to be processed in format *.AT2
//          T - period of interest//          damping - percent damping
//          [scale] optional - scale factor on ground motion
//          [fy] optional - yield strength of inelastic system
// OUTPUT : none (generate output file, see above)
//
// spawns cdm.c
//
// to compile: cc -lm spectral.c -o spectral

```

## Appendix D Visualization

### APPENDIX D.1 DATA VISUALIZATION

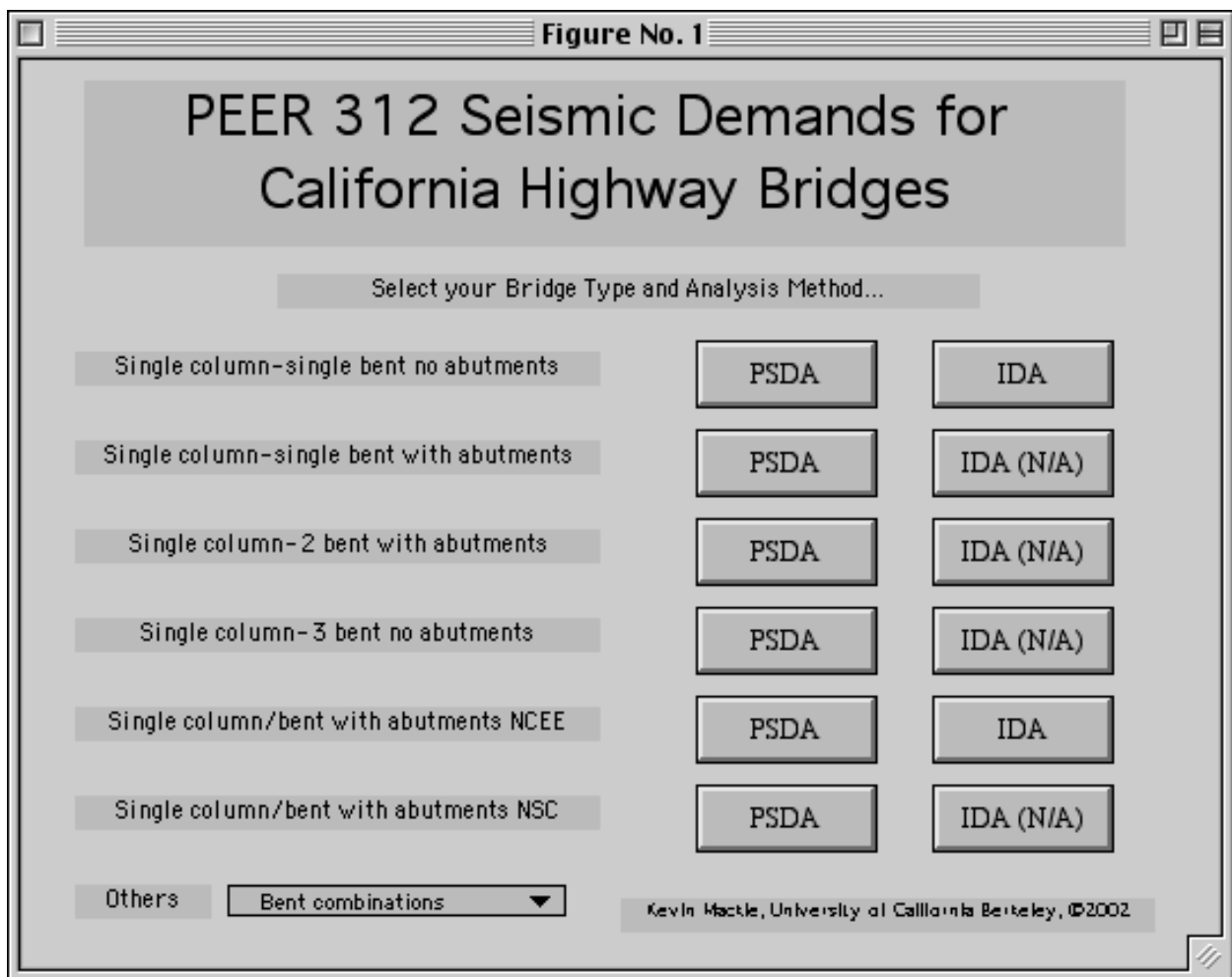


Fig. Appendix D.1 Initial screen from *Demand.m* for running all PSDMs

All of the following information is necessary for understanding the procedures used to plot the IM-EDP information for use in all PSDMs presented in this report. Data and Matlab files can be obtained from [http://peer.berkeley.edu/Products/PEERReports/reports-2003/0316\\_appCD.html](http://peer.berkeley.edu/Products/PEERReports/reports-2003/0316_appCD.html). Without modification, they can be used by starting the Matlab routine “Demand.” Functionality of this front end is described hereafter. The initial bridge geometry configuration and analysis method is selected from the available options on the opening screen (Fig. Appendix D.1).

The following is an example database file containing all the IM-EDP information for one bridge and ground motion analysis. First column data information is always first mode, while second column is second mode specific, if appropriate.

Axial load ratio	0.0444623333083
Yield disp. long.	4.0325021682
Yield curv. long.	0.000111550667782
Yield disp. trans.	5.53392109481
Yield curv. trans.	0.000112368285729
Capacity Cy long.	392.808845453
Capacity Cy trans.	394.722340908
Max_displ. in x	0.846877
Max_displ. in y	0.499815
Drift in x	0.282292333333
Drift in y	0.166605
Max_curv in long.	1.88862e-05
Max_curv in trans.	6.44566e-06
Max_moment in long.	84629.5
Max_moment in trans.	33473.2
Max steel strain	0.000933354
Max conc strain	0.00057912
Max steel stress	27.0673
Max conc stress	2.47638
residual in x	0.0243031
residual in y	0.0409245
Hysteretic energy ln.	3740.11077536
Hysteretic energy tr.	382.005859815
R (cs) long.	0.438237753644
R (cs) tran.	0.62007112188
disp. ductility long.	0.210012782306
curv. ductility long.	0.169306023671
disp. ductility tran.	0.0903184182494
curv. ductility tran.	0.0573619145134
RDI long.	0.00602680395107
RDI tran.	0.00739520844242
theta_px	0
theta_py	0
Duration	40.0
Magnitude	6.5
Distance	54.1
Strong motion durat.	18.68
PGA in x-dir	0.320
PGA in y-dir	0.233
PGA in z-dir	0.102
PGV in x-dir	16.4
PGV in y-dir	13.0
PGV in z-dir	3.1
PGD in x-dir	2.1
PGD in y-dir	3.7
PGD in z-dir	1.4

Vibration periods	0.65	0.56
Sa(T1, T2) in x-dir	255.50	325.95
Sa(T1, T2) in y-dir	144.52	143.37
Sa(T1, T2) in z-dir	57.44	40.93
Sv(T1, T2) in x-dir	26.370	29.161
Sv(T1, T2) in y-dir	14.916	12.827
Sv(T1, T2) in z-dir	5.928	3.662
Sd(T1, T2) in x-dir	2.722	2.609
Sd(T1, T2) in y-dir	1.539	1.148
Sd(T1, T2) in z-dir	0.612	0.328
Sd,in(T1, T2) x-dir	2.631	3.626
Sd,in(T1, T2) y-dir	1.830	2.069
Sd,in(T1, T2) z-dir	0.649	0.328
Arias Intensity x-dir	97.31	
Arias Intensity y-dir	77.78	
Arias Intensity z-dir	17.13	
Vel. Intensity x-dir	14.24	
Vel. Intensity y-dir	17.63	
Vel. Intensity z-dir	8.98	
Cum. Abs. Vel. x-dir	907.01	
Cum. Abs. Vel. y-dir	869.82	
Cum. Abs. Vel. z-dir	430.57	
Cum. Abs. Disp. x-dir	63.77	
Cum. Abs. Disp. y-dir	63.09	
Cum. Abs. Disp. z-dir	25.49	
RMS accel. x-dir	52.36	
RMS accel. y-dir	44.67	
RMS accel. z-dir	22.33	
Charact. Int. x-dir	1637.87	
Charact. Int. y-dir	1290.45	
Charact. Int. z-dir	456.08	
Freq. Ratio One x-dir	0.052	
Freq. Ratio One y-dir	0.057	
Freq. Ratio One z-dir	0.031	
Freq. Ratio Two x-dir	0.126	
Freq. Ratio Two y-dir	0.282	
Freq. Ratio Two z-dir	0.456	

Files such as these are then processed using the Matlab routine *ConvertFiles.m*. This routine converts the text formatted files into Matlab binary files to facilitate plotting speeds. Typically these files are all stored in a folder named *summary* in the *PlotUtil* directory. The resulting binary files are stored in a folder named *summary.mat*. In order for the plotting routine to recognize the type and name of the data to be plotted from the file, it is necessary to tell the routine named *LoadVals.m* what the order of data in the file is. This is accomplished using a 36-column array. The first 35 characters are the IM or EDP name, followed by a 0, 1, or 2. Entering a 0 groups the data line as an IM, a 1 groups the line as an EDP. A line of data not desired for plotting can be ignored by suffixing with a 2. Sample lines from the *LoadVals.m* file are shown below:

```
'Yield Energy Transverse           2';
'Maximum Displacement Longitudinal 1';
'R factor (CS) Longitudinal        0';
```

The plotting routines allow the investigation of PSDMs from both PSDA and IDA. However, it is necessary to call one or the other from the command line. To commence plotting

manually, enter either *PSDMplot* or *IDAplot*. Alternatively, these can be reached using *Demand.m*. See Figure Appendix D.2 for a screen shot of the PSDM plotting window. All *LoadVal* entries with a 0 will appear in the IM pop-up menu. All entries with a 1 will appear in the EDP pop-up menu. The user selects the IM for y-axis and EDP for x-axis, then decides whether to compare the effect of design parameters (“Parameters” pop-up) or bins of earthquakes (“Seismicity” pop-up). If “Parameters” is selected, the specific design parameter to vary can be chosen. The seismicity option uses the same subset of data points. A fit in log-log space will be made to each series of data points. The parameter plot attempts a bilinear or linear (“Fit-type” pop-up) fit, while the seismicity plots attempts a single linear fit. The Matlab window will print corresponding slope and origin values of the linear fits. It also prints out the dispersion of the data.

Further functionality is provided to analyze results from both probabilistic seismic demand analysis (PSDA), as well as incremental dynamic analysis (IDA). All the same plots are available except the “Bin Dependence” plot. This is subsequently replaced by a Typical IDA pushover curve. The program can also generate plots to indicate various statistically dependent behaviors. For the dependence of design parameter variations on the selection of bins, choose (“Bin Dependence” pop-up). All of the same colored lines (parameters are of the same value) should have a similar slope to be independent of the bin used. Further, magnitude, distance, and duration (sufficiency) dependence can be seen from the residual plots (“M Dependence,” “R Dependence,” or “Durnt Dependence” pop-ups). These plots show residuals of the EDP from the fit in log space. The dependent variable ( $M$ ,  $R$ ) is plotted in linear space.

Finally, structural demand hazard curves can be generated for any PSDM using  $S_a$  as the IM. Notice that the hazard is taken from the USGS hazard maps for the Berkeley area, this can be changed in the function *GetHazard.m*. Also notice that this feature makes no sense if a non- $S_a$  IM is selected.

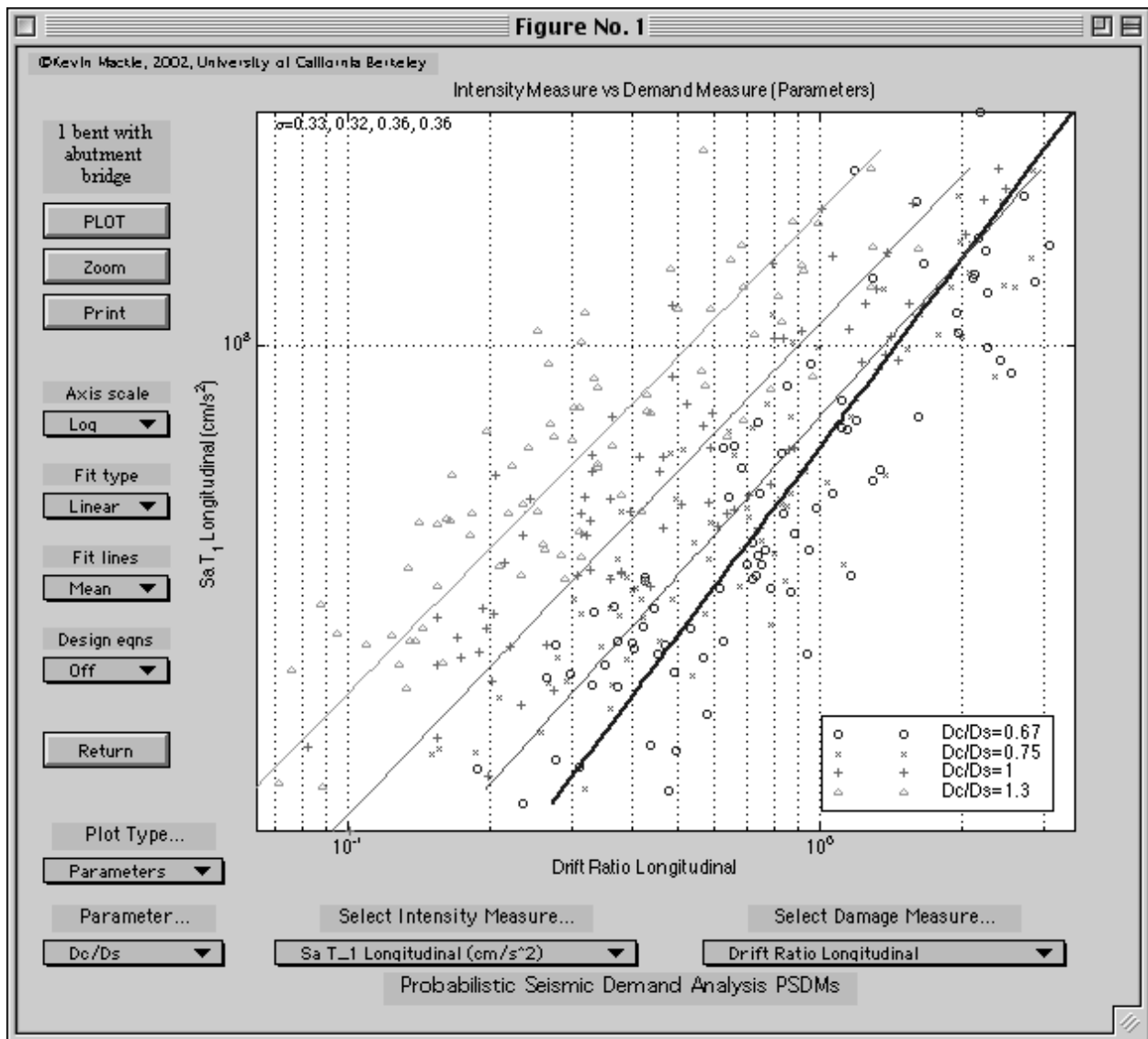


**Fig. Appendix D.2 PSDM plotting window**

Sample results printed to Matlab window from Seismicity and Parameter plots (bilinear):

```
Fits = (fits for ln(EDP)=A + B ln(IM) )
      [B1]    [A1]    [B2]    [A2]
      0.9235  -5.8730  -2.3663  17.9531
      0.4866  -3.4804   0.9283  -5.8810
      2.7567 -14.5064   0.9288  -5.7314
      2.4890 -12.1508   0.8957  -5.2269

Dispersion =
      0.3586  0.2963  0.3660  0.3003
```

For example, read off the IM, like spectral acceleration=500 cm/s<sup>2</sup> from the plot, then Eq. Appendix D.1. would give you ln(EDP)=0.34, or take  $e^{0.34}=1.40$  to find the EDP (like drift ratio)

from the linear fit. Therefore, for the model selected, an earthquake with an intensity of  $Sa_{TI}=500 \text{ cm/s}^2$  would give you a drift ratio demand of 1.4%.

$$-5.2269 + 0.8957 \cdot \ln(500) = 0.3395 \quad (\text{Appendix D.1})$$

Any of the above plots can be printed directly to a postscript file for insertion into documents using the “Print” button. Different scales can also be investigated with “Axis scale” pop-up. The default plotting option will just produce the median fit lines for each IM-DM pair. However, you can easily add the plus- and minus-one sigma distribution stripes by using the “Fit lines” pop-up.

A further feature available is the ability to generate design equations in the form of Eq. 3.2. Use the “Design equations” pop-up to turn on this feature. NOTE: this only makes sense for *period-independent* IMs, such as Arias intensity. The design equations cannot account for implicit period shifts due to design parameter variations. Therefore, you cannot apply this option to such IMs as  $Sd$  and  $Sa$ . With this noted, once the design equation feature is on, selecting PLOT will prompt you for a design parameter value. This is the design parameter for which you want to generate a specific design equation. Note that Matlab will also generate the general design equation with design parameter variables as well as this specific one. For example, for the  $D_o/D_s$  parameter, you could obtain a design equation for  $D_o/D_s = 1.15$ , which is not explicitly plotted as part of the currently available data.

Sample for bilinear  $D_o/D_s$  IM-EDP plot:

```
A{1}=-28.338*x^2+44.957*x^1-20.686*x^0
B{1}=+9.636*x^2-16.004*x^1+7.016*x^0
```

```
A{2}=+13.933*x^2-22.475*x^1+1.029*x^0
B{2}=-2.738*x^2+4.084*x^1-0.056*x^0
```

```
Design_Equation{1} =
```

```
log(EDP)=-6.462+1.355*log(IM)
```

```
Design_Equation{2} =
```

```
log(EDP)=-6.391+1.020*log(IM)
```

The  $A\{1\}$ ,  $B\{1\}$  are the coefficients for the first linear fit in the bilinear fit, and so on for  $A\{2\}$ ,  $B\{2\}$ . The variable  $x$  is for the current design parameter. The *Design\_Equation{1}* formula is for

the first linear fit at the given (eg  $x=1.15$ ) design value, already in equation form. Note that Matlab's use of log is for base  $e$ , not base 10.

The program also outputs a new set of plots from which it generated the design equation. The top plot shows information for generation of the  $A$  coefficient, the bottom plot for  $B$ . For the  $A$  plot,  $x$ 's indicate known data, pentagrams indicate the calculated fit. For the  $B$  plot,  $o$ 's indicate known data, pentagrams the calculated fit. This plot is provided for the case when the data is highly irregular and it is uncertain whether the design equation correctly captured the appropriate behavior.

## APPENDIX D.2 MODEL VISUALIZATION

Following data recombination, Tcl routines also output a fully functional OpenSees bridge model. The distinct difference being all the bridge models used for analysis are completely parametric (the models use variables only). This de-parameterized file can be used with post-processing programs such as OSP [Chadwell] to plot bridge geometry, mode shapes, displacement response, etc. These can be used to verify the assumption of longitudinal modes being fundamental and transverse modes secondary. The sample mechanism for converting parameterized files to use with such programs is as follows:

```
PrintOut $params $dir $skew $L $LoH $fy $fc $r_s $Dcs $k $wt $r_t $deck $abut $ida $gap
```

Where the *PrintOut.tcl* skeleton is:

```
# PrintOut.tcl: generates Tcl file for model with all values inserted
# Heinz Kuo, 2001/11/24
# schwmmr1@uclink4.berkeley.edu
#
# Reads the GenerateBridge.tcl script and generates the bridge
# model in a single file with all values inserted so that it may
# be ported for other uses (ie OSP)

# This program requires that GenerateBridge.tcl use the following format:
#
# 1. No comments may be made on the same line as a command
# 2. All if, elseif, else, and statements ending with ";" shall made on different lines
#    and follow the formatting:
#       if { test1 } {
#           body1
#       } elseif { test2 } {
#           body2
#       } else {
#           body3
#       }
# 3. Any command that uses an open curly and close curly should be written in
#    the form above. Currently,
#    only switch, ifelse, section, pattern, and proc's are supported.
```

```

# 4. No "{" and "}" may be used inside the test of the if/elseif statements
# 5. For switch statements, the pattern must be separate from the body --
# that is, it should be formatted like the following:
#     switch -- string {
#         pattern1 {
#             body1
#         }
#         pattern2 {
#             body2
#         }
#     }
# Switch statements may not be written as (one example):
#     switch -- string {
#         pattern1 {body1}
#         pattern2 {body2}
#     }
# 6. Cannot use a procedure that returns a value
# 7. Does not support foreach
# 8. Does not support switch loops within switch loops
# 9. Cannot source a file with two or more procedures in it.
# Must be written as two different files with the name of the procedure contained in it
# being exactly the same (case sensitive) as the name of the file that stores the procedure
# 10. No more than one command per line. i.e., you cannot write: set A 123; set B 456
# It must be written as:
#     set A 123
#     set B 456
proc PrintOut {params dir skew L LoH fy fc rho_s DcDs ksoil wt rhos_trans deck abut ida gap} {
}

```

Specifically developed for this project is a Matlab visualization routine named *Showbridge*. This routine accomplishes all the geometry, mode, and displacement plotting requirements of any OpenSees input file (Fig. Appendix D.3). *Showbridge* can be invoked in Matlab using the syntax:

```
Showbridge('BridgeModel0001.tcl');
```

Where the filename is any OpenSees input file you have created. The benefit being that *PrintOut.tcl* automatically generates *GenerateBridgexxxx.tcl* during all the parametric runs. Not only this, but it also generates the corresponding period and mode shape information and files to be used with *showbridge*. Corresponding mode shape files would be: *BridgeModel0001EIGENVALS.out*, *BridgeModel0001mode1.out*, *BridgeModel0001mode2.out*, and *BridgeModel0001mode3.out*.

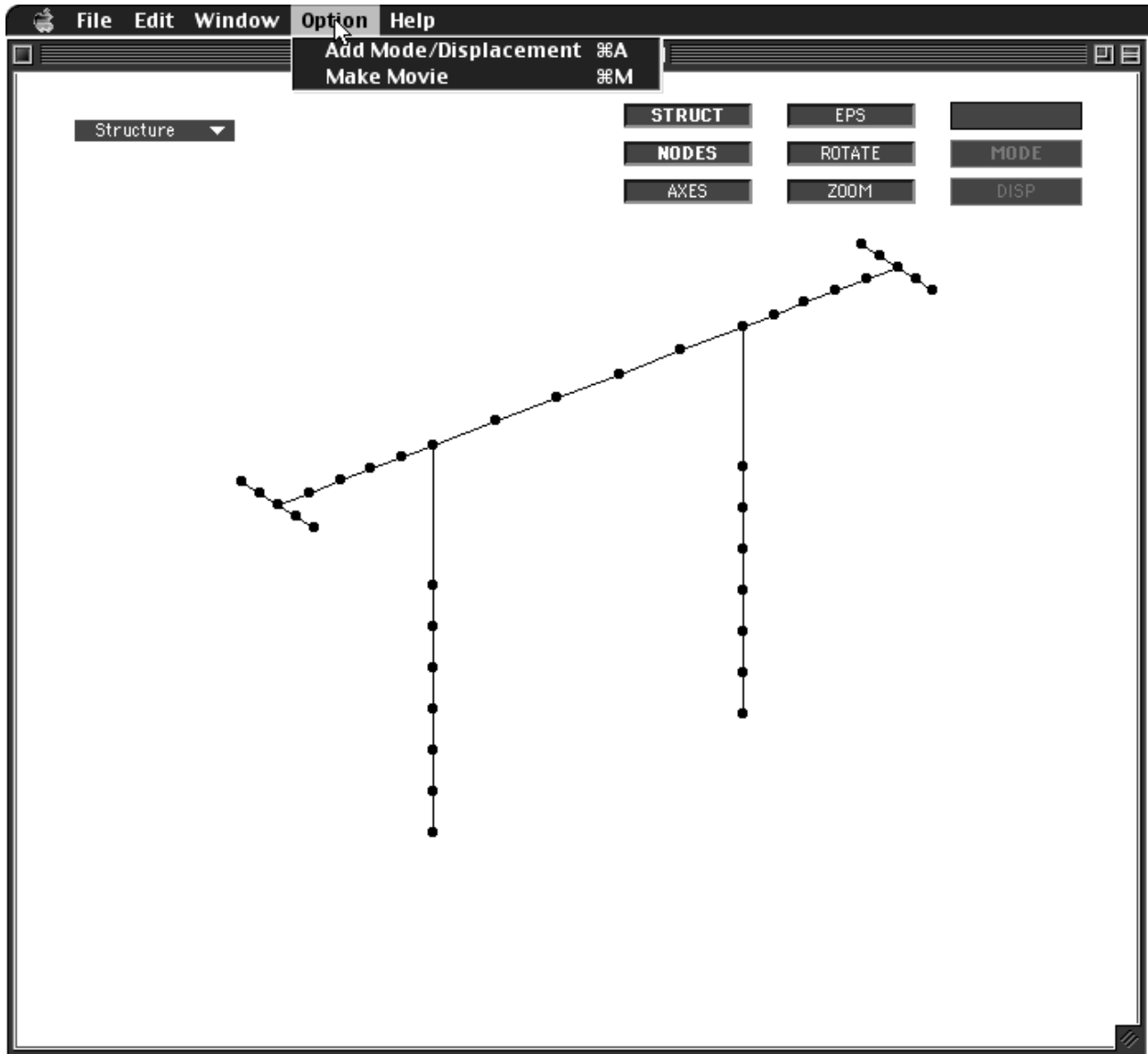


**Fig. Appendix D.3 Initial screen from *Showbridge.m* for model visualization**

The basic structure of the GUI consists of a display, the added “Option” menu, and a selection of push-buttons. When bolded, the push-button action is “on.”

- i. **STRUCT** (default on) dictates whether the (undeformed) bridge model is to be shown.
- ii. **NODES** (default off) when on, displays where the nodes are.
- iii. **AXES** (default off) when on, displays the axis.
- iv. **EPS** creates an EPS of the current plot and saves it to the working directory.
- v. **ROTATE** (default off) when on, click and hold the mouse button to rotate the axis.
- vi. **ZOOM** (default off) when on, click left button to zoom in and right button to zoom out.

vii. MODE (default on) only enabled when an eigenmode is selected. When turned off, the yellow lines depicting the mode will disappear.

viii. DISP (default off) grey dotted lines depicting the movement of the nodes from their original to deformed position are displayed.

To switch between eigenmodes, click on the pull-down menu on the top left corner and select the appropriate mode. In order to add more modes, or modify the existing ones, select the “Option” menu and select “Add Mode/Displacement.” To add a new mode, click on “Add” in the subsequent box that pops up. Fill in the information with an appropriate File and Name and press “Enter.” To modify the name, click on the appropriate mode. When the information appears, modify the appropriate information and click on “Update.” To remove a mode, select the appropriate mode and click on “Remove.” Note that this is completely general and allows for importing displacement files from any analysis, including both eigen and transient analysis.

The GUI now also contains movie-making capabilities. Select the “Option” menu and then “Make Movie.” A GUI will appear with possible modes or displacements to make a movie from. Type in the name of the output file (excluding extension) and click on “Movie.” Two scenarios exist for movie making. Mode shapes or any other static analysis with only one load step will generate an animation of increments up to this displacement. Pushover analyses or transient analyses with multiple information entries will generate a frame for each displacement entry. If the movie being made is a displacement time-history movie, you may have problems with memory. To remedy memory problems, increase the virtual memory settings on your computer.

## PEER REPORTS

PEER reports are available from the National Information Service for Earthquake Engineering (NISEE). To order PEER reports, please contact the Pacific Earthquake Engineering Research Center, 1301 South 46<sup>th</sup> Street, Richmond, California 94804-4698. Tel.: (510) 231-9468; Fax: (510) 231-9461.

- PEER 2003/16**     *Seismic Demands for Performance-Based Design of Bridges.* Kevin Mackie Božidar Stojadinović. August 2003.
- PEER 2003/14**     *Finite Element Reliability and Sensitivity Methods for Performance-Based Earthquake Engineering.* Terje Haukaas and Armen Der Kiureghian. April 2004.
- PEER 2003/13**     *Effects of Connection Hysteretic Degradation on the Seismic Behavior of Steel Moment-Resisting Frames.* Janise E. Rodgers and Stephen A. Mahin. March 2004.
- PEER 2003/12**     *Implementation Manual for the Seismic Protection of Laboratory Contents: Format and Case Studies.* William T. Holmes and Mary C. Comerio. October 2003.
- PEER 2003/11**     *Fifth U.S.-Japan Workshop on Performance-Based Earthquake Engineering Methodology for Reinforced Concrete Building Structures.* February 2004.
- PEER 2003/10**     *A Beam-Column Joint Model for Simulating the Earthquake Response of Reinforced Concrete Frames.* Laura N. Lowes, Nilanjan Mitra, and Arash Altoontash. February 2004.
- PEER 2003/09**     *Sequencing Repairs after an Earthquake: An Economic Approach.* Marco Casari and Simon J. Wilkie. April 2004.
- PEER 2003/08**     *A Technical Framework for Probability-Based Demand and Capacity Factor Design (DCFD) Seismic Formats.* Fatemeh Jalayer and C. Allin Cornell. November 2003.
- PEER 2003/07**     *Uncertainty Specification and Propagation for Loss Estimation Using FOSM Methods.* Jack W. Baker and C. Allin Cornell. September 2003.
- PEER 2003/06**     *Performance of Circular Reinforced Concrete Bridge Columns under Bidirectional Earthquake Loading.* Mahmoud M. Hachem, Stephen A. Mahin, and Jack P. Moehle. February 2003.
- PEER 2003/05**     *Response Assessment for Building-Specific Loss Estimation.* Eduardo Miranda and Shahram Taghavi. September 2003.
- PEER 2003/04**     *Experimental Assessment of Columns with Short Lap Splices Subjected to Cyclic Loads.* Murat Melek, John W. Wallace, and Joel Conte. April 2003.
- PEER 2003/03**     *Probabilistic Response Assessment for Building-Specific Loss Estimation.* Eduardo Miranda and Hesameddin Aslani. September 2003.
- PEER 2003/02**     *Software Framework for Collaborative Development of Nonlinear Dynamic Analysis Program.* Jun Peng and Kincho H. Law. September 2003.

- PEER 2003/01** *Shake Table Tests and Analytical Studies on the Gravity Load Collapse of Reinforced Concrete Frames.* Kenneth John Elwood and Jack P. Moehle. November 2003
- PEER 2002/24** *Performance of Beam to Column Bridge Joints Subjected to a Large Velocity Pulse.* Natalie Gibson, André Filiatrault, and Scott A. Ashford. April 2002.
- PEER 2002/23** *Effects of Large Velocity Pulses on Reinforced Concrete Bridge Columns.* Greg L. Orozco and Scott A. Ashford. April 2002.
- PEER 2002/22** *Characterization of Large Velocity Pulses for Laboratory Testing.* Kenneth E. Cox and Scott A. Ashford. April 2002.
- PEER 2002/21** *Fourth U.S.-Japan Workshop on Performance-Based Earthquake Engineering Methodology for Reinforced Concrete Building Structures.* December 2002.
- PEER 2002/20** *Barriers to Adoption and Implementation of PBEE Innovations.* Peter J. May. August 2002.
- PEER 2002/19** *Economic-Engineered Integrated Models for Earthquakes: Socioeconomic Impacts.* Peter Gordon, James E. Moore II, and Harry W. Richardson. July 2002.
- PEER 2002/18** *Assessment of Reinforced Concrete Building Exterior Joints with Substandard Details.* Chris P. Pantelides, Jon Hansen, Justin Nadauld, and Lawrence D. Reaveley. May 2002.
- PEER 2002/17** *Structural Characterization and Seismic Response Analysis of a Highway Overcrossing Equipped with Elastomeric Bearings and Fluid Dampers: A Case Study.* Nicos Makris and Jian Zhang. November 2002.
- PEER 2002/16** *Estimation of Uncertainty in Geotechnical Properties for Performance-Based Earthquake Engineering.* Allen L. Jones, Steven L. Kramer, and Pedro Arduino. December 2002.
- PEER 2002/15** *Seismic Behavior of Bridge Columns Subjected to Various Loading Patterns.* Asadollah Esmaeily-Gh. and Yan Xiao. December 2002.
- PEER 2002/14** *Inelastic Seismic Response of Extended Pile Shaft Supported Bridge Structures.* T.C. Hutchinson, R.W. Boulanger, Y.H. Chai, and I.M. Idriss. December 2002.
- PEER 2002/13** *Probabilistic Models and Fragility Estimates for Bridge Components and Systems.* Paolo Gardoni, Armen Der Kiureghian, and Khalid M. Mosalam. June 2002.
- PEER 2002/12** *Effects of Fault Dip and Slip Rake on Near-Source Ground Motions: Why Chi-Chi Was a Relatively Mild M7.6 Earthquake.* Brad T. Aagaard, John F. Hall, and Thomas H. Heaton. December 2002.
- PEER 2002/11** *Analytical and Experimental Study of Fiber-Reinforced Strip Isolators.* James M. Kelly and Shakhzod M. Takhirov. September 2002.
- PEER 2002/10** *Centrifuge Modeling of Settlement and Lateral Spreading with Comparisons to Numerical Analyses.* Sivapalan Gajan and Bruce L. Kutter. January 2003.

- PEER 2002/09**      *Documentation and Analysis of Field Case Histories of Seismic Compression during the 1994 Northridge, California, Earthquake.* Jonathan P. Stewart, Patrick M. Smith, Daniel H. Whang, and Jonathan D. Bray. October 2002.
- PEER 2002/08**      *Component Testing, Stability Analysis and Characterization of Buckling-Restrained Unbonded Braces<sup>TM</sup>.* Cameron Black, Nicos Makris, and Ian Aiken. September 2002.
- PEER 2002/07**      *Seismic Performance of Pile-Wharf Connections.* Charles W. Roeder, Robert Graff, Jennifer Soderstrom, and Jun Han Yoo. December 2001.
- PEER 2002/06**      *The Use of Benefit-Cost Analysis for Evaluation of Performance-Based Earthquake Engineering Decisions.* Richard O. Zerbe and Anthony Falit-Baiamonte. September 2001.
- PEER 2002/05**      *Guidelines, Specifications, and Seismic Performance Characterization of Nonstructural Building Components and Equipment.* André Filiatrault, Constantin Christopoulos, and Christopher Stearns. September 2001.
- PEER 2002/04**      *Consortium of Organizations for Strong-Motion Observation Systems and the Pacific Earthquake Engineering Research Center Lifelines Program: Invited Workshop on Archiving and Web Dissemination of Geotechnical Data, 4–5 October 2001.* September 2002.
- PEER 2002/03**      *Investigation of Sensitivity of Building Loss Estimates to Major Uncertain Variables for the Van Nuys Testbed.* Keith A. Porter, James L. Beck, and Rustem V. Shaikhutdinov. August 2002.
- PEER 2002/02**      *The Third U.S.-Japan Workshop on Performance-Based Earthquake Engineering Methodology for Reinforced Concrete Building Structures.* July 2002.
- PEER 2002/01**      *Nonstructural Loss Estimation: The UC Berkeley Case Study.* Mary C. Comerio and John C. Stallmeyer. December 2001.
- PEER 2001/16**      *Statistics of SDF-System Estimate of Roof Displacement for Pushover Analysis of Buildings.* Anil K. Chopra, Rakesh K. Goel, and Chatpan Chintanapakdee. December 2001.
- PEER 2001/15**      *Damage to Bridges during the 2001 Nisqually Earthquake.* R. Tyler Ranf, Marc O. Eberhard, and Michael P. Berry. November 2001.
- PEER 2001/14**      *Rocking Response of Equipment Anchored to a Base Foundation.* Nicos Makris and Cameron J. Black. September 2001.
- PEER 2001/13**      *Modeling Soil Liquefaction Hazards for Performance-Based Earthquake Engineering.* Steven L. Kramer and Ahmed-W. Elgamal. February 2001.
- PEER 2001/12**      *Development of Geotechnical Capabilities in OpenSees.* Boris Jeremic. September 2001.
- PEER 2001/11**      *Analytical and Experimental Study of Fiber-Reinforced Elastomeric Isolators.* James M. Kelly and Shakhzod M. Takhirov. September 2001.
- PEER 2001/10**      *Amplification Factors for Spectral Acceleration in Active Regions.* Jonathan P. Stewart, Andrew H. Liu, Yoojoong Choi, and Mehmet B. Baturay. December 2001.

- PEER 2001/09** *Ground Motion Evaluation Procedures for Performance-Based Design.* Jonathan P. Stewart, Shyh-Jeng Chiou, Jonathan D. Bray, Robert W. Graves, Paul G. Somerville, and Norman A. Abrahamson. September 2001.
- PEER 2001/08** *Experimental and Computational Evaluation of Reinforced Concrete Bridge Beam-Column Connections for Seismic Performance.* Clay J. Naito, Jack P. Moehle, and Khalid M. Mosalam. November 2001.
- PEER 2001/07** *The Rocking Spectrum and the Shortcomings of Design Guidelines.* Nicos Makris and Dimitrios Konstantinidis. August 2001.
- PEER 2001/06** *Development of an Electrical Substation Equipment Performance Database for Evaluation of Equipment Fragilities.* Thalia Agnanos. April 1999.
- PEER 2001/05** *Stiffness Analysis of Fiber-Reinforced Elastomeric Isolators.* Hsiang-Chuan Tsai and James M. Kelly. May 2001.
- PEER 2001/04** *Organizational and Societal Considerations for Performance-Based Earthquake Engineering.* Peter J. May. April 2001.
- PEER 2001/03** *A Modal Pushover Analysis Procedure to Estimate Seismic Demands for Buildings: Theory and Preliminary Evaluation.* Anil K. Chopra and Rakesh K. Goel. January 2001.
- PEER 2001/02** *Seismic Response Analysis of Highway Overcrossings Including Soil-Structure Interaction.* Jian Zhang and Nicos Makris. March 2001.
- PEER 2001/01** *Experimental Study of Large Seismic Steel Beam-to-Column Connections.* Egor P. Popov and Shakhzod M. Takhirov. November 2000.
- PEER 2000/10** *The Second U.S.-Japan Workshop on Performance-Based Earthquake Engineering Methodology for Reinforced Concrete Building Structures.* March 2000.
- PEER 2000/09** *Structural Engineering Reconnaissance of the August 17, 1999 Earthquake: Kocaeli (Izmit), Turkey.* Halil Sezen, Kenneth J. Elwood, Andrew S. Whittaker, Khalid Mosalam, John J. Wallace, and John F. Stanton. December 2000.
- PEER 2000/08** *Behavior of Reinforced Concrete Bridge Columns Having Varying Aspect Ratios and Varying Lengths of Confinement.* Anthony J. Calderone, Dawn E. Lehman, and Jack P. Moehle. January 2001.
- PEER 2000/07** *Cover-Plate and Flange-Plate Reinforced Steel Moment-Resisting Connections.* Taejin Kim, Andrew S. Whittaker, Amir S. Gilani, Vitelmo V. Bertero, and Shakhzod M. Takhirov. September 2000.
- PEER 2000/06** *Seismic Evaluation and Analysis of 230-kV Disconnect Switches.* Amir S. J. Gilani, Andrew S. Whittaker, Gregory L. Fenves, Chun-Hao Chen, Henry Ho, and Eric Fujisaki. July 2000.
- PEER 2000/05** *Performance-Based Evaluation of Exterior Reinforced Concrete Building Joints for Seismic Excitation.* Chandra Clyde, Chris P. Pantelides, and Lawrence D. Reaveley. July 2000.
- PEER 2000/04** *An Evaluation of Seismic Energy Demand: An Attenuation Approach.* Chung-Che Chou and Chia-Ming Uang. July 1999.

- PEER 2000/03** *Framing Earthquake Retrofitting Decisions: The Case of Hillside Homes in Los Angeles.* Detlof von Winterfeldt, Nels Roselund, and Alicia Kitsuse. March 2000.
- PEER 2000/02** *U.S.-Japan Workshop on the Effects of Near-Field Earthquake Shaking.* Andrew Whittaker, ed. July 2000.
- PEER 2000/01** *Further Studies on Seismic Interaction in Interconnected Electrical Substation Equipment.* Armen Der Kiureghian, Kee-Jeung Hong, and Jerome L. Sackman. November 1999.
- PEER 1999/14** *Seismic Evaluation and Retrofit of 230-kV Porcelain Transformer Bushings.* Amir S. Gilani, Andrew S. Whittaker, Gregory L. Fenves, and Eric Fujisaki. December 1999.
- PEER 1999/13** *Building Vulnerability Studies: Modeling and Evaluation of Tilt-up and Steel Reinforced Concrete Buildings.* John W. Wallace, Jonathan P. Stewart, and Andrew S. Whittaker, editors. December 1999.
- PEER 1999/12** *Rehabilitation of Nonductile RC Frame Building Using Encasement Plates and Energy-Dissipating Devices.* Mehrdad Sasani, Vitelmo V. Bertero, James C. Anderson. December 1999.
- PEER 1999/11** *Performance Evaluation Database for Concrete Bridge Components and Systems under Simulated Seismic Loads.* Yael D. Hose and Frieder Seible. November 1999.
- PEER 1999/10** *U.S.-Japan Workshop on Performance-Based Earthquake Engineering Methodology for Reinforced Concrete Building Structures.* December 1999.
- PEER 1999/09** *Performance Improvement of Long Period Building Structures Subjected to Severe Pulse-Type Ground Motions.* James C. Anderson, Vitelmo V. Bertero, and Raul Bertero. October 1999.
- PEER 1999/08** *Envelopes for Seismic Response Vectors.* Charles Menun and Armen Der Kiureghian. July 1999.
- PEER 1999/07** *Documentation of Strengths and Weaknesses of Current Computer Analysis Methods for Seismic Performance of Reinforced Concrete Members.* William F. Cofer. November 1999.
- PEER 1999/06** *Rocking Response and Overturning of Anchored Equipment under Seismic Excitations.* Nicos Makris and Jian Zhang. November 1999.
- PEER 1999/05** *Seismic Evaluation of 550 kV Porcelain Transformer Bushings.* Amir S. Gilani, Andrew S. Whittaker, Gregory L. Fenves, and Eric Fujisaki. October 1999.
- PEER 1999/04** *Adoption and Enforcement of Earthquake Risk-Reduction Measures.* Peter J. May, Raymond J. Burby, T. Jens Feeley, and Robert Wood.
- PEER 1999/03** *Task 3 Characterization of Site Response General Site Categories.* Adrian Rodriguez-Marek, Jonathan D. Bray, and Norman Abrahamson. February 1999.
- PEER 1999/02** *Capacity-Demand-Diagram Methods for Estimating Seismic Deformation of Inelastic Structures: SDF Systems.* Anil K. Chopra and Rakesh Goel. April 1999.

- PEER 1999/01** *Interaction in Interconnected Electrical Substation Equipment Subjected to Earthquake Ground Motions.* Armen Der Kiureghian, Jerome L. Sackman, and Kee-Jeung Hong. February 1999.
- PEER 1998/08** *Behavior and Failure Analysis of a Multiple-Frame Highway Bridge in the 1994 Northridge Earthquake.* Gregory L. Fenves and Michael Ellery. December 1998.
- PEER 1998/07** *Empirical Evaluation of Inertial Soil-Structure Interaction Effects.* Jonathan P. Stewart, Raymond B. Seed, and Gregory L. Fenves. November 1998.
- PEER 1998/06** *Effect of Damping Mechanisms on the Response of Seismic Isolated Structures.* Nicos Makris and Shih-Po Chang. November 1998.
- PEER 1998/05** *Rocking Response and Overturning of Equipment under Horizontal Pulse-Type Motions.* Nicos Makris and Yiannis Roussos. October 1998.
- PEER 1998/04** *Pacific Earthquake Engineering Research Invitational Workshop Proceedings, May 14–15, 1998: Defining the Links between Planning, Policy Analysis, Economics and Earthquake Engineering.* Mary Comerio and Peter Gordon. September 1998.
- PEER 1998/03** *Repair/Upgrade Procedures for Welded Beam to Column Connections.* James C. Anderson and Xiaojing Duan. May 1998.
- PEER 1998/02** *Seismic Evaluation of 196 kV Porcelain Transformer Bushings.* Amir S. Gilani, Juan W. Chavez, Gregory L. Fenves, and Andrew S. Whittaker. May 1998.
- PEER 1998/01** *Seismic Performance of Well-Confined Concrete Bridge Columns.* Dawn E. Lehman and Jack P. Moehle. December 2000.